Development of Non-Destructive Indentation Fracture Toughness Methodologies for High Strength Alloys

Case study: High strength rail steels and aluminum

by

Stephen Ifeanyi Okocha

A thesis submitted in partial fulfillment of the requirements for the degree of

Doctor of Philosophy

Department of Mechanical Engineering

University of Alberta

© Stephen Ifeanyi Okocha, 2024

Abstract

Rail derailment comprising largely from main track derailments frequently occur in the Canadian railway network. Reports have shown that some of these derailments experienced a train-initiated emergency brake application caused primarily from broken rails especially at extreme cold temperatures. These rail derailments thus require continuous monitoring of the rail structures for their integrity. However, using traditional means of estimating the structural integrity for an in-situ examination would not be feasible since samples need to be removed from existing structures. Hence, there is a desired need to adopt alternative methods for determining the structural integrity of in-service rail steels. The objective of this research project is to develop efficient, non-destructive indentation testing methodologies to establish the fracture toughness and mechanical properties of high-strength rail steels for implementation in current or potentially future technologies needed for continuous monitoring of rail infrastructures or verification of rail steel's properties. In this research project, two indentation testing methods are developed to quantify the fracture toughness of high-strength rail steels. The project can be broadly divided into two major parts.

Part I, reported in chapter 2 and 3, involves establishing the fracture toughness ($K_{IC,pred}$) of high strength rail steels using a *modified critical fracture strain model* and establishing mechanical properties of the rail steels via instrumented ball indentation test methods. 9 different rail steels were investigated to obtain the mechanical properties, which are vital parameters needed for the implementation of the *modified critical fracture strain model*. The modification to this model focused on determining the equivalent plastic fracture strain and equivalent plastic strain from tensile and indentation tests, respectively, as well as the characteristic distance needed for estimating fracture initiation. The study showed that stress triaxiality played a vital role by decreasing the ductility required to initiate fracture, which in conjunction with the prior austenite grain sizes are crucial for

establishing the characteristic distance. The $K_{IC,pred}$ defined based on the *modified critical fracture strain model* from tensile tests showed a strong correlation with K_{IC} determined from ASTM standard method. $K_{IC,pred}$ from indentation also offers the opportunity for ascertaining the fracture toughness non-destructively by focusing on the equivalent plastic strain and pressure at the tip of the indenter

In Part II, which is reported in chapter 4, 5 and 6, involved the use of both flat-end cylindrical indenter rods and spherical indenters for estimating the fracture toughness using three different indenter sizes. The 2nd method for fracture toughness estimation was based on a *modified limit load approach* using the concept of virtual load and indentation depths analysis. Critical apparent stress intensity factor via J-integral was determined by combining virtually determined J-integral in the form of an apparent stress intensity factor (K_J) and extrapolating it to zero with the contact radius to imitate a sharp crack. The first phase of Part II showed that a chamfered cylindrical indenter is preferable to a flat-ended cylindrical indenter in estimating the fracture toughness due to the lower stress singularity at the edge of the indenter. For the second phase of Part II, the study focused on investigating between the chamfered indenter and the spherical indenter since the stress constraint is continuous with increasing depth. The study showed that the *modified limit load analysis* can also be employed for spherical indenters only when the average contact pressure is replaced with hardness estimated via expansion cavity model (ECM) approach. Comparison between the chamfered indenter and spherical indenter for fracture toughness showed that spherical indenters required lower indentation depths as well as smaller plastic zone size development at the material's substrate than the chamfered indenter. For the third phase of Part II, the *modified limit load analysis* using spherical indentation is applied to rail steels.

The fracture toughness for rail steels using the *modified limit load model* via spherical indentation showed a better measurement of K_{IC} having an average value range from -2.66 – 2.51% difference

while the *modified critical strain model* approach projected an average measurement of K_{IC} range from -8.13 – 6.32% difference from the ASTM K_{IC} measurement. In the end, indentation testing offers the opportunity for ascertaining the fracture toughness of high strength rail steels thus idealizing the condition of a non-destructive testing for structural integrity assessment in the future.

Preface

This dissertation presents a comprehensive investigation into developing methodologies of using non-destructive indentation testing for fracture toughness estimation. Two distinctive methods were proposed in this research originating from the principles of contact and solid mechanics, which drives towards less complex analysis aimed for direct field application. The research conducted has culminated in the publication into two journal papers that significantly contribute to the understanding of the first approach for indentation fracture toughness estimation. The second approach, although having an additional three chapters, is still in development for future publications.

Throughout this dissertation, the integration of theoretical insights and empirical evidence aims to provide a holistic understanding of non-destructive indentation testing. Key areas from classical plasticity, theory of elasticity, small deformations and high strength materials were explored as the building blocks for the two indentation methodologies proposed in this research. The research journey has been both challenging and rewarding, requiring rigorous experimentation, extensive data analysis, and continuous refinement of methodologies. The insights attained from the non-destructive indentation testing methods detailed in these chapters of this research will particularly benefit micro-indentation testing, paving the way for more precise and less invasive evaluations of material properties of metals at microscopic levels.

I extend my deepest gratitude to my supervisors, colleagues, technicians (workshop and labs), friends and family for their unwavering support and encouragement. Their guidance and assistance has been invaluable in navigating the complexities of this research, which upheld my physical, emotional and mental state. I also acknowledge the funding bodies and institutions that provided the necessary resources to conduct this study.

This dissertation is dedicated to the relentless pursuit of knowledge and innovation in the understanding of materials and their load carrying capacities. It is my earnest hope that the knowledge gained from this research will inspire future studies both in academia and industry and lead to further improvements in non-destructive testing techniques.

Dedicated to the father, son, and the holy spirit.

Acknowledgement

First and foremost, I express my deepest gratitude to my supervisors, Drs. P-Y Ben Jar and Michael T. Hendry for their unwavering support, guidance, advice and insightful feedback throughout the journey of my doctorate. Their wealth of knowledge, expertise, support and dedication has been instrumental towards shaping my academic and personal growth.

I extend my earnest appreciation to the members of my supervisory committee and extended arm length, Zengtao Chen, James Hogan, Mustafa Gul and Benjamin Cheung, for their thoughtful suggestions, and scholarly input, which significantly enriched the quality and depth of this work. A special thanks to the staffs of the machine shop: Roger Marchand, Mitul Pater, Wade Paker, Andrew Campbell, Brent Martin, Stephen Buhlerand, Allison Probst and all those I couldn't mention their names. I am very grateful for your utmost dedication towards my career prospects in aiding my experimental specimen preparation and testing.

To the professors and academic staff at the University of Alberta, mechanical and civil engineering, whose lectures, seminars, and academic resources have provided me with a solid foundation and broadened my understanding in my field of study. Their passion for teaching and commitment to academic excellence have inspired me to strive towards this stage of my career and more in the future. Special thanks is extended to appreciation to Kevin Hodder (Ph.D.) in the Department of Chemical and Materials Engineering, University of Alberta for his support and mentorship during the metallographic specimen preparation and etching, Andre McDonald (Ph.D.) in the Department of Mechanical Engineering, University of Alberta for sharing vital information the process required for the etching process and also the technicians who helped in preparing the specimens for metallographic work.

I would like to acknowledge the non-academic staff members, including administrative personnel of mechanical and geotechnical engineering: Serena pike, Vivian Giang and Jennifer Stogowski, librarians, and IT support, whose efficiency, professionalism, and willingness to assist have facilitated the administrative aspects of my doctoral journey and ensured a conducive environment for research and learning.

I would also like to express my appreciation to the Canadian Rail Research Laboratory (CaRRL) and the University of Alberta for awarding prestigious scholarships. CaRRL is funded by the Natural Sciences and Engineering Research Council of Canada (NSERC), Canadian Pacific Railway, Canadian National Railway, the Association of American Railways – Transportation Technology Center Inc., Transport Canada and Alberta Innovates – Technology Futures.

To my friends I met from all over the world in Edmonton and Canada, the black graduate student association (BGSA), the *real ninjas 2024 group*, comprising of people from all continents of the world: John luke, Tarek, Geoffrey, Ali, Shamim, Iman, Alicia, Piotr, Amanda, Roberto, Pavan, Kanishk, Kostya, Tobby, the two Fatimas and all those I couldn't mention their names who were there before and after the pandemic period (COVID-19), I appreciate and thank you all for sticking around.

Lastly, I would like to express my sincere thanks to my family especially my mother, Anita Okocha, my elder sister and her husband, Vivian Oloruntoba and Femi Oloruntoba and my niece, Natalie Olorutoba towards their warmth encouragement towards my career and being a source of vitality and inspiration.

Table of Contents

List of Tables

List of Figures

Nomenclature

ASTM	American Society for Testing and Materials
ASM	Aerospace specification metals
CIP	Crack initiation point
CRB	Cracked round bar.
ECM	Expansion cavity model.
FE	Finite element.
HTSR	Heat-treated stress relieved
LEFM	Linear elastic fracture mechanics
MTS	Materials Test Systems
NRB	Notched round bar.
UTS	Ultimate tensile strength
VGI	Void growth index
$a_c^{'}$, $a_{c,CIP}$	Virtual NRB ligament radius and the measured contact radius at the CIP
a_c , d_c , r_c	Contact radius, diameter and radius of the unchamfered section of the indenter
$a_{c,flt}$, $a_{c,ch}$	Contact radius specifically using a non-chamfered and chamfered flat-end cylindrical indenter.
a_{cf} , h_c	Horizontal and vertical distance of the chamfered portion of the flat-end cylindrical indenter.
A_{el} , A_{pl}	Elastic and plastic area of the virtual indentation load-depth curve
C	Plastic zone size
D, d	Shoulder diameter and the ligament diameter of the NRB specimen
d_o, d_f	original and final diameter of the gauge section of the smooth tensile specimen.
*d**	Prior austenite grain size
E, E_s	Young's modulus from tensile and indentation test, respectively
Δh_e	Difference between the elastic unloading between the chamfered and non-chamfered indentation
h , $h^{'}$, $h^{''}$	Indentation depth, pre-determined offset blunting line related to J-integral, virtual indentation depth

$(h/a_c)_{CIP}$	Normalized indentation depth at CIP
J , J_e , J_p	J-integral, Elastic and plastic components of the energy per unit fracture surface area
$K_{\rho c}$, K_{JC}	Critical apparent stress intensity factor estimated via Irwin's notch analysis, and apparent stress intensity factor.
K_J, K_ρ	Stress intensity factor from J-integral via indentation and apparent fracture toughness from NRB
$K_{IC,pred(i)}$	Fracture toughness estimation using the modified critical fracture strain model
κ	Yielding constraint based on ECM and an adjusting parameter for flow curve estimation
L , L' , L_{CIP} , L_c	Indentation load, virtual indentation load, load at CIP and load at corresponding φ value
P, P_y, P_{CIP}	Indentation pressure and indentation pressure at CIP
v_s , v_i	Poisson's ratio of the specimen and indenter
η_{pl}	Plastic work factor based on specimen geometry
σ_y	Yield strength via tensile test
σ_{ys}	Yield strength estimation by indentation.
ρ	Notch root radius
K_t	Stress concentration factor
S_{max}	Maximum stiffness between the indenter and specimen
t_d	Diameter of the base tip of the chamfered diameter
β	Dimensionless correction factor
φ	critical depth needed for estimating L_c.
r^2	*Coefficient* of determination
ρ,b,t	Notch root radius, notch width, notch thickness
$\sigma_{eq}, \sigma_{eq}^f, \varepsilon_{eq}, \varepsilon_{eq}^f$	Equivalent stress &equivalent fracture stress and equivalent strain & equivalent fracture strain.
$\sigma_{eng}, \varepsilon_{eng}$	Engineering stress and Engineering strain
σ_{nom}	Nominal stress
σ_{st} , ε_{st}	Saturated stress attained via Voce Model, strain at the corresponding saturated stress.

$n_{RO(i)}$, $n_{RO(ii)}$	Strain hardening exponent for 2-stage Ramberg-Osgood's model and Hollomon's equation.
n, n_s	Strain hardening exponent via smooth tensile testing and via indentation
ε_y , ε_{pu}	Equivalent plastic strain at yield stress and UTS, respectively.
K_{HO} , K_{RO}	strain hardening co-efficient for 2-stage Ramberg-Osgood's model and Hollomon's equation.
α , β , K_T	user-defined parameters
$\sigma_{a,p}$, $\varepsilon_{a,p}$	Average plastic stress and average plastic strain, respectively
d_p, d_t, h_p, h_t	Plastic and total diameter, plastic and total indentation depth
ε_{th} , P_{th}	Damage plastic threshold equivalent strains for the uniaxial and triaxial stress state
η_{avg} , $f(\eta_{avg})$	Average stress triaxiality and stress triaxiality factor
$\varepsilon_{eq}^{f,\eta_{avg}}$, $\varepsilon_{eq}^{p,\eta_{avg}}$	Equivalent plastic fracture strain and Equivalent plastic strain
l_o^*	Characteristic distance
X_o	Microstructural distance
$\dot{R}$, $\dot{\varepsilon}_o$, R_o	Void growth rate, strain rate and average void inclusion radius, respectively
α_m , β , ψ	Microstructural-macrostructural material constants

Chapter 1 Introduction

1.1 Background and motivation

The importance of the rail industry in Canada and across the world is gaining more attention as a transportation means as seen with records of the high frequency of usage due to its operational safety, flexibility, comfort, and the growing population [1-2]. This requires continuous monitoring of the health condition of the rail structures especially for rail defects and resistance to fatigue damage for structural integrity assessment (since it is imperative for rail structures to have higher hardness and fracture toughness) [2]. However, using the conventional means of mechanical and fracture toughness in-situ examination would not be feasible for in-service structures like the rail steels since samples need to be removed from existing structure, making them unfit for their original intended purpose. This insinuates a desired need to adopt alternative methods for quickly and efficiently determine the mechanical properties like the Young's modulus, hardness, yield strength and fracture toughness of rail steels and structural members whether it being in-service or as supplied material stocks.

Despite the pros of rail industry in its operation and to the economy, several challenges arise ranging from technical issues to infrastructure problems leading to main track and non-main track train derailment that results to loss of property, life, and public confidence [2]. In fact, the work from Leishman et al. [3] investigates the Canadian main track derailment trends from 2001 to 2014 and suggests that on the Canadian main track, *joint bar and rail anchoring* and *track geometry* accounted for about 20% of derailments and 36% of derailed cars per derailment, respectively. In 2020, a report from the Transportation Safety Board (TSB) of Canada [4] presented investigations on a train derailment accident near Labuma, Alberta (Figure 1a), which resulted from broken rails caused by pre-existing detail fractures (i.e. a group of fatigue defects known as transverse detail defects (TDDs), in which the fracture plane is perpendicular to the running direction of the rail [5]), which caused damage to car (Figure 1.b). Investigations of the rail pieces showed gauge corner shelling, which is a rail head condition consisting of progressive subsurface longitudinal or horizontal separations that can crack out on the gauge side of the rail head (Figure. 1c) present on the rail head along with TDD occurrence accounting for about 70% of the rail head.

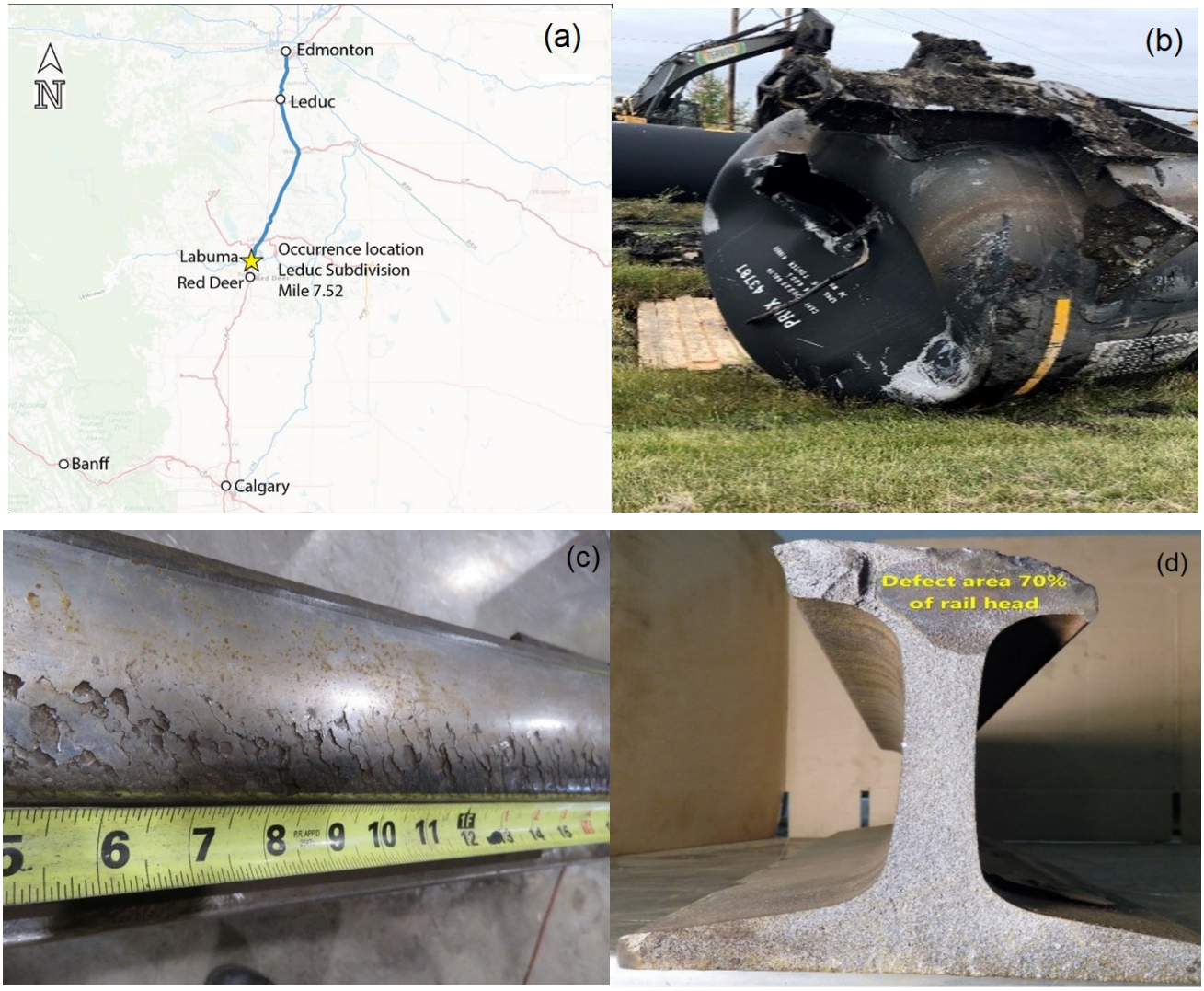

Figure 1.1 Main track derailment occurrence: (a) Location of main track derailment occurrence; (b) Damage to car PROX 43787; (c) gauge corner shelling; and (d) Transverse detail defect on rail head. Source: Transport Canada, Rail transportation safety investigation report [5].

Another concern with railway safety is the extreme condition in Canada, which can see temperatures go as low as -50°C. Many of the main track derailment investigations saw the ambient temperature below -0°C [3]. However, from current statistics [4], in 2020, the TSB recorded 205 main-track accidents, which was down from 2019 with a total of 277 indicating a 6% increase from the previous 10-year (2010–2019) average (194). The main-track accident rate in 2020 was 2.7 accidents per million main-track train miles, which was down from 3.3 in 2019 but 12% above the 10-year average of 2.4 [4]. Figure. 2(a) shows main track accidents from 2010 to 2020 showing a steep increase in main-tracks accident rates.

Main-track collisions and derailments constitute the most serious kinds of rail accidents in terms of potential risk to the public and financial loss. 70 main-track derailments were reported in 2020, which was a decrease from the 2019 total of 93, and 16% below the 10-year average of 84 Figure. 2(b) shows main track accidents from 2010 to 2020 based on collision and derailments [4].

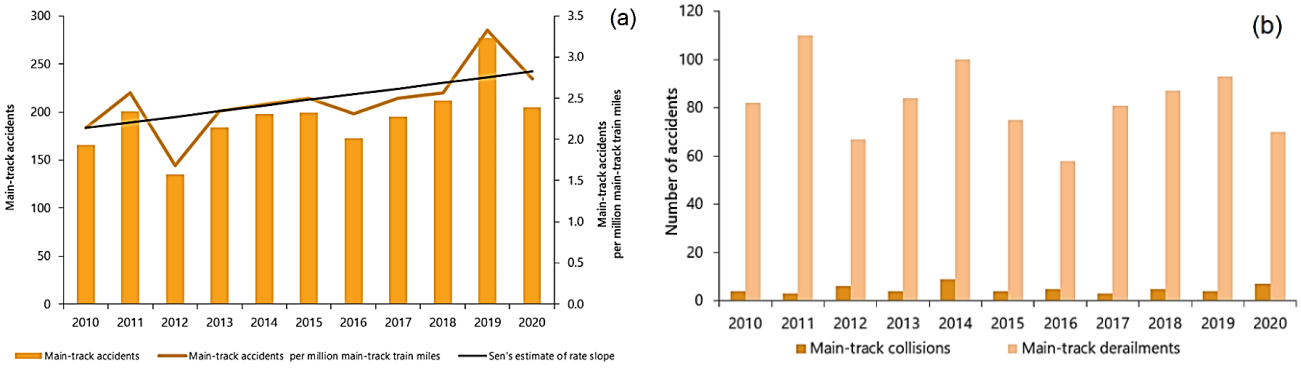

Figure 1.2 Main track derailment accidents: (a) Main-track accidents and accident rates, 2010 - 2020; (b) Main-track collision and derailment accidents, 2010 – 2020. Source: Transportation Safety Board of Canada [4].

Since broken rails and main track defects constitute a high frequency among all rail accidental issues, fracture toughness and hardness of the main track becomes a major concern as it is postulated that main tracks with higher fracture toughness along with higher strength (i.e higher hardness) would present a higher operational safety infrastructure needed for efficient operations. Hence, easy characterization of rail steels (new stocks or for investigative purposes) is needed using a simple, flexible approach.

In this research, ball and flat-ended cylindrical indentation techniques will be used to estimate the mechanical properties and fracture toughness rail steels as well as high strength aluminum. The mechanical properties like Young's modulus, yield strength, hardness and strain hardening exponents will be estimated and eventually compared with ASTM conventional approaches. The fracture toughness, which is one of the most important mechanical properties because of the frequency of broken rails and rail defects, will be attained using a modified critical fracture strain model and a virtually induced crack for ball and flat-ended cylindrical indenters, where the focus will be concentrated on the methodologies for the application in other range of materials. This will also be estimated and compared with the fracture toughness attained via the ASTM methods.

The indentation techniques will further be applied in attaining the stress-strain curve for the ball indenter to quantify the entire rail steel's responses non-destructively and consequently proffer the applicability of these techniques for in-service operations particularly in rail transportation in Canada.

1.2. Main track defects and derailment

1.2.1 Loading on rails

The forces between the train wheel and the rail head, also known as the wheel-rail interface, depends on several factors like the speed of the train and handling, car type, condition and distribution load, track design and deviations in track geometry. The most important forces are the vertical and lateral forces as seen in Figure 3, which results in a resultant force designated by the ratio of the vertical and lateral forces. A detailed view of the contact between the wheel and rail is also shown in Figure 1.3. Derailment of the train depends on this V-L ratio, which when increased beyond a certain limit, results in derailment. Different scenarios result to increasing V-L ratio, but basically stems from a combination of high lateral forces and low vertical forces. The high lateral force tends to push the wheel flange up and over the gauge face of the rail, resulting in a wheel-climb derailment.

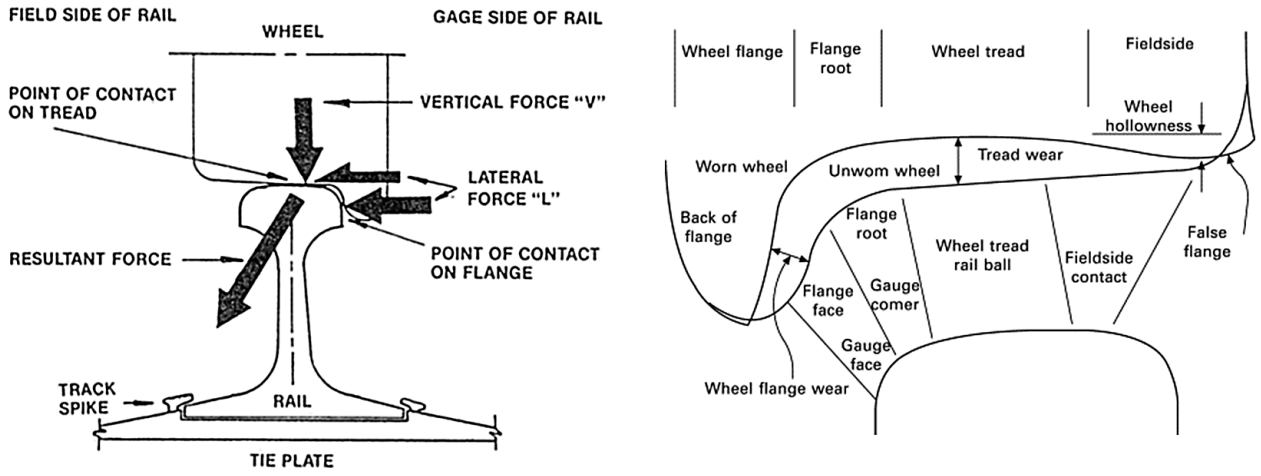

Figure 1.3 Wheel-rail interaction forces and key terminologies [6-7]. Source: Transportation Safety Board of Canada and Wheel–Rail Interface Handbook.

1.2.2 Wheel loading induced rail stresses

a. Bending stresses

The vertical and lateral forces are the main components that contribute to bending stresses. Even though lateral bending stresses contribute to the failure in rails, most of the bending stresses are contributed by the vertical bending stresses. These are primarily compressive stresses in the rail head and tensile stresses in the rail base. Although rail uplift on either side of the wheel load position leads to a reversal of stresses [2]. Based on the beam on elastic foundation (BOEF) theory for plane bending applied to rails by Zimmermann [8], the ideology of a general approach characteristically applies beams to mimic the response of rails tracks, which are supported by spring and dashpot elements that represent the kind of combined effect between the ground and the various track components [9–16]. The moments acting on the rail beam is derived as a rail considered as a continuous supported beam with a single wheel load.

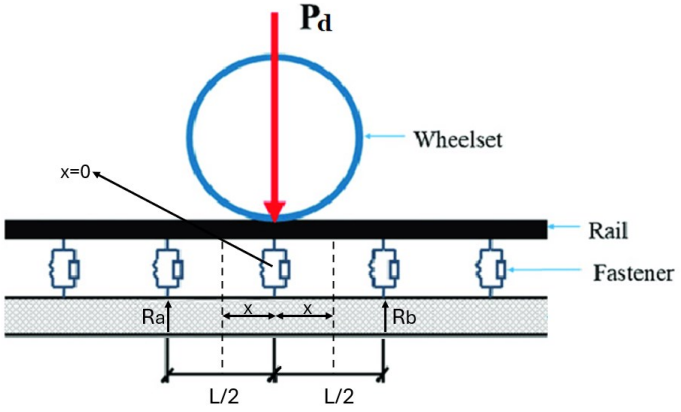

Figure 1.4 An illustration of continuous elastic foundation beam model under a single wheel load [9]

$$M_x = \frac{P^d}{4\beta_o} e^{-\beta_o x}\left[\cos\beta_o x - \sin\beta_o x\right] \qquad (1.1)$$

where $\beta_o = \sqrt[4]{\frac{K_R}{4EI}}$ is the characteristic length, K_R, the track modulus/the stiffness ratio, EI, the flexural rigidity, P^d, the dynamic bending loading and x, track position along the running axis

The maximum bending stress in the rail is thus given as:

$$\sigma_{\max}^{d} = \frac{cM_{\max}^{d}}{I} \tag{1.2}$$

where c is the distance from the neutral axis to the rail base and $M_{\max}^{d}$ is the maximum bending moment at $x = 0$

b. Shear stresses

Shear stresses are also experienced on the rail section, which causes most of the failures in bolt holes machined in the rail web for fishplate-joined rails [2, 17]. Although, shear stresses have been reduced significantly with the introduction of continuous welded rails (CWR). Shear stresses are also suggested to contribute to the ridge features seen on the surface of rail detail fractures (explained in section 1.2.3) but is advisable to neglect defect nonplanarity on the crack growth rate based on engineering mechanics principles [17]. However, with the presence of surface cracks, shear stresses contribute to mixed mode loading conditions [18].

c. Residual stresses

Rail steels also exhibit inherent residual stress, which are stresses existing within the rail structure in the absence of external loading. This can be introduced during manufacturing processes via heat treatment procedure, roller straightening, welding of rail sections off-field or welding on-field via rail installation [18]. These residual stresses depending on their origin can introduce different stress patterns comprising of tensile and compressive stresses in the head, web, or foot of the rails. Wheel load application can thus induce plastic deformation due to increased compressive stress than theoretically estimated.

d. Thermal stresses

Another form of stress that develops in rails is thermal stress, which develops due to differences between service temperatures and the “so-called” neutral temperature, which is the temperature at which rail internal forces are zero [18]. In Canada, where the temperature gets lower than the neutral

temperature of the rail at winter periods, tensile thermal stresses are developed, which adds to the wheel loading as a static load component increasing the tendency of rail fracture. However, when the service temperatures are higher than neutral temperatures, compressive stresses are built up, (also described as a 'sun kink') which can cause length of a railway (CWR) to buckles laterally [9, 18-19].

For CWR, the thermal stress, σ_T can be determined as seen in Eq. (1.3). For rails joined by fish-bolt plates, σ_T is affected due to discontinuities and geometrical deviations in the rail section and tend to have smaller values.

$$\sigma_T = \alpha_{CTE} E(T_N - T) \tag{1.3}$$

where α_{CTE} is the expansivity, T_N and T, the neutral and service temperatures, respectively.

e. Contact stresses

Contact between the wheel and rail is commonly considered as contact between two quasi-identical or convex bodies and can be divided into normal and tangential contact [9, 19]. This is also regarded as a non-conformal contact, where a contact elliptical patch as shown in Figure.1.5 located at the top of the rail is where actual contact between the rail and the wheel occurs. The contact stresses are, in general, compressive except for a transverse shearing stress that completely reverses as the rolling load passes [19-20]. The Hertzian contact theory [21-22] is used to analytically solve normal contact problems, where the contact patch is assumed to be elliptical in shape thus producing a pressure distribution in the contact area.

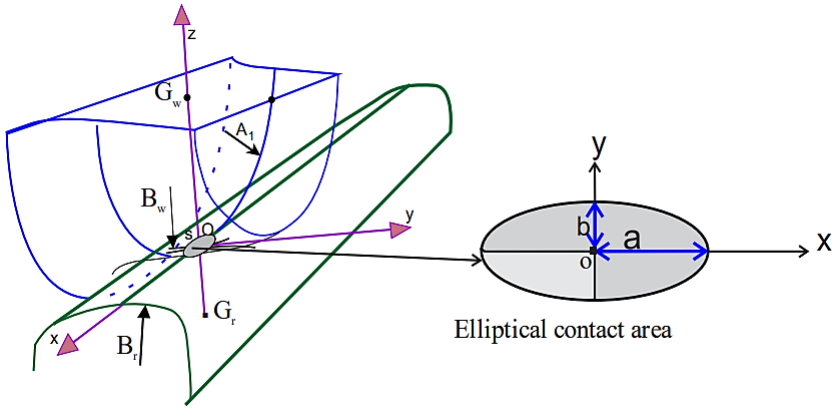

Figure 1.5 Contact elliptical patch. Source: Study of rail-wheel contact problem by analytical and numerical approaches [9].

The elliptical contact patch semi-axis 'a' and 'b' are dependent on the normal force, F_n, and E^*, which defines the elliptical contact area. Hence the pressure distribution in the contact patch, $P(x,y)$ is described using Eq. (1.4), which is parabolic in nature with x and y taken as the cartesian values of a circular radius.

$$P(x,y) = \frac{3}{2\pi ab} F_n \sqrt{1 - \left(\frac{x}{a}\right)^2 - \left(\frac{y}{a}\right)^2} \tag{1.4}$$

Further considerations of the shape of the elliptical contact patch that affects the contact area can be seen in [23].

In the consideration of the tangential wheel-rail interaction, which depends on rolling contact for low energy dissipation. The rolling contact is usually analyzed using the Kalker's 'exact theory', which is implemented in a well-known code-named CONTACT [24]. Prior to Kalker's 'exact theory', Carter [25] first studied the rolling contact problem as a 2D contact case with longitudinal creepage. Later, Johnson [22] extended Carter's theory to the 3D elliptic contact case containing longitudinal and lateral creepage. In Kalker's 'exact theory', rolling contact considers arbitrary geometry with the combination of creepage (longitudinal and lateral) and spin [23, 25]. A simple relationship of Kalker's 'exact theory' solution is expressed in Eq. (1.5).

$$\begin{aligned} F_x &= -f_{33}\xi_x \\ F_y &= -f_{11}\xi_y - f_{12}\xi_{sp} \\ M_z &= f_{12}\xi_y - f_{22}\xi_{sp} \end{aligned} \tag{1.5}$$

where $f_{11}, f_{12}, f_{22}, f_{33}$ are the creep coefficients defined by Kalker as

$f_{11} = (ab)GC_{22},\ f_{12} = (ab)^{3/2}\,GC_{23},\ f_{22} = (a/b)^2\,GC_{33},\ f_{33} = (ab)^{3/2}\,GC_{11}$,

G = Shear modulus of rigidity

C_{ij} = creepage and spin coefficient.

$\xi_x, \xi_y\ \xi_{sp}$ = longitudinal, lateral and spin creep.

A linear non-Hertzian unsteady tangential wheel-rail contact model can be readily analyzed computationally as seen in [27].

Another important consideration is the inclusion of surface roughness, which influences the wheel-rail contact [9, 21, 27]. The surface roughness causes deviations from the smooth and uniform Hertzian contact stresses causing highly localized contact pressures that yields local plastification. With further over rollings with surface roughness, very high plastic deformations are developed, which is linked as one of the major contributing factors to rail fatigue. In [28] the roughness-induced stress field and its effects were analyzed by numerical computations, twin-disc experiments and field observations. It is important to also note that there are instances of wheel-rail contact occurring at the rail edge, the contacting part of the wheel is thus concave near the flange, which entails that the wheel and rail radii are near 'matching' resulting in a conformal contact [9, 21] and thus cannot be analyzed based on Hertzian theory due to non-fulfillment of geometrical requirements. This will also lead to very high contact stresses and the development of plastification. Other deviations from the smooth distributed Hertzian contact loading are not only from the influence of dynamic effect arising from car and bogie motions but also due to the dynamic response of the track including its ballast bed and subgrade [9, 28].

Since plastification is an important material response to contact loading, it is of interest to study the induced effective stress. Here the von Mises effective stress in Eq. (1.6) can be used to estimate the induced effective stress (equivalent stress) for the maximum distortion.

$$\sigma_{eq} = \sqrt{\frac{3}{2} s_{ij} s_{ij}} \tag{1.6}$$

where s_{ij} are the components of stress deviator tensor.

To realize mechanical tests for characterizing the rail material's behaviour, one or more different constitutive laws like the Ogden hyperelastic model [30], von Mises plastic strain [31], Voce model [32], swift model [33], Hollomon's model [34] and others for elastic-plastic and strain hardening materials can be utilized. In [35], a combination of von Mises plastic strain and the nonlinear kinematic hardening model of Armstrong-Frederick was utilized to characterize R9T and 50CrMo4 steels. The non-linear kinematic hardening model of Amstrong associated with von Mises type plastic criterion is expressed in Eq. (1.7).

$$f = J_2(A) - k_y \tag{1.7}$$

where $J_2(\underline{\underline{A}}) = \sqrt{\frac{3}{2}\underline{\underline{A}} : \underline{\underline{A}}}$ and $\underline{\underline{A}} = dev(\underline{\underline{\sigma}}) - \underline{\underline{X}}$, $k_y = \sigma_y =$ tensile yield strength, considered as a constant and $\underline{\underline{X}}$ is the hardening back stress, C_H is a hardening parameter

$\dot{\underline{\underline{X}}} = \frac{2}{3} C \dot{\underline{\underline{\alpha}}}$ with $\dot{\underline{\underline{\alpha}}} = \dot{\underline{\underline{\varepsilon}}}_p - \frac{3}{2}\frac{\gamma}{C_H}\underline{\underline{X}}\dot{p}$ as the internal plastic strain rate increment and $p = \int_0^t \sqrt{\frac{2}{3}\dot{\underline{\underline{\varepsilon}}} : \dot{\underline{\underline{\varepsilon}}}}\, dt$

As elucidated earlier, wheel-rail interface phenomena predominantly encompass material yielding (plastification), which significantly influences contact geometry and surface as well as subsurface stress distributions. In this context, the Finite Element (FE) method has garnered increasing utilization. The FE methodology affords the capacity for analyzing intricate three-dimensional geometrical configurations while concurrently accommodating advanced material models. Explicit FE methods are undeniably applied to scenarios of geometrical, material, and dynamic effects. Nevertheless, when applied to the realm of rolling contact analysis, these computations expand exponentially, necessitating extensive computational resources and time commitments. The holistic exploration of challenges linked to wheel-rail rolling contact undeniably hinges on a substantial augmentation in computational power and processing speed.

A summary of the stresses on rail in motion is illustrated in Figure. 1.6 due to wheel-rail interaction.

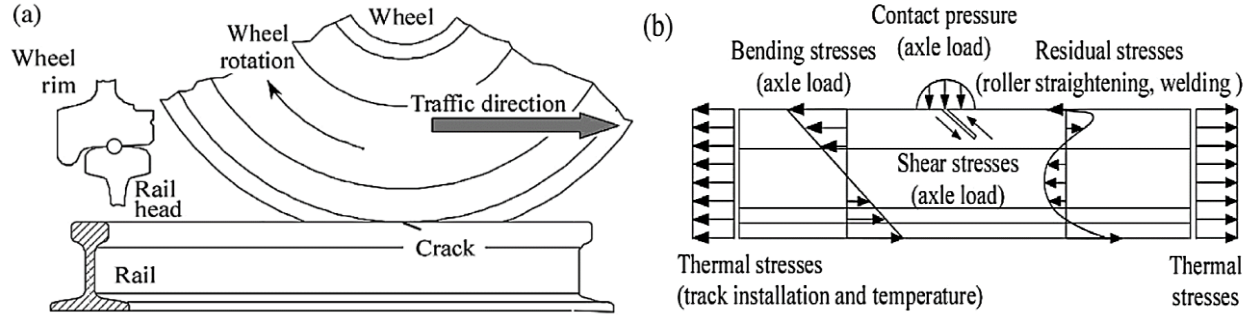

Figure 1.6 wheel-rail interaction: (a) wheel-rail illustration in motion with the presence of a crack; (b) different contact stress developed at the contact patch. Source: Introduction to the damage tolerance behaviour of railway rails–a review [18].

1.2.3 Rail and surface defects

Several types of rail defects exist based on the type and composition of rail steels, loading, track geometry cyclical loading, impact from rolling stock, rail wear, plastic flow, and environmental conditions. However, as highlighted in section 1.1, only common rail defects will be discussed in this

section especially those common to the Canadian railway main-track and how they contribute to wear and broken rails.

a. Transverse defects

Transverse defect is a progressive fracture that develops transverse to the cross-sectional area of the rail head. They occur mainly in the rails subsurface and are unnoticeable until the defect reaches the surface (crack out), thus reducing the structural integrity of the rail towards its load carrying capacity. Transverse defects are recognized by one or several following appearances: a hairline crack at right angle to the running surface, a hairline crack around the upper gage corner of the rail head, bleeding on the rail head, which is a discoloration around the developed crack caused by internal rusting and many other hairline cracks around the side of the head or at right angle by other surface defects. Some of the major transverse defects are discussed below:

i. Transverse detail fracture (TDD): This progressive fracture that starts from a longitudinal streak (separation) close to the running surface that originates at the upper gage corner and spreads transversely through the rail head. It is unnoticeable, thus leading to a catastrophic failure in the form of a broken rail leading to rail derailments. It can also occur as assisted from a surface shell, which can sometimes be visible due to the surface shell. Growth starts slow until it attains 15%, where it can become rapid around 20-60% [9, 17, 19, 35]. A reverse detail fracture may also occur where the progressive fracture starts at the bottom corner of the gage side of the rail head, spreading transversely through the head because of stress risers associated with a 'notching' condition on the *cold rolled lip*. This defect is typically associated with severely worn rail and high axle loads.

ii. Transverse fissure: This is a progressive crosswise fracture originating from a nucleus located inside the head due to imperfections in steel (shatter crack or non-metallic inclusions). Studies have shown that highly compressive stresses from contact or bending stresses do not occur on rail surface but in the sub-surface close to a distance from the contact surface [22]. This nucleus initiation starts a growth of a transverse separation. This can occur in several locations on the rail head, web or even foot. Separation is significant and occurs at a right angle to the running surface. The fissure surrounds the nucleus and shows indication of growth originating from the nucleus [17, 19, 35].

iii. Compound fissure: This is a progressive fracture originating in a horizontal split head that either turns down or up in the head as a smooth, dark, or bright surface, progressing until it is noticeably at a right angle to the length of the rail. The horizontal separation can be from an internal longitudinal seam or inclusion, developing longitudinally before turning either down, up or both ways in connection to the transverse direction. It can also occur in several locations and can be identified with both longitudinal (usually short) and transverse separations [36].

iv. Engine Burn Fracture: This is also a progressive fracture that occurs on the rail head originating from a *burn* develops downwards and has similar resemblance with a transverse or compound fissure. The burn occurs when slipping engine driver wheel rapidly heats a portion of the rail surface and followed by a rapid cooling forms, which thermal cracks. Further impact from wheels over the affected area initiates a small horizontal seam of the burned metal from the parent rail head, developing a flat spot.

A surface burn is always identified and when failure occurs, there is an absence of a nucleus. Figure. 1.7 shows an illustration of these transverse defects.

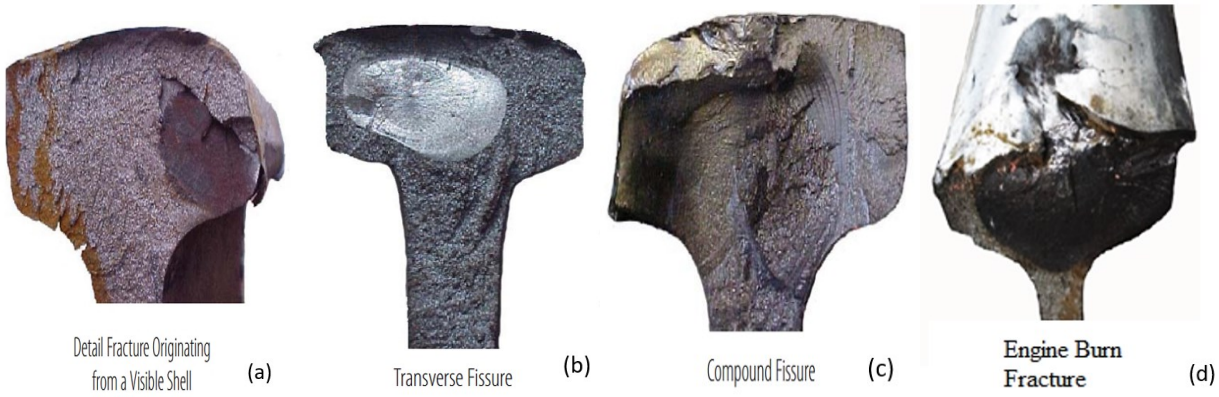

Figure 1.7 Tranverse rail defects: (a) Transverse detail fracture (TDD), (b) transverse fissure, (c) compound fissure, (d) engine burn fracture. Source: Nordco Rail Services and Inspection Technologies (NRS&IT) [36].

b. Longitudinal defects

Longitudinal cracks are special types of horizontal cracks (longitudinal separation only) induced sub-surface beneath the gauge corner, which has the potentiality of leading to breaking out of the material. The most common are the horizontal split head and vertical split head.

i. Horizontal split head:

This is a horizontal progressive longitudinal fracture, which originates internally within the rail head at about ≥ ¼ inch from the running surface [36] and can be initiated from longitudinal seams, inclusions, or segregations. Once initiated, it propagates in all directions, firstly longitudinally and horizontally, which is parallel to the running surface. Horizontal split heads are usually accompanied by a flat spot [36] and can propagate (in a curve path) downwards and initiate a transverse crack. Horizontal split head can also occur in several locations simultaneously because the initiating factor (seams, segregations, or inclusions) may exist throughout the rail.

ii. Vertical split head (VSH):

This is also another progressive longitudinal internal fracture that is found near the center of the head that either extents or runs through the starting point. They can originate from longitudinal seams, segregation, or inclusions [36]. They are also one of the dominated fatigue defects [17] along with transverse details fractures and bolt hole cracks. Figure. 1.8 shows an illustration of longitudinal defects.

Figure 1.8. Longitudinal defects: (a) horizontal split head, and (b) vertical split head. Source: Nordco Rail Services and Inspection Technologies (NRS&IT) [36].

Other rail defects can occur in the web and foot region of the rail steel but will not be covered here are the intrest is focuded on the region of coontact (head rail)

c. Surface defects

These are surface imperfections, deformations, or initiated damage on the exterior surface (sometimes close to the exterior surface) of the rail. These defects are initiated by rolling contact fatigue (RCF) conditions developed during the wheel/rail interface. Since wearing is one of the major observations during surface defects inspection, the hardness of the rail steel becomes a vital parameter to be concerned of especially during turns and curves. Some of the common surface defects are shelling, flaking, spalling, corrugation among others.

i. Shelling: This is a progressive horizontal defect (separation) that normally occurs beneath the cold-worked region around the gage corner of the rail. This may lead to cracking out mainly at the upper level of the gage side at any level (also known as gage corner shelling). This defect normally extends longitudinally at an angle to the rail axis relating to the amount of wear created. The shells can also propagate downwards in the transverse direction causing defect (also known as detail fracture from swelling, see Figure.6a). The gage corner shelling is mostly initiated from subsurface fatigue phenomenon in conjunction with high contact stresses, thermal and residual stresses at the contact patch around the throat of the wheel and the gage corner [36 -37]. They appear as dark spots, which are irregularly spaced on the gage side (see Figure.8a). They occur mostly in curved areas of the rail line [37].

ii. Flaking: This is a progressive horizontal separation in the form of flakes, scaling or chipping of small silver occurring only on the running surface near the gage corner. The flakes are not so deep when compared with shelling, however. It is predominant on the high side of curves and switch points. It is sometimes caused by poor maintenance schemes in the form of grinding or an improper lubrication [39].

iii. Spalling: While spalling is sometimes referred to as flaking, spalling is a localized degradation on the running surface with an appearance of black spots. They are generally displacements from the parent metal, which originates from high contact stresses in conjunction with RCF (cyclic loading). Initially, they can be referred to as flaking [36] but with further loading, materials are displaced and are easily seen during rail head inspection.

iv. Corrugation: This is the formation of oscillatory profile (ripples) on the running surface of a rail caused by long-term interactions between vehicle wheels and rails. They can be related to plastic flow and generally causes aggressive vibrations in the structures of vehicles and tracks, causes noise, induce building vibrations, support the reduction of service life of structural parts of the vehicles and tracks, affects comfort level of ride, and affect the wheel/rail dynamic forces

especially in improper loading of the vehicle [39–42]. Causes and development of corrugation are related to several factors, but some studies suggest that pinned-pinned resonance, torsional vibration of a wheelset or fastening system stiffness [43-44], where the influence of plastic flow is also considered as a possible saturation mechanism [43, 45] . In terms of maintenance, rail grinding was seen to be an effective maintenance method for correcting rail corrugation, rolling contact fatigue, and wear defects [42, 46]. Figure.1.9 shows an illustration of the four types of surface defects discussed for proper identification.

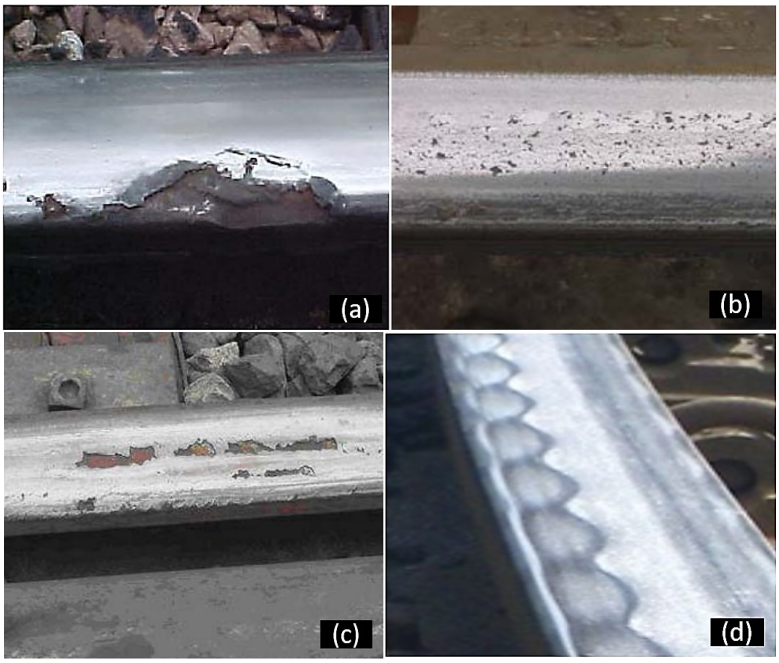

Figure 1.9 Different surface defects: (a) Shelling, (b) flacking, (c) spalling, and (d) corrugation. Source: Nordco Rail Services and Inspection Technologies (NRS&IT) [36].

1.3 Literature review

1.3.1 stress concentration

The inevitability for structures to be free of notches, seams or cracks has almost a zero likelihood. These discontinuities can cause serious issues due to the highly developed stress concentration thus local stresses can develop beyond the yield strength of the material leading to the more complex theory of plasticity and in special conditions with ductility limit, a catastrophic fracture. The macroscopical elastic behavior of isotropic materials is characterized by three elastic constants, the Young's modulus (E), shear modulus (G) and Poisson's ratio (v) based on the relationship of E =

$2G(1 + \nu)$ on which the homogenous stress distributions can be characterized by Hooke's law. However, with the presence of these discontinuities (notches and/or cracks), an inhomogeneous stress distribution is developed at the 'root of the notch'. The stress concentration, K_t is thus estimated as the ratio of the peak stress at the root of the notch to the nominal stress of the specimen provided the condition is based on linear elastic material behaviour [47–50]. Figure 1.10 shows an inhomogeneous stress distribution of a hole within a plate.

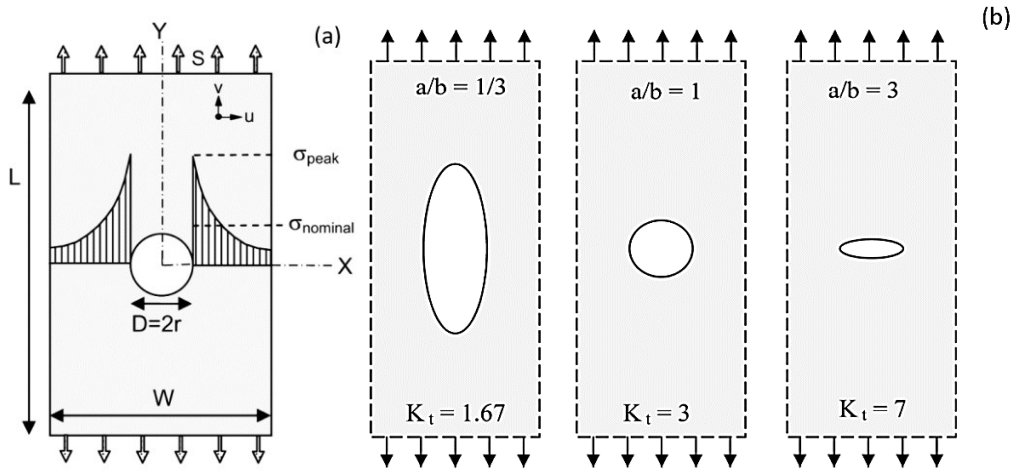

Figure 1.10 Stress concentration in holes: (a) plate with central hole, and (b) effect of the hole on K_t under tension
Source: Stress Concentration at Notches [51].

$$K_t = \frac{\sigma_{\max}}{\sigma_{nom}} \tag{1.8}$$

The peak stress (σ_{max}) can be derived from different loading types include tensile, torsional, bending or even combined loading. For complex loadings, finite element (FE) modeling can be introduced. As seen in Figure 1.10(b), the shape and orientation of the hole or notch within the specimen affects the K_t value, which is a classical problem in the theory of elasticity [49]. A circular hole has a K_t value of 3 for an infinite plate, which makes it a special case. Although, a structure in practice with a circular hole will have a lower value due to geometrical conditions of the plate having a finite dimension. For an elliptical hole with semi-axes a and b, the equations for the peak stress and K_t with a notch root radius, ρ, are expressed in Eq. (1.9a) as shown in [51]:

$$\sigma_{nom} = \sigma_{nom}\left(1+2\frac{a}{b}\right) = \sigma_{nom}\left(1+2\sqrt{\frac{a}{\rho}}\right) \tag{1.9a}$$

$$K_t = 1 + 2\sqrt{\frac{a}{\rho}} \tag{1.9b}$$

Further modifications of the analytical equation for the estimation of K_t depending on the nature of the notches (sharp or shallow) are presented in [51-52].

1.3.2 Stress analysis of notches and cracks

The elastic stress field close to a crack or notch was developed by Irwin [54] and William [55] based on stress intensity factor, K_I, which is used to predict the stress states. The stress components for a *mode I failure mode* have the form:

$$\begin{aligned}
\sigma_{xx} &= \frac{K_I}{\sqrt{2\pi r}}\cos\frac{\theta}{2}\left(1-\sin\frac{\theta}{2}\sin\frac{3\theta}{2}\right)\\
\sigma_{yy} &= \frac{K_I}{\sqrt{2\pi r}}\cos\frac{\theta}{2}\left(1+\sin\frac{\theta}{2}\sin\frac{3\theta}{2}\right)\\
\tau_{xy} &= \frac{K_I}{\sqrt{2\pi r}}\sin\frac{\theta}{2}\cos\frac{\theta}{2}\cos\frac{3\theta}{2}\\
\tau_{xz} &= \tau_{yz} = 0\\
\sigma_{zz} &= \begin{cases} 0 & \text{plane stress} \\ \nu(\sigma_{xx}+\sigma_{yy}) & \text{plane strain} \end{cases}
\end{aligned} \tag{1.10}$$

where r is radius from the tip of the sharp crack or notch and θ the angle of inclination in the polar coordinate positioning the state of the stress field.

Irwin [54] also discovered in 1957 that any stress state could be reduced to three independent stress intensity factors, which are *mode I*, *mode II,* and *mode III* fracture modes. Figure 1.10 shows an illustration of the three fracture modes in practical terms.

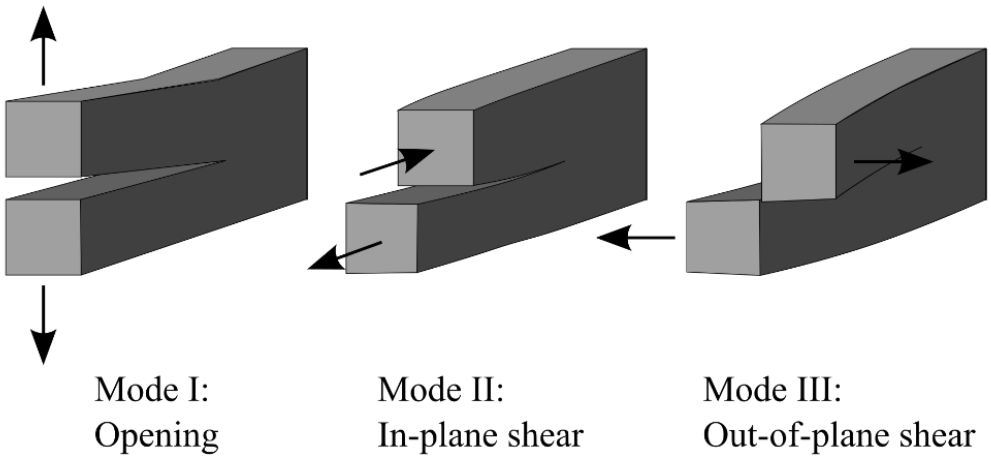

Figure 1.11 Three fracture modes. Source: Fracture Mechanics: Fundamentals and Applications [56].

In the case where σ_{max} exceeds the yield strength of the material, plastic zone develops at the root of the notch or crack due to blunting effect. However, if the plastic zone at the tip of the crack is relatively small to the crack length and the entire body in stress, the stress state at the crack tip can be assumed to be experiencing elastic stresses in a term called small scale yielding (SSY) [56] because the material outside the dissipative region is very large and elastic and is thus referred as linear elastic fracture mechanics (LEFM). For larger plastic deformation (or plastic zone) in comparison to the entire body, the criteria of LEFM becomes invalid leading to elastic-plastic fracture mechanics (EPFM) [55-56]. Irwin [54] proposed a fracture criterion, which states that crack growth occurs when the stress intensity factor reaches a critical value (K_C). The validity of the criterion for K_{IC} requires that nonlinearity around the crack tip is ignored due to their relatively small size, which are well contained in the K-dominance zone around the crack tip. This critical value is a material constant also known as the fracture toughness and highly depends on the thickness of the specimen, where thin specimens (plane stress) results in a larger plastic zone making K_c value quite larger than expected and thicker specimens (plane strain) results in smaller plastic zone that can meet the criteria of SSY. At certain geometrical conditions and appropriate thickness, K_c becomes insensitive to thickness and thus fracture toughness is known. For a mode I fracture, the fracture toughness is termed as K_{IC} and can be attained using standard fracture toughness tests.

1.3.3 Standard fracture toughness tests

According to the ASTM, standard fracture tests can be attained for metallic materials using ASTM E399 [58], which is a 3-point single edged notch bend (SENB) test involving the criteria and

procedures for specimen dimension, procedure for mechanical test, fatigue pre-cracking and measuring pre-cracked length from post fractured specimen. Apart from the SENB test, other standard tests are available which involve the compact test, the disk-shaped compact test, the middle tension specimen, and the arc-shaped tension specimen. Attaining K_{IC} using standard tests is quite challenging due to the difficulty in material preparation, laborious techniques, multiple material tests and ultimately cost. Standard tests are also not encouraged for newly developed alloys, where material stock is limited. In fact, the work from Yu et al. [59] suggests about 6 months to complete testing for K_{IC} for rail steels. Figure1.12 shows different standard fracture toughness tests according to ASTM [references].

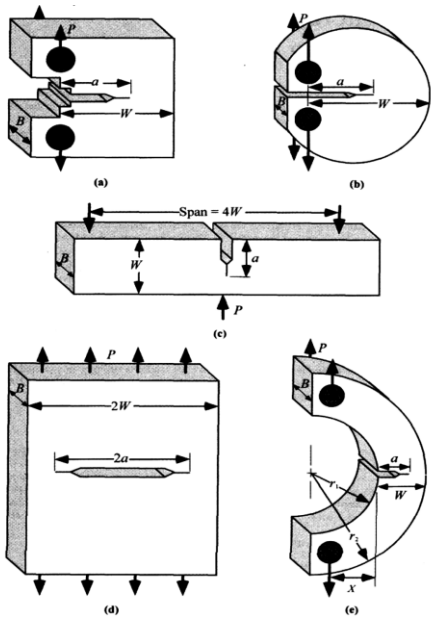

Figure 1.12 Standardized fracture mechanics test specimens: (a) compact tension (CT) specimen, (b) disk-shaped compact tension specimen, (c) single-edge-notched bend (SENB) specimen, (d) middle tension (MT) specimen, and (e) arc-shaped tension specimen. Source: T.L. Anderson [56].

Another concern is when in-service equipment is to be re-tested for the K_{IC} values, sample extraction becomes practically impossible since the in-service structure would be deemed nonapplicable for its intended purpose. This becomes a driving motivation for this study to develop new approaches for K_{IC} estimation using non-destructive testing approaches. In the further sections, different theories for fracture toughness will be examined as the building block for developing a non-destructive fracture toughness method.

1.3.4 Iwrin's stress intensity solution for notches

As already stated, Irwin [54] proposed a fracture criterion for K_C. However, despite the stress states between a sharp crack tip and a notch nip are similar, finding a relationship between crack and notches for K_{IC} estimation can be challenging. Irwin [54] thus proposed a limiting relationship to correlate between a notch and crack. Eq. (1.11) is the connection between the geometrics and mechanics of a sharp crack and a notch.

$$K_\rho = \lim_{\rho \to 0} \frac{\sqrt{\pi}}{2} K_t \cdot \sigma_{nom} \sqrt{\rho} \tag{1.11}$$

Irwin proposes that using different notch root radii, a notch can be likened to a sharp crack by extrapolating the notch root radii to zero and thus the stress intensity factor becomes critical ($K_{\rho c}$) and can be regarded as an approximate K_{IC} value.

1.3.5 Critical fracture stress and strain models

With the advent of fracture toughness studies, different models are being generated from the foundations of Griffin's [60] and Irwin's [54] prepositions in conjunction with different material behaviors. For brittle materials, where plastic deformation is extremely negligible or absent, Ritchie et al. [61] postulated the critical fracture stress model with the observation that cleavage cracks propagated in an unstable manner when the tensile σ_{max} ahead of a stress concentrator exceeded a critical value, σ_{eq}^{f},which was relatively independent to strain rate and temperature [60–62]. This unstable slip-initiated cleavage ahead of sharp cracks along with the knowledge of the asymptotic Hutchinson, Rice, and Rosengren (HRR) [56] crack tip singularity theory for elastic-plastic stress distribution is achieved over some microstructural distance known as the *characteristics distance* (l_o^*). Ritchie proposed l_o^* to be equivalent to twice the average grain diameter. The critical fracture stress model also depended on the yield and fracture stresses. Eq. (1.12) describes the critical fracture stress model proposed by Ritchie et al. [61], which is solely depends on the HRR asymptotic crack tip singularity, and correspondingly does not reflect the refinements in the stress distribution derived from more recent finite element solutions [61].

$$K_{IC} = \varphi^{-((N+1)/2)} l_o^{*1/2} \left[\frac{\sigma_f^{((N+1)/2)}}{\sigma_y^{((N+1)/2)}} \right] \tag{1.12}$$

where, $\varphi = f(N)\left[\frac{(1-\nu^2)}{\varepsilon_o i}\right]^{1/(N+1)}$ is the amplitude of the stress singularity, and I, $f(N)$, and φ are functions of hardening exponent, N [61].

The establishment of the critical fracture strain model was also proposed by Ritchie et al. [61], which was used in describing and predicting the fracture toughness K_{IC} for ductile materials. The critical fracture strain model was based on the development of the plastic strain (ε_p^*) from a tensile notch test and from the microstructural point of view. For a circumferentially tensile test, the equivalent plastic strain can be estimated as shown in Eq. (1.13).

$$\varepsilon_p^* = 2\ln\left(a_o/a_f\right) \tag{1.13}$$

where a_f and a_o are the current cross-section radius and initial cross-section radius, respectively.

Assumption of SSY criterion is also considered, where the plastic zone of a small crack tip relates to the stress intensity factor [60, 63]. The equivalent plastic strain ε_p^*, as shown in Eq. (1.13) is also defined as a function of a microstructural distance ahead of the crack tip (X_o) and the crack tip opening displacement (CTOD) as shown in Eq. (1.14a).

$$\varepsilon_p^* = \frac{1}{\alpha_m}\frac{\delta}{X_o} \tag{1.14a}$$

where α_m is a constant relating microstructural and macrostructural strain depending on the stress triaxiality effect.

However, fracture is expected to occur when this equivalent plastic strain reaches a critical value. This occurs at the weakest point (point of flaw) along the grain boundary or around the inclusion particle [61]. As X_o becomes critical, it becomes the characteristic distance (l_o^*) within the microstructure at which fracture initiates. Hence, the equivalent plastic strain develops into the equivalent plastic fracture strain at that l_o^* value, as shown in Eq. (1.14b).

$$\varepsilon_f^* = \frac{1}{\alpha_m}\frac{\delta_c}{l_o^*} \tag{1.14b}$$

It is important to note that ε_f^* depends on the stress triaxiality of the material, depending on the process of fracture. Hence, by combining the relationship between the critical value of CTOD (δ_c) with the K_{IC} based on SSY criterion, as shown in Eq. (1.15) and the equivalent plastic fracture strain in Eq. (1.16), the critical fracture strain model is developed as explained by Ritchie et al. [61] in Eq. (1.16).

$$\delta_c = \gamma_m \left(K_{IC}^2 / E\sigma_y \right) \tag{1.15}$$

where γ_m is a material constant, E the Young's Modulus and σ_y yield strength of the material.

$$K_{IC,pred} = C_m \sqrt{E\ \sigma_y\ l_o^*\ \varepsilon_{eq}^{f,\eta}} \tag{1.16}$$

Eq. (1.16) recommends that fracture toughness can be estimated for any ductile material once the material properties and the characteristic distance are known. Haggag et al. [64-65] estimated C_m to have a value of three for steels only with the condition of replacing $\varepsilon_{eq}^{f,\eta}$ with the material's strain exponent (n). This replacement of strain hardening exponent (n) with $\varepsilon_{eq}^{f,\eta}$ by Haggag, $K_{IC,pred} = C_m \sqrt{E\ \sigma_y\ l_o^*\ n}$, is said to have no basis for justification in the critical fracture strain model, only on the basis that n is directly proportional with ε_f^* in a smooth tensile test for many ductile materials. Hence, the usage of n provides the means of predicting the fracture toughness non-destructively.

1.3.6. J-integral and Limit Load analysis

For elastic-plastic fracture toughness estimation, works from Rice [67], Begley and Landes [68] showed that the *energy rate* interpretation of the J-integral, which is a parameter needed for characterizing the plane strain fracture resistance of ductile materials is fundamental theory needed. The J-integral can be decomposed into the elastic and plastic part for a SENB specimen [69].

$$J = J_e + J_p = \frac{(1-v^2)}{E} \cdot \left(\frac{L_s}{BW^{1/2}} Y\left(\frac{a}{W} \right) \right)^2 + \eta_{pl} \frac{2}{B(W-a)} \tag{1.17}$$

where W is the test piece width, B, the test piece thickness, a, the crack length, L_s, the applied load, η_{pl} is the plastic component of deformation energy also known as the plastic work factor.

The elastic J-Integral J_e can be determined by using parameters from the linear elastic fracture mechanics (LEFM) [56, 58].

For the limit-load analysis, Miller [70] reviewed the maximum load required for the fracture of structures with dents using different loadings. This is to determine a lower bound to the limit load of a structure before the onset of large plastic deformations (plastic collapse). This is used for establishing design factors to the limit load of a structure. For tensile notched round bar (NRB) specimens with an axisymmetric sharp notch, Miller [70] showed that the limit load constraint factor, ω, based on Tresca's yield criteria is 2.85 [70] for deep sharp notches as seen in Eq. (1.18)

$$\omega = \frac{L}{\pi b^2 \sigma_y} = \begin{cases} 2.85 & b\,R < 0.35 \\ R/b & b\,R > 0.35 \end{cases} \tag{1.18}$$

where L is the limit load, σ_y, the yield strength of the structure with b and R the notch and nominal radius of the NRB specimen. The limit load causes the plastic collapse suggests that fracture toughness can be estimated once L is known.

1.3.7. Indentation testing

The use of indentation technique has gained popularity both in laboratory and industrial applications. The ability to measure mechanical properties non-destructively for structural integrity assessment and monitoring purposes gives it more viability towards research and development. Although it was initially meant for measuring the hardness of materials, its application has expanded to measuring Young's modulus, yield and tensile strength, creep, and fracture toughness. The theoretical concepts have been developed over decades which has seen significant improvement in understanding the mechanics of indentation techniques. Some of these theoretical concepts include pile-up and sink-in effect, stress relaxation, loading and unloading, elastic relaxation, deformation regimes, damage mechanics and compliance effects.

a. Hertz's contact law

In the field of contact mechanics, Hertz [22] was the first to study the contact of deformable solids and found an analytical solution for two axisymmetric objects based on the conventional principles

of the theory of elasticity and continuum mechanics. In Figure. 1.13, the elastic contact of a sphere with an elastic half-space is shown (with the assumption of no plastic deformation), which describes the deformation of a rigid spherical indenter that causes a contact area of radius by an indenter of radius, *R*. The contact radius, a_c between the spherical indenter and the specimen can be computed using Eqn. (1.19) under the assumptions of Hertz's contact law, which requires both surfaces to be conformal, linear elastic with small deformations that requires loading only in the normal direction [21-22].

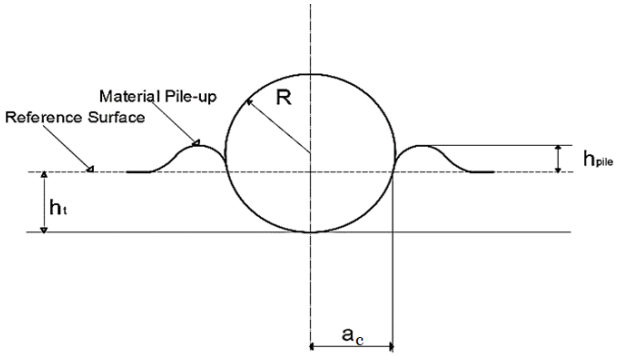

Figure 1.13. Schematics of contact of a sphere with an elastic half-space

$$a_c = \sqrt{Rh_t} \tag{1.19}$$

The applied force, *L* causing the deformation is related to h_t as expressed below [1].

$$L = \frac{4}{3} E_r R^{1/2} h_t^{3/2} \tag{1.20a}$$

where $$\frac{1}{E_r} = \frac{(1-\nu_s^2)}{E_s} + \frac{(1-\nu_i^2)}{E_i} \tag{1.20b}$$

E_r is the reduced modulus resulting from the combined modulus from the contact between the indenter and specimen on the assumption that there exist elastic deformations in both the indenter and the specimen during the contact, E_s the modulus of the specimen, E_i the modulus of the indenter, ν_s and ν_i the Poisson's ratios of the specimen and indenter, respectively.

Johnson [22] resolved the distribution of normal pressure in the contact area as a function of distance from the center of the circle that results in the maximum pressure. The normal pressure distribution is expressed in Eq. (1.21)

$$\sigma_{zz}(r,0) = p_o\left(1-\frac{r^2}{a^2}\right)^{\frac{1}{2}} \qquad r \le a \tag{1.21}$$

where σ_{zz} is the mean normal pressure acting on the surface by the indenter, *a* the contact radius, p_o the maximum pressure.

The normal force causing the deformation can also be expressed as a function of the normal pressure distribution on the deformed surface.

$$P = \int_0^a \sigma_{zz}(r,0)2\pi r(dr) = \frac{2}{3}p_o\pi a^2 \tag{1.22}$$

Combining Eqs. (1.19), (1.20) and (1.22), the contact radius and the total indentation depth are related to the applied load P in Eq. (1.23).

$$a^3 = \frac{3LR}{4E_r} \tag{1.23a}$$

$$d_t = \frac{a^2}{R} = \left(\frac{9L^2}{16E^2{}_rR}\right)^{1/3} \tag{1.23b}$$

It is to be noted that in Eq. (1.22), the maximum contact pressure (p_o) will be located at the center point of the contact area in the z-axis just below the contact region. The analytical solutions for stresses beneath the surface of an elastic half-space indented by a spherical indenter are shown in Appendix 1.

b. Sneddon's solution for contact stiffness.

Sneddon's solution resolved the relation between load, L, and penetration depth, *h*, in the indentation process using an axisymmetric Boussinesq problem for an arbitrary profile [1]. For a flat punch, Sneddon found a simple relationship between *L* and *h* as shown in Eq. (1.24), which involves the

Poisson's ratio and shear modulus of the specimen in an elastic half-space derived from the distribution of pressure under the punch and the shape of the boundary from the deformed half-space.

$$L = \frac{4\mu a}{1-v} h \tag{1.24}$$

where a is the contact radius, μ the shear modulus and v the Poisson's ratio of the specimen.

Once the relationship in Eq. (1.24) is differentiated dL/dh between L and h of about 20-50% of the unloading curve, Sneddon found that the contact stiffness (S_{max}) can be estimated. Eq. (1.25) shows the relationship between the S_{max} and E_r, resulting in a general model for the elastic contact between a rigid, axisymmetric punch and an elastic half-space.

$$S_{\max} = \frac{2\beta}{\sqrt{\pi}} \sqrt{A_c} E_r \tag{1.25}$$

$S_{\max}$ is attained from the initial slope of the unloading curve of L-h as shown in Figure 1.14, $\sqrt{A_c}$ is the measured contact area, and β is a geometric correction factor for different indenter shapes and related to the bodies of revolution. To make Eq. (1.25) applicable to all indenter types, Kings [70] proposed the values of β for different indenters: for a triangular indenter, it is 1.034, for a square-ended indenter 1.012, and for a circular indenter 1. This is under the condition that modulus and Poisson's ratio of the material are known.

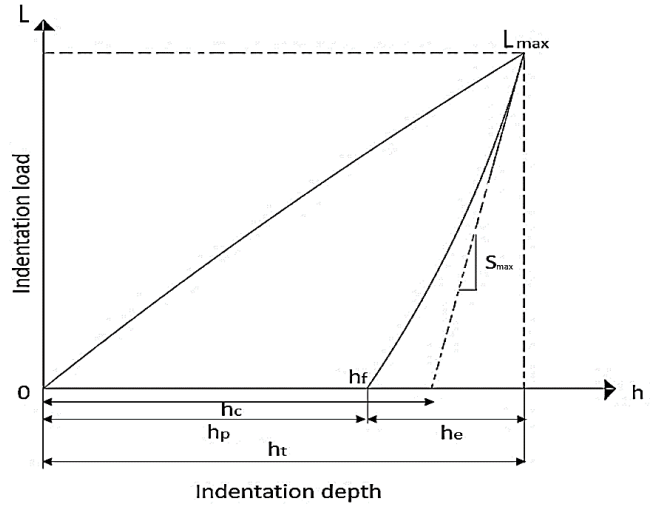

Figure 1.14. A typical loading- unloading curve showing the estimation of S_{max}

1.3.8. Gaps in fracture toughness measurement using indentation for high strength rail steels

Despite extensive research on the measurement of fracture toughness for high strength rail steels, earlier studies have shown notable gaps in the characterization of high strength rail steels of its mechanical properties and fracture toughness using indentation-based methods. Although existing research has acknowledged the influence of stress triaxiality on the damage evolution during indentation for rail steels, the critical damage parameter (D_{cr}) often has equivalent similarity with a standard tensile specimen. The work from Yu et al. [72 -73] demonstrated that the specific work of fracture at the crack tip can be replaced by the specific indentation energy by determining a critical indentation depth using the corresponding value of damage modulus from a tensile specimen with that of indentation. Although, the rail steels showed a good ranking and trend with fracture toughness attained using standard testing via ASTM approach, the K_{Ind} value for each rail was about one order of magnitude bigger than the corresponding K_{Ic} value. The literature so far still requires more in-depth exploration and incorporation of stress triaxiality for fracture toughness measurement in high strength rail steels via indentation.

Another notable gap is the uncertainty surrounding the use of an *'adjusting parameter* (*k*)*'* to relate indentation-compression test and tensile test for reconciling the critical damage parameter for fracture toughness measurement [72 -73]. Firstly, it is not clear if this *adjustment parameter* (*k*) is related to hydrostatic pressure sensitivity, damage induced effect or simply just a multi-axial stress effect. Secondly, the use of this *adjusting parameter* is limited to a small range of high strength rail steels with limited microstructural orientation (i.e pearlite, bainitic, martensite, etc.) and as such does not offer more insights on the physical meaning of this adjusting parameter for tensile-indentation flow curve measurement for reaching the critical damage parameter needed for fracture toughness measurement.

Another gap in the literature is the full comprehension of the fracture toughness measurement of high strength steels with the presence of notches (sharp or circular) via indentation. Works in [74-75] show the use of small punch tests (SPT) or flat-end indentation with the presence of notches in circular specimens for high strength steels, which captures different notch mouth opening displacement of at crack initiation for the different high strength steels. However, the complexities of the notches are still not very clear as the formation of SPT does not necessarily favor the formation of a single crack neither does it show a proper crack propagation as seen in standard tests (SENB or CT). Moreover,

this approach cannot be applied for in-service static or rotatory equipment as introduction of notches or cracks defeats the notion of non-destructive testing.

In general, the current indentation-based methods of estimating fracture toughness still need more insights, refinements and robust data analysis before it can be standardized for automation in industrial settings needed for a quick, efficient and flexible method of non-destructive testing.

1.4. Aim and Objectives of this study.

The overall goal of this research is to use a non-destructive indentation testing approach to develop fracture toughness methodologies to ascertain the fracture toughness of high strength alloys. Nine high-strength rail steels and one high strength aluminum alloy (AL2024-T351) are tested and used to compare the outcomes with results obtained from traditional ASTM approaches. The specific objectives include:

I. Determining the mechanical properties of high strength steel and high strength aluminum via indentation testing.
II. Comparing different indentation techniques for fracture toughness estimation
III. Estimating the hardness using suitable hardness approaches
IV. Establishing the stress and strain fields produced from indentation and comparing with tensile test's stress-strain relationship.
V. Observing the stress fields within the material sub-surface via indentation for plastic zone size estimation.

Where is your revision to repond to Dr. Jahed's comment: 'offer a concise statement that explains how your approach differs from, builds upon, or advances the current state of the art.

At the end of every chapter starting from chapter 2 and also added at the end of this section.

The thesis will be divided into six major chapters in line with the stages of this project.

Chapter 2 focuses on the experimental approach of using ball indentation technique to attain the mechanical properties of nine rail steels. The outcome of the ball indentation test relies on the experimental work conducted by Yu. [59] based on the ASTM approach as a reference. Mechanical properties like the Young's modulus, E_s, yield strength, σ_{ys} and strain hardening exponent, n_s are estimated with emphasis laid on the hardness behaviour on the surface and sub-surface of the rail head. For further analysis, the tensile flow curve was estimated via ball indentation by including an

adjusting parameter (κ) and relates to E_s which offers to insight the development of the plastic zone beneath the indenter tip to tone down the effect of multi-axial stresses and increased stresses from the contact between the indenter and the rail steel.

The study presented in Chapter 3 focuses on developing a model for fracture toughness estimation by looking into tensile tests and indentation tests. The methodology requires implementing a modified version of the critical strain model, where stress triaxiality is included on a void growth model for ductile failure mechanics (nucleation, growth, and coalescence) as well as the equivalent plastic fracture strain. For the tensile test, the n as well as the n_s from indentation tests were looked upon to investigate the viability of fracture toughness to be estimated from a non-destructive approach. The same nine rail steels were examined with the works of Yu et al. [57], which were used as a reference for the K_{IC} based on ASTM procedures.

In Chapter 4, in order to alienate some of the limitations of the spherical indentation, cylindrical flat-end indenters were introduced to investigate its viability for fracture toughness estimation. Two types of cylindrical flat-end indenters of 3 different sizes each were used in the study. The first set of flat-end indenters describes the tip to be non-chamfered while the other type was chamfered at 45^o. As a substitute to rail steels, a high strength aluminum alloy (AL2024-T351) was introduced due to the high pressure that can be developed at the contact region of the indenter when indenting rail steels, which can cause the non-idealization of the indenter as a rigid material. The AL2024-T351 used although has similar fracture toughness with rail steels, they have a lower hardness value making it feasible for study with lower load requirements. The ideology for the fracture toughness estimation is to relate flat-end indentations, geometrically, as what is obtainable in a tensile notch round bar (NRB) specimen test virtually based on isotropic material deformation and J-integral using a newly developed modified limit load analysis. The fracture toughness was estimated using a limit load function to relate the stress intensity factor estimated from J-integral with the contact radius of the flat-end indenter.

Chapter 5, which is an extension from chapter 4, describes the application of the newly developed modified limit load analysis for fracture toughness using spherical indentation. This was applied to AL2024-T351 showing the ability for fracture toughness to be estimated. Unlike the chamfered flat-end cylindrical indenter, the spherical indenter was likened to the pre-cracked single edged notch bend (SENB) specimen test, where the indentation load-depth is likened to a virtually determined

force-displacement curve of the SENB specimen. The chapter also addresses the challenge of using spherical indentation, where indentation size effect (ISE) is predominantly present especially for smaller sized spherical indenters, which causes localized hardness of the substrate. A solution was provided by replacing the contact pressure with pressure attained using an expansion cavity model (ECM) for the procedure of fracture toughness measurement. In the end, the indentation depth needed for fracture toughness between the chamfered flat-end cylindrical indentation and the spherical indentation is compared with preference given for lower indentation depth, where both chamfered flat-end cylindrical indentation and the spherical indentation present their pros and cons towards the goal of non-destructive testing.

In Chapter 6, the understanding of the application and the challenges arising from spherical indentation for fracture toughness of AL2024-T351 is then applied to rail steels. Although another challenge arose from attaining high stress intensity factors generated from the modified limit load analysis for rail steels, a good trend was observed with K_{IC}. A solution was proposed for the inclusion of stress triaxiality factor to the plastic components of the J-integral via indentation, which saw the fracture toughness estimated very close to K_{IC}. The Brinell hardness was also estimated based on the spherical ECM showing the evolution of indentation hardness with the representative strain (ratio of the contact radius to the radius of the indenter), where the Brinell hardness was estimated using a combined approach involving spherical ECM and von-Mises criteria. In the end, hardness and fracture toughness for the rail steels saw close values with conventional testing approach but still needs further study.

Chapter 7 summarizes the main contributions of this project and offers recommendations for future studies that have the potentially for actualizing the non-destructive testing for mechanical and fracture toughness testing for an investigation or condition-based maintenance purpose for high strength rail steels and metal alloys.

The methods offered in this work consider the inclusion of pressure dependency in terms of stress triaxiality in the plastic energy component from indentation on existing analytical models (critical strain model and limit load analysis) for the measurement of fracture toughness for rail steels. The stress triaxiality effect within the models presented aided in balancing the extensive plastic deformation that occurs during indentation, thereby reducing the equivalent plastic strain needed for micro-fracture initiation.

Chapter 2 Indentation Testing Method for Determining Mechanical Properties and Tensile Flow Curve of High-Strength Rail Steels[1]

2.1 Introduction

It is imperative to determine the structural integrity of newly manufactured or in-service metallic structures as this gives vital information about their ability to perform adequately in the designed operating conditions [72–74]. In order to determine the integrity of structures, inspections to reveal the mechanical properties, information about flaws and residual stresses are required [72, 75–77]. Although achieving some of these inspection procedures are done non-destructively, the mechanical properties like yield strength and tensile strength are mostly obtained based on destructive test methods following the standards of the American Society for Testing and Materials (ASTM) using specified specimen dimensions. Further challenge comes for in-service static structures like railways, pipelines, pressure vessels and nuclear reactors, where continuous monitoring is required due to varying factors like deviation from operating conditions, age, and external stresses. It is important to determine and monitor the structural integrity of these in-service metallic structures with an alternative, cost-effective and non-destructive approach. Currently, the non-destructive approaches are based on acoustic emission (AE) or ultrasonic testing [81], which could not quantify accurately the change of mechanical properties such as tensile strength and fracture toughness.

One non-destructive technique that has the potential to quantify the mechanical properties is the instrumented ball indentation technique. Although in this study, specimens were cut out of parent material, the principles developed could be applied to structures in service. In this way, the degree of damage introduced by the indentation is far less than that attained during a destructive tensile test. Our definition of non-destructive is that cracks, fracture, or propagation of any crack within the material is not initiated during testing.

[1] This chapter has been published in the following publication:

Okocha, S. I., Yu, F., Jar, P. Y. B., & Hendry, M. T. (2023). Indentation Testing Method for Determining Mechanical Properties and Tensile Flow Curve of High-Strength Rail Steels. Experimental Mechanics, 63(5), 839-852.

Additionally, the indentation depth of the test could be quite minimal by using indenters of small diameter. Therefore, the maximum indentation damage could be further reduced. Notable researchers have used this technique to characterise the mechanical properties and flow curves of different metallic structures [72, 79, 80–87, 88–90]. As early as the 19th century, the indentation technique was used for estimating elastic properties based on Hertz contact law [85] and Sneddon's elastic solution [94] while Tabor [90] pointed out the relationship between the hardness (Vickers and Brinell) and yield stress for metals in a plastic state. Furthering the work from Tabor, possibility has been shown for estimating mechanical properties in the elastic-plastic regime during indentation. One outstanding outcome was from the work of Doerner and Nix [96], where they utilized the data from indentation load and depth to estimate the elastic and plastic properties of a material. This created the bridge for improving the method for accuracy and precision as seen from the works of Oliver and Pharr [97] and Pharr, Oliver and Brotzen [98] for the proper estimation of contact depth due to the effect of sink-in and pile-up. The contact depth can be estimated with the assumption that the contact periphery sinks in a manner that can be described for an indentation process of a flat elastic half-space by rigid punches of simple geometry [98]. Francis as mention in [80, 84, 96] made some notable changes in estimating the representative or average stress (σ_r) from the pressure applied by the indenter on the material using a stress constraint (δ) that varies based on the deformation regimes experienced via spherical indentation. Using statistical analysis, Francis discovered that δ is a continuous function of the plastic zone development beneath the indenter tip, which was characterized by the material and geometric changes during the indentation. Haggag et al. [64 - 65] added some notable changes to the models established in Francis' work to describe the stress constraint during indentation, for establishing the σ_r required for stress-strain extraction from indentation. However, the methods [80, 84, 96] were only applied to establishing the stress-strain relationship for low carbon steels, by employing numerical approaches that showed a strong correlation with uniaxial tensile test data on the basis of the Hooke's law and the Hollomon's equation. It is not clear if their approach is suitable for high strength steels which exhibit lower ductility and different deformation behaviours from low carbon steels [73]. Although the work of Herbert et al. [100] could not properly reproduce the stress-strain curve for AL6061-T6, the works in [101-102] were able to obtain the stress-strain curves. However, the works of [101-102] utilized a different stress and strain constraint as suggested by Tabor and required the use of an inverse analysis via finite element computations, which included a finite-stiffness spring in series with the indenter

that provides support for assuming it to be rigid. This approach required lots of computation before finding the required specification of bounds for the model parameters, and limit on the number of iterations can be attained.

In the present work, possibility of using indentation testing to determine mechanical properties and the stress-strain relationship that are conventionally obtained from monotonic tensile test is researched upon for nine high strength rail steels. The mechanical properties attained via the indentation testing are in good correlation with results from conventional destructive tests and thus show practicability and applicability for stock rail characterization and/or railway track inspection, as well as other in-service static structures. An approach of adding an *adjusting parameter* (κ) from conventional indentation-based analytical model is suggested to account for the differences between indentation-based and tensile flow curves of different heat-treated high strength steels. A relative correlation was seen between κ and young's Modulus attained via indentation (E_s), which opens the avenue for stress-strain curve to be obtained using only analytical models for high strength steels.

At the end, κ is included in the expression for parameter ϕ to reconcile the difference in the plastic zone development and/or pressure sensitivity of indentation as compared to tensile loading. This in turn helps provide a quick means for determining the flow curve of the rail steels, which in standard test, is obtained in a destructive manner. Once successfully developed, the indentation loading has the potential be used for monitoring metals in service or serve as an alternative to the destructive testing for determining mechanical properties for new high-strength alloys.

2.2. The principle of instrumented ball indentation test

2.2.1 Mechanical properties determination

2.2.1.1 Young's modulus

Several studies have investigated the use of ball indentation techniques to determine mechanical properties of materials which range from Young's modulus (E), yield strength, hardness (H) and fracture toughness [21, 73, 85, 97–106]. The Young's modulus and hardness was specifically attained by focusing on the accurate measurement of the contact area and stiffness between the indenter and specimen from the unloading indentation curve while the yield strength focused more on understanding the deformation stages via indentation and identifying the initial yielding deformation stage. For the fracture toughness, a strain energy density method was deployed, which required

attaining a critical energy from indentation from a critical indentation depth at fracture point that is associated with a critical void volume fraction of ductile materials. The indentation process requires loading and unloading of the ball indenter into the specimen's surface [22] to estimate its mechanical properties. Figure 2.1 shows the schematics of a loaded and unloaded specimen. From the loaded scenario in Figure 2.1(a), the material pile-up defines the extent at which contact is attained in the material which defines the contact radius (a_c) as a function of the indentation depth. Once the indenter is unloaded from the specimen, there is an elastic recovery, resulting in the difference between the projected diameter (total diameter, d_t) and plastic diameter (d_p) along with the total depth (h_t) and plastic depth (h_p). Conventionally, Young's modulus is attained during unloading by the well-known method established by Oliver and Pharr [94, 95, 100], as expressed in Eq. (2.1) derived from the simple Sneddon's linear elastic solution between the indentation load and depth [21, 70, 105, 107].

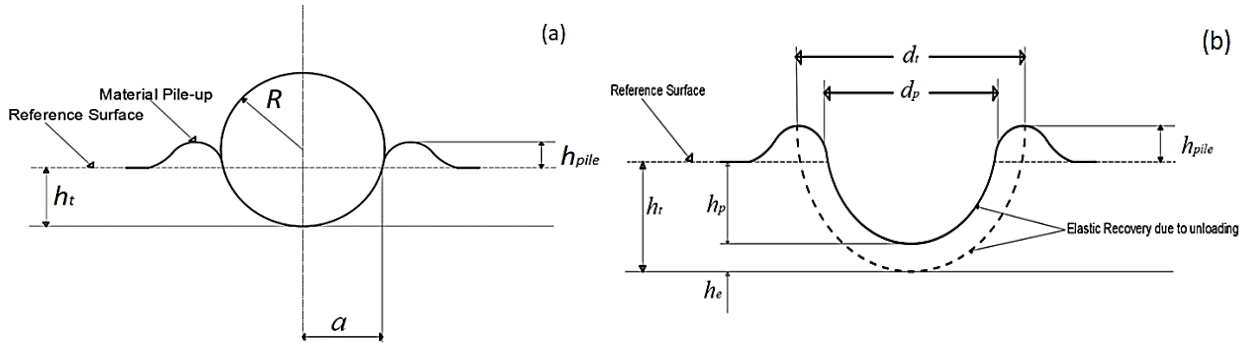

Figure 2.1Ball indentation testing illustration: (a) Loading of spherical indenter on a specimen, and (b) after-effect of an unloaded specimen.

$$E_r = \frac{\sqrt{\pi}}{2\beta}\frac{S_{\max}}{\sqrt{A(h_c)}} \tag{2.1}$$

where E_r is the reduced modulus as a result of contact between the indenter and the specimen, S_{max} is the stiffness between the indenter and the specimen and is derived from the initial slope of the unloading curve at the maximum depth, β is a geometric factor for different indenter shapes, performed by Kings [70] and taken as 1 for indenters with a circular profile, and $A(h_c)$ is the projected contact area experienced during the indentation process, of which the accuracy depends on the proper measurement of the contact depth and can be obtained using a geometrical relationship between the contact depth and diameter of the ball indenter [97]. The Young's modulus of the specimen (E_s) can thus be calculated using Eq. (2.2), if Young's modulus of the indenter (E_i) and

Poisson's ratios of the indenter (v_i) and specimen (v_s) are known. For cases where both E_s and v_s are unknown especially for newly developed materials, a relationship among the Vicker's hardness (H_v), E_s and v_s can be established, which is then combined with Eqs. (2.1) and (2.2) to determine E_s and v_s, as demonstrated by Zorzi and Perottoni [112]. This is seen from the relationship of H_v with the product of the squared Pugh's modulus ratio and shear modulus [40, 42]. In this study, however, the v_s for the rail steels is known to be 0.3, from the work by Yu et al. [73, 104], and is used in Eq. (2) to determine E_s.

$$E_s = \frac{1-v_s^2}{\frac{1}{E_r} - \frac{1-v_i^2}{E_i}} \tag{2.2}$$

2.2.1.2 Yield strength

According to Haggag et al. [65-66, 74], yield strength (σ_y) can be estimated using multiple indentation cycles by relating the total indentation pressure to the total indentation diameter (d_t) created within the material such as carbon steels, aluminium and titanium alloys that exhibit Lüders bands. Value for d_t can be attained geometrically as a function of the total indentation depth (h_t) and diameter of the indenter ($D=2R$), as seen in Eq. (2.3).

$$d_t = 2(h_t D - h_t^2)^{0.5} \tag{2.3}$$

With d_t determined, the relationship between the total indentation pressure, defined as P/d_t^2, and the total indentation diameter ratio (d_t / D) can be expressed using Eq. (2.4):

$$P / d_t^2 = \Psi_P (d_t / D)^{m-2} \tag{2.4}$$

where m is the Meyer's exponent according to the Meyer's Law [113]. The yield stress (s_y) can then be estimated using the value of Ψ_P in Eq. (2.4), multiplied by β_m which is a material constant for carbon steels and is taken as 0.2285 [65-66]. For materials that do not show Lüders bands, such as rail steels used in this study, a specific indentation cycle that shows the onset of E_s degradation should be used to determine the Ψ_P value in Eq. (2.4) in order to calculate the σ_y value. The determination of Ψ_P is explained later, in section 4.2.1 of this chapter.

2.2.1.3 Hardness

Hardness (H_M) as a mechanical property helps determine the scratch resistance or the plastic response on the surface of materials. Hardness has been shown to relate empirically to [101, 108–110] based on the slip line theory [107] for materials subjected to indentation processes. The Brinell hardness (H_B), based on the ball indentation processes, is the most popular method for the hardness measurement and its value is defined using Eq. (5) [108-109]. H_B is now a standard in ASTM E10 for measuring and comparing hardness of different materials [114]. For rail steels, H_B plays a vital role as it is used to quantify the wear resistance and load type of rail steels on which recommendations for operational speeds are made in order to maximize the useful life of the rails [115].

$$H_B = \frac{2P}{\pi D(D - \sqrt{D^2 - d^2})} \tag{2.5}$$

where d is the measured diameter of indent during the indentation process. Since d was not directly measured in this work, it was derived from $A(h_c)$, as $A(h_c) = \pi d^2/4$ and $A(h_c)$ can be determined from the contact depth (h_c) with a given indenter diameter. The hardness (H_M) expressed as $H_M = P / A(h_c)$, can still be used to express the relationship between P and h_c.

2.2.2 Effect of pile-up on contact depth and area

A challenge in the indentation process is the accurate determination of contact area, $A(h_c)$, as a function of contact depth for the E_s estimation. Doerner and Nix [96] presented the determination of E_s using indentation load-depth data, which was found to be not accurate enough but Oliver and Pharr [97] showed that the accuracy of E_s depends on the accurate measurement of $A(h_c)$ due to the presence of pile-up or sink-in effects generated from the indentation processes. Other researchers found the dependency of pile-up and sink-in effects on the strain hardening exponent (n) of the material [65 ,111], from the observation that materials with smaller n values exhibit pile-up phenomena for spherical indentation due to the plastic zone becoming less confined locally, hence having less resistance to dislocation motion. On the other hand, sink-in is caused by large restrictions to dislocation movement which leads to little or no spreading of the plastic zone in the material, and eventually results in the sink-in effect [94-95, 112]. It is important to put into consideration the pile-

up or sink-in effects for indentation processes for estimating h_c and $A(h_c)$ before E_s can be accurately determined.

Value for h_c is determined by including both the additional height caused by the pile-up and subtraction of the elastic recovery once the specimen is unloaded [111, 113-114], as seen in Eq. (2.6) which indicates that the accurate h_c determination requires accurate characterization of the pile-up effect (the second term) and the elastic recovery effect (the third term).

$$h_c = h_t + h_{pile} - \in \frac{P_{\max}}{S(h_{\max})} \tag{2.6}$$

where $\in$ represents a geometrical constraint and is taken as 0.75 for parabolic or spherical indenters [97], $h_{\max}$ and $P_{\max}$ the maximum indentation depth and force, respectively, attained via experiments, and h_{pile} the height of the pile-up with reference from the surface of the un-indented specimen. With the accurate h_c value, $A(h_c)$ can then be estimated using Eq. (2.7) for spherical indenters and then applied to Eq. (1) for determining E_r.

$$A\left(h_c\right) = \pi\left(Dh_c - h_c^2\right) \tag{2.7}$$

2.3 Materials and Methods

2.3.1 Materials

Materials used in the experiments are high strength rail steels, which are known for their high yield and tensile strengths in contrast to low carbon steel. Additionally, when compared to other steels, high strength steels possess hard wearing and resistance to cracking achieved by careful choice of the chemical composition and control over the cooling rate of the hot rail [115]. Table 1 shows the rail steels used in this study, provided by the Canadian National (CN) Railway Company and an undisclosed company (COMPX). Due to the confidentiality of the rail steels provided by COMPX, they are not mentioned in this paper. A total of nine rail steels were used to generate the required data for estimating the mechanical properties of the rail steels via the instrumented ball indentation testing.

Table 2.1 Rail samples and their microstructures

Rail Name /Identification number	Microstructure	Locations*	Company
JP	Deep head hardened	H, F	CN
EV	Deep head hardened	H, F	CN
CZ	-	H, F	CN
Rail #RCN (Control)	Micro head hardened	H	COMPX
Rail #2	Hypereutectoid	H	COMPX
Rail #3	Hypereutectoid	H	COMPX
Rail #4	Head hardened perlite	H	COMPX
Rail #5	Head hardened perlite	H	COMPX
Rail #6	Micro head hardened	H	COMPX

⁎ *H:Rail head, F: Base of the rail*

2.3.2 Mechanical tests

2.3.2.1 Tensile tests

The tensile properties were obtained from the previous work by Yu et al. [73, 114]. Tensile tests were conducted on smooth dog-bone specimens in the longitudinal direction of the rail steels following the recommendations of ASTM E8/E8M [120]. Results from the tensile tests, such as E, σ_y, ultimate tensile strength (UTS), the stress-strain relationship, the strain hardening exponent (n) and fracture strain ($\varepsilon_f{}^*$), were used as a reference to evaluate accuracy of results from the indentation tests.

2.3.2.2 Indentation Tests

The indentation tests were carried out using an in-house-designed indentation test equipment as shown in Figure 2(a) for extracting the *P-h* curves of the rail steels, as illustrated in Figure 2(b). The specimen was extracted from one-half of railhead with 10mm in thickness without any flaw. The ball indenter is made of tungsten carbide with a diameter of 1.19mm, having mechanical properties of E_i of 480GPa, and ν_i of 0.28. Eqs. (2.1) – (2.7) were used to estimate the mechanical properties of the rail steels. Ten different indentation cycles were performed on each rail steel sample at 5 different locations (a total of 50 indents per rail steel) in which the average values were used to represent the mechanical properties via indentation. The ten indentation depths were 0.04, 0.06, 0.09, 0.12, 0.18, 0.24, 0.3, 0.36, 0.42, and 0.48 mm as a displacement-controlled experimentation. Crosshead speed of 0.1 mm/min was used at both loading and unloading stages. The indentation load was recorded

with a resolution of 0.01N using an MTS load cell while the indentation depth was measured using a clip-on extensometer with a resolution of 3μm. With a careful observation through optical microscopy, h_{pile} can be measured. This was achieved using a digital optical microscope of 320X magnification and a digital dial indicator with a resolution of 2.54μm. To achieve this, vertical position of an un-indented flat surface near the indent was recorded to serve as a reference point. The vertical position of the pile-up section was then recorded in the same procedure. Difference of the readings from the reference represents the local height of the pile-up (h_{pile}). An average based on five h_{pile} measurements for each indent was determined for the use in Eq. (2.6).

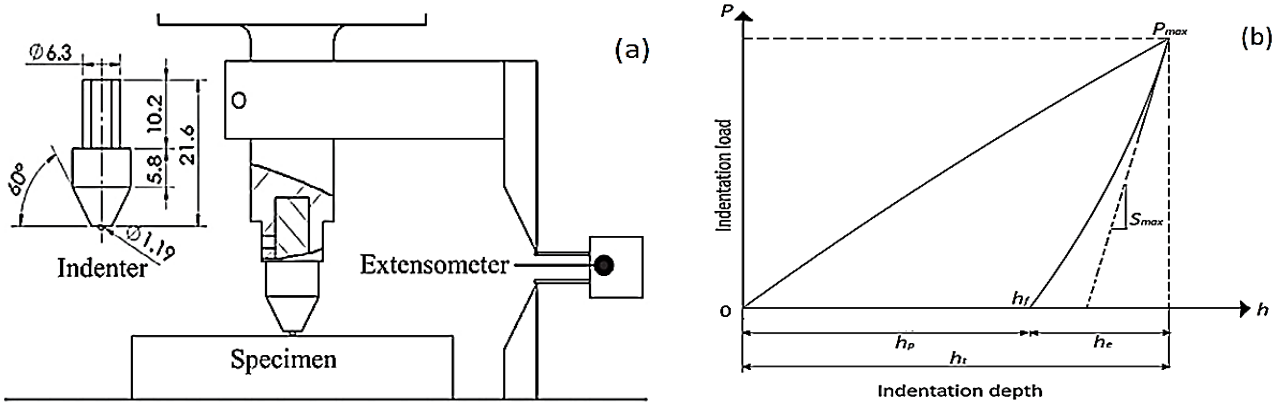

Figure 2.2 Schematics of the instrumented indentation test: (a) illustration of the in-house developed ball indentation equipment [2], and (b) a typical loading-unloading curve showing the estimation of S_{max}.

2.4. Results

2.4.1. Tensile test of smooth specimens

Outcomes from the tensile tests, coupled with the extensometers, are the force-displacement and force-diameter relationships, which were used to calculate the true stress-strain relationship. Figure 2.3 shows the true stress-strain relationship for JP, EV, and CZ rail steels, with the point of fracture marked as 'X' as the fracture stress (σ_f) and strain (ε_f). Table 2 provides a summary of all rail steels and their mechanical properties from the tensile tests. As reported by Yu et al. [119], the equivalent stress-strain curves were established in finite element (FE) modelling so that the model could regenerate the experimental load-elongation curve and cross-section reduction through an iterative procedure.

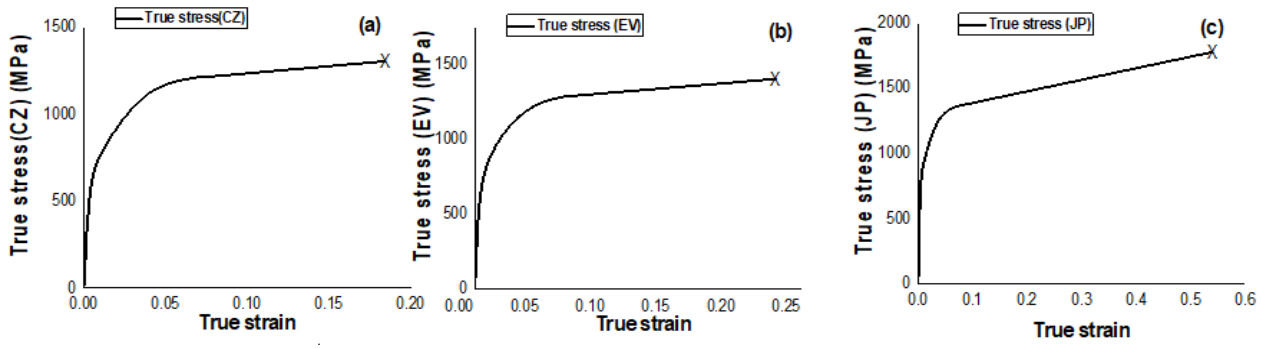

Figure 2.3. Typical true stress-strain diagram for the rail steels: (a) CZ, (b) EV, (c) JP [114]

The Young's modulus was attained from the linear elastic regime of the stress-strain curve, while the yield strength is attained using the corresponding engineering stress at 0.2% of the plastic strain [99, 116–118]. The Voce model [73, 114] was used to determine the strain at onset of necking (ε_n), as well as ultimate tensile stress (σ_{UTS}) while the Holloman's model [73, 114] was used to attain the strain hardening exponent (n) and the strength coefficient constant K.

Table 2.2 Average tensile properties for the nine rail steels for both rail head (H) and base of the rail (F)

Rails	Location	E (std_dev) (GPa)	σ_y (MPa)	σ_{UTS} (MPa)	n	σ_f (MPa)	ε_f
JP	H	200 (18)	820	1330	0.086	1776	0.504
EV	H	196 (13)	714	1207	0.085	1468	0.301
CZ	H	193 (8)	632	1130	0.082	1303	0.183
Rail #2	H	200 (9)	941	1580	0.03285	1735	0.260
Rail #3	H	200 (8)	925	1529	0.0399	1682	0.241
Rail #4	H	185 (9)	943	1544	0.05009	1782	0.466
Rail #5	H	190 (6)	936	1498	0.01003	1678	0.638
Rail #6	H	220 (4)	887	1492	0.05485	2003	0.514
Rail # RCN	H	200 (7)	870	1473	0.05027	1699	0.381
JP	F	196 (3)	693	1168	0.0904	1481	0.345
EV	F	187 (4)	655	1143	0.07	1404	0.295
CZ	F	205 (2)	635	1135	0.075	1307	0.201

H:Rail head, F: Base of the rai, std_dev :Standard deviation

2.4.2 Non-destructive indentation test

2.4.2.1 Determination of E_s, H_B, and σ_y

Determining E_s using indentation tests requires the use of Eqs. (2.1) and (2.2). At first, the load-indentation depth curves of different cycles were obtained, and E_r calculated with the consideration of the load frame compliance (C_f). In this study, C_f was determined using a standard hardness testing block with H_B of 203MPa (HBW 10/3000) and Young's modulus of 210GPa. The stiffness S_{max} of each cycle was calculated based on the slope (dp/dh) of the power-law relationship using $P = B\left(h_t - h_f\right)^m$ of the initial unloading curve (i.e. the upper 50% of the *P-h* data [20, 22, 41]) where the parameters *B* and *m* were attained by using a least-squares fitting procedure. It should be noted that the stress relaxation caused a small load decrease at constant indentation depth, as shown in Figure 2.5. This occurred when the indenter was held at a given stroke for approximately 15s before unloading started. This part of the unloading curve was not used in the calculation of S_{max}.

Once the S_{max} is attained, Eqs. (2.1) and (2.2) are used to determine E_r and then E_s values for each rail steel. As the number of the loading cycle increases, the calculated E_s value decreases due to in-situ indentation induced damage with the increase of indentation depth [125]. Figure 4(a) shows the E_s degradation for JP, EV and CZ steels as indentation depth increases, and Figure 4(b) compares *E* value for each rail steels with their corresponding estimated indentation E_s values. The line of equality shows how well the indentation results compare with tensile outcomes detailing the extent of deviation amongst the nine rail steels. The deviation of E_s for Rail #4 (R#4 in Figure. 2.4(b), according to Shuman et al. [103], can be attributed to the reverse plasticity added to the elastic recovery during unloading, which results in increase of the apparent elastic modulus. Although the reverse plasticity should have occurred in all rail steels to cause a slight increase of their apparent E_s values, it is not clear why such an increase is very significant for R#4 and needs further investigation.

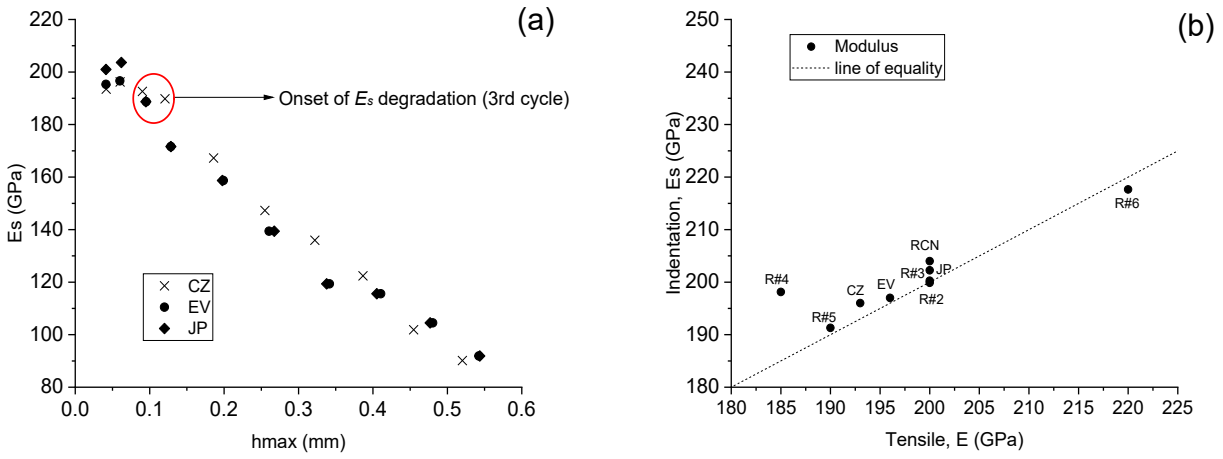

Figure 2.4 Estimation of E_s via indentation: (a) degradation of E_s with increase of indentation depth (h_{max}), and (b) comparison between tensile E and indentation E_s

H_B of the rail steels was also determined according to the guidance of ASTM E10-18 [113] using Eq. (5). Following ASTM E10-18 [113] guidance, the average H_B values and their standard deviation were determined at small indentation depths using the designated test force corresponding to the force-diameter ratio for the indenter of 1.19mm in diameter. As shown in Figure 2.5, the H_B values were found to be within the range of H_B for high-strength rails according to ASTM A1 – 00 [126].

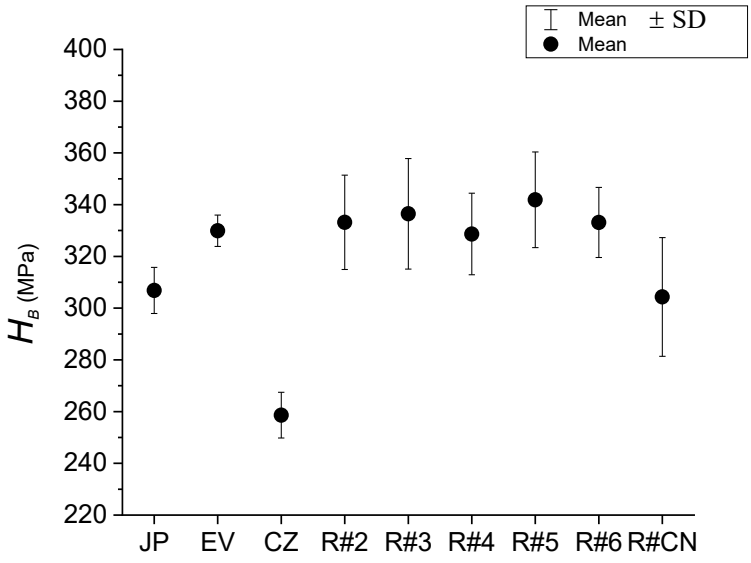

Figure 2.5 Average H_B for the rail steels.

In order to investigate the evolution of hardness through the depth of the rail steels, the H_B was estimated as a function of the indentation depth. Figure 2.6 illustrates the variation of H_B on the railhead from the original cross-sectional surface as a function of depth. The figure shows that JP and R#2 are the hardest rail steels, with the former showing a larger hardness variation than the latter, followed by EV, R#3 and R#5. CZ which had no heat treatment has the lowest hardness.

The hardness evolution with the increase of indentation depth can be characterized into two sections. The first section (I), with h_{max} below 0.18 in Figure 2.6, shows an increase in hardness with the increase of h_{max} due to localized hardening effect, as reported in the works of Swadener et al. [127], Pharr et al. [128] and Voyiadjis and Yaghoobi [129] on nano-indentation of single crystalline and polycrystalline materials. According to the indentation size effect (ISE) [122-124] movement of the initial nucleation and evolution of geometrically necessary dislocations (GNDs) beneath the indenter can be blocked at the grain boundaries, causing a local hardening and pile-up stresses as seen in section I of Figure 2.6. Once this pile-up stress attains a critical value, the dislocations dissociate to the next grain, causing reduction in the hardness as seen in section II of Figure 2.6 [127]. Nix & Gao [130] also developed the strain plasticity gradient law by relating the square of hardness degradation and inverse indentation depth in section (II) of Figure 2.6.

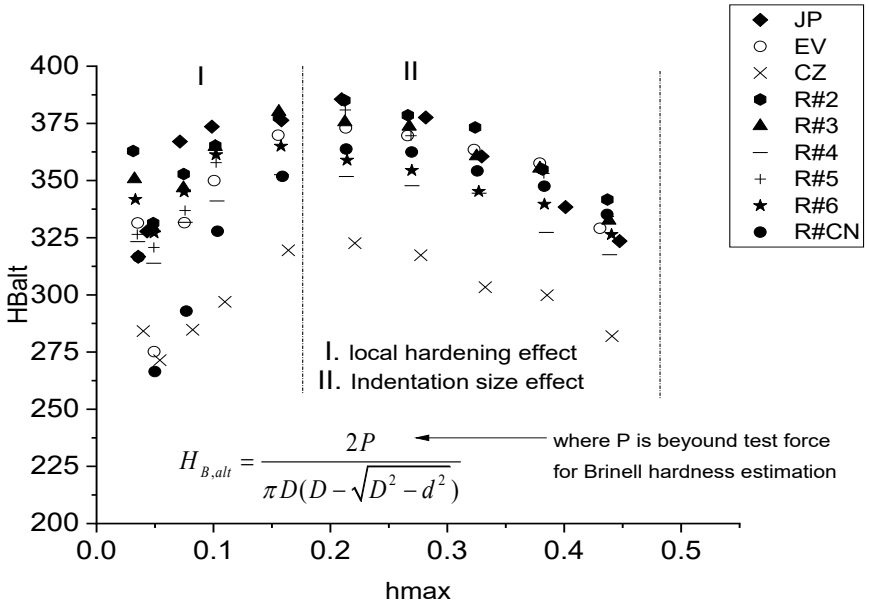

Figure 2.6 Evolution of hardness with indentation depth showing local hardening effect and hardness degradation

The σ_y values for the rail steels are also estimated via indentation by implementing Eq. (2.4). Figure 2.7(a) shows the plot and procedure for determining the σ_y value, using data for JP rail as an example. Note that the procedure used here is similar to the work by Haggag et al. [65, 74] but in this work only the cycle that shows the onset of E_s degradation, as indicated in Figure 2.4(a) is used to determine the σ_y value. In the work by Haggag et al., on the other hand, all indentation cycles were used to estimate σ_y values. Figure 2.7(b) summarizes σ_y for the nine rail steels via the indentation tests and compares the values with those via tensile tests.

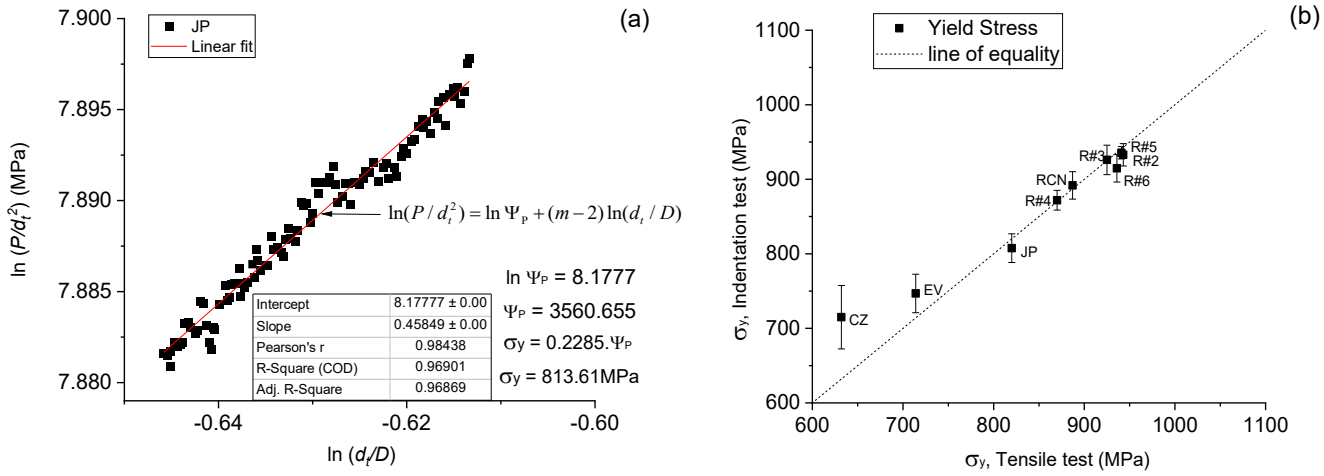

Figure 2.7 Estimation of σ_y via indentation: (a) σ_y estimated from parameter Ψ_P for JP rail steel, and (b) comparison between tensile σ_y and indentation σ_y for the nine rail steels.

2.4.2.2 Determination of elastic-plastic flow and strain hardening exponent

A power law equation, as expressed given in Eq. (2.8) below, has been suggested to express for the stress-strain relationship in the plastic regime for metallic materials [65, 74, 109, 126]. However, the use of the indentation process to determine the strain hardening exponent (n_s) can be quite challenging because the indentation loading introduces multiaxial stresses as opposed to the uniaxial stress in tensile test of smooth specimens.

$$\sigma_{a,p} = K_s \varepsilon_{a,p}^{n_s} \tag{2.8}$$

where K_s is the strength coefficient via the indentation test, and $\sigma_{a,p}$ and $\varepsilon_{a,p}$ the average stress and average strain in the plastic regime respectively.

Understanding evolution of the average stress and the average strain in the plastic regime of the indentation deformation requires a proper characterization of the entire deformation regime. Park and Pharr [132] conducted FE analysis of the indentation deformation using a spherical indenter in the elastic-plastic transition regime. Their study suggested the use of the relationship between two parameters, $\delta = p_m/\sigma_r$ and $\Lambda = E_r a / \sigma_y R$, to characterize stress-strain curve under spherical indentation, and described the difference among deformation regimes that occurred during indentation. Hence, evolution of δ and Λ in the indentation process is essential and needs to be understood for estimation of the stress-strain curve for the rail steels [22, 74, 127]. In general, values for δ are considered to increase from elastic deformation to fully plastic deformation [66, 81, 127-128].

Park and Pharr [132], based on the Hertzian contact law, suggested that yielding is quickly initiated beneath the surface at the initial indentation stage, at $\Lambda = 2.52$ and δ slightly less than 1.1 when the material recovers elastically after removal of the load. This is consistent with the suggestion by Mesarovic and Fleck [133] using FE modelling, that yielding is initiated when $\delta \approx 1.07$ and $\Lambda \approx 2.5$. With a further load increase, the deformation regime becomes transitional as the plastic zone continues to evolve and spread outwards and upwards, though still being constrained by the surrounding elastic regime until δ reaches 1.5 and Λ reaches 3.5 [132]. Before this point is reached, the elastic-plastic region is believed to experience pseudo-Hertzian characteristics, i.e. the elasticity-dominated transition regime which is affected by n_s of the material. However, Mesarovic and Fleck [133] did not observe the pseudo-Hertzian characteristics. Rather, their observation has suggested that the plot of δ versus Λ shows no obvious departure from linearity at the onset of yield until d reaches 1.6 [133] . The study of Park and Pharr [132] suggested that variation of n_s in the elastically dominated transitional regime is reflected by the variation of the slope values for the deformation responses to the indentation loading.

Increase of the load beyond the elasticity-constrained transitional regime causes the plastic zone to break out of the indented surface, corresponding to the regime at which the effect of plasticity becomes apparent when δ reaches 2.1 and Λ reaches 10 [132]. After this point, the transitional regime

becomes plastically dominated but is still constrained by the surrounding elastic regime. Studies from Oliver and Hernot [82] suggested that effect of plasticity becomes apparent when Λ reaches 12, similar to the study in [132]. However, with a further increase of the loading, additional plastic zone grows and spreads laterally on the indentation surface till the plastic zone is fully developed (i.e., in the full plastic regime). This full plastic regime is sometimes defined by a sharp deviation of the slope in the plot of δ versus Λ. Park and Pharr [132] suggested that for metals, Λ for the full plastic regime is in the range from 50 to 200. Other works suggested a different range of Λ values. For instance, Johnson [22] showed that for elastic-plastic indentation, the full plastic regime started at $\Lambda = 40$, while Mesarovic and Fleck [133] suggested that for materials with a wide range of E_r/σ_y values, Λ is in the range from 40 to 50 for the full plastic regime. Pane and Blank [134] considered $\Lambda = 80$ for σ_y/E_r values in the range from 0.001 to 0.0017 while Taljat and Pharr [135] suggested the use of $\Lambda = 110$ for elastic–perfectly-plastic materials with $n_s = 0$ and a friction coefficient $\mu = 0.2$ to define the initiation of a full plastic regime. It is believed that the range of Λ values for the full plastic regime lies on the ductility responses and fracture toughness of the metals. Steels with higher fracture toughness or larger E/σ_y values, such as low carbon steels, tend to have larger Λ values than steels with lower facture toughness or smaller E/σ_y values, such as high strength steels [84]. For the deformation to transit from elastic to plastic regimes under spherical indentation, Haggag et al. [77] showed that the typical δ values in a range from 1.12 to 2.87 are needed to establish the average stress σ_r [74, 126].

In the current study, stress (σ_t) and plastic strain (ε_p), defined by Eqs. (2.9) and (2.10) respectively, are used to establish the stress-strain curves from instrumented ball indentation tests and compared with the stress-strain curves established from the standard tensile test.

$$\sigma_t = \frac{P}{A(h_c)\delta} \tag{2.9}$$

$$\varepsilon_p = 0.2\frac{d_p}{D} \tag{2.10}$$

where d_p is the diameter of the indentation after unloading. Note that in this work, d_p value is estimated using Eq. (2.11) [66, 74, 78, 87]. Further insight into d_p is seen in Appendix 2

$$d_p = \left\{ \left[3PR\left(4h_p^2 + d_p^2\right) \right] / \left[E_r \left(4h_p^2 + d_p^2 - 4h_p D\right) \right] \right\}^{1/3} \quad (2.11)$$

To calculate σ_t using Eqn. (2.9), δ value is needed. Among the analytical approaches used to determine the δ value, some approaches require the prior knowledge of n_s [86, 126, 131-132] while the others do not [22, 65, 74, 77, 79, 97, 133]. In this study, a set of analytical equations based on the work by Haggag et al. [65, 74] are used to determine the δ values, as shown in Eq. (2.12).

$$\delta = \begin{cases} 1.12 & \phi \le 1 & \text{elastic} \\ 1.12 + \tau \ln \phi & 1 < \phi < 27 & \text{transition} \\ \delta_{\max} & \phi > 27 & \text{plastic} \end{cases} \quad (2.12)$$

where ϕ as defined in Eq. (2.13), is used to characterize the development of the plastic zone beneath the indenter, τ as defined in Eqn. (2.14), is a multiplicative constant to represent the incremental development of the plastic zone, and $\delta_{\max}$ is a parameter proportional to strain rate (α_m) introduced in the test, as shown in Eq. (2.15). For quasi-static strain rates the proportionality between $\delta_{\max}$ and α_m is taken as 2.87 [65, 74].

$$\phi = \varepsilon_p E_s / 0.43\sigma_t \quad (2.13)$$

$$\tau = (\delta_{\max} - 1.12) / ln(27) \quad (2.14)$$

$$\delta_{\max} = 2.87\alpha_m \quad (2.15)$$

It should be noted that σ_t in the transition regime (i.e., for f values between 1 and 27) needs to be attained via iterations.

By employing Eqn. (2.12), a plot of δ versus Λ for the nine rail steels is shown in Figure 2.8. The figure suggests that full plastic regime is developed in the rail steels when Λ reaches 50.

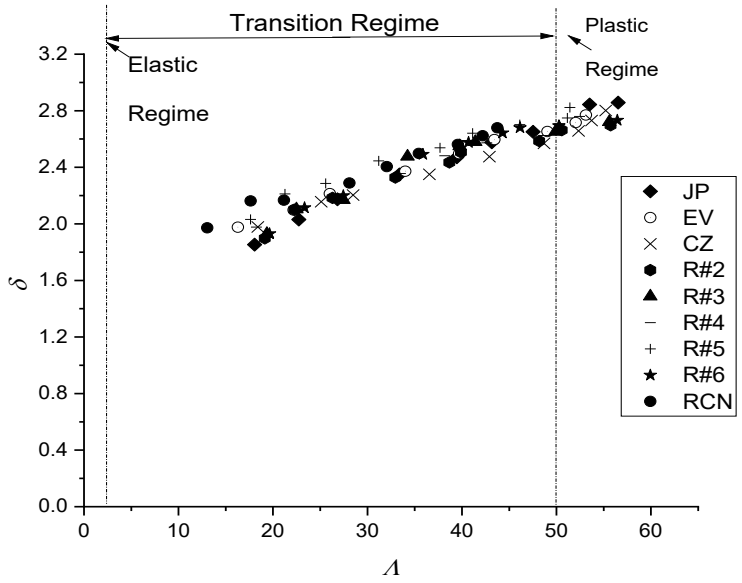

Figure 2.8. Plot of the elastic-plastic regime for the 9 rail steels.

Haggag's model suggests that δ value ranges from 2.03 to 2.86 with a linear increase in the deformation regime, suggesting a gradual increase in the flow properties with the increase of indentation depth. In this study, full plasticity occurs when $\Lambda > 50$ which is consistent with other studies [81, 127-128]. Note that the relationship between δ and Λ for the rail steels, based on Haggag's model, is similar to the relationship between δ and Λ for other materials [81, 127-130].

To further characterize the mechanical behaviour of the rail steels in indentation, n_s needs to be estimated. To attain n_s, Eq. (2.8) was used in the log-log scale to relate the average stress and average strain for $\Lambda > 50$. In this study, in the full plastic regime $\sigma_{a,p}$ is taken as σ_t from Eq. (2.9) and $\varepsilon_{a,p}$ taken as ε_p from Eq. (2.10). It is important to note that only the last two loading cycles of indentation tests conformed with Eq. (2.8) and were used to estimate n_s values, in contrast to all loading cycles reported by Haggag et al. [65, 74]. This is possibly caused by the high multiaxial stress state and localized hardening that occurred beneath the indenter for rail steels. As an example, Figure 2.9(a) shows the estimated n_s for JP rail steel which was attained from only a small fraction of the loading indentation cycle while Figure 2.9(b) shows the comparison between n_s from indentation and tensile tests for the nine rail steels.

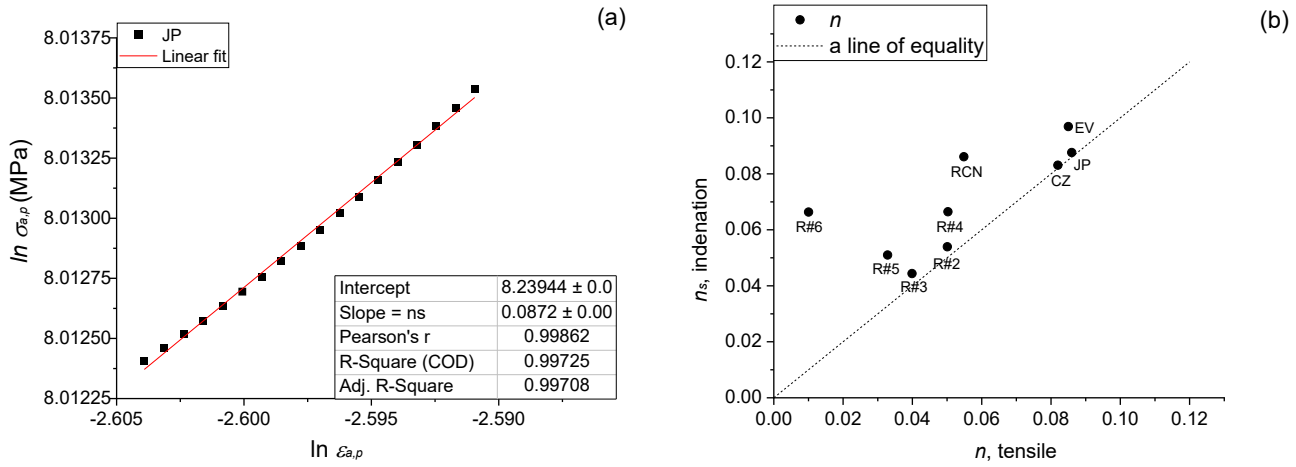

Figure 2.9 Estimating n_s for the rail steels: (a) Exponent of the power-law equation for JP rail steel, and (b) comparison between tensile n and indentation n_s for the 9 rail steels.

2.4.2.3 Establishing the tensile stress-strain field

The flow curve estimated via indentation method is compared with stress-strain curve from tensile test for JP rail steel, as shown in Figure 2.10(a). The transition from elastic to plastic deformation is quite similar between the two curves, signifying that the same type of constitutive equation as seen in [73, 114] can be used for both tensile and indentation tests (i.e. Hooke's law for elastic response, Voce equation for obtaining saturated stress (σ_s) for elastic-plastic response and Hollomon's equation and power law for full plastic response). However, the indentation stress-strain curve shows higher stress values, compared to tensile counterpart, possibly attributed to the multiaxial stress state that occurs during the indentation. As already discussed, other potential reasons for the higher stress values can be attributed to the imperfect indenter effect as suggested in some works [131] and ISE [122-124]. However, studies from [72, 139]suggest that the higher stress is attributed to pressure-sensitivity (hydrostatic pressure) of the rail steels in compression as to tensile test. Flow curves for JP, EV and CZ under indentation are presented in Figure 2.10(b) and compared with their tensile stress-strain curves. Figure 2.10(b) indicates the viability of estimating the tensile stress-strain curves from indentation loading and to determine if they follow a similar sequence notwithstanding the higher stress values experienced via indentation. It can be seen in Figure 2.10(b) that the ranking order from indentation flow curve estimation follows the same sequence with tensile stress-strain curve for the three rail steels.

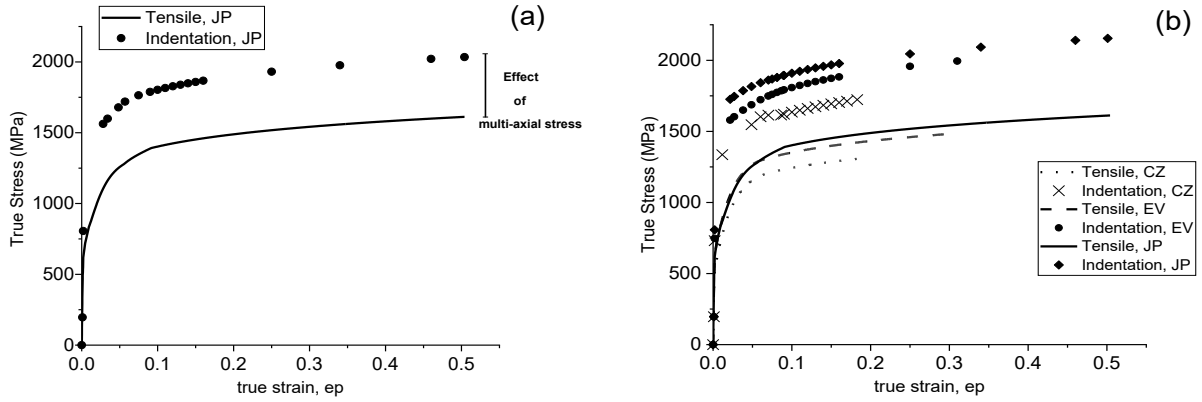

Figure 2.10. Flow curve estimation via indentation: (a) difference between tensile and indentation flow curves estimation for JP rail steel, and (b) sequencing tensile and indentation stress-strain curves for JP, EV and CZ rail steels.

To match the indentation flow curve with tensile stress-strain curves, the indentation stress values are adjusted by adding a correcting parameter (κ) to ϕ in Eq. (2.13) to account for the high stress triaxiality effect [73, 104], as expressed in Eq. (2.16). The modified parameter, ϕ_k, describes the role of material properties and geometric constraints during indentation on the stress response to deformation. A summary for the process for attaining the approximate flow stress and its limits before and after the incorporation of κ are shown in Figure 2.11, which shows the iterative steps required.

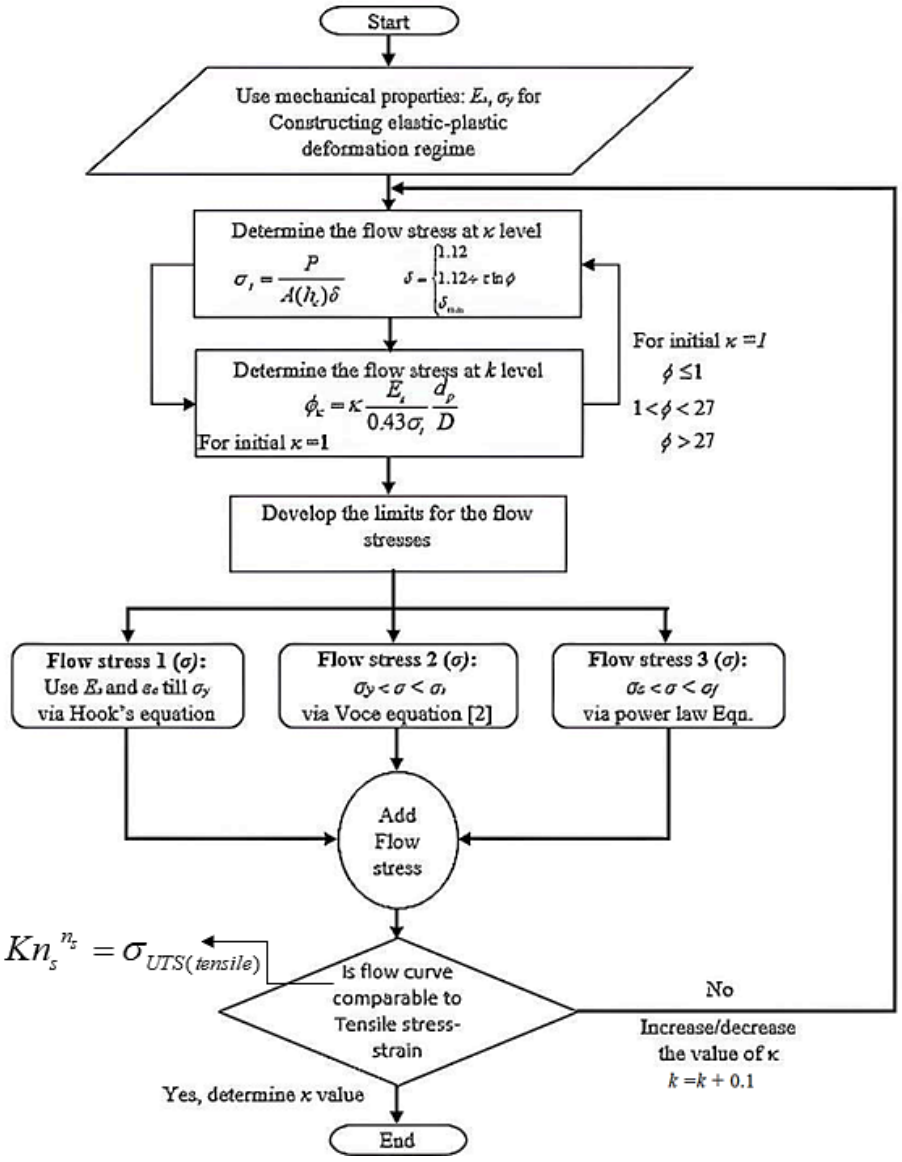

Figure 2.11. A flow diagram for obtaining the approximate tensile stress-strain via spherical indentation.

Figure 2.12 shows the stress-strain field generated via indentation for the nine rail steels using ϕ_k in Eq. (2.16). Table 3 summarizes all κ values for the nine rail steels. It is important to note that values for κ were determined only for the spherical indenter of 1.19mm in diameter. Further studies are needed to examine how the indenter size affects the κ values.

$$\phi_\kappa = \kappa \frac{E_s}{0.43\sigma_t}\frac{d_p}{D} \tag{2.16}$$

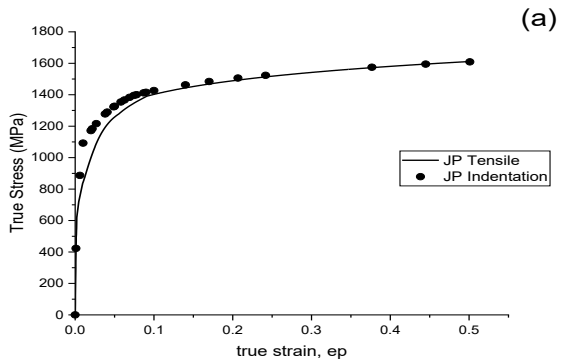
(a)
True Stress (MPa)
true strain, ep
JP Tensile
JP Indentation

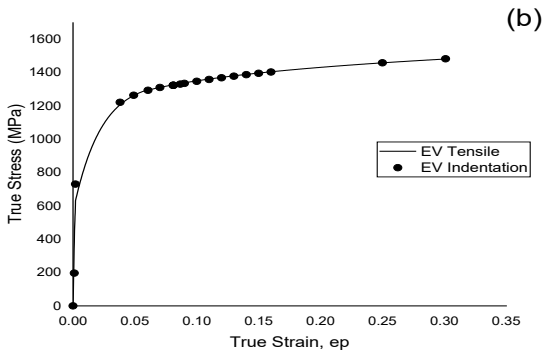
(b)
True Stress (MPa)
True Strain, ep
EV Tensile
EV Indentation

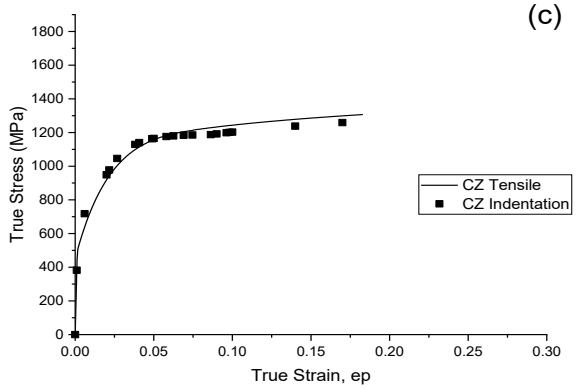
(c)
True Stress (MPa)
True Strain, ep
CZ Tensile
CZ Indentation

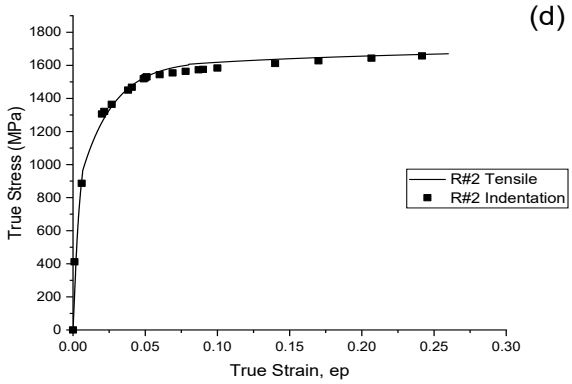
(d)
True Stress (MPa)
True Strain, ep
R#2 Tensile
R#2 Indentation

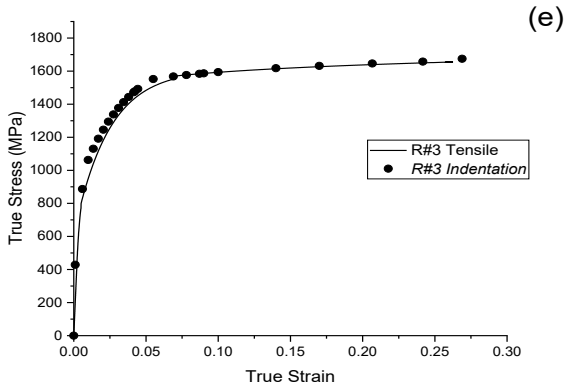
(e)
True Stress (MPa)
True Strain
R#3 Tensile
R#3 Indentation

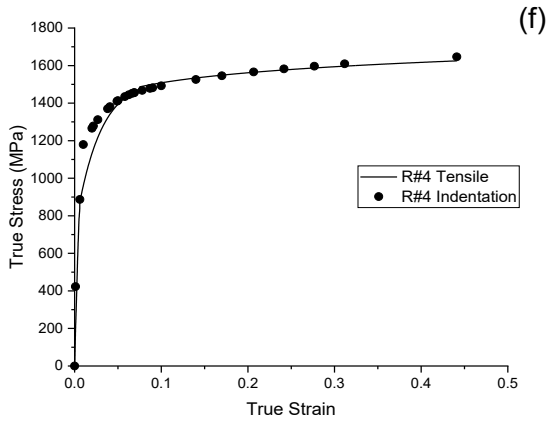
(f)
True Stress (MPa)
True Strain
R#4 Tensile
R#4 Indentation

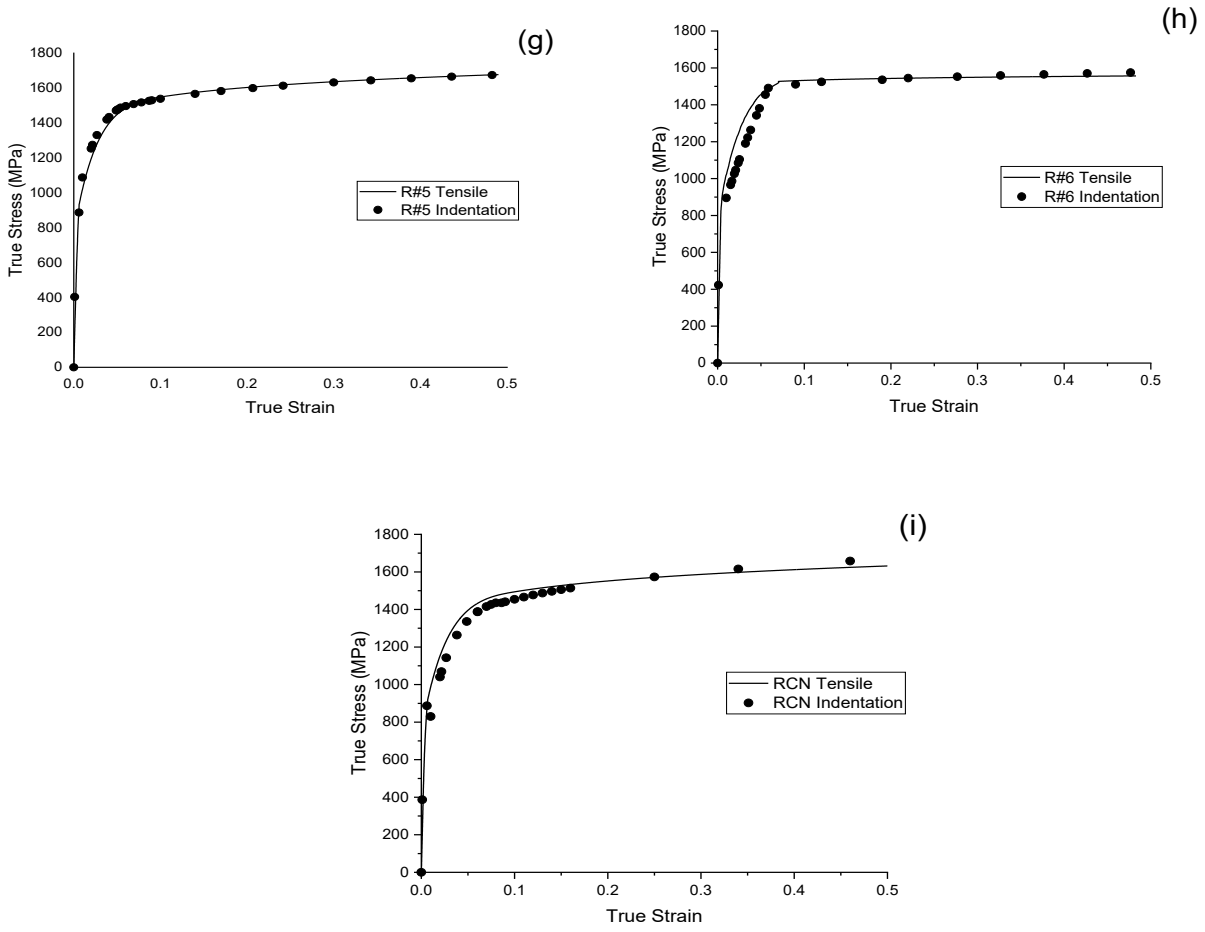

Figure 2.12. Combined true stress-strain estimation (tensile and ball indentation) of high-strength steels: (a) JP, (b) EV, (c) CZ, (d) R#2, (e) R#3, (f) R#4, (g) R#5, (h) R#6, and (i) RCN.

Table 2.3 The adjusting parameter, κ, for the nine rail steels for indenter diameter of 1.19mm.

	JP	**EV**	**CZ**	**Rail #2**	**Rail #3**	**Rail #4**	**Rail #5**	**Rail #6**	**Rail RCN**
k	4.2	4.5	4.5	3.0	2.8	2.5	3.3	2.5	4.8

The κ values are also compared with an average Young's modulus, E_s, from different indentation tests for the nine rail steels, as shown in Figure 2.13. The correlation between κ and E_s suggests that Young's modulus has some contributions to variation of k values. Hence, κ value can be estimated based on E_s, and then tensile stress-strain curves for the high-strength rail steels can be constructed

using results from indentation loading, especially in a local region that cannot be obtained using the conventional standard tensile test. This possibility needs to be further studied.

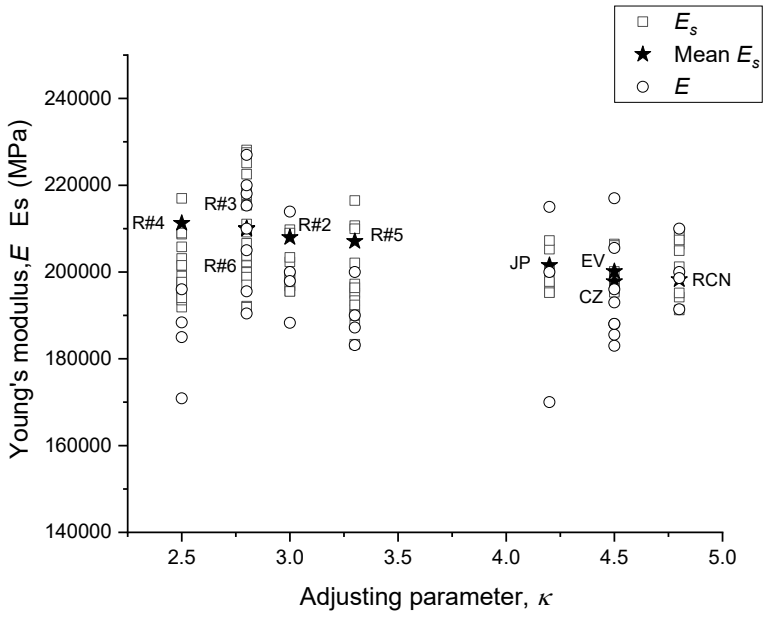

Figure 2.13 Relationship between κ and E_s, E

2.5. Discussion

In view of determining the mechanical properties and flow curves of rail steels via indentation, three considerations are discussed in this section. The first consideration focuses on the estimation methodology of σ_y for high strength rail steels in contrast to low carbon steels reported by Haggag et al. [65, 74]. The second consideration discusses on the local hardening effect seen at the initial stage of hardness estimation before subsequent hardness and modulus degradation while the third consideration focuses on the role of k on estimating tensile stress-strain via indentation.

The σ_y was attained using the immediate cycle at the onset of E_s degradation rather than the entire indentation cycles as done in [65 -66 ,77 ,134]. For the high strength steels, the Voce tensile constitutive equations as reported in Yu et al. [73, 104] fits with the deformation stage where plastic strain increases as a result of an increase in the hydrostatic stress till it reaches the saturation stress, σ_s, before the plastic flow occurs. Hence, using the entire indentation cycles after the E_s degradation for σ_y prediction as done in [65 -66 ,77 ,134] would give a wider expected range of σ_y values.

Considering that σ_y and hardness measure the same property for the onset of plastic deformation, the hardness of the rail steels was measured using H_B. Figure 2.6 shows an initial rise of H_B before it reduces with the increase of depth. This behaviour is also experienced by of Swadener et al. [127], Pharr et al. [128] and Voyiadjis and Yaghoobi [129], signifying occurrence of the local activities that results in the local hardening effect in the region of initial rise of hardness while the first point of reduction of H_B with increasing depth translates to the onset of plastic deformation. Based on ISE, local hardening and pile-up stresses attributes to this behaviour coupled with multi-axial stresses from the indenter's tip which are potentially responsible for the high stresses experienced in the flow curve estimation as well as the large damage (modulus drop) experienced. According to the works of Chen et al. [141] and Zhang et al. [137], little damage could be introduced by the combined shear and compressive deformation alone under the indentation loading. However, decrease of E_s value in the range to 48-50%, as observed in this study, indicates the possible presence of other damage mechanisms, which may involve movement of initial nuclei and evolution of GNDs beneath the indenter. Chen et al. [141] and Zhang et al. [137] also attributed the increase in damage to the nucleation of the secondary voids and shear softening coupled with the existing voids.

The high stresses experienced in the flow curve estimation can be seen in Figure 2.10 which shows a similar pattern experienced for the rail steels. Figure 2.12 shows the flow properties estimated via indentation, which are in good agreement with the tensile stress-strain for the rail steels. This is achieved by including the correcting factor, k, to take into account the effect of multi-axial stresses on the stress-strain relationship via indentation. The relationship seen in Figure 2.13 suggests k to be a function of the rail steels' average Young's modulus. The reason for larger k is not fully understood since we do not have all information about the rail steels like the alloying composition. However, the concept of indentation plastometry [142] suggests that the fitting parameter for estimating flow stress is 'unique' for each material. This initiates that some mechanical properties are responsible for different fitting parameters (k) during flow stress estimation via indentation [142]. It is apparent that k might be related to other material properties and geometric changes (size of the indenter) and needs to be disassociated into parameters like hardness, stress triaxiality and possibly damage parameter due to indenter size in further studies.

2.6 Conclusions

In this chapter, the instrumented ball indentation tests were conducted to determine the mechanical properties for 9 rail steels non-destructively by using the load-depth data extracted from the experimentation. This was achieved using conventional contact mechanics principles. The main conclusions can be summarised as follows:

1. The estimation of E_s, $\sigma_{y,}$ H_B, n_s show that mechanical properties of metallic materials can be determined non-destructively. Values for the E_s, $\sigma_{y,}$ H, n_s match those attained from tensile data according to the works of Yu et al. [73, 104], showing the potentiality of indentation testing approach. Although the indention method in "monitoring metals in service" has not been fully validated for all materials, the initial value of E_s as well as its deterioration have the potential of providing an opportunity for structural health monitoring due to age, external loading, or unfavourable operating conditions.

2. The flow curve determined via the ball indentation approach is in good agreement with the tensile stress-strain relationship for the rail steels according to the works of Yu et al. [73, 104]. The stress constraint factor, δ, is continuous during the development of the elastic-plastic deformation regimes and should be adequately determined for estimating the average stresses needed for estimating the flow curve via indentation. However, the inclusion of k as an adjusting parameter shows the possibility of capturing the approximate flow properties of high strength steels that are subjected to multi-axial stresses. Attaining the flow stress is significant due to extracting uniaxial flow properties for material characterization (analytically or numerically) using an easy multi-axial loading approach (spherical indentation), which overcomes the challenges of using multiple specimens according to ASTM procedures, saves time and labour cost and ultimately provides flexibility using a miniature specimen.

In conclusion, mechanical properties as well as the stress-strain curve for high strength rail steels is predicted using only *analytical approach* of indentation force-depth curve, which is attractive for industrial application without the need for complex methodologies like FE modelling or continuum damage modelling (CDM). However, further insights on the characterization of k are required on a wider spectrum of high strength steels to enable its inclusion in the analytical procedures for flow curve estimation.

Chapter 3 Use of A Modified Critical Fracture Strain Model for Fracture Toughness Estimation of High Strength Rail Steels[2]

3.1 Introduction

Over the past decades, there has been substantial research work in the rail industry concerning rail derailments, which proposes that derailments are majorly caused by broken rails [4, 6, 137–141]. In fact, the work from Leishman et al. [3] suggests that on the Canadian main track, joint bar and rail anchoring and track geometry accounted for about 20% of derailments and 36% of derailed cars per derailment respectively. In 2020, a report from the Transportation Safety Board of Canada [5] presented investigations on a train derailment accident near Labuma, Alberta, which resulted from broken rails caused by pre-existing detail fractures (i.e. a group of fatigue defects known as transverse detail defects (TDDs), in which the fracture plane is perpendicular to the running direction of the rail [3]). Since broken rails constitute a high frequency among all rail issues, fracture toughness of the main track becomes a major concern, and it is postulated that main tracks with higher fracture toughness along with higher strength would present a higher operational safety condition. However, the challenges associated with using the standard methods for fracture toughness estimation, developed by American Society for Testing and Materials (ASTM) [58, 69], include the difficulty in specimen preparation, long specimen preparation time, and increasing cost related to multiple specimen preparations, which discourage the use of these standards. Hence, the need to develop new, efficient, and effective methods for estimating fracture toughness cannot be overemphasized [66, 73, 104, 142–147].

In the effort of developing simplified specimens (crack-less specimens) for fracture toughness estimation of ductile materials, one of the earliest approaches involves the work of Brown [153], which invariably considers the circumferentially notched cylindrical specimen as a fracture toughness screening test for ductile materials using the Irwin's stress intensity factor solution [154].

[3] This chapter has been published in the following publication:

Okocha, S. I., Yu, F., Jar, P. Y. B., & Hendry, M. T. (2023). Use of a modified critical fracture strain model for fracture toughness estimation of high strength rail steels. Theoretical and Applied Fracture Mechanics, 127, 104069.

Although, employing the circumferentially notched cylindrical specimen is not generally accepted as a standard for measuring K_{IC}, the substantial discrepancies between fracture toughness from circumferentially notched cylindrical specimen and K_{IC} is still being investigated. Further approaches using smooth tensile specimen for fracture toughness estimation are presented from the works of Haggag and Nanstad [66] and Oh [149], where the former applies a modified critical fracture strain model originating from Ritchie et al.[155] preposition of microstructural instability based on the localization of strain between large voids for A515 grade 70 Steel and A533 grade B Class 1 Steel while the latter [149], used the dynamic fatigue life model, which emphasized the use of specific surface energy for predicting the fracture toughness of 4340 steel, 2024 T3 aluminum and 7075 T6 aluminum. The outcome of the measured fracture toughness was consistent with the results obtained from ASTM E1820 and ASTM E399 methods [58, 69]. However, the lethargy coefficient and the atomic bonding forces required for fully utilizing the dynamic fatigue life model can be quite challenging to determine, especially for newly developed materials since there may be little information (properties) available.

Further advances in non-standardized fracture toughness estimation of ductile materials involves the works of Go and Swartz [156] using different energy methods to measure fracture toughness in terms of a critical energy release rate, which was attained using the J-integral method, the stress intensity factor method and the modified Peterson's method, all showing consistency for both extended and non-extended cracks. Yang et al. [109] further applied the energy method to miniature disk samples by considering the influence of geometrical constraints for small punch tests (SPT) based on membrane stretch analysis and categorizing the total energy into the elastic deformation energy, plastic deformation energy and fracture energy. This was done to effectively test miniature samples extracted from in-service components with the aim of characterizing, non-destructively, the fracture toughness of in-service materials. However, estimating the equivalent strain for the SPT posed a challenge because strain calculation by microscopic observation is not most suitable for direct strain measurement [103, 152-153]. The strain energy density (SED) criterion developed by Sih [159] for mixed-mode crack scenarios is another means of determining fracture toughness. This approach is to determine the strain energy per unit volume required before fracture of the specimen. Since Sih's criterion also considers the direction of crack propagation and modes of failure, it differs from the classical Griffith theory of fracture [155], as the latter does not consider crack propagation and different failure modes but rather focuses on the energy required to cause fracture. Other researchers

[98, 114, 155] also applied the SED criterion to predicting fracture for both micro and macro applications. Xue et al. [104] applied the SED criterion as a non-destructive indentation test for determining fracture toughness of high strength stainless steel. The predicted fracture toughness showed strong correlation with experimental values, which provides an opportunity for measuring the fracture toughness of materials, non-destructively. However, the use of a constant void volume fraction and determination of the critical damage value for ductile materials in the SED may vary for different ductile materials. Pertaining to non-destructive testing methods, the ball indentation technique has proven to be effectively used for ascertaining the structural integrity [65,98, 111, 114, 156–158] of materials while some researchers have explored into applying ball indentation for fracture toughness determination of both brittle and ductile materials [65, 73, 104, 111, 156–158]. Haggag et al. [65-66] showed that estimated fracture toughness ($K_{IC,\ pred}$) using an automatic ball indentation (ABI) test was averagely 0.4% higher and 0.425% lower than the measured K_{IC} for A533 Grade B Class 1 and A515 grade 70, respectively, at room temperature, using a modified critical fracture strain model. However, the approach does not work for all steels (for example, using mechanical properties from rail steels used in this study) especially when steels manufactured using low, medium, or high carbon contents are taken into consideration.

The above materials [65-66,103,150] have very high ductility and fracture toughness (>100MPa.m$^{0.5}$), which differ from values seen in rail steels. For rail steels, Yu et al. [73, 104] measured the fracture toughness using ball indentation technique for high strength rail steels via a continuum damage mechanics (CDM) approach. The $K_{IC,pred}$ result showed a good trend with K_{IC} for different rail steels but was estimated at some magnitude higher than the ASTM K_{IC} values.

Amongst some of the above approaches [65, 66, 73, 98, 104], the critical fracture strain approach proposed by Ritchie [65, 104-105] considers the microstructural perspective of ductile materials, thus providing a potential for further investigation of K_{IC} estimation in the microstructural scale. Two well-known methods that consider the microstructural contribution towards K_{IC} estimation are the *critical stress model* and the *critical strain model* [105]. The former postulated by Ritchie et al. [61, 150] following the classical Griffith principle for brittle materials, elucidates that fracture only occurs when the local maximum principal stress (σ_{yy}) at some specific microstructural characteristic size-scale, known as the characteristic length (l_o^*), exceeds the fracture stress (σ_f). Value for this l_o^* developed ahead of the crack tip, which either extends through an intergranular fracture mechanism

[150, 159–163] or grows from one grain to another [164–166], is proposed to be two times the average grain diameter (d^*) for brittle materials [61]. However, for ductile materials, where the failure mechanism follows a process of void nucleation, growth, and coalescence ahead of the crack tip with nucleation initiating mostly from non-metallic inclusions [159, 161, 165, 169, 171-172, 174–176] , Ritchie et al. [61] suggested the l_o^* to have a larger magnification factor of d^* than that for a brittle material. In the attempt to understanding the mechanisms of ductile fracture in metals and the characteristic distance relationship, Hahn and Rosenfeld [173-174] observed that fractured surfaces of ductile unnotched tensile metallic bars displayed a fibrous, dimpled appearance, suggesting that the failure process followed a sequence of plastic deformation, void nucleation from hard particles within the ductile matrix, growth of the voids and their subsequent coalescence, which transited from an *'internal microcrack'* to a visually seen macroscopic crack [173-174] that provides more insights to the size of the l_o^* for ductile materials.

Following the suggestions in [173-174], Ritchie et al. [61] described the fracture toughness using a critical fracture strain model, proposing that the characteristic distance is multiple of the average grain size, 5 and 7 times of the average grain diameter for SA533B-1 and SA302B steels, respectively. Additionally, Ritchie et al. [61], Yu et al. [73, 104], Hancock and Mackenzie [180] and others [176-177] also noted a strong relationship between plastic strain and stress triaxiality (η), i.e. the ratio of mean stress to equivalent stress, ahead of the crack tip or notched specimen. This should be taken into consideration depending on the applied loading approach to make the proposed model applicable to less ductile materials.

In the present work, the fracture toughness of nine rail steels is estimated using two different loading types. Firstly, using tensile test results by simulating the effect that would occur in a sharp crack tip before and at the onset of fracture and secondly, using the instrumented ball indentation technique, both based on a newly modified critical fracture strain model. This modified critical fracture strain model includes the consideration that η plays a vital role in reducing the strain to failure while at the same time contributing to the growth of voids via the void growth index (VGI) model from crack initiation sites. Further investigation on the significance of the strain hardening exponent, n, for predicting the accumulative effective plastic strain for fracture toughness estimation for both tensile and indentation approaches are conducted. For the indentation testing, further investigation into the equivalent plastic strain for fracture initiation is based on the plastic regime of the von Mises stress

evolution and also based on the similarity with pressure sensitivity flow seen at the onset of necking on a smooth tensile specimen, $\varepsilon_{ind}^{p,\eta}(\sigma_u)$. At the end, consistency between K_{IC} and $K_{IC,pred}$ for the nine rail steels is discussed for smooth tensile specimens both destructively and non-destructive. Also, the opportunity for further study on the ball indentation techniques for fracture toughness estimation with focuses on the equivalent plastic strain during indentation is discussed.

3.2. Development of the Theoretical Framework

3.2.1 Mechanical properties via tensile test and indentation test

Before $K_{IC,pred}$ can be estimated, it is important to attain the mechanical properties which include Young's modulus (E), yield strength(σ_y), l_o^* and plastic strain evolution. The tensile test requires using a standard smooth specimen such as the type designated by ASTM in which the sample is subjected to a uniaxial force until failure (and/or fracture) [119] while indentation test process requires loading and unloading of the ball indenter into the specimen's surface [22, 73, 104]. Figure 3.1 shows the schematics of a loaded and unloaded specimen during the indentation test. For the loading scenario, as shown in Figure 3.1(a), extent of material contact is defined based on the contact radius (a_c) as a function of the indentation depth (h_t). Once the indenter is unloaded, as shown in Figure 3.1(b), an elastic recovery occurs, resulting in the difference between the projected diameter (total diameter, d_t, based on the size of material pile-up) and plastic diameter (d_p), along with the total depth (h_t) and plastic depth (h_p).

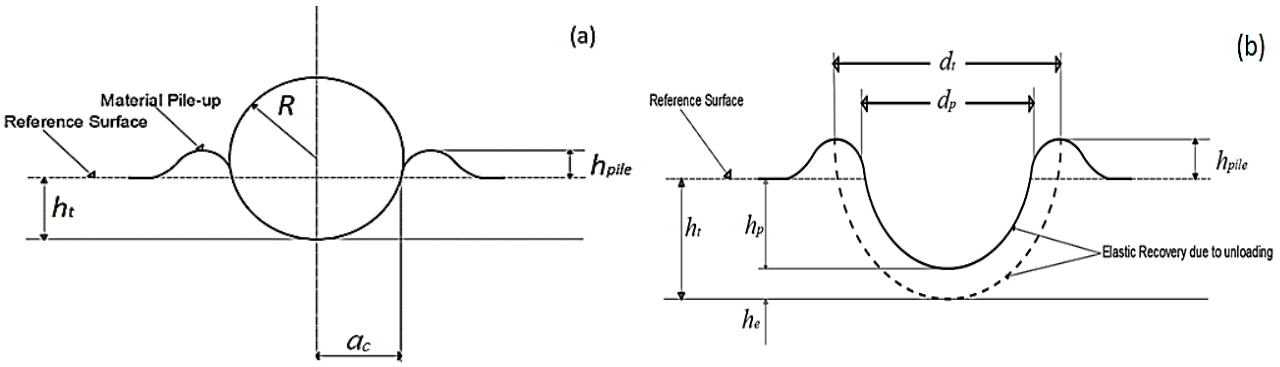

Figure 3.1Ball indentation testing illustration [183]: (a) loading of a spherical indenter on a specimen, and (b) after-effect of an unloaded specimen.

The indentation-determined Young's modulus (E_s) is attained following the methodology offered by Oliver and Pharr [97] and Sneddon's solution [94] on the basis of Hertz contact theory [22], which provides the idealization of an indenter as a rigid body experiencing elastic recovery at the initial portion of the unloading curve [97], in the range from the first 20 to 50% of the overall unloading curve. Determination of the indentation yield strength (σ_{ys}) follows the procedure provided by Haggag et al. [65-66] which considers the total indentation pressure and normalized total indentation depth, extrapolated to zero in the log-log scale.

A power law equation, as given in Eq. (3.1) below, is used to express the average stress-strain relationship in the plastic regime [65-66, 120, 126]. However, using the indentation process to determine the strain hardening exponent (n), similar to that from uniaxial testing, can be quite challenging because the indentation loading introduces large multiaxial stresses as opposed to uniaxial stress in tensile test of smooth specimens. Thus, n_s is regarded as a *pseudo-strain hardening exponent* in this paper, which is the equivalent plastic strain developed at the tip of the indenter that is subjected to triaxial stress state.

$$\sigma_{a,p} = K_s \varepsilon_{a,p}^{n_s} \tag{3.1}$$

where K_s is the strength coefficient via the indentation test, while $\sigma_{a,p}$ and $\varepsilon_{a,p}$ the average plastic stress and average plastic strain, respectively, in the fully plastic regime (i.e when Λ is $\geqslant 50$).

However, understanding the evolution of the average stress and the average strain in the plastic regime of the indentation deformation requires a proper characterization of the entire deformation regime [183]. For the entire indentation process, the average stress (σ_t) and the average plastic strain (ε_p), defined by Eqs. (3.2) and (3.3) respectively, are used to establish the stress-strain curves from instrumented ball indentation tests using data from load (P) and indentation depth (h_t) as depicted in Figure 3.1(b) that creates an indent with a contact depth, h_c (the depth of actual contact between material and indenter at maximum load), which is required to eventually estimate the contact area $A(h_c)$ [94, 178].

$$\sigma_t = \frac{P}{A(h_c)\delta_s} \tag{3.2}$$

$$\varepsilon_p = 0.2\frac{d_p}{D} \tag{3.3}$$

Note that in this study, d_p value is estimated iteratively using Eq. (3.4) [66, 78, 114, 148, 178] and δ_s the stress constraint factor, a continuous quantity that varies as the deformation regime of indentation changes from elastic to fully plastic and ranges from 1.12 - 2.87 as recommended in [66, 178- 179] for ball indentation.

$$d_p = \left\{\left[3PR\left(4h_p^2 + d_p^2\right)\right] / \left[E_r\left(4h_p^2 + d_p^2 - 4h_p^2 D\right)\right]\right\}^{1/3} \tag{3.4}$$

Hence, to attain n_s in Eq. (3.1), $\sigma_{a,p}$ is taken as the values of σ_t from Eq. (3.2) and $\varepsilon_{a,p}$ as the values of ε_p from Eq. (3.3), but only when the deformation regime for the rail steels is considered as fully plastic [178].

3.2.2 Definition of the equivalent plastic strain for fracture initiation

To understand the equivalent plastic strain under different loading scenarios, factors affecting plastic deformation like the η should be taken into consideration. Taking an instance for a circumferentially notched round tensile (CNRT) specimen, the initial η at the centre of the specimen can be expressed by the Bridgman's proposed approximate formula [185] as seen in Eq. (3.5).

$$\eta = \left(1 + 2\frac{R}{a}\right).\ln\left(1 + 2\frac{2}{2R}\right) \tag{3.5}$$

where a is the minimum cross-section radius and R, the notch root radius. However, in this study, following the suggestions in [73, 104, 181-182], the η value at the sharp crack tip is determined based on the concept of an *average stress triaxiality* (η_{avg}) as seen in Eq. (3.6), which considers the variation of η values with the evolution of plastic strain within the vicinity of the deformed region of the loaded specimen, and is expressed as:

$$\eta_{avg} = \frac{1}{\varepsilon_{eq,\max}^p} \int_0^{\varepsilon_{eq,\max}^p} \eta(\varepsilon_{eq}^p) d\varepsilon_{eq}^p \tag{3.6}$$

where $\eta(\varepsilon_{eq}^{p})$ is the evolution of η as a function of ε_{eq}^{p}. Also, looking at the CNRT specimen during the loading based on the diametric changes, the equivalent plastic strain (ε_{p}^{*}) already affected by the η, developed on notched specimen can be estimated as shown in Eq. (3.7)

$$\varepsilon_{p}^{*} = 2\ln\left(a_o/a_c\right) \tag{3.7}$$

where a_c and a_o are the current cross-section radius and initial cross-section radius, respectively.

In Eq. (3.7), values for ε_p^* was supported in [61, 114, 169, 175-176, 183] to strongly rely on the effect η developed by different notch root radius geometries, which as a critical factor is also responsible for the rate of void growth during ductile deformation and fracture. Hence, to account for the role of η_{avg} on the development of ε_p^***,** one of the nonlinear continuum damage models (CDM) provided by Bonora [104, 114, 184-185], which relies on the damage dissipation potential (F_D) following the kinetic law of damage evolution, is employed to provide a means of coupling the effect of η_{avg} with uniaxial fracture strain (ε_f^*) [104, 114, 184-185]. Bonora's model suggests that material strain to failure is reduced for positive high hydrostatic stresses by including a multiaxial stress state in the loading history. With Bonora's model [184-185] used in predicting the damage evolution at different η, we can rely on the assumption that the failure mechanism of void nucleation, growth and coalescence is same for both uniaxial and multiaxial stress states [181, 184–186] and for an isotropic material, the absolute value of $\eta$is employed for both tensile and compressive loadings. Hence, Eq. (3.8) is used to relate η_{avg} and the equivalent plastic fracture strain, $\varepsilon_{eq}^{f,\eta_{avg}}$. It is to note that nucleating strain, which can result from the de-cohesion of particles from the rail steels' matrix is governed by cleavage fracture [189] while the matrix experiences a larger strain before macro fracture and is thus governed by an equivalent plastic strain criterion. Hence, in defining the energy required to de-bond particles (non-metallic inclusions) from the matrix to attain the nucleating strain, an equivalent stress criterion must be used as seen in Appendix 3.

$$\varepsilon_{eq}^{f,\eta_{avg}} = \frac{p_{th}}{f\left(\eta_{avg}\right)^{\gamma}}\left(\frac{\varepsilon_f^*}{\varepsilon_{th}}\right)^{\frac{1}{f\left(\eta_{avg}\right)^{1-\gamma}}} \tag{3.8}$$

where ε_{th} and P_{th} are the damage plastic threshold equivalent strains for the uniaxial and triaxial stress states, respectively, obtained from [73, 104], and are taken to have the same value of 0.002 for

the rail steels [73, 104] while $f(\eta_{avg})$, the average triaxiality factor is expressed in Eq. (3.9) as a function of the Poisson's ratio of the specimen (v_s) and η_{avg}. γ is the stress triaxiality sensitivity and depends on the stress state of the material in deformation. The value of 0.002 for ε_{th} and P_{th} were taken conservatively as Young's modulus degradation based on the repeated loading and unloading of a smooth tensile specimen occurred way before the necking strain (close to the onset of yielding). Also, the damage evolution as a function of equivalent plastic strain from short, notched gauge specimens showed that damage initiation occurred from equivalent strains close to 0.002 as seen in Appendix 3 for different locations of the notch. Since the loading is quasistatic, the critical damage at fracture is low, the damage softening of material flow can be ignored [189]. Thus, γ can be taken as arbitrarily and taken as zero ($\gamma = 0$). Further explanations are expressed in Appendix 3.

$$f\left(\eta_{avg}\right) = \frac{2}{3}\left(1+v_s\right) + 3\left(1-2v_s\right)\left(\eta_{avg}{}^2\right) \tag{3.9}$$

For this work, other than $\varepsilon_{eq}^{f,\eta_{avg}}$ developed from tensile test to simulate the equivalent plastic strain during fracture in a sharp crack tip, as seen in Eq. (3.8), an equivalent plastic strain ($\varepsilon_{eq}^{p,\eta_{avg}}$) is introduced as the '*critical equivalent plastic strain'* which is attained by replacing ε_f^* from Eq. (3.8) with the strain hardening *exponent* (attained by uni-axial testing, *n*), in the aim of estimating the effective accumulated plastic strain for micro ductile fracture initiation [173-174]. The reason for this definition is focused on the opinion that firstly, although there are no cracks or obvious fracture formed at the deformation stage during uni-axial tensile testing, where *n* can be estimated, there are possibilities of micro-coalescence within the material's microstructure. The work presented by Yamada et al. [187-188] suggests that *n* could be a new parameter for estimating the equivalent plastic strain that corresponds to the ductile crack initiation limit. The work [187] focuses on two steels (SM400B and HT780) for this notion, where failure mechanism is governed by the growth of major voids and linked through several micro voids, at high stress triaxiality of which *n* was used for evaluating ductile crack initiation limit for steels. It is seen in [187] that the locus between $\varepsilon_{eq}^{p,\eta_{avg}}$ and η at the centre of the notched section is largely dependent on *n* and thus suggests that *n* is an important factor for fracture definition. Following the application of Mohr-Coulomb fracture criterion for ductile crack initiation limit [189-190] and the concept presented by Yamada et al. [187], the influence of *n* on the estimation of the equivalent plastic strain required for ductile crack initiation

for several steels is demonstrated. However, this influence did not follow the same trend for aluminium (AL2024-T351) due to a different ductile failure mechanism and/or the size of the initial voids within the microstructutre as reported in [187]. Thus, it is essential that the influence and application of 'n' is taken with caution for the estimation of $\varepsilon_{eq}^{p,\eta_{avg}}$ required for ductile fracture initiation for different materials other than steel.

In addition, as to why 'n' should be considered in Eq. (3.8), to replace ε_f^*, the work from Li et al. [195] Extended model for void growth and coalescence also showed that Gb 35CrMo steel began to fail microstructurally after the peak stress, that is, when the theoretical onset of necking was attained leading to a process for crack formation (from cavity initiation to cavity coalescence). This concept of failure at the peak stress is also supported by the theoretical work provided by Pardoen and Hutchinson [196] on the mechanism of void growth and coalescence, which suggests that for materials with large initial aspect ratio of the cell, λ_o, (i.e. ratio of the radial and axial half-lengths of the cell) within a representative volume element (RVE), the onset of void coalescence coincides with the peak stress in a tensile test at low stress triaxiality, which consequently is due to the onset of void coalescence localization processes [191-192].

Hence, by replacing ε_f^* in Eq. (3.8) with n as shown in Eq. (3.10), $\varepsilon_{eq}^{p,\eta_{avg}}$ for micro fracture initiation can be estimated. This is aimed in predicting the effective accumulated plastic strain for fracture toughness estimation prior to an obvious macro fracture that follows the kinetic law of damage evolution. For now, this assumption is applied to steels that obey or have regions within its stress-strain relationship following the Hollomon's equation [34, 114], where 'n' is implemented as a principal factor that estimates the equivalent plastic strain for micro fracture initiation.

$$\varepsilon_{eq}^{f,\eta_{avg}} = \frac{p_{th}}{f\left(\eta_{avg}\right)^{\gamma}}\left(\frac{n}{\varepsilon_{th}}\right)^{\frac{1}{f\left(\eta_{avg}\right)^{1-\gamma}}} \tag{3.10}$$

Hence, 3 different parameters, $\varepsilon_{eq}^{f,\eta_{avg}}$, $\varepsilon_{eq}^{p,\eta_{avg}}$ and n_s, are used in this paper to define the material state for fracture initiation, which will be investigated for their applicability to estimating the fracture toughness of high strength rail streels.

3.2.3 Characteristic distance relationship with plastic strain and VGM model

The description of characteristic distance (l_o^*) as reported by Rice and Johnson [197] provides one of the first presentations of relating microstructural activities to macro fracture, where a '*microstructural distance'* is the distance between two nucleated and growing voids before coalescence, and is described as the mean particle spacing of non-metallic inclusions [197]. Using the slip-line approach [197], microfracture was related to macro fracture as seen in Eq. (3.11a), where the plastic strain relates to the crack tip opening displacement (CTOD), δ, and the microstructural distance, X_o, ahead of the blunting crack tip.

$$\varepsilon_p^* = \frac{1}{\alpha_m}\frac{\delta}{X_o} \tag{3.11a}$$

where α_m is a material factor.

As deformation continues, X_o becomes critical, resulting to the l_o^* and thus fracture is initiated. Thus Eq. (3.11a) is changed to Eq. (3.11b) to depict the fracture occurrence. However, it is to note that the relationship between ε_p^* and δ/X_o is largely non-linear as presented in [157, 193].

$$\varepsilon_f^* = \frac{1}{\alpha_m}\frac{\delta_c}{l_o^*} \tag{3.11b}$$

Since the relationship between ε_p^* and δ/X_o is largely non-linear in most instances, the value of α_m can be attained by taking a tangent of the values of δ/X_o corresponding to the ε_p^* values depending on the stress triaxialty level. Although few reports [194-195] have suggested ε_p^* to be related with δ/X_o linearly, it is possible that this linear relationship only occurs for plastic strain accumulation without damage consideration [184-185]or perhaps at a constant stress triaxiality level. Though several parameters like the void spacing, colony size, prior-austenite grain sizes, lamellar spacing and more [200] are situated within the microstructure of materials especially steels, the need for determining l_o^* using fewer microstructural parameters is necessary.

Further investigation on the evolution of X_o to l_o^* indicates that an important concept affecting the actualization of l_o^* is the void growth mechanism. McClintock [200] developed the analysis of a long cylindrical hole for an ideal plastic solid which was then modified by Rice and Tracey [83, 201] by

using the Rayleigh-Ritz approach for obtaining the solution for an isolated spherical void surrounded by an ideally deformed plastic matrix as seen in Eq. (3.12).

$$\frac{\dot{R}}{\dot{\varepsilon}_o R_o} \approx A \exp\left[\beta \cdot \eta\right] \tag{3.12}$$

where A =0.427 for $\eta \geq 1$ [84] and A =0.283 for $\eta \leq 1$ [83] and β =3/2 [83-84], and $\dot{R}$, $\dot{\varepsilon}_o$, R_o are the void growth rate, strain rate and average void inclusion radius, respectively.

Eq. (3.12) was found to be a very good approximation for a stress state of low h values. However, Huang [84] modified Eq. (3.12) for consideration of high η values and came up with A =0.427. Further studies [200–202] saw the development of the critical void growth ratio (ratio of the final void size at the point of fracture to the initial void size), which over the loading history and accumulated plastic deformation serves as a material parameter that quantifies the critical void ratio without considering effects of some microstructural parameters such as the void nucleation strains at the primary inclusions, void-to-void interactions, localization in the intervoid ligaments, development of secondary void nucleation within the material's matrix and change in propagating direction in growth of voids ahead of the blunt crack tip [204]. Eq. (3.13) expresses the critical void growth index, $(VGI)_C$, which is taken as the theoretical critical point for void coalescence from the void growth model in Eq. 3.12.

$$(VGI)_c = \phi_c = A.\varepsilon_f^* \exp\left(\beta \cdot \eta\right) \tag{3.13}$$

Hence, to relate l_o^* with Φ_c, following suggestions from Garrison [207] and Garrison and Thompson [208] and also Rice and Johnson's suggestion [197] which identifies X_o as the average distance to the three-dimensional nearest neighbour (also as a microstructural distance) from the primary voids, the expectation is that $l_o^* = f(X_o, \varepsilon_f^*.\eta)$. The l_o^* can then be expressed in Eq. (3.14):

$$l_o^* = \frac{\psi X_o \phi_c}{\varepsilon_f^*} \tag{3.14}$$

where ψ is a material constant.

Studies have suggested that ductile fracture mechanism would initiate from grain boundaries or non-metallic inclusion deposits [161, 169, 171-172, 174–176]. Since non-metallic inclusions were not looked upon in this study due to their difficulty in matrix distribution, the prediction of the critical void growth for estimating l_o^* as seen in Eq. (14) is based on the microstructural distance, X_o, which is the distance between two voids along the prior austenite grain boundary, which is being assumed to be approximate to d^* ($X_o \approx d^*$) in this study. Hence, combining Eq. (3.13) and Eq. (3.14), l_o^* can be expressed in Eq. (3.15) for high stress triaxiality scenario. (i.e A =0.427 [84])

$$l_o^* = d^* \cdot A \exp\left(\beta.\eta_{avg}\right) \tag{3.15}$$

Where β is taken as 1 to relate l_o^* to the microstructural distance and stress triaxiality only. The equivalent plastic strain needed for fracture initiation is already satisfied and is coupled with l_o^* to replicate the damage plastic stretch ($l_o^*\ \varepsilon_{eq}^{f,\eta_{avg}}$) required for fracture initiation. The ψ seen in Eq. (3.14) will be inclusive to the estimation of the modified critical fracture strain model.

3.2.4 Development of modified critical fracture strain model

In predicting $K_{IC,}$ one would consider the small-scale yielding (SSY) approximation as a prerequisite for the basic assumption in Irwin's linear elastic fracture mechanics principles [56], since the materials of concern show very small plastic deformation at the crack tip during fracture (i.e. high strength structural metals e.g. rail steels for this work) [56, 104]. Hence by considering the SSY criteria for fracture toughness definition, the relationship between K_{IC} and δ_c can be expressed using Eq. (3.16) [56].

$$\delta_c = \gamma_m \left(K_{IC}^2 / E\sigma_Y\right) \tag{3.16}$$

where γ_m is a material constant that considers plane-strain condition for K_{IC} estimation [56].

It is important to note that $\gamma_m = \dfrac{4}{m\pi}$ is a general form for both plane-stress and plane-strain conditions [56], where it defines CTOD at the end of a strip-yield zone of a very limited zone [56], m is a

dimensionless constraint factor, and is a function of yield and tensile strength [209], yield strain and *n* [210].

Hence, by combining Eq. (3.11b) and Eq. (3.16) as a means of relating micromechanics and macro fracture for K_{IC} estimation, a critical fracture strain model for ductile failure $\left(K_{IC} = \text{constant}\sqrt{E\sigma_y l_o^* \varepsilon_f^*}\right)$ can be established. The modification to this model is seen in Eq. (3.17), where the principal factors to determine the K_{IC} lies on the limited plastic deformation, which is a function of the l_o^*, the stress triaxiality experienced at the plastic zone size, and the elastically strained region of the material defined by the Young's modulus and yield strength of the material.

However, the 3 different equivalent plastic strains are incorporated to replace ε_f^* to investigate their effect on the modified critical fracture strain model. The replacement of ε_f^* with $\varepsilon_{eq}^{f,\eta_{avg}}$, $\varepsilon_{eq}^{p,\eta_{avg}}$ and n_s are to investigate the estimation of K_{IC} for smooth tensile specimen, destructively (i.e. till fracture strain, Eq. 3.17i) and non-destructively (i.e. till *n,* Eq. 3.17ii) and indentation testing (Eq. 3.17iii), respectively.

$$K_{IC,pred(i)} = \begin{cases} \mathrm{C}_m \sqrt{E\sigma_y l_o^* \varepsilon_{eq}^{f,avg}} & \text{i} \\ \mathrm{C}_m \sqrt{E\sigma_y l_o^* \varepsilon_{eq}^{p,avg}} & \text{ii} \\ \mathrm{C}_m \sqrt{E\sigma_y l_o^* n_s} & \text{iii} \end{cases} \tag{3.17}$$

where C_m is a material parameter: $C_m = \sqrt{\frac{\alpha_m}{\gamma_m}}$, E_s and σ_{ys} are Young's modulus and yield strength attained via indentation. Hence, Eq. (3.17) provides a means of predicting the fracture toughness by considering different equivalent plastic strains from tensile, Eq. 3.17 (i) and Eq. 3.17 (ii), and indentation testing, Eq. 3.17 (iii).

In this work, a modified prediction model for *m* needed for the estimation of γ_m is being suggested from the averages of low strength steel (σ_y ~ 400MPa) and very high strength steel (σ_y ~ 1200MPa) in accordance with Pereira et al. [210]. It is to note that the experimental data was extracted from Pereira et al. [210], modelled and used to estimate the expected experimental data for the rail steels. *m* is attained using the averages from ASTM model used at 400MPa and 1200MPa steel, HRR model

at 1200MPa and McMee King's model at 400MPa to give an approximate model at 800MPa. Eq. 3.18 shows the relationships between these models with 'A' signifying 1200MPa and 'B' signifying 400MPa. Hence, with the values of *n*, m^* can be estimated using Eq. 3.18. The application of Eq. 3.18 is seen in section 3.4.4, where the different relationships of the models used are shown.

$$m^* = \frac{\frac{1}{2}(ASTM(A) + HRR(A)) + \frac{1}{2}(ASTM(B) + McMee\ King(B))}{2} \tag{3.18}$$

where ASTM (A), ASTM (B), HRR(A) and McMee King (B) models are the relationships between *m* and *n* (from tensile test).

3.3. Materials, Experiments and Simulation

3.3.1 Materials

Materials employed for this study are high strength rail steels, which are known for their high yield and tensile strengths due to the alloying components and heat treatment activities during the manufacturing process. Table 1 shows the rail steels used in this study with their microstructures which were attained using different heat treatments, provided by the Canadian National (CN) Railway Company and an undisclosed company (COMPX). Due to the confidentiality of the rail steels provided by COMPX, their names are not mentioned in this paper. A total of nine rail steels were used to generate the required data for estimating the mechanical properties [58] and fracture toughness via the instrumented ball indentation testing. The rail steels used in this study are similar in the manufacturing process and composition that have been used in the previous work by Yu et al. [73, 104, 114].

Table 3.1 Rail samples and their microstructures

Rail Name /Identification number	Microstructure	Locations*	Company
JP	Deep head hardened	H, F	CN
EV	Deep head hardened	H, F	CN
CZ	-	H, F	CN
Rail RCN	Micro head hardened	H	COMPX
Rail #2	Hypereutectoid	H	COMPX
Rail #3	Hypereutectoid	H	COMPX
Rail #4	Head hardened perlite	H	COMPX
Rail #5	Head hardened perlite	H	COMPX
Rail #6	Micro head hardened	H	COMPX

* *H:Rail head, F: Rail foot*

3.3.2 Mechanical tests

3.2.1 Tensile and single edge notched bend (SENB) tests

The tensile properties were obtained from the previous work by Yu et al. [73, 104, 119]. Tensile tests were conducted on smooth dog-bone specimens in the longitudinal direction of the rail steels following the recommendations of ASTM E8/E8M [120]. Results from the tensile tests, such as E, σ_y, ultimate tensile strength (UTS), the stress-strain relationship, the strain hardening exponent (n) and fracture strain ($\varepsilon_f{}^*$), were used as a reference to evaluate the accuracy of results from the indentation tests and developing the constitutive equation for FE modelling [73, 104, 114]. Figure 3.2(a) illustrates the positions on the rail head where the dog-bone specimens, with dimensions given in Figure 3.2(b), were extracted. The stress-strain was also conducted to understand the nature of the failure mechanism experienced at the fracture of the rail steels. More details of the stress-strain curves and the fractured surface are shown in Appendix 7 and Figure. A6.

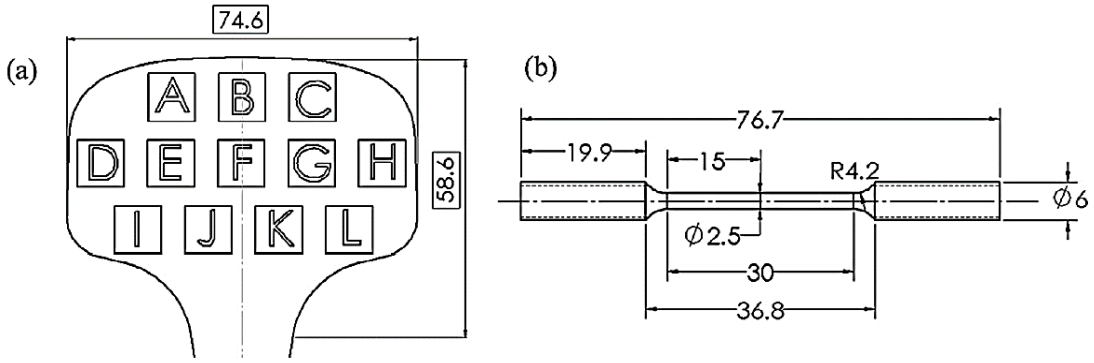

Figure 3.2.Tensile test specimens: (a) sampling locations on the cross section of railhead, and (b) dimensions and geometry of the tensile specimen [73].

The SENB tests were also conducted from previous work by Yu et al. [73, 104, 114] as shown in Figure 3.3. The SENB tests were conducted according to ASTM E399 [58] to measure K_{IC} for the nine rail steels, as a reference to validate $K_{IC,pred}$. The dimensions and methodology for the SENB specimens are recorded in [73, 104, 114]. Data for the SENB specimens were also used to determine η_{avg} values using Eq. (3.6) via FE modelling.

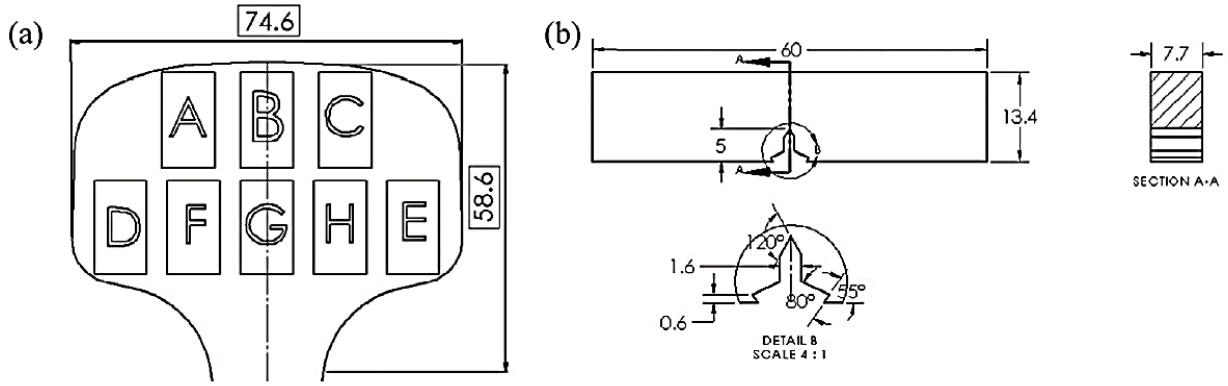

Figure 3.3. Single-edge-notched bend (SENB) specimens: (a) sampling locations on the cross section of railhead, and (b) dimensions and geometry of the SENB specimen [73].

3.2.2 Indentation tests

The indentation tests were carried out using an in-house-designed indentation test equipment as shown in Figure 3.4(a) for extracting the P-h_t curves of the rail steels, as illustrated in Figure 3.4(b).

The study to attain the mechanical properties for the nine rail steels has been achieved on a previous study [183].

The specimen was extracted from one-half of railhead with 10mm in thickness. The ball indenter is made of tungsten carbide with a diameter of 1.19mm, having mechanical properties of E_i of 480GPa, and v_i of 0.28.

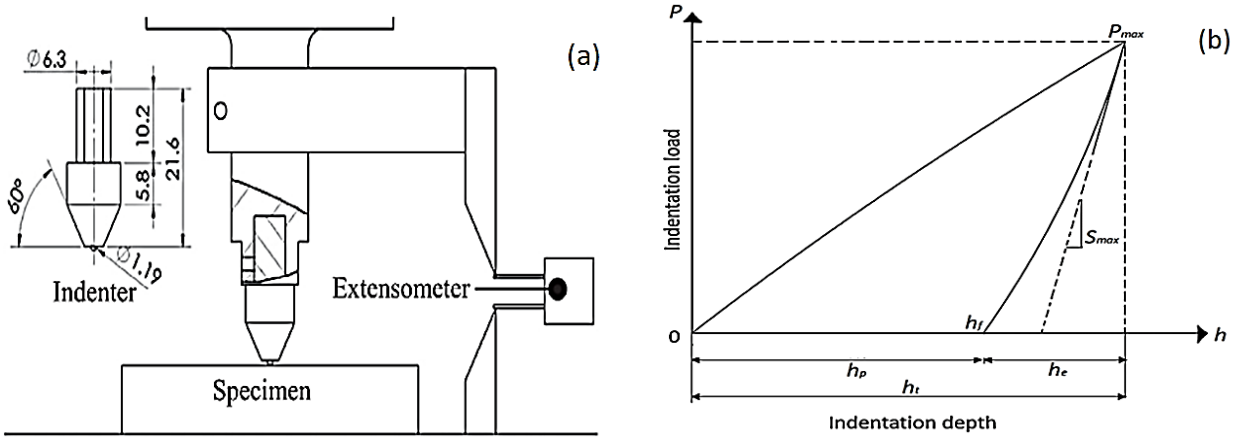

Figure 3.4. Schematics of the instrumented indentation test: (a) illustration of the in-house developed ball indentation equipment [73], and (b) a typical loading-unloading curve showing the estimation of S_{max} [183].

3.3.3 Microstructural analysis

Three rail steels provided by CN, i.e. the top three shown in Table 3.1 were extracted from the rail head and foot following the dimensions as shown in Figure 3.5(a) and held firmly in a cup fused with an epoxy-resin hardener mixture as shown in Figure 3.5(b) for the microstructural test (MT). The remaining six steels in Table 3.1 were only extracted from the rail head and prepared for MT test similar to the 'CN' specimens. The test specimen extracted was followed by grinding and polishing using SiC paper grits (240-1200mm) and diamond suspension (1mm) respectively, according to the procedures of ASTM E3 [95] to achieve a perfectly-flat and polished surface on the test specimens. To reveal the microstructure from the specimens' surface and grain boundaries, an etching process using 2% Nital etchant [211-214] was used for an average of 15 seconds via the dipping (immersion) technique. It was found that the dipping method in the etching process gave a more reliable outcome than the swabbing method due to the uniformity in etching initiation on the surface of the rail steels. Revealing the microstructures of rail steels are quite challenging, hence, by applying visual inspection (VI) procedure, an indication of a timely and controlled etched surface is revealed with the

instantaneous change on its polished surface. The etching process was immediately halted (after the instantaneous change) with cold distilled water. To view the microstructure, an optical microscope (OM) was used and the images were analyzed using ImageJ software [215]. Each sample collected from the head and foot of the rail steels were examined using 5 fields of optical images, each provided with 5 lines, to determine the average grain sizes, d^*, on three different locations per rail sample (via mean intercept method to be further described). Hence a total of 27 samples from 3 locations of the 9 rail steels, 135 optical field images and 675 lines were used.

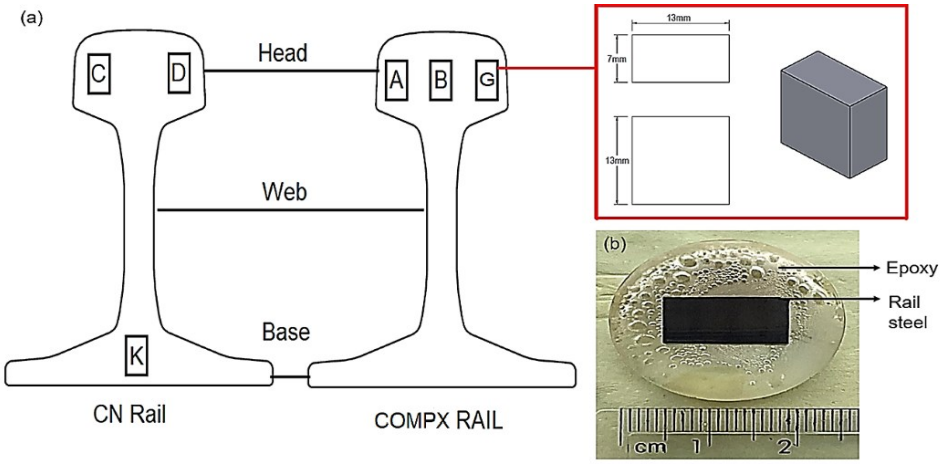

Figure 3.5. Indentation samples: (a) Location on the specimen for MT and (b) samples mounted to epoxy for metallographic examination.

The mean intercept length ($\bar{l}$) of the rail steels were calculated from the microstructure using the mean intercept line method [216]. Eq. (3.19) describes the relationship between $\bar{l}$ and the number of grains intercepted (N) following the ASTM E112 guidelines while Eq. (3.20) shows the relationship between the mean intercept length and the ASTM grain Number (G) [216]. Once G is calculated using Eq. (3.20) as depicted in ASTM E112, d^* can estimated using the relationship table correlating G and d^* as seen in ASTM E112 [216].

$$\bar{l} = \frac{L}{MN} \tag{3.19}$$

$$G = \left(-6.6643858 \log_{10} \bar{l} \right) - 3.288 \qquad \bar{l} \text{ in mm [98]} \tag{3.20}$$

where L is the total test lines and M the magnification of the test field [216].

In order to attain d^*, the image revealed from the OM is directly imported into ImageJ for image analysis. Here, the contrast is firstly adjusted to properly reveal the microstructure of the different fields. Five random lines of equal lengths were used for the analysis to cut across the microstructure, as shown in Figure 3.6(a). The lines started about half-way a grain and ended also about half-way a grain. These half-way grains were taken as 0.5 grain each and signified by the red circles. Also, grains that intersect the lines tangentially were considered as 0.5 grain and signified by blue lines while every other grain that is entirely crossed by the line were taken as whole grains and signified as yellow circles. In Figure 3.6(b) shows a closer look at the austenite grains being observed and manually counted to show demarcations between the austenite grains by their grain boundaries. Once the different grain counts are identified, Eq. (3.19) and Eq. (3.20) are used to attain $\bar{l}$ and G, respectively. It is essential to know that the average grain diameter estimated (d^*) in this work is equivalent to the prior-austenite grain size measured within the microstructure [216].

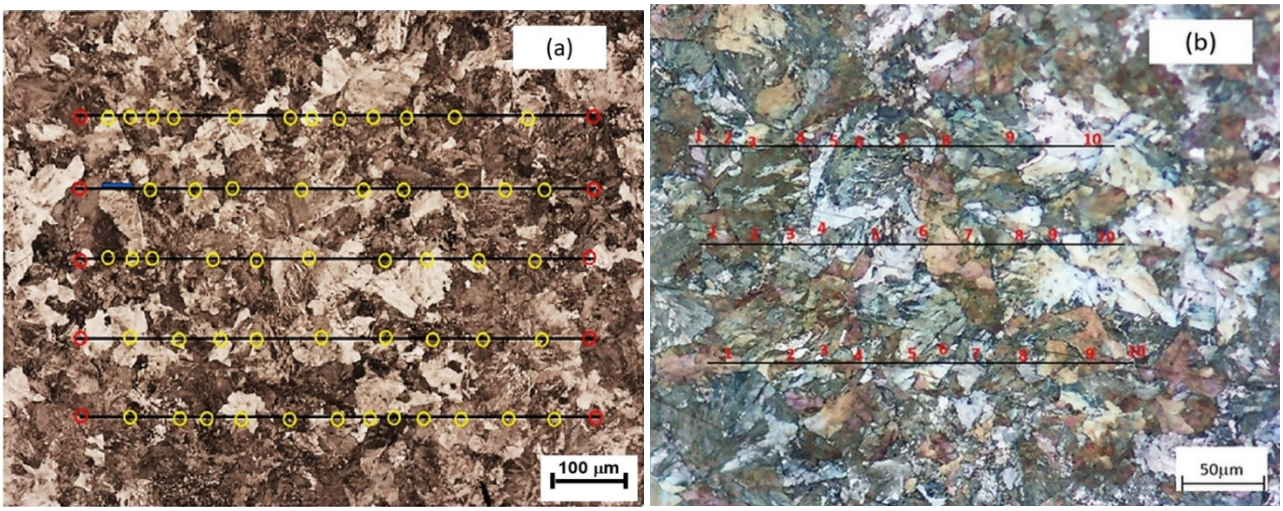

Figure 3.6. Microstructure of the rail steel: (a) Average grain diameter determination using mean intercept line method, (b) Counting of the austenite grains

The rail steels were then examined using a Zeiss Sigma field emission scanning electron microscope (FESEM) with a scanning voltage of 10kV and aperture size of 30µm for taking SEM images through the device's secondary electron (SE) detector. A magnification ranging from 2,000 – 40,000X were used for SEM images to investigate the nature of the grains present in the rail steels.

3.3.4 Finite element modelling

Finite element (FE) modelling of SENB and indentation tests were carried out using ABAQUS/CAE 6.14 standard analysis. FE simulations were first carried out by Yu et al. [119] on the SENB specimen to determine the evolution of η as a function of the equivalent plastic strain since the direct measurement of the equivalent plastic fracture strain cannot be carried out on the SENB specimen. The equivalent plastic strain's value of the smooth tensile specimen was used instead from an extrapolation of the measured fracture strain to the stress triaxiality that matches that of sharp notch tip. The constitutive equation from the smooth tensile test was used in imitating the deformation behaviour of the rail steels in the SENB simulation [73, 104]. The SENB FE model was created according to the dimensions of the SENB specimen as described in Figure 3.3, which was designed using 2D modelling as shown in Figure 3.7, with 36,340 quadrilateral 8-node elements and 109,910 nodes in plane strain condition. The sharp notch tip had a quarter-circular profile, with an initial radius 0.1mm, determined based on the strip yield model [217] and falls within the range of practical fatigue crack size [122]. The boundary conditions were set to mimic the experimental setup. A friction coefficient of 0.35 based on the classical Coulomb's law was used as the penalty for the tangential behaviour on the contact pins with a hard contact as the normal behaviour, which was attained by iterating the output of force-depth from FE modelling with experiment.

FE modelling of indentation tests was then carried out following the set-up as described in Figure 3.4(a), where the ball indenter is attached unto an in-house indentation creating indents on the specimen at prescribed depth. The specimen is modelled as a cylinder with a radius of 12.5 mm and height of 7 mm. The model consists of 22,795 linear quadrilateral elements of type CAX4R and 65,097 nodes. The minimum element size at the contact region is 3µm as shown in Figure 3.7, which was obtained through a mesh sensitivity analysis as further seen in Appendix 4. To depict the nature of the indenter, as described in section 3.2.2, the ball indenter was modelled as an analytical rigid body with a radius of 0.595mm. A contact surface was placed between the ball indenter and the specimen in the condition of small sliding, "hard" normal contact, and tangential friction of 0.3, which was obtained also by iterating the output of force-depth from FE modelling with experimental force-depth curve. The boundary conditions were set to be the same as those for the testing, i.e., with the bottom of the specimen supported and the indenter moving down at a specified displacement rate to specific indentation depths.

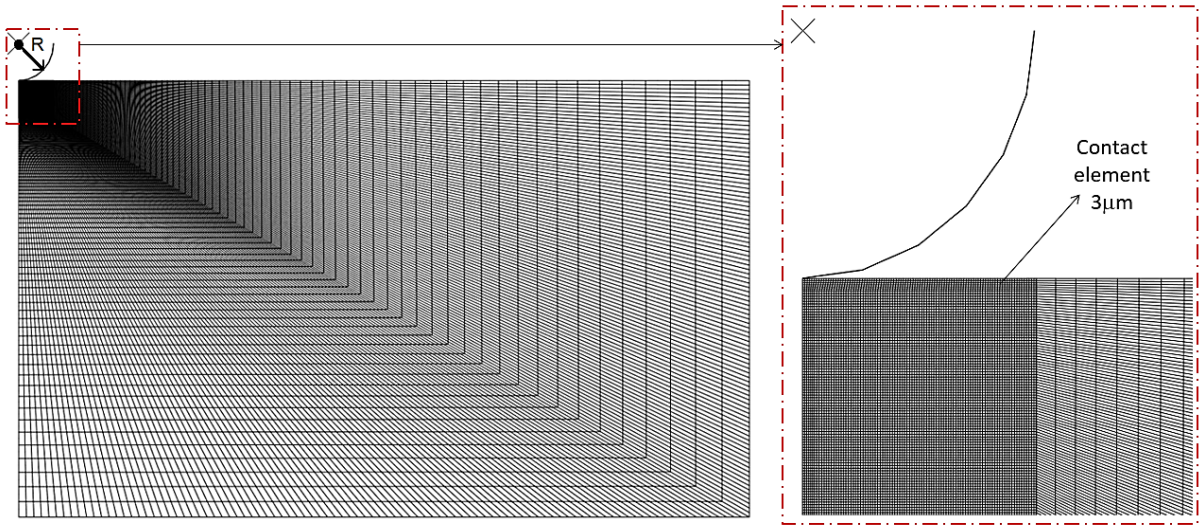

Figure 3.7 FE modelling and mesh orientation of the indentation testing using a rigid indenter.

3.4 Results and Discussion

3.4.1 K_{IC} from SENB

A summary of the K_{IC} attained using the SENB is expressed in Table 3.2 as obtained from the works [73, 104, 114]. Information concerning the plane-strain condition, provisional force and specimen crack lengths are also reported in [73, 104, 114] while the force to crack mouth opening displacement (CMOD) curves for the 9 rail steels are presented in Appendix 5. 9 rail samples were extracted from the rail head for the K_{IC} estimation while the specimens that met the criteria for K_{IC} definition (# of specimens) as specified in ASTM E399 [58] are highlighted and their mean taking as the K_{IC} of the different rail steels. It is to note that the K_{IC} values and standard deviation (Std Dev) used as reference for the nine rail streels as seen in Table 3.2 are samples attained only from the rail head since this is the area of interest of direct contact between the rail wheels and main track. The K_{IC} for the foot rail is used as part of a collective comparison between K_{IC} and d^* seen in section 3.4.3.

Table 3.2 A summary for K_{IC} results from SENB as reference for $K_{IC,pred}$

Rail	**JP**	**EV**	**CZ**	**R#2**	**R#3**	**R#4**	**R#5**	**R#6**	**RCN**
# of specimens	6	5	6	8	6	5	5	7	5
K_{IC} (MPa.m$^{0.5}$)	39.42	41.73	34.32	37.85	35.28	42.28	41.16	41.40	42.34
Std Dev	1.44	1.29	0.62	2.52	1.84	1.33	2.21	2.65	3.35

The variations in K_{IC} can be attributed to the heat treatments and manufacturing procedures on the rail head resulting to non-uniformity of material properties across the depth of the rail but specifically to improve the properties of the main track at the contact location. This variation is minimal in CZ rail because of the uniformity in microstructure after the hot rolling process. i.e. no heat treatment procedure for surface hardening was done on CZ.

3.4.2 Stress triaxiality (η) and equivalent plastic strains

In order to attain the η_{avg}, FE modelling of the SENB test were conducted from the works [114]. For the determination of the stress triaxiality of the SENB, the average values were determined via FE simulation from Yu et al. [114]. Although high η_{avg} is attained for the nine rail steels, the differences are suggested to be an effect from the difference in the fracture strain and plastic strains developed at the notch root in describing the failure site. This failure site criterion is also suggested by Yu et al. [114] and other researchers [213–215] on the basis that micromechanics failure is based on material constants and its microstructural parameter in the form of its characteristic length. Based on the work from Yu et al. [114], Alves and Jones [181] and Bonora et al. [188], failure sites are attributed to fracture strain and stress triaxiality based on continuum damage mechanics (CDM) [214–215]. To attain the η_{avg}, the numerical force-displacement relationship is matched with experimental force – crack mouth opening displacement (CMOD) by optimizing the elastic-plastic properties and friction parameters to imitate the SENB behaviour. The η_{avg} at ambient temperature utilized by Yu et al. [114] was used based on the strip yield method [217] for the rail steels as shown in Figure 3.8 (with JP rail steel as an example) using Eqn.(3.6). At high stress triaxiality (> 2–3) as seen in Figure 3.8, brittle cleavage fracture is promoted and at the same time, the creation of dimple formation is experienced within an otherwise ductile fracture mechanism.

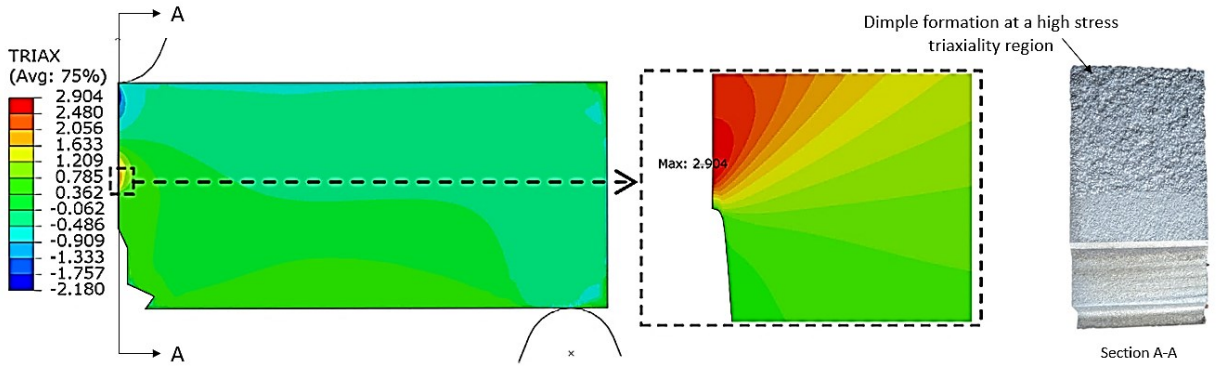

Figure 3.8 Stress triaxiality distribution ahead of the sharp notch tip of SENB specimen at the onset of fracture [114]

For the indentation test, the η_{avg} is also estimated via FE modelling and compared with the outcomes from SENB FE simulation to determine the applicability of η_{avg} from SENB in the indentation model. The evolution of triaxiality with plastic strain is extracted from the 2D axisymmetric FEA configuration of the indentation test as depicted in Figure 3.9. Since the indentation testing does not encounter cracks or load drop like the conventional fracture toughness tests of high strength materials, the initiation point under the indenter tip to arrest the simulation was at the maximum indentation depth. It is observed that η ranges from 0.76 to − 3.36 (-ve η), hence, the region (element) where the maximum η was observed at the maximum depth was used in relating the loading history between η and the equivalent plastic strain. Following the suggestion of Lee et al. [184], which considers the similarity of η between SENB and the tip of the spherical indenter, the η_{avg} of the indentation test is also calculated using Eq. (3.6) and is compared with SENB outcome to observe if the η_{avg} of the SENB test can be implemented for indentation model as seen in Table 3.3 shows the η_{avg} from the indentation simulation being closely matched with the η_{avg} of the SENB simulation with no more or less than ±10% of the SENB outcomes.

Even though the elastically strained region under indentation is compressive in contrast to tensile around the crack tip of SENB test, it is commonly accepted that the compressive and tensile deformations are equivalent when there are no cyclic deformation inclusive in the loading history [222] and with the criteria of the principle of isotropy. With the knowledge of η_{avg} from SENB test to be implemented for both tensile and indentation tests, the three equivalent plastic strains (n_s, $\varepsilon_{eq}^{f,\eta_{avg}}$, $\varepsilon_{eq}^{p,\eta_{avg}}$) can be known for this study using Eqs. (3.1), (3.8) and (3.10) respectively. Figure 3.9(a) shows an example of the force-indentation depth curve via experimentation and ABAQUS simulation as well as the evolution of η with equivalent plastic strain in Figure 3.9(b). The calculated η_{avg} value for RCN rail steel as a representative of the other rail steels is also shown in Figure 3.9.(b). The contour plot of the indentation process of the stress triaxiality evolution as the indentation depth increases is seen in Figure 3.9 (c) showing the maximum stress triaxiality developing at a region beneath the indenter tip with respect to the equivalent plastic strain. Appendix 6 shows the indentation load and depth for all 9 rails.

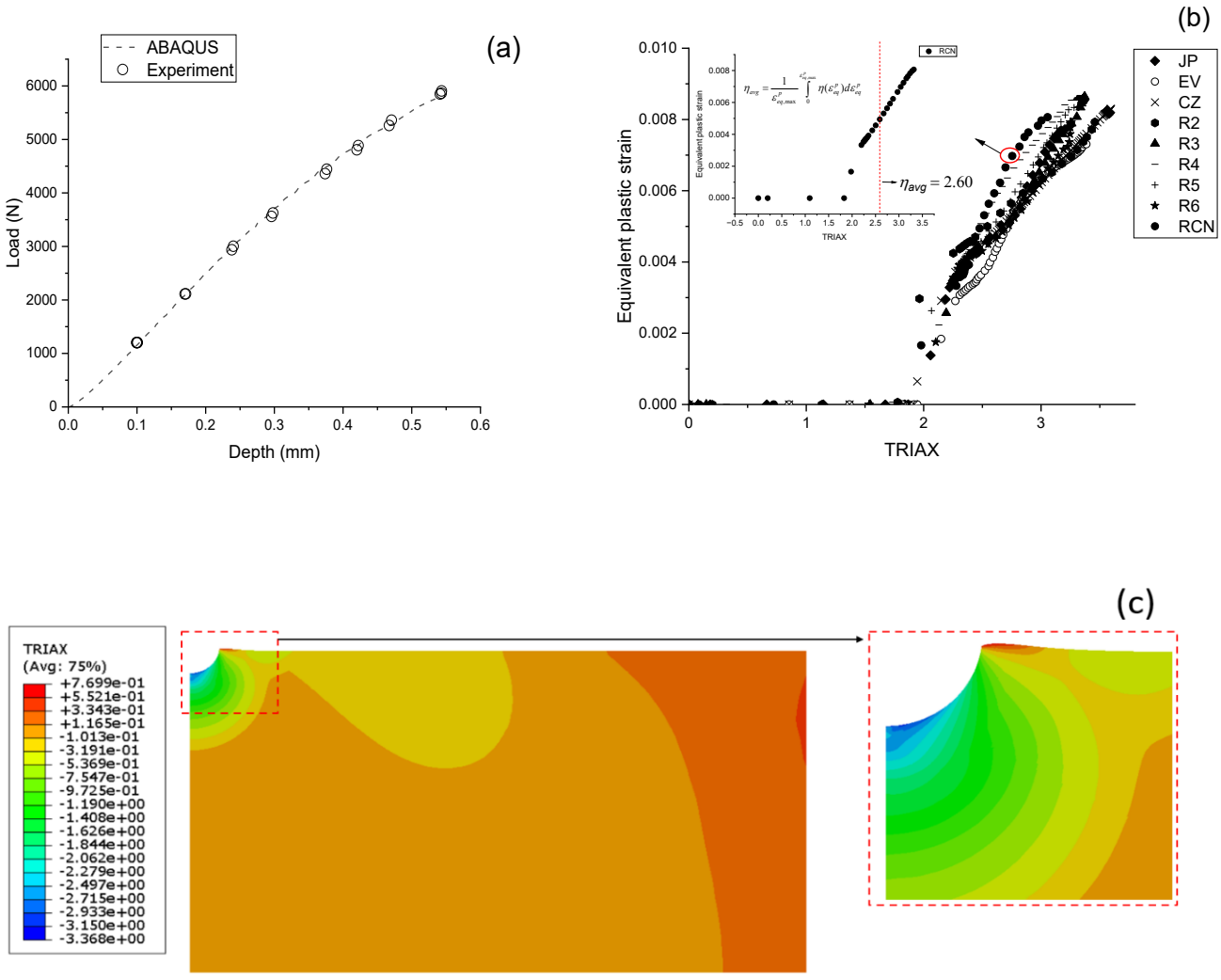

Figure 3.9 Numerical simulation outcomes: (a) Calibration of indentation force-depth for JP rail steel, (b) Evolution of plastic strain with stress triaxiality and average triaxiality, (c) Stress triaxiality contour plot of the indentation testing

The high η_{avg} experienced both in the SENB specimen and indentation testing indicates that the rail steels, although fails in a ductile manner fall within linear elastic fracture mechanics (LEFM) criteria with a sharp crack. More ductile materials like low and medium structural steels, which fall within the elastic-plastic fracture mechanics (EPFM) region have low η_{avg} (can be insensitive), making failure governed by the flow properties [56].

With the theoretical significance of n_s for the indentation testing, $\varepsilon_{eq}^{p,\eta_{avg}}$ and $\varepsilon_{eq}^{f,\eta_{avg}}$ for tensile tests, the equivalent plastic strains for ductile fracture initiation can be estimated and investigated.

Table 3.3 η_{avg} *and* $\varepsilon_{eq}^{p,\eta_{avg}}$ for the nine rail steels

	JP	EV	CZ	R#2	R#3	R#4	R#5	R#6	RCN
η_{avg} **(SENB) [104, 114]**	2.60	2.80	2.84	2.681	2.85	2.69	2.63	2.71	2.65
η_{avg} **(Ind) [178][216]**	2.60	2.56	2.73	2.64	2.65	2.62	2.71	2.62	2.60
% difference	0	-8.57	-3.87	-1.53	-7.02	-2.60	3.04	-3.32	-1.89
ε_f^*	0.5040	0.3010	0.1830	0.2600	0.2410	0.4660	0.6380	0.5140	0.3810
n [73,114]	0.086	0.085	0.082	0.03285	0.0399	0.05027	0.05009	0.01003	0.05485
n_s [178]	0.0876	0.0969	0.0831	0.051	0.04436	0.06644	0.05396	0.06636	0.08612
$\varepsilon_{eq}^{f,\eta_{avg}}$	0.00370	0.00326	0.00307	0.00334	0.00314	0.00354	0.00375	0.00355	0.00352
$\varepsilon_{eq}^{p,\eta_{avg}}$	0.00304	0.00288	0.00284	0.00269	0.00265	0.00280	0.00284	0.00236	0.00286

3.4.3 Microstructure outcomes

3.4.3.1 Prior austenite grain size

The images in Figure 3.10 show the OM microstructures of the nine rail steels and a sample of a polished surface. By employing visual inspection (VI), as described in section 3.3.3, the prior austenite grain sizes were identified following the boundaries between grains (seen as different colours and demarcations within the microstructure) and consequently d^* was estimated. As seen in Figure 3.10, CZ rail has its prior austenite grain boundaries visible at 100μm because no surface hardening was introduced. Other rails had their d^* estimated at 50μm except for EV rail which was very visible at 100μm due to its large d^* values. Although EV rail was deep head hardened, same as JP rail, d^* for the former was larger than that for the latter, and the former has a larger K_{IC} as seen in Table 1 following the postulated provided by *ASM International* [173].

Figure 3.10 shows the images of the rail steels viewed under OM and an image of a polished non-etched surface.

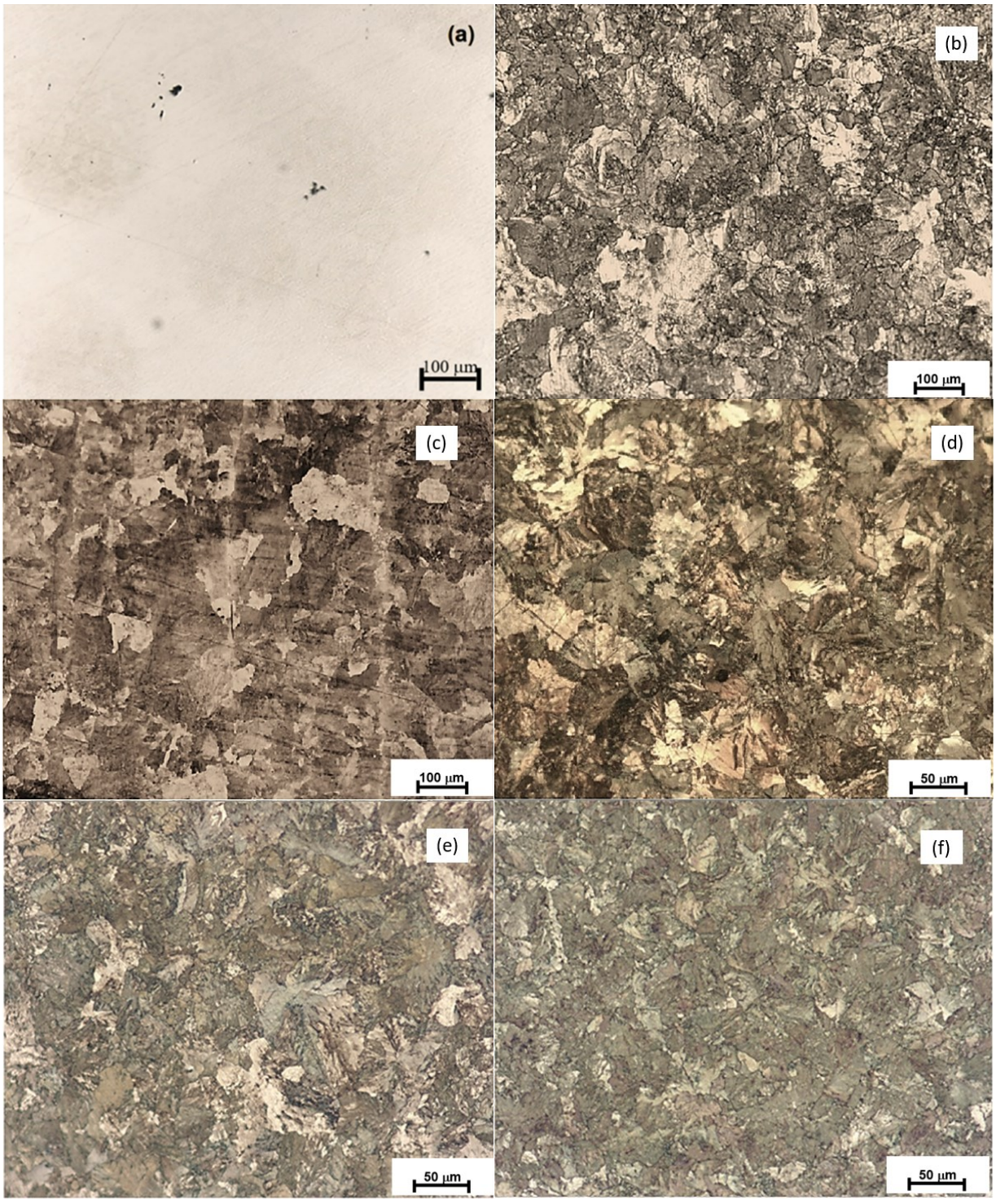
(a)
100 µm
(b)
100 µm
(c)
100 µm
(d)
50 µm
(e)
50 µm
(f)
50 µm

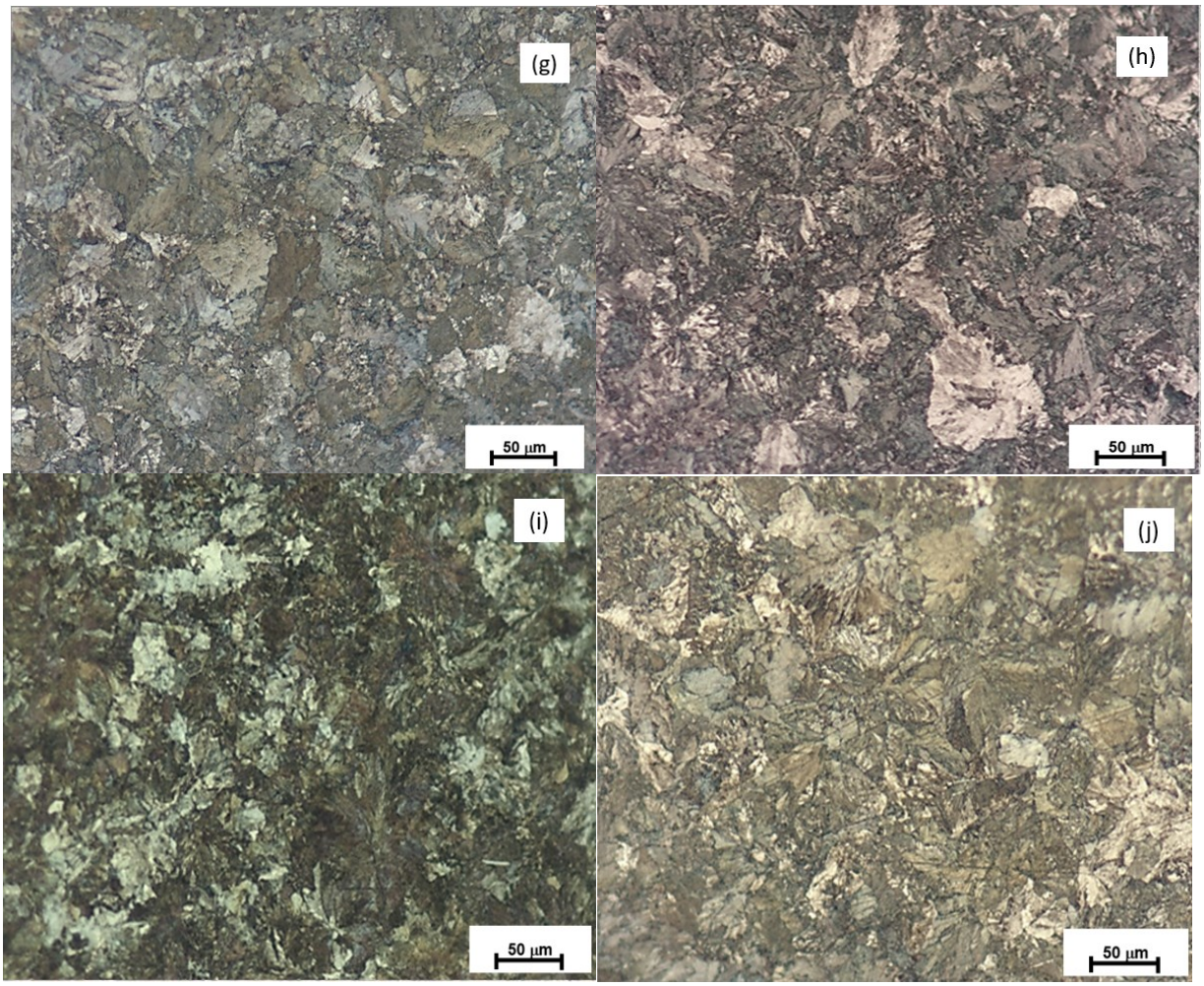

Figure 3.10 Images of specimens under the OM: (a) Image of the polished unetched specimen with presence of inclusions, (b) Image of CZ rail steel specimen (c) Image of EV rail steel specimen, (d) Image of JP rail steel specimen, (e) Image of R#2 rail steel specimen, (f) Image of R#3 rail steel specimen, (g) Image of R#4 rail steel specimen, (h) Image of R#5 rail steel specimen, (i) Image of R#6 rail steel specimen, (j) Image of RCN rail steel specimen under the OM.

By using the mean linear intersection method [216] as described in section 3.3.3, the average grain diameters were calculated. Table 3.4 shows the different estimated $\bar{l}$, G and d^* using the mean linear intercept method from ASTM 112 guidelines.

Table 3.4 Different values of mean intercept length ($\bar{l}$), ASTM number (G) and average grain diameter (d^*)

Rails Steels	Location	Microstructural parameters		
		$\bar{l}$ (mm)	G	d^* (mm)
JP	C (H)	43.692	5.746	0.0581
	D (H)	44.037	5.723	0.0583
	K (F)	42.105	5.853	0.0580
EV	C (H)	69.199	4.419	0.0788
	D (H)	69.479	4.407	0.0791
	K (F)	67.938	4.471	0.0774
CZ	C (H)	51.248	5.285	0.0492
	D (H)	51.444	5.277	0.0496
	K (F)	51.230	5.290	0.0474
Rail #2	A (H)	43.88	5.733	0.0499
	B (H)	44.148	5.716	0.0502
	G (H)	43.411	5.764	0.0493
Rail #3	A (H)	40.812	5.950	0.0456
	B (H)	38.345	6.122	0.0432
	G (H)	38.151	6.138	0.0429
Rail #4	A (H)	52.563	5.213	0.0592
	B (H)	51.259	5.285	0.0577
	G (H)	52.092	5.238	0.0587
Rail #5	A (H)	51.497	5.272	0.0584
	B (H)	51.128	5.295	0.0580
	C (H)	49.253	5.400	0.0561
Rail #6	A (H)	51.267	5.285	0.0577
	B (H)	51.943	5.248	0.0585
	C (H)	52.536	5.214	0.0592
Rail #Contrl	A (H)	55.586	5.051	0.0633
	B (H)	56.336	5.012	0.0642
	C (H)	55.842	5.038	0.0636

A relationship between K_{IC} and $\sqrt{d^*}$ is seen in Figure 3.11, showing that larger grain sizes fairly correspond to higher fracture toughness, supporting an argument presented by [61, 65-66]. This notion, however, still stands as an argument in metallographic studies with different opinions. K_{IC} measurement in metals always show a scattered behaviour [218-219], creating the scenario of a questionable proportional relationship with $\sqrt{d^*}$. As seen in Figure 3.11, the variation of K_{IC} in the head and foot regions does not correlate closely with the grain sizes of rail steels. For instance, JP, R#4, R#5, and R#6 rail steel has a very close range of d^* values but the variations in K_{IC} values are quite large while rail EV show the largest d^* but not the largest K_{IC} value than other rail steels. This certainly indicates that although the knowledge of d^* can anticipate a proportional relationship with K_{IC}, it is not enough to quantify K_{IC} but rather can be used for categorization as other mechanical parameters are needed for K_{IC} approximate quantification.

However, to look further into why a relative relationship between K_{IC} and $\sqrt{d^*}$ can occur, researchers [176, 220-221] recognized a direct relationship of prior-austenite grain sizes with K_{IC} to heat treatment processes. The heat treatment processes were varied based on austenite temperatures and controlled cooling rates to result in the outcome of K_{IC}. In 1963, Couque et al. [227] distinguished the effect of ferrite and prior austenite grain sizes based on their cooling rates and austenite temperatures (1000 -1500 ^{o}C) as to the behaviour of the plane-strain fracture toughness. Their study [227] showed that temperatures between 23^{o}C and 60^{o}C had coarser austenite grains having higher K_{IC} than finer austenite grain sizes. In 1975, Chaudhuri and Brook [225] attributed the increase of fracture toughness with increasing austenite grain sizes at tempering temperatures done at 200^{o}C within the range of 10 - 55mm for 12% Cr steel, which exhibited dimpled rupture fracture mode [220]. According to Werner [221], the measured K_{IC} of α-Fe steel (alpha alloyed irons) and Fe-Cr-Ni-N steel were studied with changes in austenite grain sizes. The former showed a barely dependent change with increase in grain sizes for α-Fe (i.e. a relative increase in K_{IC} with austenite grain sizes) and the latter, a decrease in K_{IC} for Fe-Cr-Ni-N steel with increase in austenite grain sizes according to the Hell-Petch relationship. Pacyna and Mazur [228] also investigated the effect of grain sizes by varying the austenite temperature to fracture toughness for tool steel (hot-work and type 6-5-2), showing higher austenite temperature resulting to larger d^* resulted to a slight increase in fracture toughness after austenitizing from

higher temperatures of about 1050ºC. This direct proportional effect from their work [228] revealed that the ratio of the mean linear intercept length ($\bar{l}$) and the diameter of the plastic strain zone (d_y) formed ahead of the propagating crack can increase with fracture toughness only when the ratio is greater than 1 (i.e. $\bar{l}/d_y > 1$), which can only be controlled by adjusting the austenite temperature. These observations are in-line that larger grain sizes can be somewhat related to larger K_{IC} as seen in Figure 3.11.

In this study, as seen in Figure 3.11 and Table 3.1, deep head hardened (DHH) rails steels have larger d^* values than micro head hardened rails, next to head hardened pearlite before hyper eutectoid rail steels. The reason why JP has a lower d^* values than EV, even with both being DHH rail steels is not clear at this stage and could be related to the procedures of manufacturing. CZ, however, with no hardening treatment procedure on the rail surface and a relatively uniform microstructure, has the lowest K_{IC} and Std Dev values as seen in Table 3.2, yet having larger d^* values than R#3. However, in general, it can be said that heat treatment procedures improved the K_{IC} values, reflected in their d^* values as compared to hyper-eutectoid treated and no heat treatment rail steels of R#2 and R#3, and CZ respectively.

Although recommendations from *ASM International* [173] suggests that K_{IC} increases with grain sizes for only ferrite materials (as opposed to Hell-Patch strengthening theory [229] for aluminum and other metals), Kavishe [230] (thesis work, Pg. 82) provides a range for the austenite grain sizes of pearlitic rail steels for this suggestion to be valid, which recommends perlite steels with d^* ranging from 28-88μm provides a relative linear relationship with K_{IC}. Above this range, K_{IC} becomes insensitive to further increase of d^*. However, this still needs further study as different heat treatment procedures and alloying components are likely to vary this range. Some other studies also [231 -235] look into the micromechanical behaviour of steel and how it affects parameters affecting fracture.

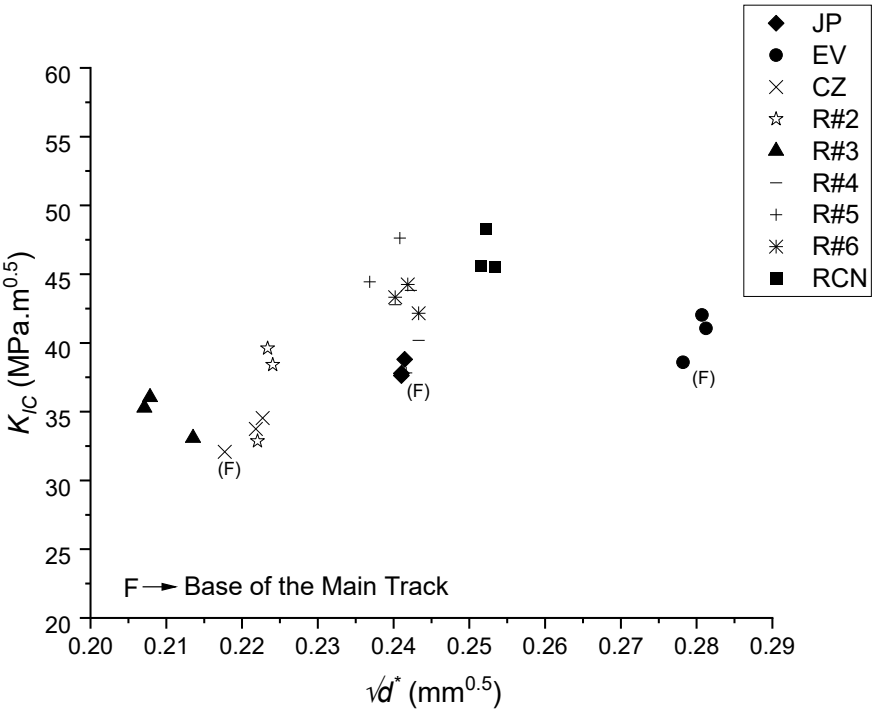

Figure 3.11 Prior-austenite grain size relationship with ASTM K_{IC} of nine different rail steels

3.4.3.2 Phases of the rail steels

The initial microstructure of the examined rails were fully pearlitic as shown in Figure 3.12. It can also be observed that random orientation of ferrite/cementite exhibited alternating lamellae colonies with some portions having larger ferrites than cementite's and vice versa. The interlamellar spacing and the pearlite colony sizes as seen at the 1mm magnification constitute the microstructural physical properties of an austenite grain size. Non-metallic inclusions were not examined in this study, but the microstructure showed signs of indications of non-metallic inclusions present within the ferrite matrix at a random orientation and as such is subject to more studies.

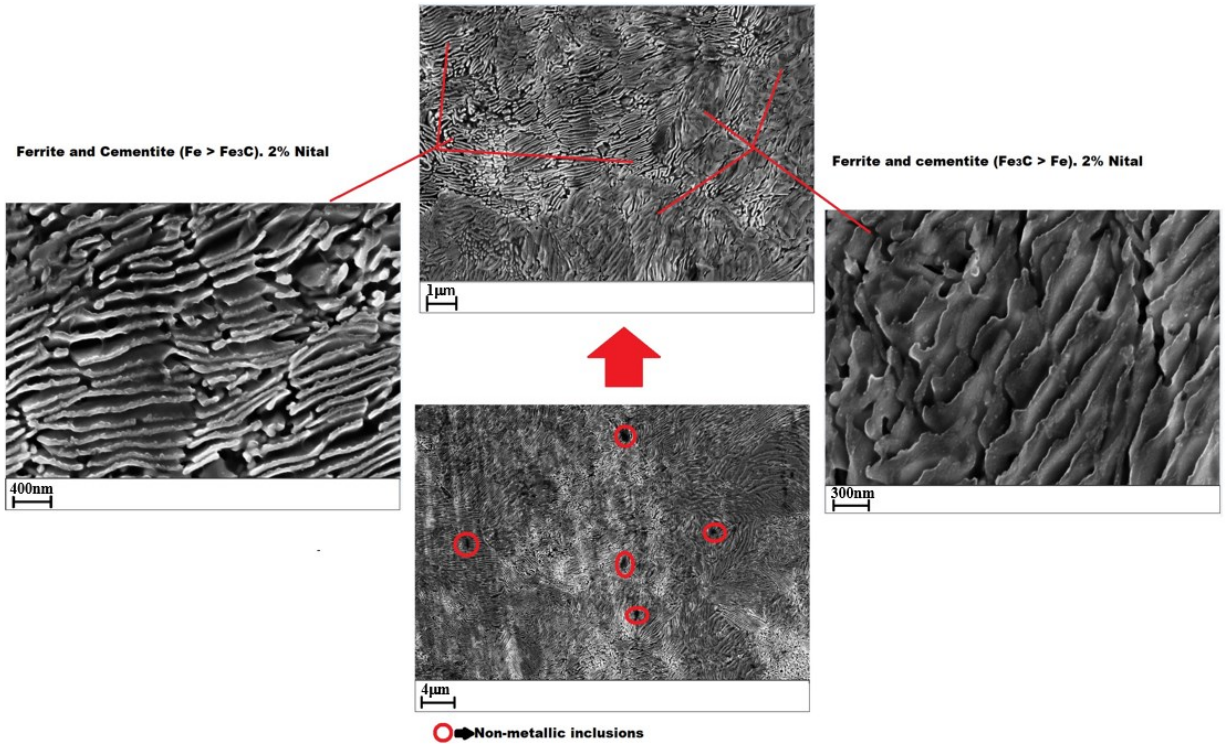

Figure 3.12 Pearlite structures of rail steels (RCN rail as an example)

3.4.4 Estimating C_m, γ_m and α_m

To estimate C_m, γ_m and α_m are meant to be known as seen in Eq. (3.17). To attain γ_m, m (constraint factor) is required since it is challenging to estimate m without performing an ASTM standard test for fracture toughness estimation. However, works from Pereira et al. [210] shows the relationship between n and the constraint factor, m, using different models, where the ASTM and the Hutchinson-Rice-Rosengren (HRR) singularity-based prediction model results were agreeable to experimental outcomes [210]. This invariably means the knowledge of n is sufficient to estimate m using the appropriate models provided in [210].

In Figure 3.13(a), the prediction models from ASTM, McMee-King and HRR are presented to show the relationship with n of the rail steels while Figure 3.13(b) shows the application of the models from Figure 3.13(a) in attaining m^* for the rail steels using Eq. (3.18). Once m^* is known, γ_m can be attained using $\gamma_m = \frac{4}{\pi m^*}$ originating from SSY criteria [56]. According to Pereira et al. [210], the ASTM approach agrees reasonably well with experimental data and thus the estimated

m^* was based on ASTM data with some modifications. Since at 1200MPa, the ASTM prediction values over estimates the experimental data, the HRR model [210] was merged with ASTM model since the HRR [210] approach underestimates the experimental data from $n < 0.1$. This is to get an attempt to attain a closer approximation to the experimental outcome of m vs n. The same approach was applied to the 400MPa low strength steel projections with ASTM. Here, the McMee-King's [210] model was merged with ASTM model since McMee-King's [210] model overestimates the experimental data from $n < 0.1$ and the ASTM approach underestimates the experimental data. Figure 3.13(b) shows how the different models were merged to attain an average model that was used for high strength steels for this study, which has an approximate of 800MPa yield strength. It is seen that from $n > 0.08$, the predicted values of m^* matches closely the experimental values.

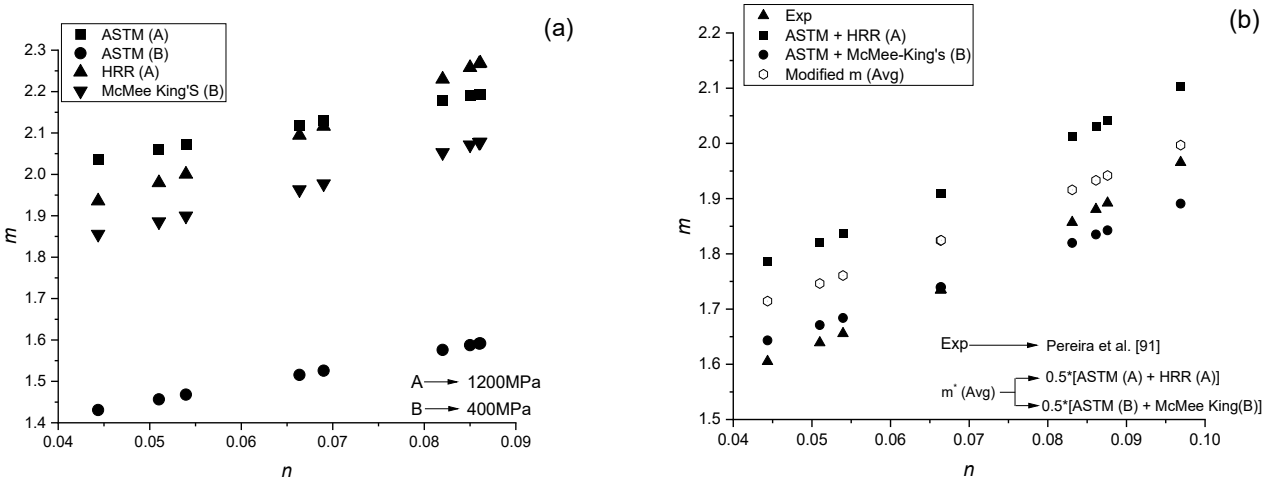

Figure 3.13 Correlation between m and n: (a) low and very high strength steel of 400 and 1200MPa [205], respectively, and (b) an average of 800MPa for high strength steel applications.

With the knowledge of m^*, δ_c can be estimated using Eq. (3.16) along with the knowledge of K_{IC} values of the nine-rail steels from Table 3.2. As shown in Table 3.5, the ratio of l_o^*/δ_c for the nine rail steels are very high ranging from 50-60 as compared from the recommendations by Rice and Johnson [197]. The high ratio can be further correlated to microstructural activities like the coalescence of secondary micro voids [197], which occurs for materials under high η. Garrison [197] also explains the mechanism of *void sheet coalescence,* which considers the linking up of very small secondary phase particles (smaller than the primary inclusions) with primary voids and

the blunting crack tip during fracture initiation. However, the values of l_o^* attained for the rail steels fall within the limit of experimentally attained l_o^* values seen in literature [225-226] as seen in Table 3.5. A ratio between l_o^*/d^* gives a range of 5-7 for all the rail steels as seen Table 3.5, which falls within the range suggested by Haggag and Nanstad [66] and Ritchie et al. [61] for ductile materials.

Table 3.5- Relationship between l_o^*, d^* and δ_c for the nine rail steels.

	JP	**EV**	**CZ**	**R#2**	**R#3**	**R#4**	**R#5**	**R#6**	**RCN**
d^*	0.0581	0.0788	0.0492	0.0499	0.0456	0.0592	0.0584	0.0578	0.0633
m^*_{avg}	1.9325	1.9268	1.9096	1.6620	1.6937	1.7427	1.7418	1.5682	1.7652
γ_m	0.659	0.661	0.666	0.766	0.751	0.730	0.731	0.812	0.721
δ_c (m)	6.27E-6	8.09E-6	6.16E-6	5.83E-6	5.06E-6	8.11E-6	6.91E-6	6.76E-6	7.29E-6
l_o^* (mm)	0.3340	0.5532	0.3597	0.3109	0.3367	0.3724	0.3462	0.3706	0.3827
l_o^*/δ_c	53.31	68.40	58.47	53.33	66.59	45.91	50.10	54.86	52.53
l_o^*/d^*	5.749	7.022	7.308	6.234	7.382	6.290	5.924	6.418	6.044

To attain α_m as expressed in Eq. (3.11), which is a dimensionless parameter that relates micro fracture with macro fracture, the work of Rice and Johnson [192] is employed in this study. The slope on the non-linear relationship for a small range of plastic strain, according to suggestions from [150, 193-194], is rather used that corresponds to the η at the loading condition. Figure 3.14(a) shows the linearized portion of Rice and Johnson's [192] outcome, chosen for a small range of X_o/δ values at high η. The slope (0.1878) as seen in Figure 3.14(a), which is equivalent to $1/\alpha_m$ value. This is used along with γ_m to attain C_m using $C_m = \sqrt{\frac{\alpha_m}{\gamma_m}}$. The values of C_m match closely to Haggag and Nanstad's [66] suggestion for C_m values for carbon steels, where all the C_m values for the nine rail steels are approximately 3. Figure 3.14(b) shows the values of C_m for the nine rail steels.

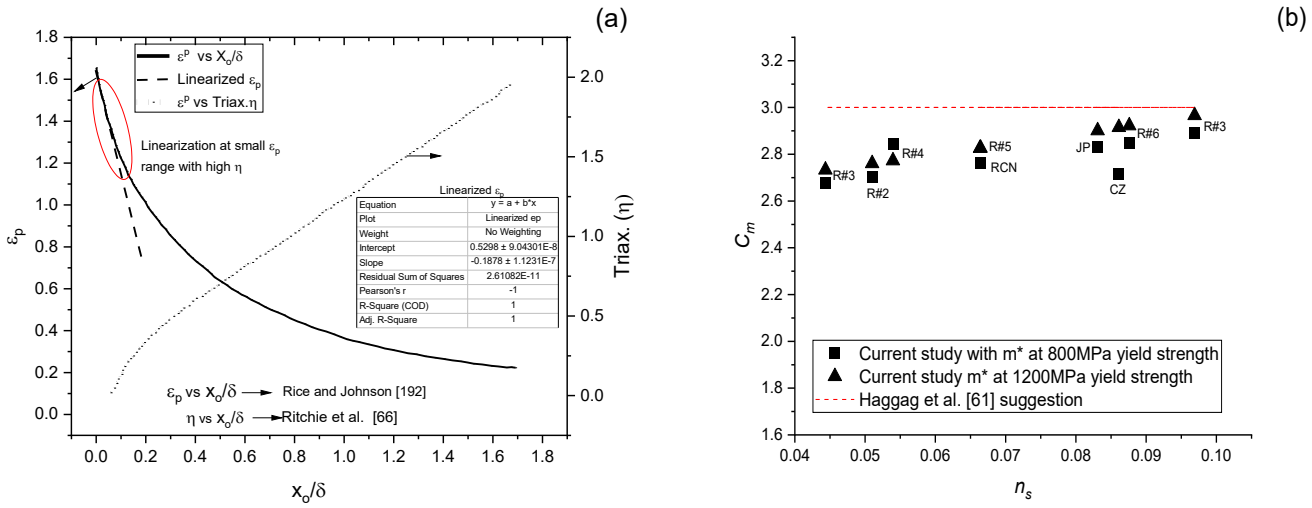

Figure 3.14 Determination of α_m *and* C_m*:* (a) Linearization of plastic strain and X_o/δ at high stress triaxiality [66], and (b) relationship between C_m and n

3.4.5 Usage of modified critical fracture strain model

3.4.5.1 Estimating $K_{IC,pred}$ via modified critical fracture strain model

The tensile testing of these rail steels as described in [183] and shown in Appendix 7 resulted in diffuse necking and dimple formation. This is evidence that ductile failure was the dominant fracture mechanism. Thus, by utilizing Eq. (3.17), the estimation of $K_{IC,pred}$ can be attained. Table 3.6. shows the different predicted $K_{IC,pred}$ for the rail steels using one location on the railhead based on the three critical fracture strain models. The K_{IC} values as seen in Table 3.1 is used to compare with $K_{IC,\text{pred}}$ as seen in Figure 3.15, showing the utilization of the modified critical fracture strain model on the rail head (A→for COMPX and C→CN rail steels). Values of mechanical properties E_s, σ_{ys} and n_s are obtained from the work of Okocha et. al. [183] while values of mechanical properties E, σ_y are obtained from Yu et. al. [73, 104]. Hence, Table 3.6 shows a summary of the mechanical properties and fracture toughness estimations for the nine rail steels.

Table 3.6 Summary of parameters for estimating fracture toughness.

Parameter	JP	EV	CZ	R#2	R#3	R#4	R#5	R#6	RCN
E (GPa)	200	195	193	200	200	185	190	220	200
σ_y (MPa)	820	714	632	941	925	943	936	887	870
E_s (GPa)	201.53	200.11	197.79	207.97	209.91	211.22	207.05	210.06	198.27
σ_{ys} (MPa)	807.59	746.84	718.15	935.57	926.01	871.92	932.89	904.74	891.81
d^* (mm)	0.0581	0.0788	0.0492	0.0499	0.0456	0.0592	0.0584	0.0578	0.0633
m^*_{avg}	1.9325	1.9268	1.9096	1.6620	1.6937	1.7427	1.7418	1.5682	1.7652
Rv/Ro	5.7625	7.0383	7.3255	6.2487	7.3992	6.3052	5.9380	6.4325	6.0579
l_o* (mm)	0.3582	0.4529	0.3320	0.3023	0.3046	0.3876	0.3750	0.3781	0.3983
C_m	2.843	2.838	2.828	2.637	2.663	2.701	2.699	2.561	2.718
$\varepsilon_{eq}^{f,\eta_{avg}}$	0.00370	0.00326	0.00307	0.00334	0.00314	0.00354	0.00375	0.00355	0.00352
$\varepsilon_{eq}^{p,\eta_{avg}}$	0.00304	0.00288	0.00284	0.00269	0.00265	0.00280	0.00284	0.00236	0.00286
n_s [178]	0.0876	0.0969	0.0831	0.051	0.04436	0.06644	0.05396	0.06636	0.08612
$K_{IC,Pred(i)}$	41.91	40.69	31.53	36.34	35.42	41.79	42.68	41.44	42.45
$K_{IC,Pred(ii)}$	37.99	38.25	30.32	32.62	32.54	37.16	37.14	33.79	38.26
$K_{IC,Pred(iii)}$	203.14	229.86	177.01	144.40	136.46	186.00	168.73	176.83	211.64

The outcomes from $K_{IC,pred(i)}$ show a relative difference with K_{IC} with its values closely matching the fracture toughness via ASTM approach. This opens an avenue for fracture toughness to be estimated via uni-axial tensile test of smooth specimens if the η_{avg} of the sharp crack tip from the SENB specimens is known. Thus, despite the failure mechanism being in the LEFM regimen, it was clear that ductile failure mechanism ruled the fracture of the specimen even though cleavage fracture is promoted. Appendix 7 shows the combined true stress and strain for the 9 rail steels and a sample of the fractured surface of the rail steel. Values from $K_{IC,pred(ii)}$, although conservatively close to K_{IC} values do not show a good trend. It is rational to consider the equivalent plastic strain for micro ductile fracture ($\varepsilon_{eq}^{p,\eta_{avg}}$) for the development $K_{IC,pred(ii)}$ as an avenue for non-destructive testing for fracture toughness estimation. The lower values of $K_{IC,pred(ii)}$ than $K_{IC,pred(i)}$ can be a function of the constraint factor, m^*, values and needs to be investigated.

For the indentation outcome ($K_{IC,pred(iii)}$), the work done by Yu et al. [73], which proposes to predict K_{IC} (for the same rail steels and indenter size, 1.19mm) also showed a strong correlation but with several times higher outcome than the K_{IC} values. The method requires identifying a critical h_c based on the specific indentation energy and damage accumulation under the indenter where E_s degradation must attain some critical point similar to the degraded E from a fractured smooth round tensile specimen [73]. It is likely that the difference between the stress triaxiality between the smooth tensile specimen and the indentation process resulted to the higher value of K_{Ind} [73] estimated even though it showed a good correlation with K_{IC}.

In this work, the expression, $\sqrt{\sigma_y l_o^* n_s}$ from the modified critical fracture strain model is considered as the specific indentation energy, which is still large and thus results to the larger fracture toughness estimation. The challenge with $\sqrt{\sigma_y l_o^* n_s}$ comes with the n_s being quite larger than the expected equivalent plastic strains since the influence of the high η and multiaxial stresses are already contributing to the development of n_s [104] and l_o^* simultaneously [196, 198-199, 201-, 202]. Further studies in using indentation for fracture toughness is required as this will thus promote the non-destructive testing of structural steels be it static, in-service or rotating equipment via indentation.

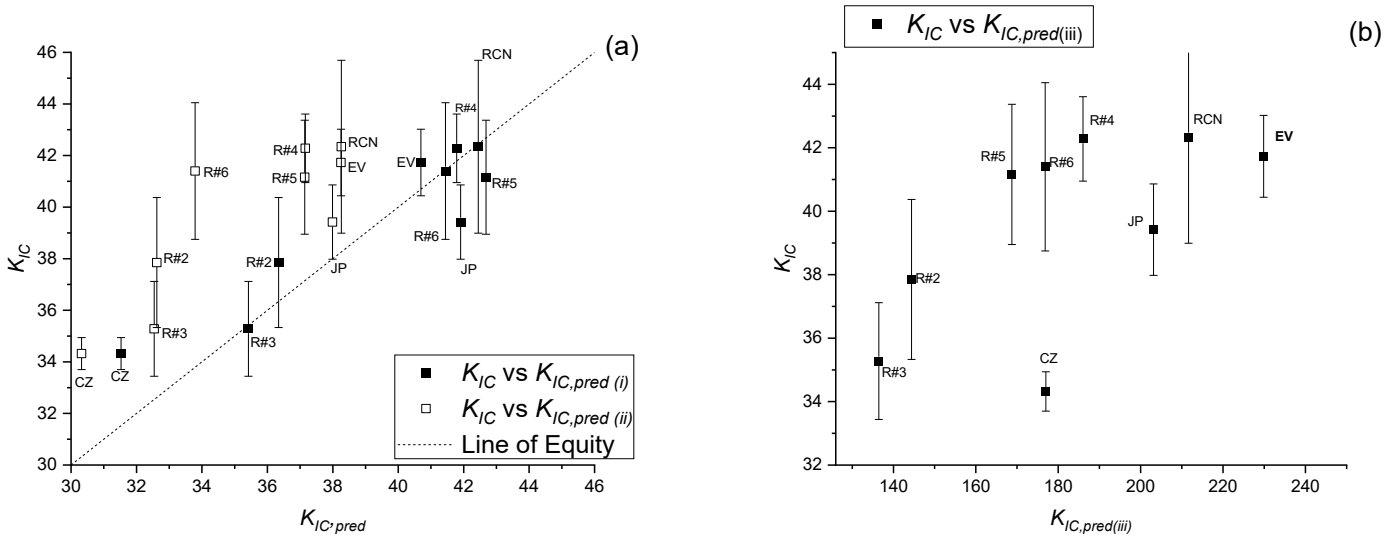

Figure 3.15 Comparison between K_{IC} and $K_{IC,\ pred}$: (a) K_{IC} and $K_{IC,\ pred}$ from tensile test, (b) K_{IC} and $K_{IC,\ pred}$ from indentation test

From Figure 3.15(a) we can see a relative similarity between $K_{IC,pred(i)}$ and K_{IC} for the rail steels, with only CZ and JP not falling within the line of equality and thus needs to be investigated while the outcomes of $K_{ICpred(ii)}$, although shows a promising trend with K_{IC} is lower than the expected value. Figure 3.15(b) is focused on the indentation test, where the fracture toughness does not relatively follow a trend with K_{IC} and is some magnitudes higher than K_{IC} values. More investigation is required to understand the reasons for the deviations and finding ways on improving the overall prediction capabilities of the modified critical fracture strain model.

3.4.5.2 Correcting $K_{IC,pred(ii)}$ and $K_{IC,pred(iii)}$ for fracture toughness estimation

As seen in section 3.4.5.1, the estimation of fracture toughness $K_{IC,pred(ii)}$ underestimates K_{IC} due to the constraint factor, m^*, being estimated from fractured tests [205] attained using J-integral (J) and CTOD at different points along the resistance curves [205], thus making C_m have a lower value. To correct this effect, suggestions from Haggag et al. [61,65], which estimates C_m to be 3 for carbon steel is being used. This higher value of C_m is thus applied for Eq 3.17(ii), where $\varepsilon_{eq}^{p,\eta_{avg}}$ is considered for non-destructive smooth tensile specimens, which is advantageous for application in micro-specimens.

For the indentation test, the value of n_s is attained from the average plastic stress and plastic strain found under the tip of the ball indenter, which is multi-axial in nature. A suggestion for estimating n from the ball indentation at this stage is firstly, using FE modelling to assess the evolution of the von Mises stress to the equivalent strain for the nine rail steels and then estimating n by using least square method of the log-log scale of Hollomon's equation at the plastic region of the curve (just 5% of the curve in the plastic region), which is regarded as the *adjusted pseudo strain hardening exponent* (n_s^*). Figure 3.16 shows the evolution of the von Mises stress to equivalent strain (a combination of the logarithmic strain and equivalent plastic strain for this work via *ABAQUS field output parameters*) curve attained via FE modeling for the nine rail steels along with the comparison between n_s^* and n (Figure 3.16(j)).

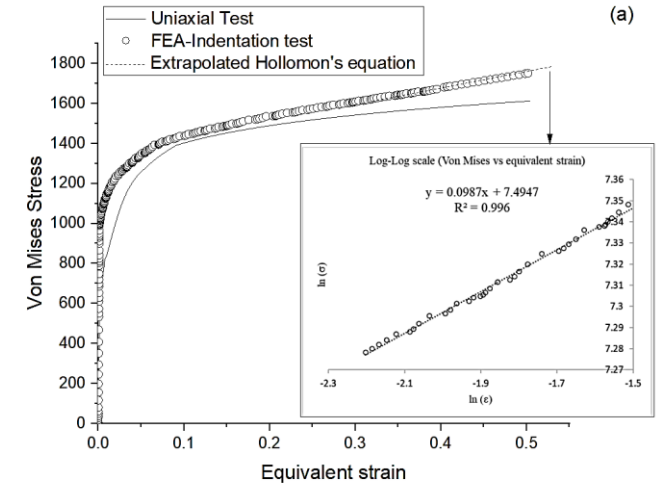
(a)
Uniaxial Test
FEA-Indentation test
Extrapolated Hollomon's equation
Von Mises Stress
Equivalent strain
Log-Log scale (Von Mises vs equivalent strain)
y = 0.0987x + 7.4947
R² = 0.996
ln (σ)
ln (ε)

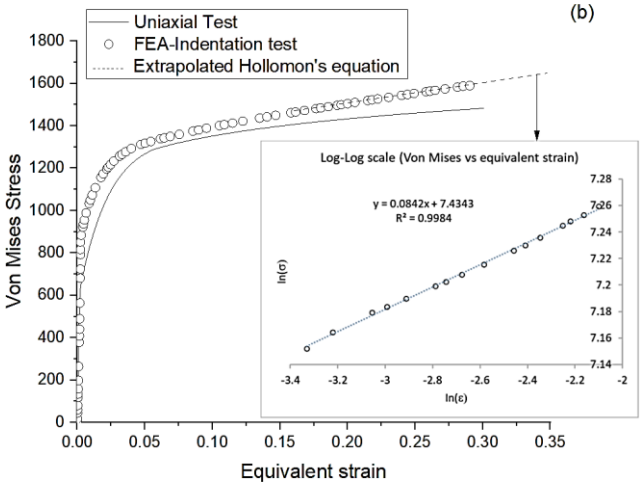
(b)
Uniaxial Test
FEA-Indentation test
Extrapolated Hollomon's equation
Von Mises Stress
Equivalent strain
Log-Log scale (Von Mises vs equivalent strain)
y = 0.0842x + 7.4343
R² = 0.9984
ln(σ)
ln(ε)

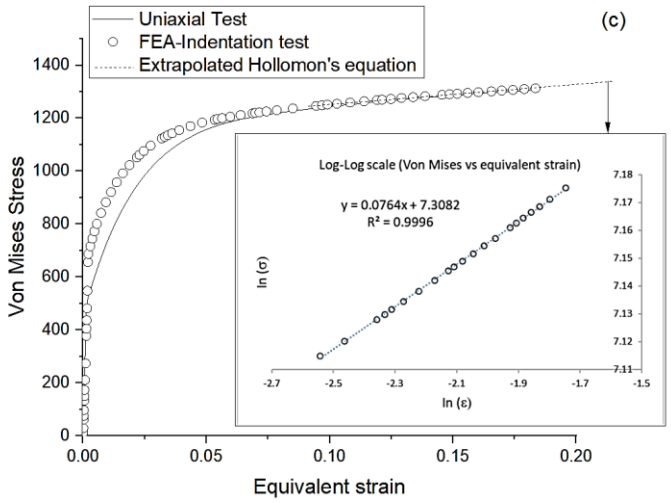
(c)
Uniaxial Test
FEA-Indentation test
Extrapolated Hollomon's equation
Von Mises Stress
Equivalent strain
Log-Log scale (Von Mises vs equivalent strain)
y = 0.0764x + 7.3082
R² = 0.9996
ln (σ)
ln (ε)

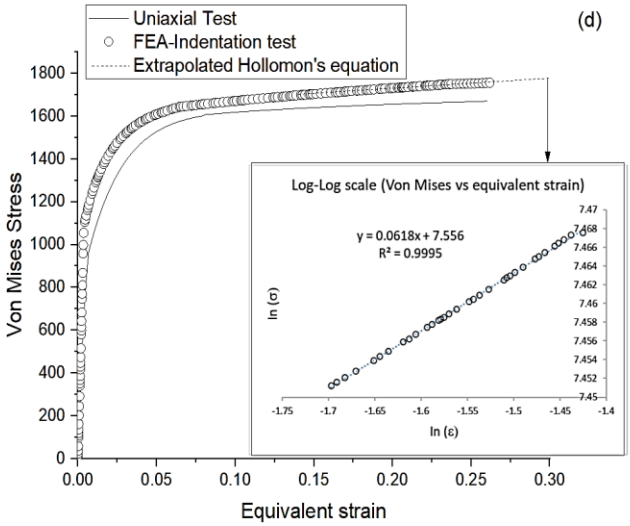
(d)
Uniaxial Test
FEA-Indentation test
Extrapolated Hollomon's equation
Von Mises Stress
Equivalent strain
Log-Log scale (Von Mises vs equivalent strain)
y = 0.0618x + 7.556
R² = 0.9995
ln (σ)
ln (ε)

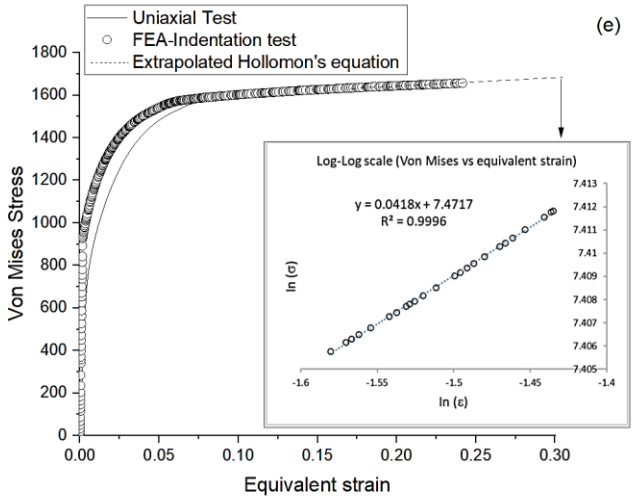
(e)
Uniaxial Test
FEA-Indentation test
Extrapolated Hollomon's equation
Von Mises Stress
Equivalent strain
Log-Log scale (Von Mises vs equivalent strain)
y = 0.0418x + 7.4717
R² = 0.9996
ln (σ)
ln (ε)

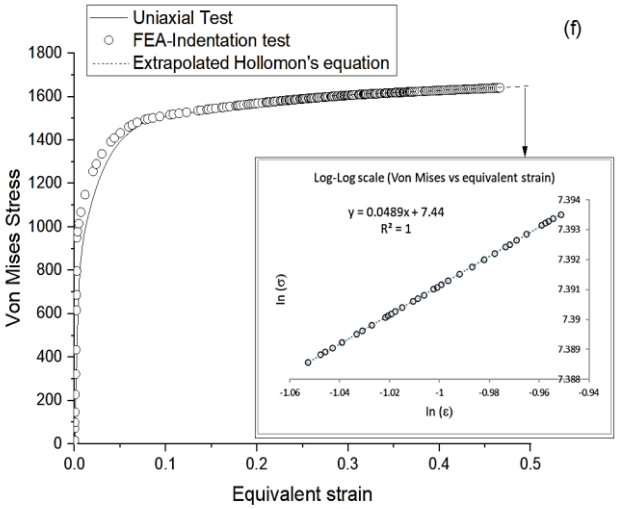
(f)
Uniaxial Test
FEA-Indentation test
Extrapolated Hollomon's equation
Von Mises Stress
Equivalent strain
Log-Log scale (Von Mises vs equivalent strain)
y = 0.0489x + 7.44
R² = 1
ln (σ)
ln (ε)

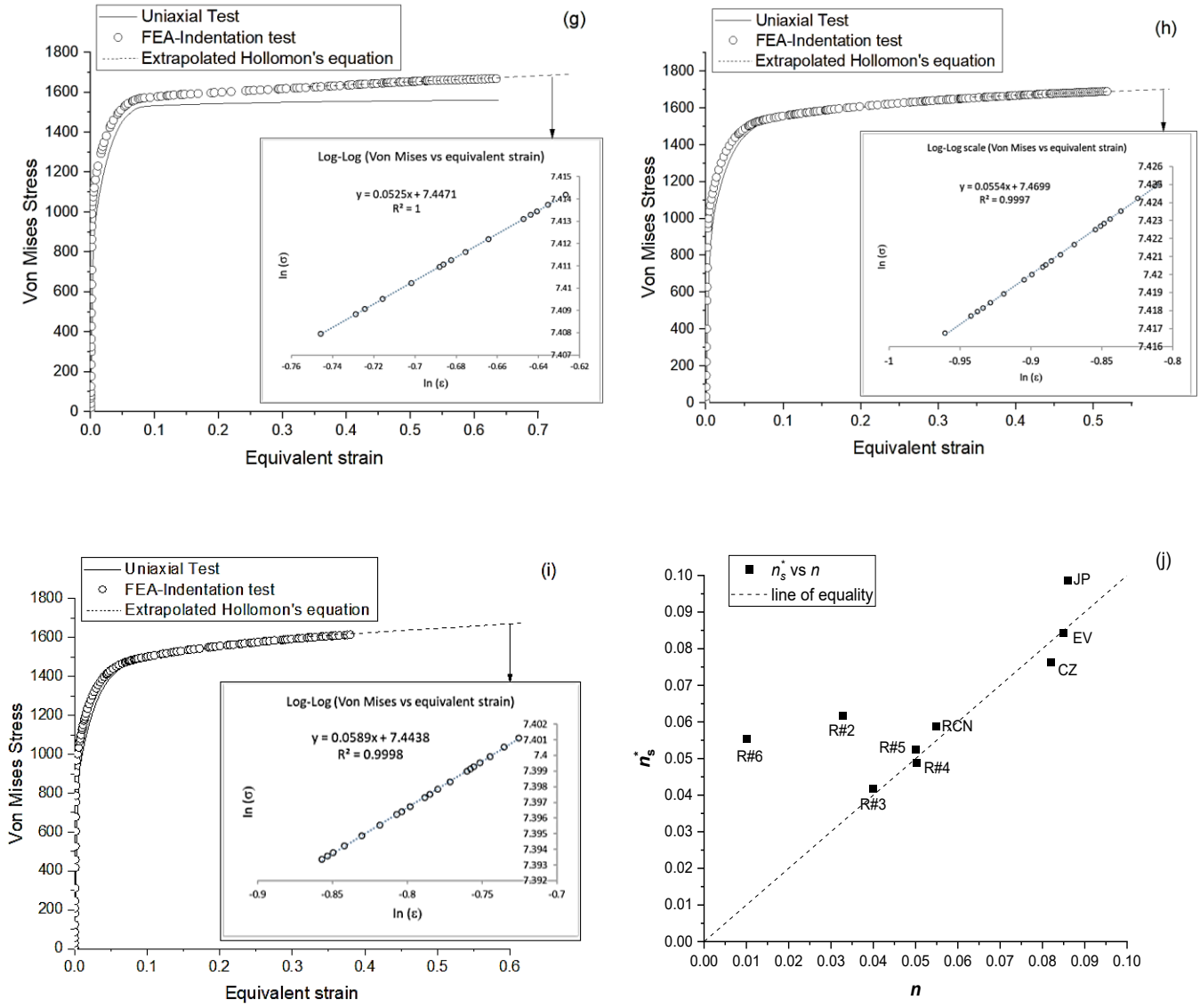

Figure 3.16. Combined von Mises vs equivalent strain (tensile and FEA-indentation) of high-strength steels: (a) JP, (b) EV, (c) CZ, (d) R#2, (e) R#3, (f) R#4, (g) R#5, (h) R#6, (i) RCN, and (j) comparison between n *and* n_s^* for the 9 rail steels.

For simplicity interests in industrial applications, it can be suggested that using Haggag et. al.'s [61, 65] preposition of C_m equivalent to 3 for this study, $K_{IC,pred(ii)}$ can easily be attained as seen in Figure 3.17(a) while Figure 3.17(b) shows the estimation of $K_{IC,pred(iii)}$ when $n_s^* \approx n$ (assumption of proportional loading [183-184]) for the estimation of the equivalent plastic strain for ductile fracture initiation using Eq. (3.10). However, the assumption of $n_s^* \approx n$ based *on proportional loading* needs to be looked further.

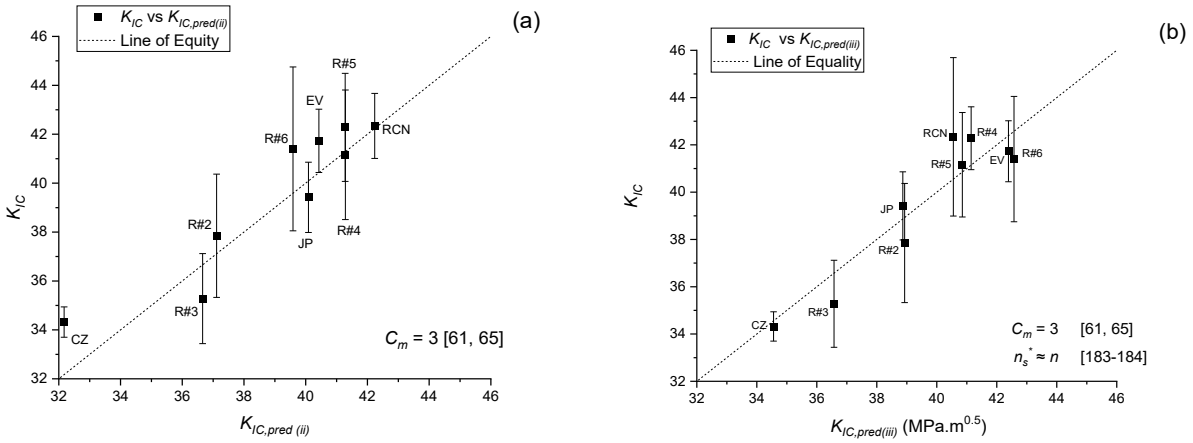

Figure 3.17 Correcting the comparison between K_{IC} *and* $K_{IC,\ pred}$*: (a)* K_{IC} *and* $K_{IC,\ pred(ii)}$ from tensile test based on *n, (b)* K_{IC} *and* $K_{IC,\ pred(iii)}$ from indentation test based on $n_s^* \approx n$ for the estimation *of a new* $\varepsilon_{eq}^{p,\eta_{avg}}$

Looking further into determining the equivalent plastic strain for fracture initiation via indentation is to consider the development of hydrostatic stress at the indenter's tip based on the pressure (hydrostatic) developed in a smooth tensile test. Values of stresses at the onset of necking as well as at the onset of fracture are taken from experimental data in [73, 104, 178] to depict the pressure developed in a smooth tensile specimen for the 9 rail steels. Figure 3.18 (a) and (b) shows the pressure developed at the gauge section from the onset of necking and the onset of fracture. In Figure 3.18(a), the stress distribution is uniform across the gauge section due to the constant η value *(*η=1/3*)* present in the gauge section. However, the necking stage introduces an increased non-uniform deformation and non-uniform η, leading to an unstable pressure distribution across the gauge section as seen in Figure 3.18(b). Hence the pressure at the von mises stress before the onset of necking will be used in this study for characterizing the smooth tensile specimen. The pressure before the onset of necking, P_u, and the theoretical pressure before the onset of fracture, $P_f = (\sigma_y/3)$, from the smooth tensile test is then translated to indentation testing via FE modelling. Since fracture occurred at the center of the specimen, a 0.1% taper was introduced at the center of the specimen to ensure necking occurs at the center of the specimen.

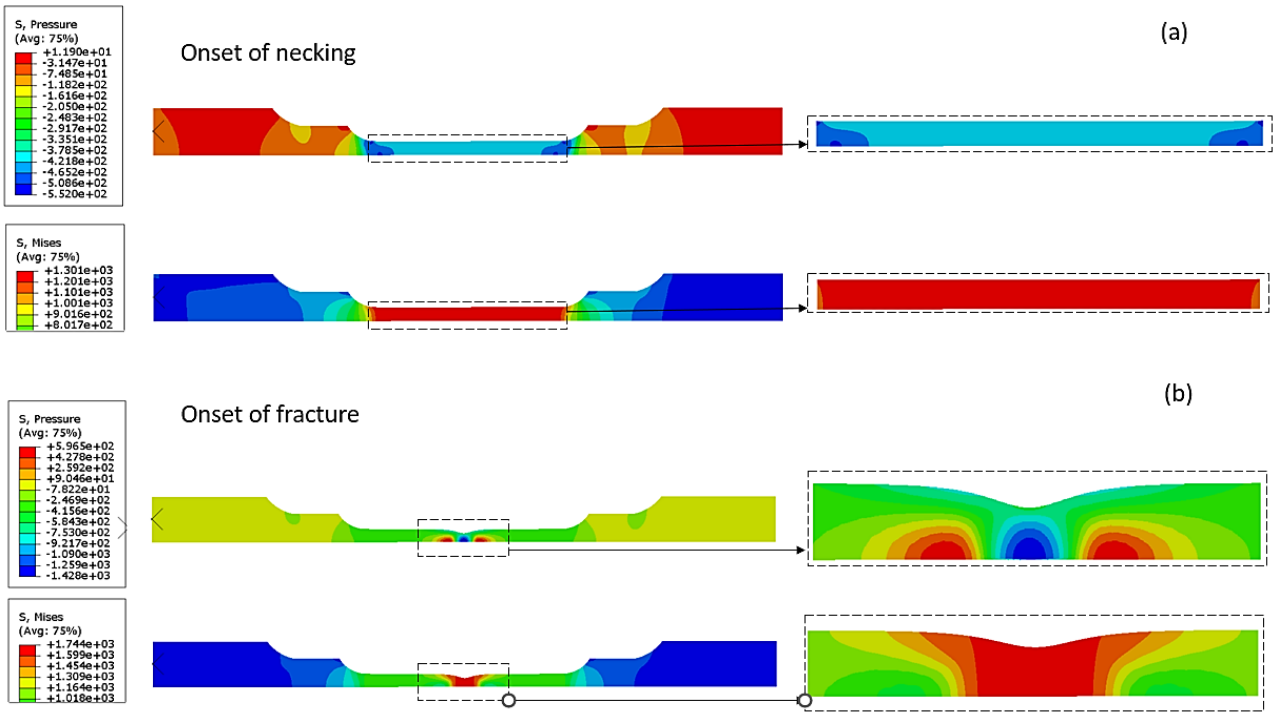

Figure 3.18. Pressure (hydrostatic) and equivalent stresses on gauge section of smooth tensile specimen: (a) At the onset necking; (b) At the onset of fracture.

To estimate the equivalent plastic strain via indentation at the pressure corresponding to the onset of necking, $\varepsilon_{ind}^{p,\eta}(\sigma_u)$, and onset of fracture, $\varepsilon_{ind}^{p,\eta}(\sigma_f)$, the pressure evolution over the equivalent plastic strain via indentation is considered by taking the values of P_u and P_f from the smooth tensile test and correlating them to indentation via FE modelling. The contour plot of the pressure distribution at the maximum indentation depth is seen in Figure 3.19. showing the maximum hydrostatic pressure developed at the tip of the indenter.

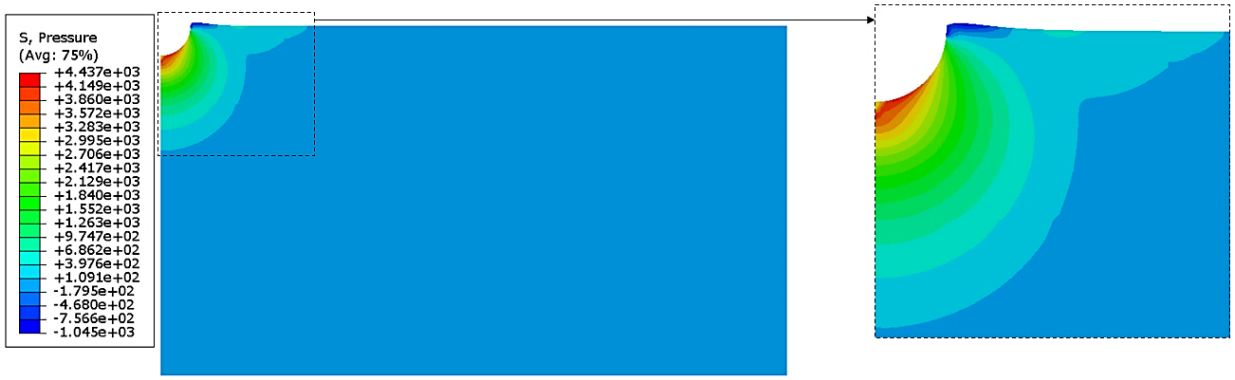

Figure 3.19. Hydrostatic pressure distribution of the indentation testing

By locating the P_u, and P_f on the evolution of indentation pressure to equivalent plastic strain, $\varepsilon_{ind}^{p,\eta}(\sigma_u)$ and $\varepsilon_{ind}^{p,\eta}(\sigma_f)$ can be identified vis FE modelling. Figure 3.20 shows the evolution of indentation pressure and equivalent plastic strain for the 9 rail steels and the comparison between $\varepsilon^{p,\eta}$ and $\varepsilon_{ind}^{p,\eta}(\sigma_u)$ for the 9 rail steels. The $\varepsilon_{ind}^{p,\eta}(\sigma_u)$ shows only a relative correlation between rails JP, EV, R#2 and R#3 with a large deviation from $\varepsilon^{p,\eta}$ while other rails show a larger deviation from the $\varepsilon^{p,\eta}$.

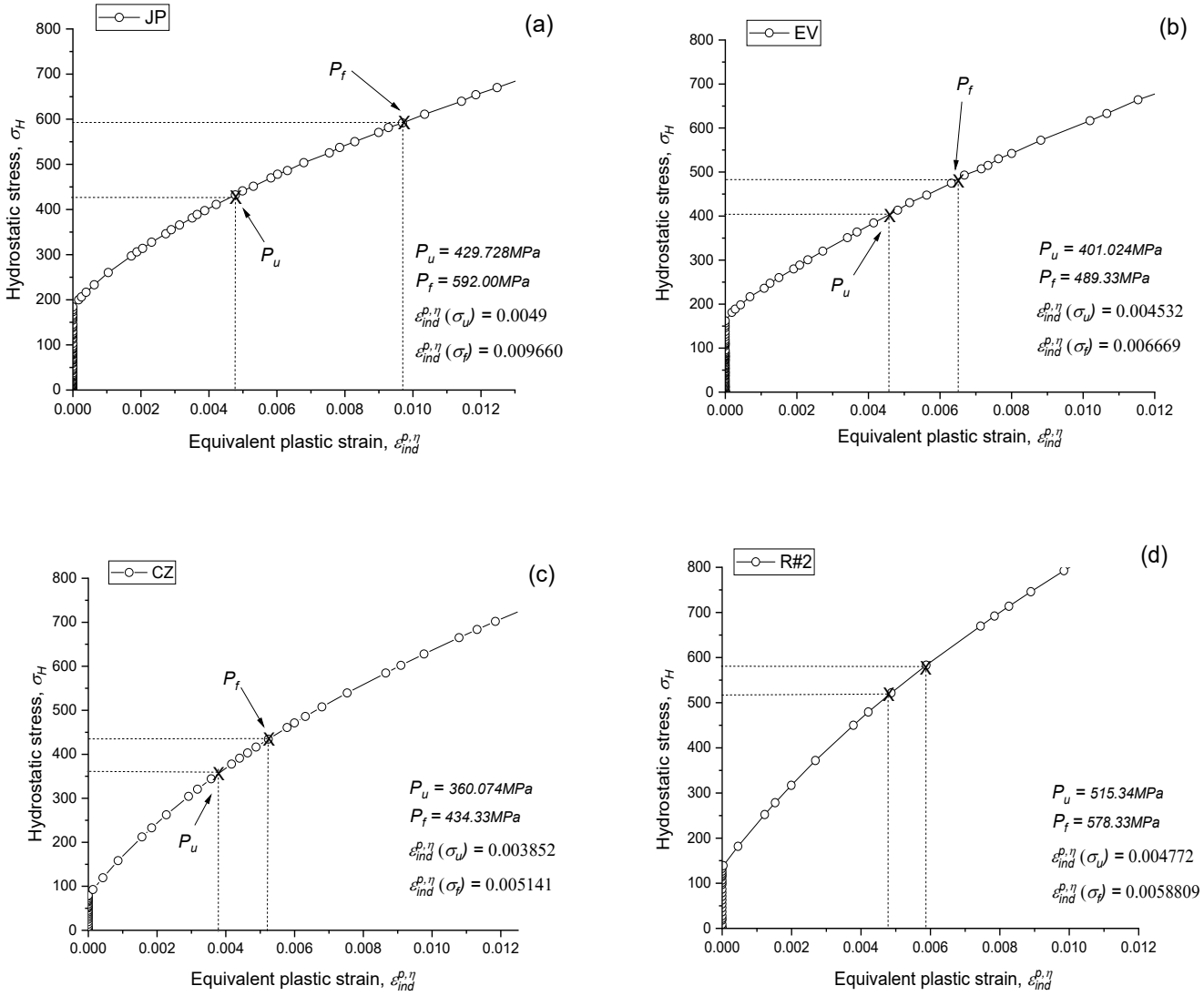

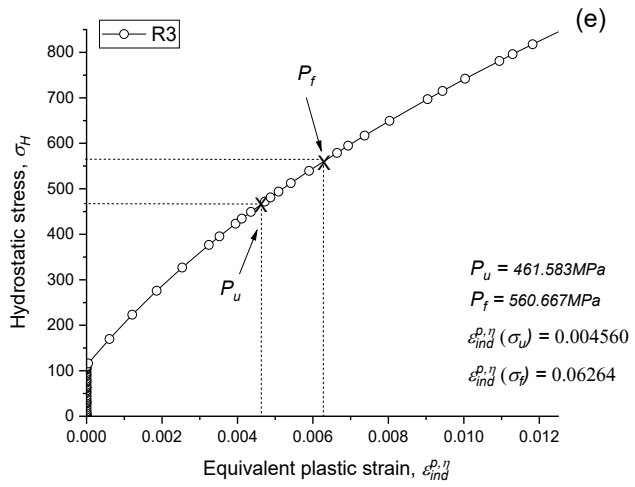
(e)
R3
Hydrostatic stress, σ_H
Equivalent plastic strain, $\varepsilon_{ind}^{p,\eta}$
P_f
P_u
P_u = 461.583MPa
P_f = 560.667MPa
$\varepsilon_{ind}^{p,\eta}(\sigma_u)$ = 0.004560
$\varepsilon_{ind}^{p,\eta}(\sigma_f)$ = 0.06264

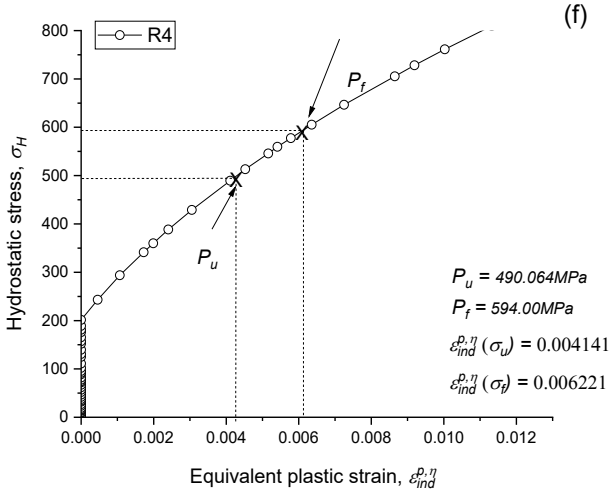
(f)
R4
Hydrostatic stress, σ_H
Equivalent plastic strain, $\varepsilon_{ind}^{p,\eta}$
P_f
P_u
P_u = 490.064MPa
P_f = 594.00MPa
$\varepsilon_{ind}^{p,\eta}(\sigma_u)$ = 0.004141
$\varepsilon_{ind}^{p,\eta}(\sigma_f)$ = 0.006221

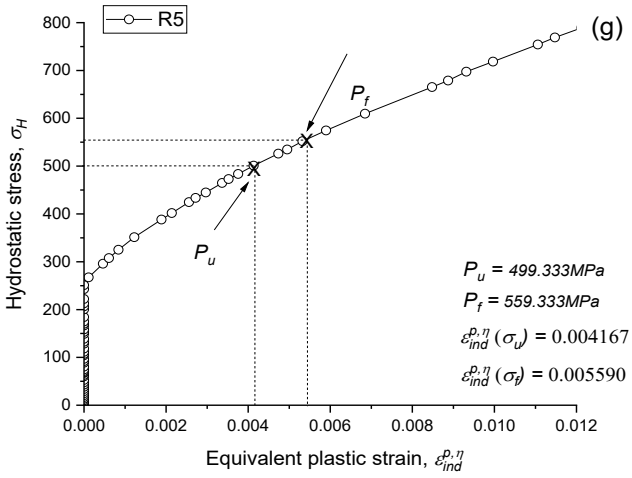
(g)
R5
Hydrostatic stress, σ_H
Equivalent plastic strain, $\varepsilon_{ind}^{p,\eta}$
P_f
P_u
P_u = 499.333MPa
P_f = 559.333MPa
$\varepsilon_{ind}^{p,\eta}(\sigma_u)$ = 0.004167
$\varepsilon_{ind}^{p,\eta}(\sigma_f)$ = 0.005590

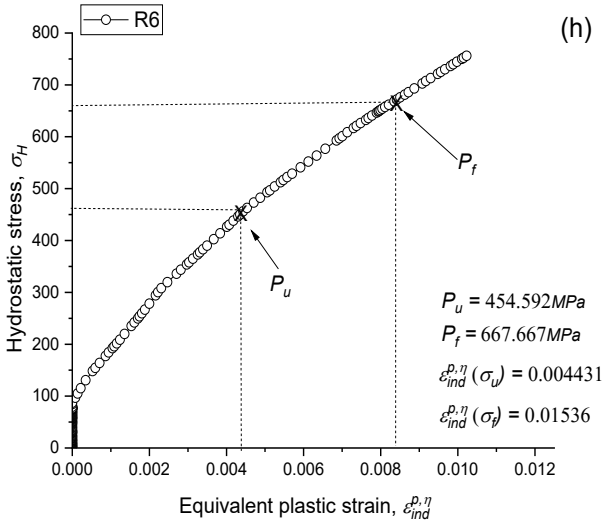
(h)
R6
Hydrostatic stress, σ_H
Equivalent plastic strain, $\varepsilon_{ind}^{p,\eta}$
P_f
P_u
P_u = 454.592MPa
P_f = 667.667MPa
$\varepsilon_{ind}^{p,\eta}(\sigma_u)$ = 0.004431
$\varepsilon_{ind}^{p,\eta}(\sigma_f)$ = 0.01536

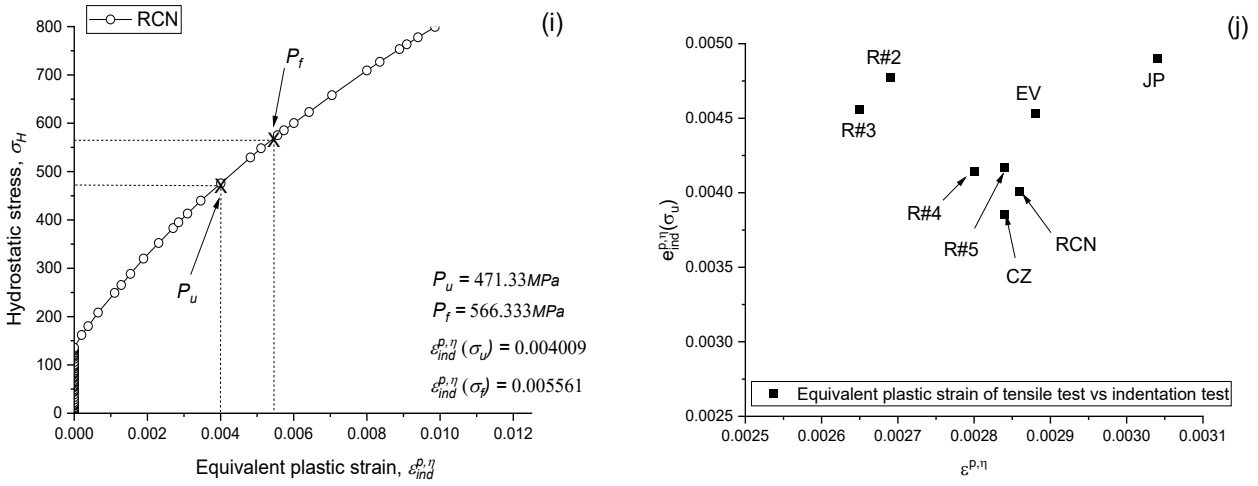

Figure 3.20 Evolution of indentation pressure and equivalent plastic strain for the 9 rail steels vis FE modelling: (a) JP, (b) EV, (c) CZ, (d) R#2, (e) R#3, (f) R#4, (g) R#5, (h) R#6, (i) RCN, and (j) comparison between $\varepsilon^{p,\eta}$ and $\varepsilon_{ind}^{p,\eta}(\sigma_u)$ for the 9 rail steels.

With the values of $\varepsilon_{ind}^{p,\eta}(\sigma_u)$, it can be used with Eq.(3.17iii) to estimate the fracture toughness. Figure 3.21. shows values of $K_{IC,pred(iii)}$ attained with and without the use of C_m =3 [61,114]. Although the relationship between $K_{IC,pred(iii)}$ and K_{IC} is relative, the values are quite close to K_{IC} values, thus showing the estimation of $\varepsilon^{p,\eta}$ and K_{IC} via indentation. This offers a promising future for fracture toughness estimation using a ball indenter for high strength steels and should be investigated even further.

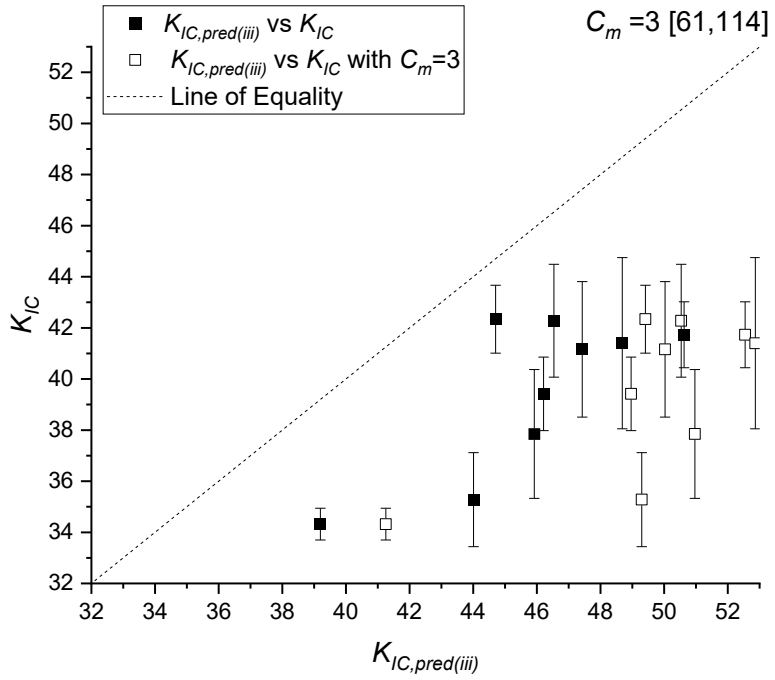

Figure 3.21 Fracture toughness estimation for indentation testing

Based on K_{IC} estimation via the indentation method, Figure 3.17(b) provides the opportunity for fracture toughness estimation, non-destructively via estimating $K_{IC,pred(iii)}$better than the outcome from Figure 3.21. The approach of defining $\varepsilon_{eq}^{p,\eta_{avg}}$ by considering $n_s^* \approx n$ [183] in conjunction with Eq. 3.10 provided a consistent outcome with K_{IC} estimation, thus indicating that the estimation of n_s^* is negligibly influenced by the multi-axial stresses at that stage (plastic regime) of the rail steels' material deformation. This suggests that there was very little or no increase in the plastic constrain, δ_s needed for increasing the multi-axial stresses that contributed to the $s_{a,p}$ [65,178, 150]. Thus, the preposition of $n_s^* \approx n$ can be acceptable. However, in Figure 3.21, the deviation between $K_{IC,pred(iii)}$ and K_{IC} can be due to the difference in the η during the tensile test (during the onset of necking as seen in Figure 3.18a) and the indentation test resulting in the difference between $\varepsilon_{ind}^{p,\eta}(\sigma_u)$ and $\varepsilon_{eq}^{p,\eta_{avg}}$. This, however, requires further studies.

3.5 Conclusions

In this chapter, fracture toughness was estimated and investigated using the modified critical fracture strain model for 9 high strength rail steels, where 3 proposed viewpoints involving tensile destructive tests, tensile non-destructive tests and indentation test are suggested. The main conclusions can be summarized as follows:

1. The η_{avg} plays a major role in controlling the fracture behavior for high strength rail steels both in indicating the l_o^* and the equivalent accumulated plastic strain.
2. The study suggests that γ is insensitive to ε_{th} and p_{th} as the value of p_{th} is close to ε_{th} for a short-gauge, notched specimen as seen from the works by Yu et al. [139]. We assumed in this study that $p_{th} = \varepsilon_{th}$. However, at high stress triaxiality as those seen in SENB and indentation testing, further investigation is needed in determining the dependency of η *to* p_{th} based on the γ.

3. The usage of η_{avg} in the modified critical fracture strain model is dependent on the materials' deformation and fracture behavior. For the rail steels with little plastic deformation, the magnitude of η_{avg} was used similar to the η_{avg} experienced at the sharp crack tip of a standard SENB specimen. (i.e materials that follow the LEFM principles have high η while very ductile material as used by Haggag et al. [61,114] are quite insensitive to η_{avg}.

4. At high η, the high pressure for fracture initiation requires that the equivalent accumulated plastic strain is reduced thus suggesting the quick micromechanism of void nucleation, growth, and coalescence when compared to low η.

5. The microstructural information regarding the distance between voids along the prior-austenite grain boundaries for rail steels is important in estimating $K_{IC,pred}$, where l_o^* can also depends on the prior-austenite grain size. Concern must be taken as not all ductile failure mechanism follows this theory for the definition of l_o^* in this work and is affected

by the initial sequential distribution of voids/non-mettalic inclusions within the material's matrix.

6. Achieving $K_{IC,pred}$ non-destructively in this study requires n to be attained via tensile test as this is estimated into $\varepsilon_{eq}^{p,\eta}$ needed in the modified critical fracture strain model. Using ball indentation technique still needs further study as n_s for high strength rail steels is in a multi-axial stress state, which has been affected by the η. $\varepsilon_{ind}^{p,\eta}(\sigma_u)$ also shows promising signs of using indentation test for fracture toughness estimation.

7. For simplicity and quick industrial application, C_m can be taken as 3 for carbon steels and as suggested by Haggag et al. [61, 114], when n is considered for the application of the modified critical fracture strain model for tensile test.

In conclusion, fracture toughness is proposed to be measured for high strength steels using mechanical properties (Young's modulus and yield strength) with the inclusion of stress triaxiality both with the equivalent plastic strain and the characteristic length either for tensile or indentation tests. However, the stress triaxiality to be considered is that similar to a sharp crack tip, similar to what is experienced in an SENB specimen or the tip of a spherical indenter as long as the material in question follows the conditions of linear elastic fracture mechanics. The constant C_m was also seen to vary with different materials depending on their strain hardening exponent values. However, for a nondestructive approach (i.e using n or n_s instead of the equivalent plastic fracture strain) C_m is suggested to be a constant value of 3.

Chapter 4 Fracture Toughness Measurement of AL2024-T351 using Flat-end Cylindrical Indenter via Modified Limit Load Analysis[3]

4.1 Introduction

For metallic materials, indentation testing for fracture toughness measurement is a relatively recent development, gaining significant attention in the past few decades [65-66, 73, 104,111,146,155-157, 236-240]. With each indenter type providing an advantage and/or disadvantage over the others, the spherical indenter has gained more popularity due to its simplicity, reduced sensitivity to surface imperfections, reduced pile-up/sink-in effects, applicability, easy calibration, provision of the Hertzian elastic contact with indented material and predictability in stress-strain behavior [66, 178]. However, challenges arise when more than shallow indentation is needed because of the limited depth capabilities [241] associated with the spherical indenter. Thus, another indenter type is needed, which in this study is a cylindrical indenter with a flat end to overcome the limitation of shallow indentation depth, yet with the ability to characterize the mechanical properties and fracture toughness of ductile materials. Another major concern lies with the limitation that most methodologies of the indentation approaches for fracture toughness measurement have been developed for low carbon, low strength metals which have the critical stress intensity factor (K_{IC}) higher than 100MPa.m$^{0.5}$. Furthermore, advancing the indentation methodology for fracture toughness measurement would eliminate the challenges faced by the conventional fracture toughness testing approaches by the American Society for Testing and Materials (ASTM) like ASTM E1820 [58] and E399 [69], where K_{IC} measurement requires high cost from preparation of multiple specimens, difficulty in material preparation and the associated long time for the specimen preparation. For fracture toughness measurement using flat-ended indentation, very few studies have been conducted.

---

[3] This chapter is being prepared with the title shown below, for publication in a technical journal.

Okocha, S. I., Yu, F., Jar, P. Y. B., & Hendry, M. T. (2023). Fracture Toughness Measurement of AL2024-T351 using Flat-end Cylindrical Indenter via Modified Limit Load Analysis.

Early works from Foulds et al. [146] estimated K_{IC} using a small punch test based on the concept of material toughness being a function of the material's stress-strain properties [146]. Ju et al. [145] measured the K_{IC} of structural steel using small punches by inducing a sharp crack in the specimen to simulate the condition of an infinite plate with a small sharp crack to be tested and subjected to a uniform bending stress generated by the punch. Martínez-Pañeda et al. [74] developed a novel methodology using a small punch indentation on notched specimens to assess the fracture resistance through a critical value of the notched mouth displacement, while Hurst et al. [242] focused on creating a plane-strain condition in a circular notched disc for fracture toughness estimation using the Rice-Merkle analytical model [242].

Recently, Kim et al. [238] predicted the critical stress intensity factor from J-integral (K_{JC}) of in-service structures using geometric similarity between a test using a cylindrical flat-end indenter and a cracked round bar (CRB) by assuming that the load–depth curve of the indentation test is same as the load–displacement curve of the CRB tensile test. This approach [238] requires the determination of the crack initiation point (CIP), which provides the critical load to fail a structure with defects as defined by Miller [70] without employing any notch or crack in the specimen. Outcomes show that the methodology provided by Kim et al. [238] was suitable for low strength metals as the results showed only around 20% difference from the actual fracture toughness results.

In this work, we evaluate the feasibility of using a flat-ended indenter to estimate fracture toughness, which is firstly to determine whether a chamfer is needed along the circumference of the flat end for the indentation test, and then comparing outcomes of fracture toughness from an indentation test with that from a notched round bar (NRB) under tensile loading. Based on the similarity between indentation loading using a flat-ended indenter and tensile loading on NRB, critical loading for crack initiation under indentation was determined using results from NRB based on the Irwin's limit load analysis [243]. In the end, fracture toughness attained using a method proposed in ASTM STP 1360 [244], also supported by MATWEB's extensive library for AL2024-T351 [245], is used to validate K_{JC} measurement using the chamfered cylindrical flat-end indenters.

4.2. Theory and calculation

4.2.1 Critical indentation energy for K_{JC} estimation

The critical J-integral-based stress intensity factor (K_{JC}) is defined using the virtually determined J-integral method [235].

$$K_{JC} = \lim_{a_c^{'} \to 0} K_J = \sqrt{\frac{J \cdot E_s}{(1-\nu_s^2)}} \tag{4.1}$$

The above expressions imply that the virtual J-integral (J) consists of the elastic (J_e) and plastic (J_p) parts of the load-depth curve as seen in Eq. (4.2)

$$J = J_e + J_p = \frac{(1-\nu_s^2)}{E_s} \cdot \left(\frac{L^{'}}{2a_c^{'}\sqrt{\pi a_c^{'}}} \right)^2 + \eta_{pl} \frac{A_{pl}}{\pi \left(a_c^{'} \right)^2} \tag{4.2}$$

where $a_c^{'}$ is the virtual indentation contact radius, A_{pl} the plastic area of the virtual indentation load-depth curve, η_{pl} the plastic work factor which is a function of the specimen geometry, derived from NRB specimens [244], L' the virtual indentation load, and ν_s the Poisson's ratio of the specimen.

In this study, the approach for estimating J is also applied to direct indentation data of multiple indenters, where the virtual parameters are replaced with direct indentation parameters.

4.2.2 Crack initiation point and indentation virtual load-depth curves

The work by Miller [70] provided extensive elaboration on the load required for a structure with a defect to fail. For a NRB specimen under tension, Miller [70] expressed the pressure at the crack initiation point using Tresca's failure criteria. However, due to the conservativeness of the plastic yield surface based on the Tresca's failure criteria for ductile metals, Kim et al. [238] expressed the indentation pressure at CIP (P_{CIP}) using the criterion shown in Eq. (4.3), which was used as a principal factor for failure of metallic structures.

$$P_{CIP} = \frac{L_{CIP}}{\pi \left(a_c \right)^2} = 3.285 \cdot \sigma_y \tag{4.3}$$

where L_{CIP} is the load corresponding to the CIP, a_c the contact radius for which the value depends on the indenter type, and σ_y the yield strength of the material.

To have a geometrically similar state between indentation and NRB specimens, the indentation load and depth must be normalized, so that their values can be related to those for the NRB specimens in tension. However, this similarity is under the assumption of isotropic material properties so that flow stress is same in tension and compression in all material directions. Figure 4.1(a) compares the non-chamfered flat-end indenter scheme to CRB specimens in tension, and Figure 4.1(b) chamfered flat-end indenter scheme to NRB specimens in tension.

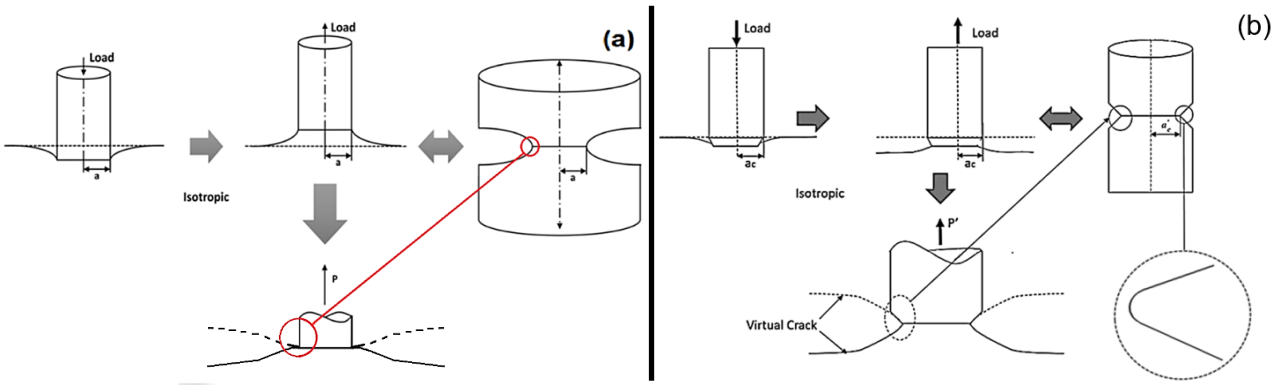

Figure 4.1. Geometrical similarity between flat-end indenters and tensile specimens: (a) non-chamfered indenter with a CRB specimen [238], and (b) chamfered indenter with an NRB specimen.

Based on the geometrical similarity between the flat-end indentation and NRB and CRB specimens (i.e. the stress singularity in a non-chamfered flat-end indenter can be regarded as being similar to that experienced in a CRB during deformation and similarly the stress singularity in a chamfered indenter especially during deformation being similar to that in a NRB specimen), it is perceived that deformation introduced by chamfered and non-chamfered indentation and that generated by tension of NRB and CRB specimens, respectively, are similar especially after the displacements are normalized using the expression given in Eq. (4.4).

$$\frac{h'}{a_c'} = \left(\frac{h}{a_c}\right)_{CIP} \tag{4.4}$$

where h and a_c are the indentation depth and contact radius depending on the indenter type, $\left(\frac{h}{a_c}\right)_{CIP}$ the normalized indentation depth at the corresponding P_{CIP}, while h' and a_c' the virtual indentation depth and virtual indentation contact radius, respectively, as to be detailed later according to the suggestions from Kim et al. [238]. Note that Eq. (4.4) is used for representing the virtual indentation testing due to the similarities in geometry from NRB specimen.

The average stress generated by the indentation load, as expressed in Eq. (4.5), is required for establishing the similarity between indenters of different sizes (for both non-chamfered and chamfered).

$$P = \frac{L}{\pi a_c^2} \tag{4.5}$$

4.2.3 Irwin's notch analysis and stress concentration factor for NRB specimens

The geometrical and mechanical connection between the mechanics of a sharp crack and notch was established by Irwin [243] as seen in Eq. 4.6(a) while Eq. (4.6b) describes the stress concentration at the notch root for a shallow elliptical notch [52, 246–248].

$$K_{\rho c} = \lim_{\rho \to 0} K_\rho = \lim_{\rho \to 0} \frac{\sqrt{\pi}}{2} K_t \cdot \sigma_{nom} \sqrt{\rho} \tag{4.6a}$$

$$K_t = 1 + 2\sqrt{\frac{t}{\rho}} \qquad \text{[52, 246–248]} \tag{4.6b}$$

where $K_{\rho c}$ is the critical K_ρ from NRB specimens, K_ρ the apparent stress intensity factor, K_t the stress concentration factor (SCF) due to the presence of a notch, σ_{nom} the nominal stress, ρ the notch root radius and *t* the notch root depth (to be defined and depicted later in section 4.3.3).

4.2.4 Measurement of mechanical properties via indentation

4.2.4.1. Yield strength estimation

Firstly, to attain the contact area needed for pressure estimation, the contact region of the indenter type must be considered. Eq. (4.7) expresses estimation of the contact areas for the non-chamfered and chamfered indenters as well as the corresponding contact radius. Figure 4.2 shows an illustration of the indenter contact region for both the non-chamfered (F) and chamfered (CH) cylindrical flat-end indenters.

$$a_{c,CH} = \frac{t_d}{2} + h_c \tan\theta \quad \text{i}$$

$$a_{c,F} = \frac{d_c}{2} \quad \text{ii}$$

$$A_{CH} = \pi\left[\frac{t_d}{2} + h_c \tan\theta\right]^2 \quad \text{iii} \qquad (4.7)$$

$$A_F = \pi\left[\frac{d_c}{2}\right]^2 \quad \text{iv}$$

where A_F and A_{CH} are the contact areas for the non-chamfered and chamfered indenters, respectively, while $a_{c,F}$ and $a_{c,CH}$ are the corresponding contact radii.

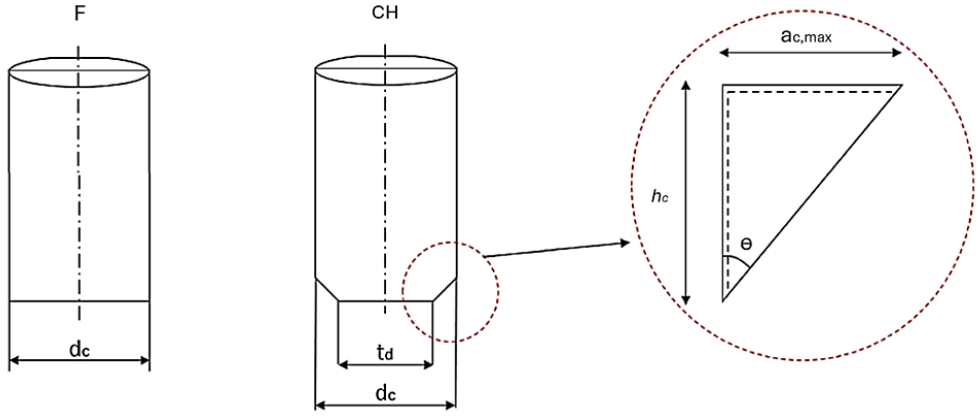

Figure 4.2 Indenter geometry for non-chamfered and chamfered flat-end cylindrical indenters

Measurement of yield strength from an indentation test using a cylindrical flat-end indenter has followed a series of suggestions from the previous works [249,–255]. In [255], the approach for the yield strength estimation is drawn from a flat-end cylindrical indenter with a rounded edge in which the force corresponding to a critical depth (φ) for full contact (the indentation depth at which full contact occurs between the circular profile of the circumference of the indenter and the substrate) is required in conjunction with κ (a yielding constraint factor) based on the expansion cavity model (ECM) for estimating the yield strength [253-254] for elastic-plastic materials. In this current work, however, value for φ and the corresponding force (L_c) in the indentation load-depth curve that are needed to estimate the yield strength via indentation (σ_{ys}). φ is determined based on the tangential intersection of the elastic and plastic deformation stages of the indentation

load-depth curve. Eq. (3.8) expresses the approach for estimating the σ_{ys} value, once φ is determined.

$$\sigma_{ys} = \frac{1}{\kappa}\frac{L_c}{\pi a_c^2} \tag{4.8}$$

where κ = 2.2 based on the ECM [255], L_c and a_c the load and the radius, respectively, at the corresponding φ value depending on the indenter size.

In our study, the estimated σ_{ys} values are compared using both indenter types, which are based on 2 hypotheses. Firstly, at a certain plastic indentation stage (or indentation depth), plastic deformation developed within the material would have an average contact pressure about six times the shear strength of the material. This criterion was suggested by the approach proposed by Eason and Shield [256], where contact pressure is about three times the tensile yield strength. The second hypothesis is that the elastic-plastic boundary to indicate the yielding of the substrate is independent of substrate modulus and hardening response [255]. Hence σ_{ys} estimation in this current study is made applicable for the chamfered indenter as seen in [255] with rounded edge on the basis of radius at infinity.

4.2.4.2. Plastic zone size

The plastic zone size and its shape development are used to characterize the plastic deformation behaviour for ductile materials due to a local stress field exceeding the yield strength of the material. For a cylindrical indenter, with the increase of indentation load, plastic zone size (*C*) is developed within the material's sub-surface. The work in [254-258] illustrates the shape of the plastic zone for the spherical and conical indenters with all having similar shapes of *C*. For flat-end indenters, the evolution of *C* does not follow an expanding spherical model as described in [255]. Johnson [22] proposed a model for relating the mechanical properties of elastic-perfectly plastic materials with *C*, in which shape of the plastic zone is spherical in nature for a cone indenter. However, the model cannot be employed for general elastic-plastic materials because of the influence of the strain hardening exponent (*n*) and the lack of the relationship between the indentation depth and *C* [22]. As a result, in this study, finite element (FE) modelling was used to estimate *C* at different indentation depths based on the constitutive equation that governs the

material's deformation behavior, where strain hardening exponent (*n)* is considered as a factor for defining the magnitude of *C*.

4.3. Experiment testing and simulation details

4.3.1 Materials and test program

A test program was conducted in ambient temperature. Smooth and notched dog-bone specimens were used for tensile tests while cylindrical disks for indentation tests. The material used in these tests was AL2024-T351. Note that although our study is meant to focus on rail steels with the objectives of finding quicker and efficient ways for determining fracture toughness as compared to ASTM standards [58, 69], choosing AL2024-T351 is because its fracture toughness is similar to rail steels as seen in our pervious works [73, 104, 236, 178] yet having a lower hardness value so that tungsten carbide rod is hard enough to be used as a rigid indenter. In this study, tungsten carbide rods were force-fitted into a 4140-heat treated, stress relieved (HTSR) steel. The indenters were ground with a diamond grinding wheel to achieve the chamfered tip for the chamfered flat-end cylindrical indenter. An MTS hydraulic universal testing machine (MTS 810) was used for both tensile and indentation tests.

Results from smooth tensile tests were used to establish the mechanical properties like yield strength as well as the constitutive equations for the deformation. Different expressions were used to represent the constitutive equations for elastic and plastic deformations, calibrated using a FE model to mimic the relationship between load and displacement from the smooth tensile specimens at room temperature, while the notched specimens were used to establish K_t and $K_{\rho c}$ in Eq. (4.6). The indentation tests were used for estimating yield strength and fracture toughness.

4.3.2 Smooth tensile specimens

The smooth tensile tests were conducted according to the guidelines of ASTM E8/E8M [58] to establish the mechanical properties of the AL2024-T351. The specimen gauge section was made to be 5 times the gauge diameter as shown in Figure 4.3. The specimens were tested at a crosshead speed of 8.5 x 10^{-3}mm/s, equivalent to an initial strain rate of 2.36 x 10^{-4}/s. Each specimen had an extensometer attached to measure the elongation and for the strain calculation.

For the elastic deformation of the smooth tensile specimens, engineering stress-strain relationship was converted to true stress-strain from the applied force and axial strain from the extensometer. For the plastic deformation, the minimum cross section after the ultimate tensile strength (UTS) was used to determine the equivalent fracture strain, ε_{eq}^{f}, after the specimen fracture using Eq. (4.9) as suggested in [57].

$$\varepsilon_{eq}^{f} = 2\ln\left(d_o/d_f\right) \tag{4.9}$$

where d_o is the original diameter in the reduced gauge section, and d_f the corresponding diameter measured at the minimum cross section after the test.

The equivalent fracture stress $\left(\sigma_{eq}^{f}\right)$ was also attained by considering the load recorded at the onset of fracture (F_f) and the minimum cross-sectional area after the test. Other parameters attained were E, yield strength and UTS. Three smooth specimens were used for the tensile test and their average values were determined.

$$\sigma_{eq}^{f} = \frac{F_f}{A_f} \tag{4.10}$$

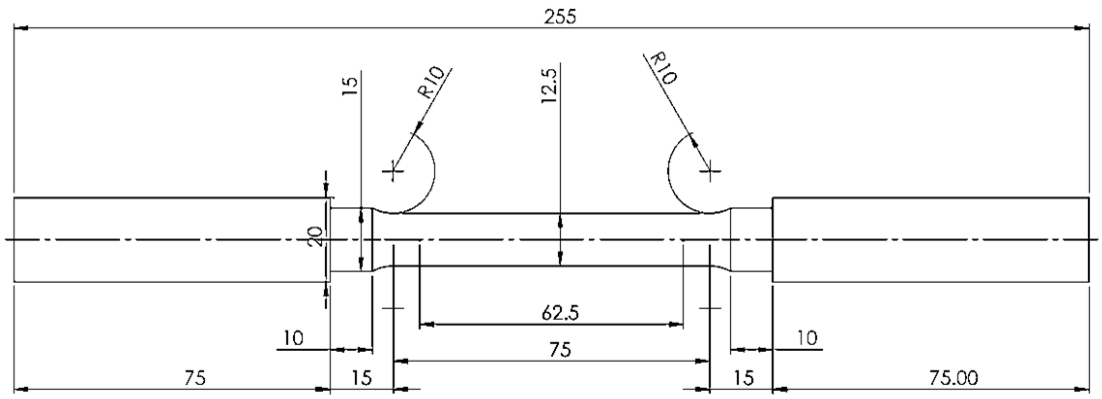

Figure 4.3 Geometry and dimensions of the smooth tensile specimen, all in mm

4.3.3 Notched round bar tensile test

The notched round bar (NRB) specimens were machined as a modification of the smooth tensile specimens, where the overall dimensions were same with the smooth tensile specimens. the NRB included a V-notch at the center of the specimens, which was machined using a punch press to selectively remove unwanted material circumferentially to introduce stress concentration at the notch root. The shoulder diameter (D), ligament diameter (d), and notch root depth (t), as shown in Figure 4. 4, were kept constant with the change of notch radius (ρ) and notch width, b for three different notch types. The NRB specimens were also tested at a crosshead speed of 8.5 x 10^{-3}mm/s. Three specimens per notch type were conducted until failure to capture the load-axial displacement relationship.

Table 4.1 shows the differences in dimensions that distinguish the three notch root radii selected for the NRB geometries.

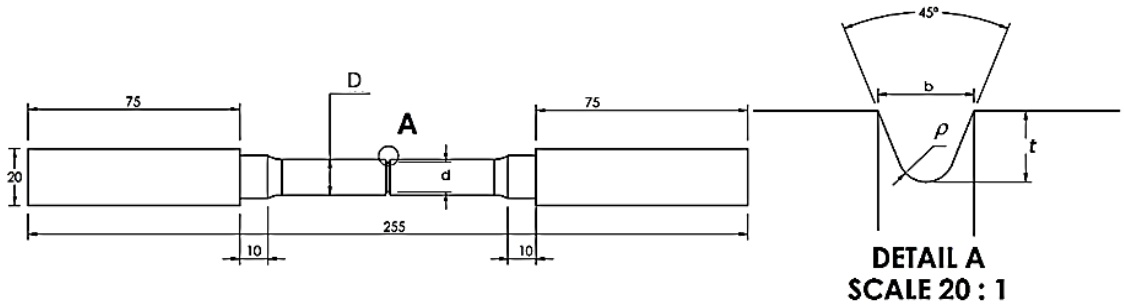

Figure 4.4 Geometry and dimensions of the NRB specimens in mm

Table 4.1. Dimensions of the different types of NRB specimens

NRB TYPE	***D***	***d***	***t***	***b***	***r***
NRB A				1.70	0.5
NRB B	12.5	10	1.25	1.43	0.3
NRB C				1.17	0.1

4.3.4 Indentation tests

The indentation tests were conducted using an MTS machine in which tungsten carbide indenters were fitted unto the MTS machine's grip. A 4140 HTSR steel, which acted as an intermediate

between the grips of the MTS machine and the indenter was first drilled of the size close to but smaller than the indenter diameter, and had an interference fit with the indenter by thermally expanding the drilled hole to allow the indenter to be slid into the hole to have a force fitted grip. Three different indenter sizes were considered, which were cylindrical tungsten carbide rods of 3, 5, and 6.35mm with Young's modulus (E_i) of 630GPa and Poisson's ratio (v_i) of 0.21. A multiple of about 3.5 times the minimum spacing required for indentation, according to ASTM E10 [113] and ASTM E18 [259], was considered in choosing the diameter and thickness of the cylindrical specimens. Figure 4.5 shows the indentation test set-up and specimen dimensions used, which was for only one indentation test to be conducted in each specimen. In the end, 6 indentation tests were carried out on different specimens for each indenter size, for both the non-chamfered and chamfered indenter types in 3 rounds of experimentation, resulting in a total of 108 indentation tests. It should be noted that indentations performed using the chamfered indenter did not exceed h_c value shown in Figure 4.2. The load levels were between 1000N -35000N for both indenter types of which the indentation depth was recorded directly from the load cell of the MTS machine. It is to note that the indentation depth from the MTS machine is a representative of the total depth accounting from the specimen and the machine's stiffness. Further work for accounting for the load frame compliance is seen in Appendix 8

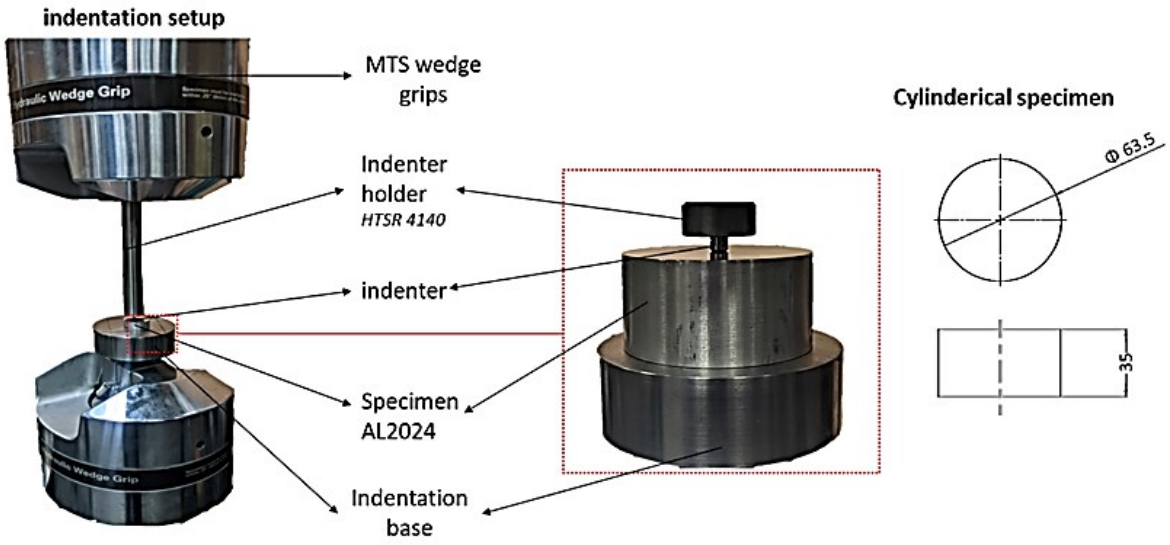

Figure 4.5. Indentation test set-up and specimen geometry

4.3.5 FE modelling of indentation test

FE modelling of indentation test was carried out following the set-up as described in Figure 4.5 using ABAQUS v6.14 standard. The aim of the FE modelling is to estimate the plastic zone size (C) at different indentation depths, especially at the depth corresponding to the CIP where the C is extracted by measuring the vertical (maximum) evolution of the plastic zone size from the tip of the indenter in the specimen's sub-surface. Due to the difficulty in analytically establishing a_c accurately when plasticity has been fully developed for the cylindrical indenters [250], a_c was measured directly via FE modelling as a function of the indentation depth to approximate the exact contact radius experimentally rather than the implementation of analytical models. This is needed for determining the approximate size of the hydrostatic core (i.e the plastic zone size within the boundary of the contact radius) during indentation for measuring the evolution of the plastic zone size. For the FE modelling, only the chamfered cylindrical indenter was considered, as discussed further in section 4.4.3.

The indenter was modelled as an axisymmetric 2D rigid body while the specimen was modelled as an axisymmetric 2D cylinder with radius of 31.75 mm and height of 35 mm. The model (SPECIMEN) consisted of 20,437 linear quadrilateral elements of type CAX4R and 60,970 nodes while no elements were used for the indenter. The minimum element size at the contact region was 3μm as shown in Figure 4.6 using mesh sensitivity analysis as further seen in Appendix 4. The chamfered cylindrical indenter was modelled as an analytical rigid body following the dimensions of each type of chamfered indenters, as depicted in Table 4.2. A contact surface was placed between the chamfered indenter and the specimen in the condition of finite sliding, "hard" normal contact, and tangential friction of 0.35, which was obtained also by iterating the output of force-depth from FE modelling with experimental force-depth curve of the chamfered indentation. The boundary conditions were set to be the same as those for the testing, i.e., with the bottom of the specimen supported and the indenter moving down at a specified displacement rate to specific indentation depths.

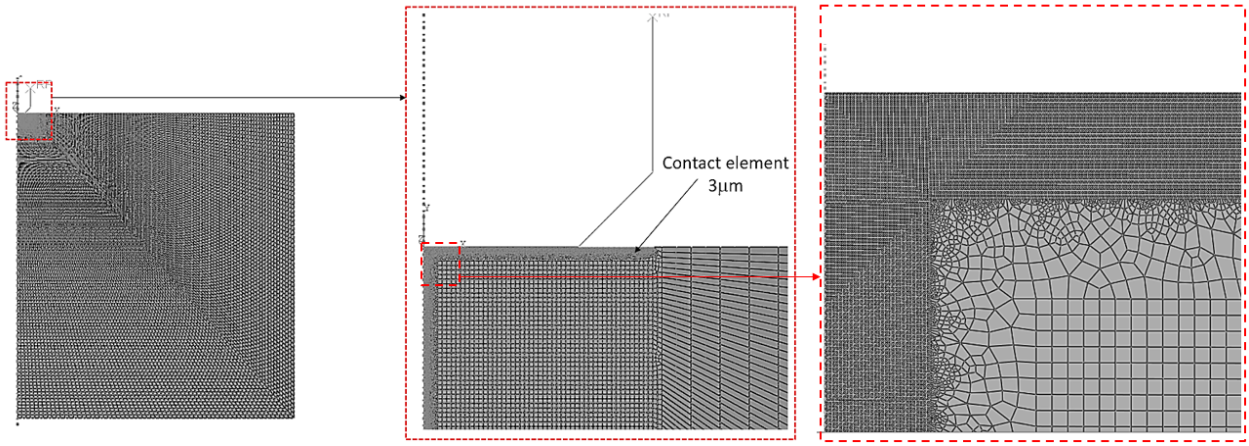

Figure 4.6 FE modelling and mesh orientation of the indentation testing using a chamfered cylindrical indenter.

Table 4.2. Chamfered cylindrical indenter parameters for the different indenter sizes.

Indenter size (d_c)		**3.00mm**	**5.00mm**	**6.35mm**
$a_{c,max}$	Contact radius of the chamfered region	0.69	0.90	0.91
h_c	Contact depth of the chamfered indenter	0.69	0.90	0.91
θ (o)	Angle of the chamfered region	45	45	45
t_d	Diameter of the non-chamfered region	1.63	3.38	4.61
t_d/d_c		0.54	0.68	0.73

where h_c , $a_{c,max}$, θ, t_d and d_c are as expressed in Figure 4.2.

In the FE modelling, Eq. (4.11) which consists of four expressions was used to represent the constitutive equation for the entire stress-strain range to capture the deformation behaviour of AL2024-T351. This includes the plateaued regions and the nonlinear deformation behaviour experienced.

$$\varepsilon_{eq}\left(\sigma_{eq}\right)=\begin{cases}\dfrac{1}{3\alpha}2\left(1+\nu\right)\dfrac{\sigma_{eq}}{E} & \varepsilon_{eq}<\varepsilon_{st} \quad \text{(a)}\\ \dfrac{\sigma_{st}}{E}\left(\dfrac{\sigma_{eq}}{\sigma_y}+\beta\left(\dfrac{\sigma_{eq}}{\sigma_y}\right)^{\frac{1}{n_{RO(i)}}}\right) & \varepsilon_{st}<\varepsilon_{eq}<\varepsilon_y \quad \text{(b)}\\ \dfrac{\sigma_{eq}-\sigma_y}{K_T}+\varepsilon_u\left(\dfrac{\sigma_{eq}-\sigma_y}{\sigma_u-\sigma_y}\right)^{n_{RO(ii)}}+\varepsilon_y & \varepsilon_y<\varepsilon_{eq}<\varepsilon_u \quad \text{(c)}\\ \dfrac{\sigma_{eq}^{n}}{K_{HO}} & \varepsilon_{eq}>\varepsilon_u \quad \text{(d)}\end{cases} \tag{4.11}$$

where $\varepsilon_{eq}\left(\sigma_{eq}\right)$ is the equivalent strain as a function of the equivalent stress (σ_{eq}) while α, β and K_T are user-defined parameters, σ_{st} and ε_{st} the saturated stress and strain, respectively while ε_y and ε_u, the equivalent plastic strain at yield stress and UTS, respectively, with ε_y determined from tensile test, $n_{RO(i)}$ and $n_{RO(ii)}$ the strain hardening exponents corresponding to the 1st and 2nd stages of Ramberg-Osgood's model [260-262], respectively, and K_{HO} and n, the stress coefficient and strain hardening exponent, respectively in accordance with the Hollomon's model [34].

In the four expressions of Eq. (4.11), Eq. (a) incorporates the elastic portion represented by Hooke's law, Eq. (b) is the first stage of the modified Ramberg-Osgood equation originating from Ramberg-Osgood's elastic-plastic model [262], taking account of the plastic plateau developed in the stress-strain curve, Eq. (c) is the 2nd stage of the modified Ramberg-Osgood equation considering the uniform plastic deformation for the occurrence of the plastic plateau before the ultimate stress, and Eq. (d) is the Hollomon's equation covering the non-uniform deformation. With thses parameters determined, the constitutive equations provide details about the vital information such as the strain hardening exponents, saturated stress and strains and how they characterize the deformation behaviour of AL2024-T351, especially for studying local deformation via indentation.

4.3.6 Fracture toughness estimation

The fracture toughness estimation using indentation test results followed a series of procedures from the force-displacement curve to the critical stress intensity factor expressed in Eq. (4.1). To attain K_{JC}, indentation load and depth are normalized and the CIP location estimated, after which

the corresponding h/a_c is used as the basis for relating the experimental data to virtual normalization of the indentation as expressed in Eq. (4.4). According to the work by Kim et al. [238], the intersection point of the J–R curve [58, 263] is regarded as the crack initiation point, where h' = 0.2mm is used for attaining the virtual contact radius with the indenter having the indentation profile similar to the notch geometry in the CRB specimens.

In this study, in order to account for CIP in the indentation test for the estimation of J, h' was varied to approach zero in decremental steps thus calculating different a_c' values with geometric similarity with NRB specimen [244, 264]. Once a_c' is determined, a new virtual load (L') –virtual depth (h'') curve can be extracted from the normalized indentation curves (P vs. h/a_c) as expressed in Eqs. (4.12) and (4.13), and from these new estimated virtual curves, K_J can be estimated from J using Eq. (4.1). The limit to halting h' is when the newly constructed curve is similar with negligible changes to the previous $L'-h''$ curve., and at this stage, the $L'-h''$ curve has the slope of the elastic and plastic deformation sections indistinguishable from each other, while the experimentally determined indentation curve shows a clear change in the slope between the elastic portion and plastic portion of the load-depth curve.

$$L' = P \cdot \pi \left(a_c' \right)^2 \tag{4.12}$$

and

$$h'' = \left(\frac{h}{a_c} \right) \cdot a_c' \tag{4.13}$$

Note that Eq. (4.4) suggests smaller a_c' as h' tends to zero, which is under the assumption of negligible stress-concentration-induced inhomogeneity when ligament radius becomes small.

A flow chart is presented in Figure 4.7 to illustrate the steps for determining K_{JC}.

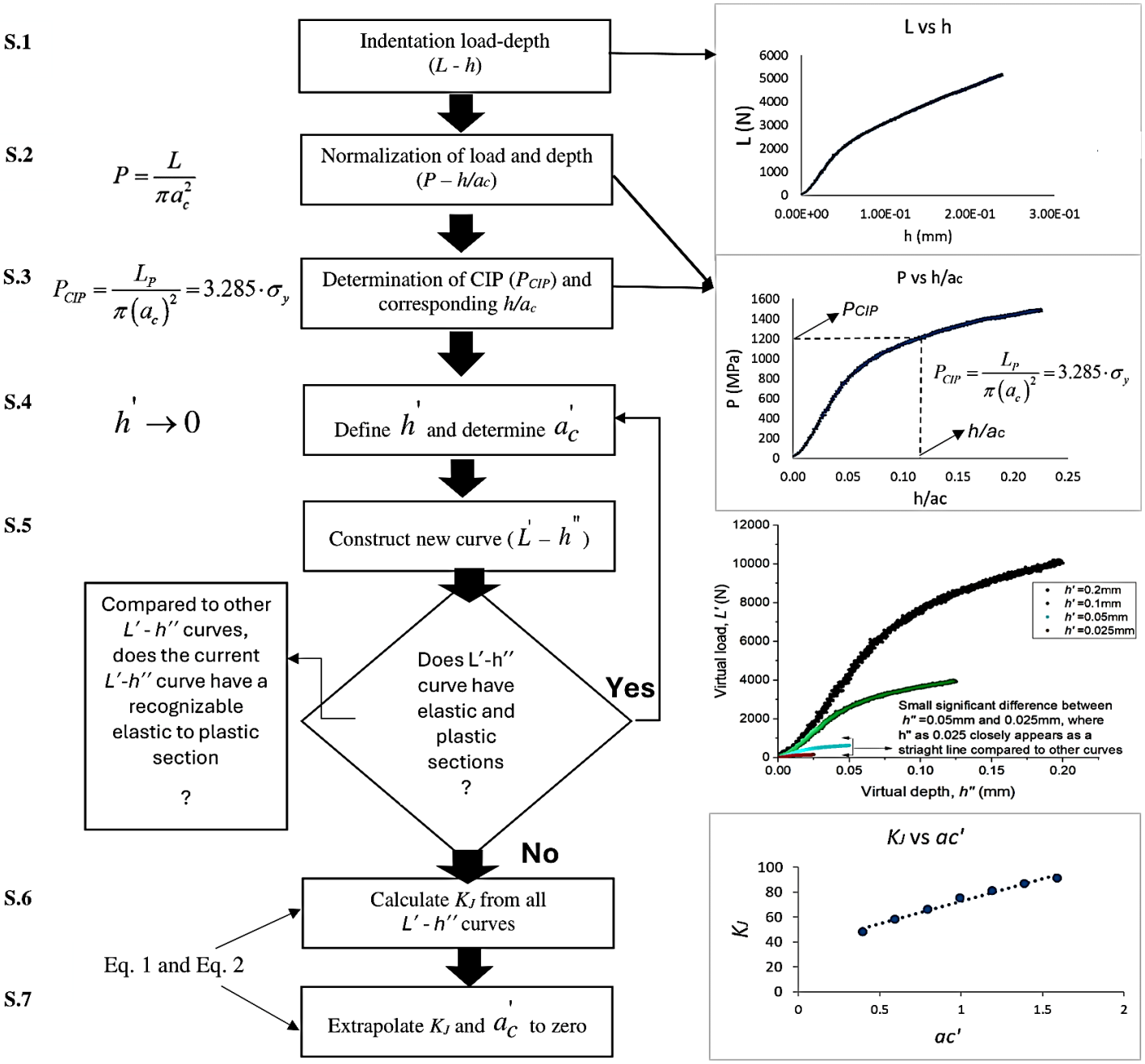

Figure 4.7. Procedure for determining the K_{JC} using indentation test results.

4.4. Results

4.4.1 Smooth specimen in tension

4.4.1.1 Mechanical testing results

Figure 4.8 illustrates the conversion of an engineering stress-strain curve from the experiment to the true stress-strain curve. The fracture characteristics were also attained by investigating the fractured specimen for the evaluation of σ_{eq}^{f} and ε_{eq}^{f}. Table 4.3 shows the summary of the average (Avg) and standard deviation (S.D) of the mechanical properties attained from conducting 3 different tests, which is comparable with results obtained from literature [244].

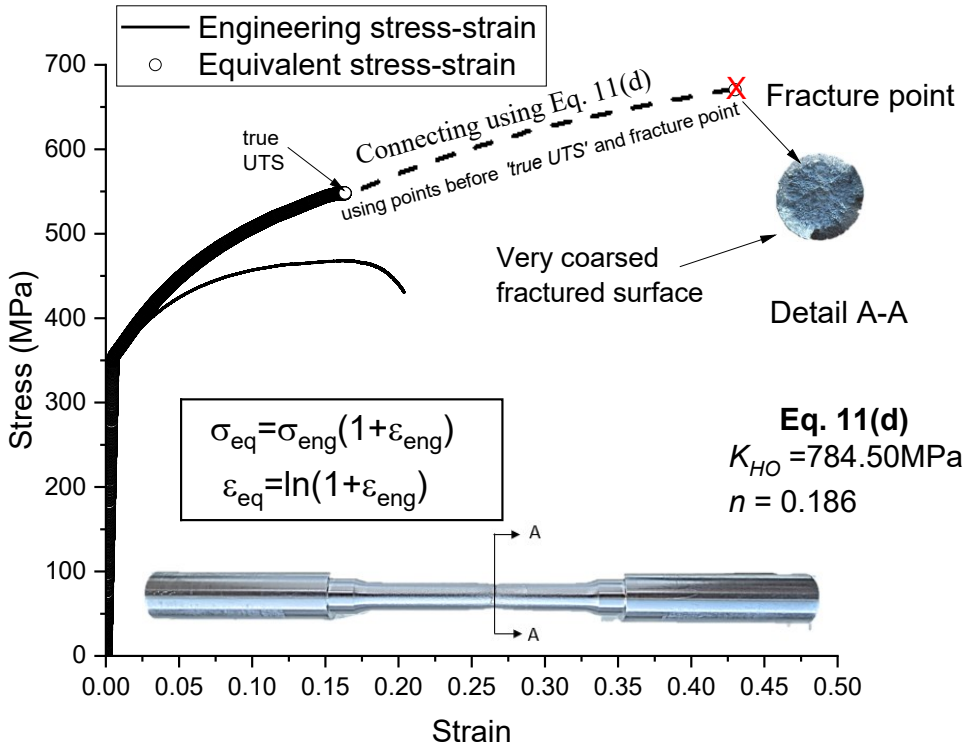

Figure 4.8 Engineering and Equivalent stress-strain curves of AL2024-T351.

Table 4.3. A summary of the mechanical properties attained from the tensile test.

	F_f (KN)	D_f (mm)	σ_{eq}^{f} (MPa)	ε_{eq}^{f}	E (MPa)	σ_y (MPa)	UTS (MPa)
Avg	53.52	10.08	670.39	0.43	71016	360.53	468.03
(S.D)	(6.36)	(0.003)	(3.37)	(0.02)	(669)	(1.99)	(3.31)

4.4.1.2 Constitutive modelling

Parameters in Eq. (4.11) were adjusted iteratively so that the true stress-strain curve generated could fit the experimental data. In the fitting process, the uniform portion of the plastic deformation was captured using both the 1st modification of the Ramberg-Osgood equation, Eq. 4.11(b), and then the 2nd Ramberg-Osgood equation, Eq. 4.11(c), while the remaining part of the curve before the fracture point was captured using Eq. 4.11(d), the Hollomon's model. Values for n and K_{HO} in Eq. 4.11(d) were determined so that the equation could be used to fit the experimental data from the point equivalent to UTS while predicting the remaining points to the fracture point. Figure 4.9 shows the portion of the equivalent stress-strain curve that was fit using Eqs. 4.11(b), 4.11(c) and 4.11(d), respectively, with Table 4.4 summarizing the values for the parameters in Eq. (4.11).

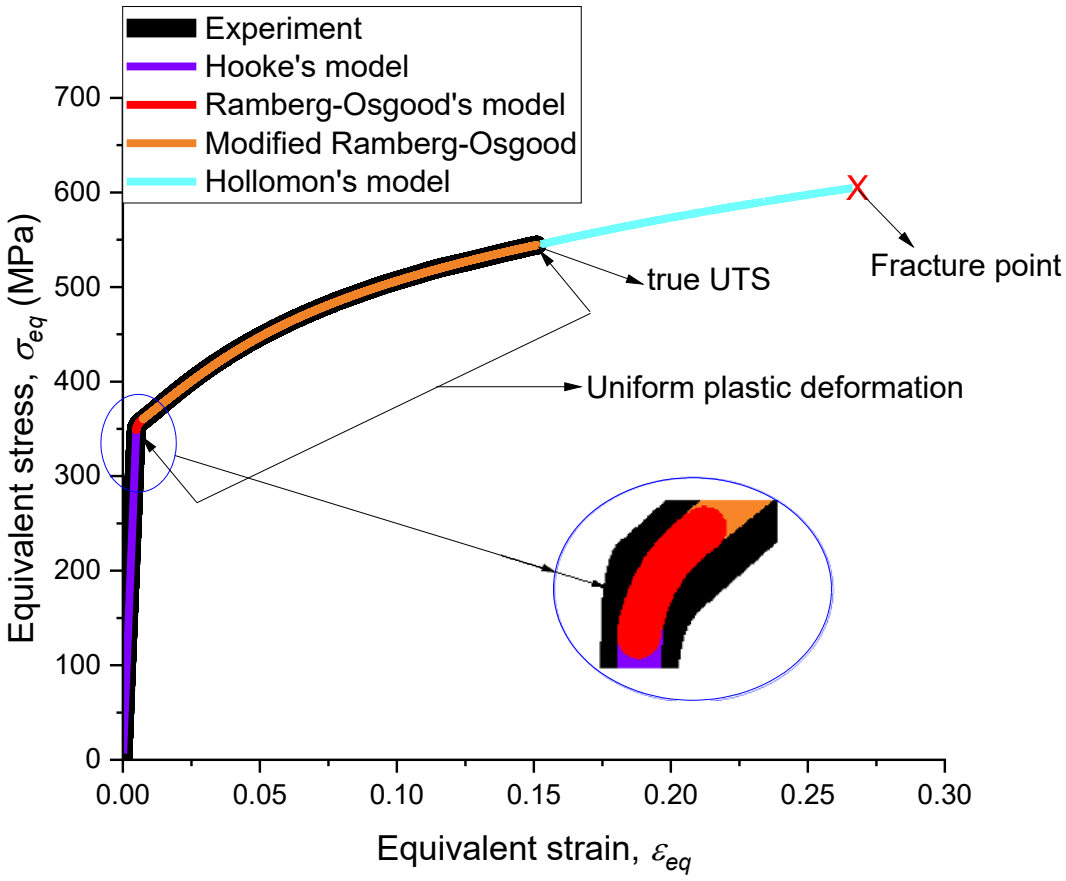

Figure 4.9. The corresponding true stress–strain curve via constitutive modelling of the entire material deformation.

The deformation saw a plateau in the plastic region, also seen in [265–267], in which the stress before or after the yield point builds up to a maximum value and deviates suddenly with a lower slope as seen in Figure 4.9. The modification of the 1st Ramberg-Osgood equation required σ_{eq} originally used in [260, 262] to be replaced with σ_{st}, since the Voce hardening law constitutive model [32] was able to mimic the stress-strain curve of the plateau region. Hence, the values of σ_{st} and ε_{st} were attained using the Voce model [32], which identifies the saturated stress and the corresponding saturated strain respectively, in an elastic-plastic material deformation [32, 178] that initially progresses beyond yield but decreases once the steady state condition is achieved as the total plastic strain continues up to instability (true UTS) as seen in Figure 4.9

Table 4.4. Parameters of constitutive equations for the entire stress-strain curve

Parameters	**value**	**Parameters**	**value**
E (MPa)	71016	σ_u (MPa)	469.70
v	0.33	ε_{pu}	0.01107
α	0.9	ε_y	0.007361
σ_y (MPa)	360.5	K_T	2308.0
β	0.004702	$n_{RO(ii)}$	3.366
σ_{st} (MPa)	334.10	K_{HO} (MPa)	784.5
$n_{RO(i)}$	0.01539	n	0.186

4.4.2 NRB specimen in tension

4.4.2.1 Force-displacement

Sample curves of force verses axial displacement for each type of NRB specimens are shown in Figure 4.10. The results show that all 3 types of notches provided the same general trend with the largest notch radius (ρ = 0.5mm) generating fracture at the largest load and displacement. All specimens broke into two halves showing a rather fine fractured surface with traces of dimples as compared with tensile specimens in Figure 4.8. This fractured surface demonstrates the effect of stress triaxiality (ratio of mean normal stress to von Mises stress) contributing to the ductile fracture mechanism, characterized with a brittle cleavage fracture as well as dimple formation within an otherwise ductile fracture. Since the ratio d/D and other factors like t, notch angle and

notch type were kept the same among the specimens used in this study, as shown in Table 4.1, different notch radii are used as the sensitivity parameter for affecting the stress concentration towards the NRB ductility.

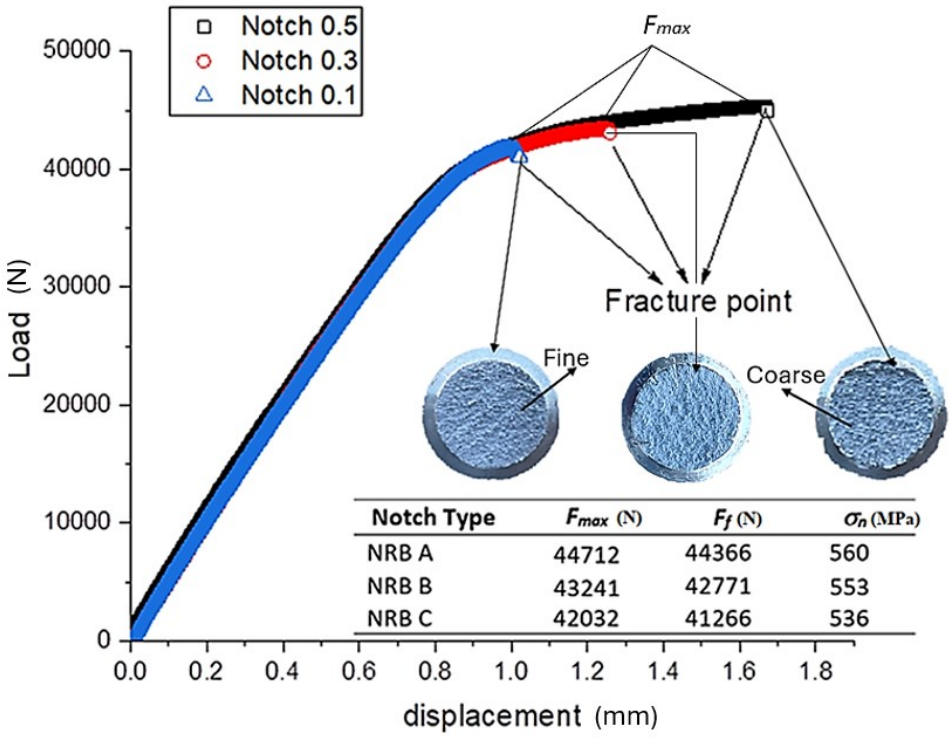

Notch Type	F_{max} (N)	F_f (N)	σ_n (MPa)
NRB A	44712	44366	560
NRB B	43241	42771	553
NRB C	42032	41266	536

Figure 4.10. A sample of force-displacement outcome from NRB specimens

Figure 4.10 indicates that the NRB specimens with ρ = 0.5mm are more ductile than those with ρ = 0.3 and 0.1mm due to the lower stress concentration and stress triaxiality [104] at the root of the notch. However, all NRB specimens failed instantaneously after attaining the maximum force with little or no softening. Two important forces are identified from the force-displacement curve in Figure 4.10: the maximum force (F_{max}) and the fracture force (F_f). While the former is used for estimating the nominal stress (σ_{nom}) needed for the apparent fracture toughness, the latter evaluates the equivalent stress at fracture based on the notch root radius size for NRB specimens. The fracture toughness estimated using the Irwin's elastic solution [243] in Eq. 4.6(a) for the NRB specimens was similar to the fracture toughness estimated in ASTM STP 1360 [244] (AL2023-T351) which also used the Irwin's elastic solution, and the Aerospace specification metals (ASM) MATWEB's library [245]. However, in [244] no information was given about the specimen extraction orientation for the fracture toughness measurement, only that the specimen was

extracted from a 50mm thick AL2024 block. In this study, specimens were extracted from a rod stock in the longitudinal-radial (L-R) orientation, where crack propagation was along the radial direction of the cross section. In view that it could not be confirmed whether the fracture toughness from the L-R orientation for our specimens correlates to the L-T, L-S or a combination of L-T and L-S orientations of a block specimen shown in [244-245], the $K_{\rho c}$ estimated is accepted under the assumption of the presence of flaws or secondary phase particles in our specimens can represent either the L-T or L-S orientation of a specimen from an AL2024-T351 block.

4.4.2.2 K_t and $K_{\rho c}$

The K_t developed within the notch root radius was calculated as an elliptical sharp notch according to the criteria seen in [32, 52, 246-247], where sharp notches are predominantly controlled by the t/ρ factor under the condition that $2\rho/d \leq 0.1$ and $2t/D \leq 0.8$ as seen in Table 4.5. For blunt notches that do not meet this condition, Noda et al. [32] proposed a different analytical model for K_t estimation. Table 4.5 shows the geometrical parameters relating to the different types of NRB specimens.

Table 4.5. A summary of the NRB parameters using Eq. 6(b)

NOTCHED SPECIMEN	**NRB A**	**NRB B**	**NRB C**
D		12.5	
d		10	
t		1.25	
2t/D		0.2	
ρ	0.5	0.3	0.1
2 *ρ/d*	0.1	0.06	0.02
***K_t*: Eq. 6(b)**	**4.16**	**5.08**	**8.07**

In estimating critical K_ρ (i.e., $K_{\rho c}$) using Eq. 4.6(a), the maximum load (F_{max}) for the NRB specimens was used to determine σ_{nom} in Eq. 4.6(a) [243]. Following the work shown in [52, 246-248], correlations between K_ρ and $\rho^{0.5}$ are shown in Figure 4.11 signifying the critical value for K_r as r approaches zero. The result using Eq. 4.6(a) shows the $K_{\rho c}$ =33.05MPa.m$^{0.5}$ as seen in Figure

4.11, which is similar to the value attained in ASTM STP 1360 [244] and [245] in the T-L direction.

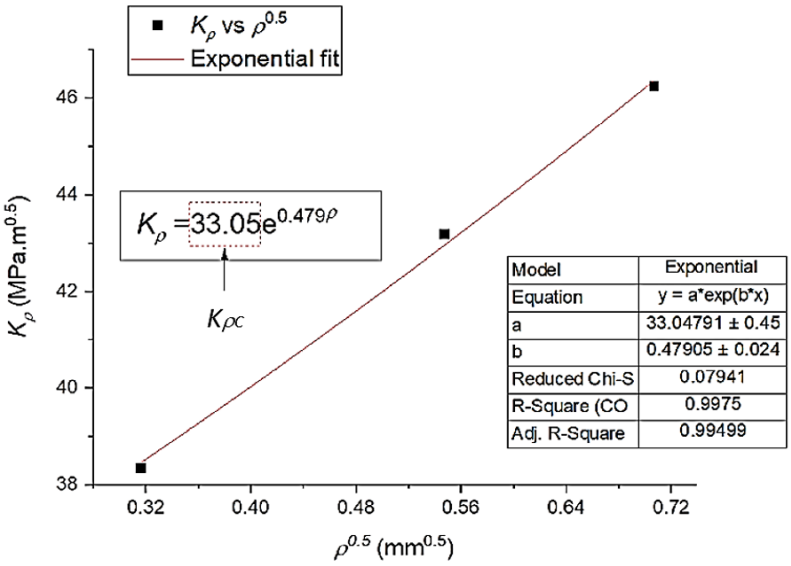

Figure 4.11. NRB notch analysis for K_ρ *vs* $\rho^{0.5}$

Note that the reason for correlating K_ρ and $\rho^{0.5}$ with an exponential function is of no particular reason but just a direct replication of the procedures done in [244]. In general, using NRB for fracture toughness estimation may not provide outcomes equivalent with K_{IC}, however for this material (AL2024-T351), using the Irwin's elastic solution for NRB is suitable for fracture toughness estimation equivalent with K_{IC}.

4.4.3 Indentation testing

4.4.3.1 Loading-unloading indentation

The indentation tests conducted involved the use of chamfered and non-chamfered flat-end indenters of three different sizes. It is to note that the load-depth curves presented here were after the calibration of the load-depth results by considering the load frame compliance of the test set-up. The process of calibrating the test setup and obtaining the load frame compliance is detailed in Appendix 8. Six loading-unloading curves were obtained for each type of indenter as shown in Figures 4.12 (a) to (f), revealing the difference between the results from the chamfered indenter tip and those from the non-chamfered indenter tip.

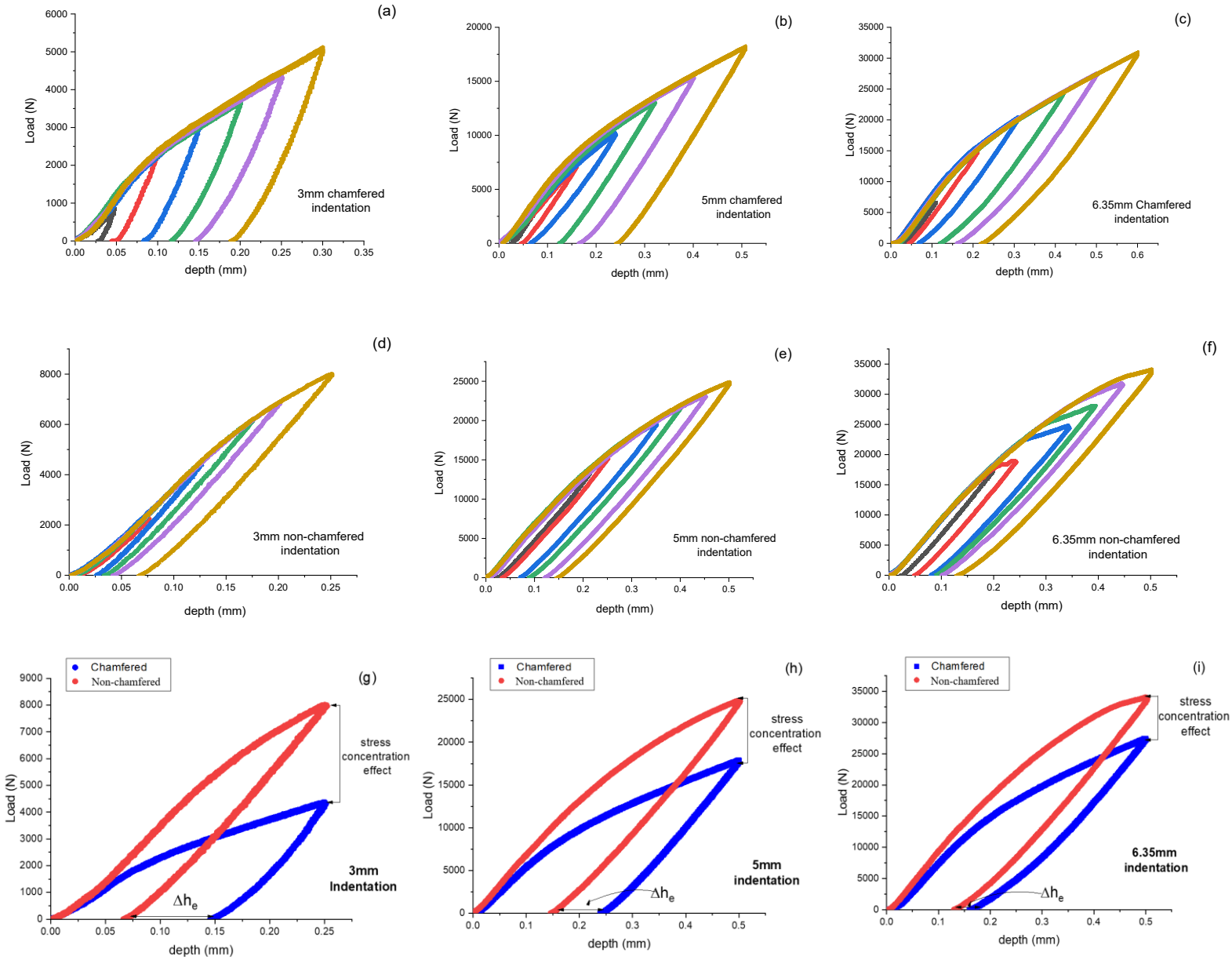

Figure 4.12. Indentation load-depth curves: (a) 3mm chamfered indenter, (b) 5mm chamfered indenter, (c) 6.35 chamfered indenter, (d) 3mm non-chamfered indenter, (e) 5mm non-chamfered indenter, (f) 6.35 non-chamfered indenter, (g) 3mm chamfered and non-chamfered indenters showing the difference in stress concentration, (h) similar comparison as shown in (g) but using 5mm indenters and (i) similar comparison as shown in (g) but using 6.35mm indenters.

The curves in Figure 4.12 (g), (h) and (i) compare results from the chamfered and non-chamfered indenters of the same diameters. The figures suggest that at the similar depths, less force is required for the chamfered indenter due to the less stress concentration initiated at the tip of the indenters. However, while this observation holds it is noticed that as the indenter size increases, the stress

concentration effect is reduced, as well as Δh_e which is the difference in the elastic recovery between the two indenter types.

4.4.3.2 Yield strength estimation

As shown in Eq. (4.3), the yield strength (σ_y) as reported in Table 4.4 is an important parameter for determining the CIP load *(L_p)*. Therefore, it is preferable if the yield strength could be estimated from the indentation test as well. In this work, Eq. (4.8) is used to determine the yield strength (σ_{ys}) using both the non-chamfered and the chamfered flat-end indenters to examine their feasibility of estimating accurately the σ_y value. It is to note that the indentation curves obtained for this purpose were smoothened to reduce noises in the experimentally measured data. An example of the smoothening process is shown in Appendix 9.

For the estimation of σ_{ys} using Eq. (4.8), identification of the critical indentation depth (φ) is required to determine the corresponding L_c and a_c values (the latter for the chamfered indenters). As shown in Figure 4.13, the j values were determined from the intersection of two tangent lines for the elastic and the plastic stages of the L-h curve. And the corresponding L_c and a_c at $h = \varphi$ were used in Eq. (4.8) to estimate σ_{ys}. Maximum (Max) and minimum (Min) values for σ_{ys} determined are summarized in Table 4.6 for all indenter sizes and types.

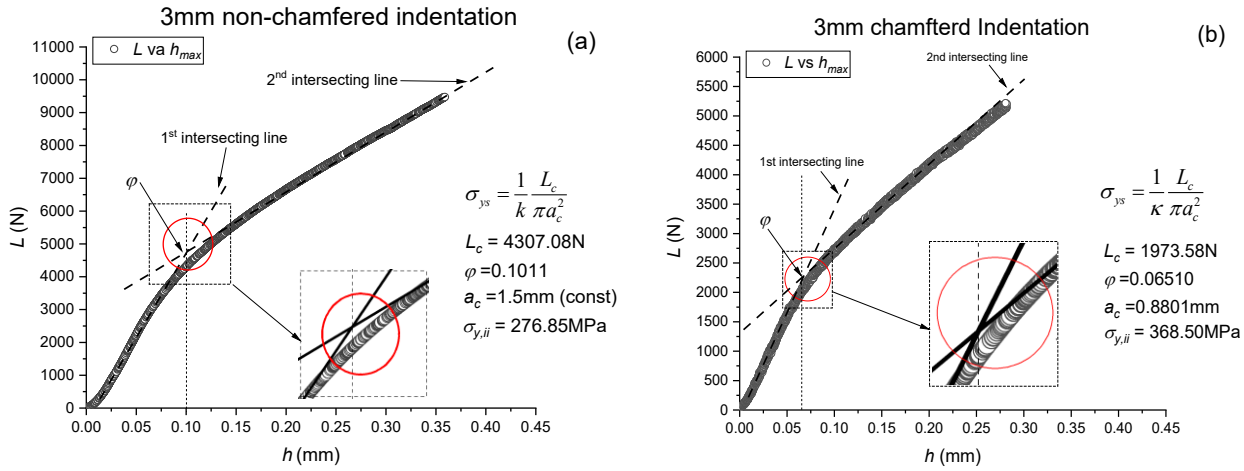

Figure 4.13 Yield strength estimation: (a) 3mm non-chamfered indentation, and (b) 3mm chamfered indentation.

Table 4.6 Yield strength estimation for different indenter sizes.

		3mm (F)	5mm (F)	6.35mm (F)	3mm (CH)	5mm (CH)	6.35mm (CH)
σ_{ys} (MPa)	***Max***	*279*	*284*	*275*	*379*	*373*	*372*
	Min	276	277	260	377	369	368

Table 4.6 suggests that values for σ_{ys} determined using the chamfered indenters of all sizes used here are close to σ_y measured from the tensile test (360MPa). However, for the non-chamfered indenter, the σ_{ys} values are much lower than the σ_y value. This raises questions on the validity of using the non-chamfered indenters for the yield strength estimation. As a result, only the chamfered indenter is considered below for determining P_{CIP} that is needed to estimate K_{JC} in this study.

4.4.3.3 Plastic zone of chamfered flat-end indentation

Using the function 'AC YIELD' in the ABAQUS, the plastic zone developed beneath the indenter could be represented by the actively yielding region. Figure 4.14 shows that for a 3mm chamfered indenter with a plastic zone (in red color in the electronic version) is developed from the circumference of the contact surface at the end of the indenter and grows towards the center of the contact surface. Figure 4.14(a) shows that the stress field develops a ring-like pattern initially, and with the increase of indentation depth, as shown in Figure 4.14(b), the ring is evolved into a half of an ellipsoidal shell, surrounding a region that is still subjected to a compressive stress state below the yield point. As shown in Figures 4.14(c) and 4.14(d), with the further increase of the indentation depth, the plastic zone evolved into an ellipsoidal solid under the indenter. It is to note that the plastic zone development process depicted in Figure 4.14 is representative of the plastic zone development using the chamfered indenters of all sizes used in this study.

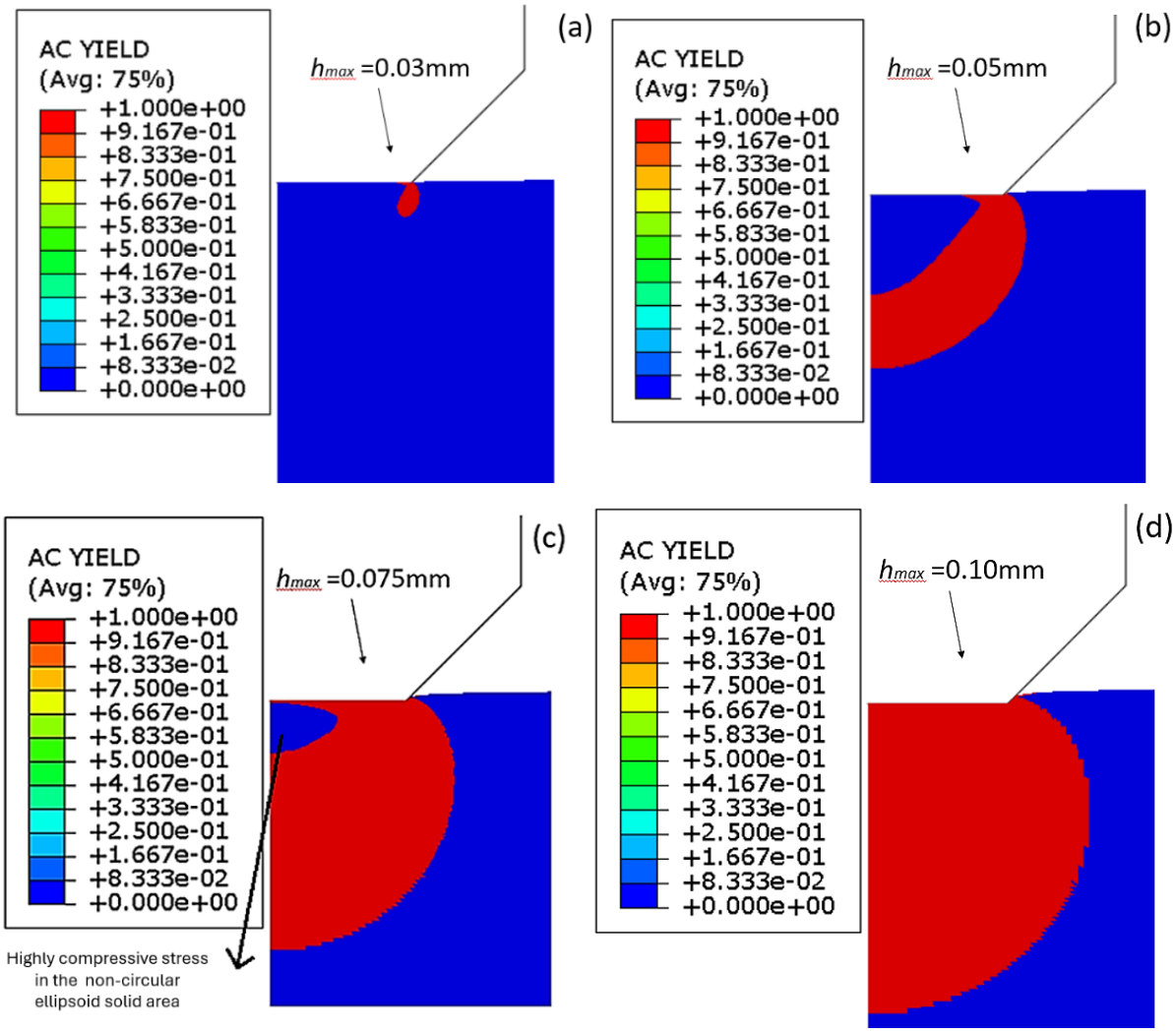

Figure 4.14 Plastic-zone development of the chamfered indentation using 3mm indenter as an illustration.

4.4.4 Fracture toughness

As described in Figure 4.7, the *L-h* curve is converted to the P-h/a_c curve using Eq. 4.4 and 4.5 from which the P_{CIP} and corresponding $h/a_{c,CH}$ are determined based on Eq. 4.3. Figure 4.15 shows examples of the location of P_{CIP} and its corresponding h/a_c value from the three chamfered indenters.

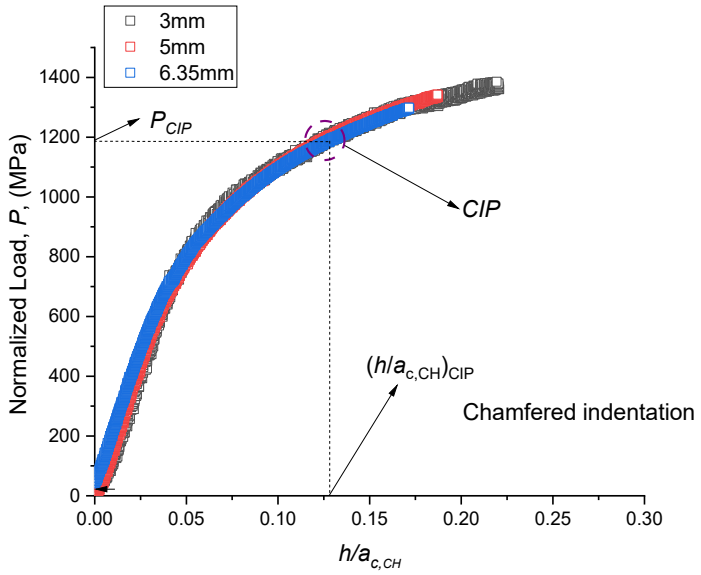

Figure 4.15 Identification of P_{CIP} and the corresponding $h/a_{c,CH}$ from the normalized indentation curves

The P-$h/a_{c,CH}$ curves shown in Figure 4.15 suggest that the same P_{CIP} can be identified with different indenter sizes used in this study. Therefore, for the use of indentation as a non-destructive means of testing, it is possible to use indenters of small sizes (micro-indenter sizes) to minimize the indented area. Hence, as described in step 4 (S.4) in Figure 4.7, also Eq. (4.4), different a_c' values could be determined by varying the values of h' from 0.2mm down to 0.05mm, and the corresponding virtual load-depth curves ($L'-h''$) could be constructed using Eqs. (4.12) and (4.13). Figure 4.16(a) summarizes these virtual $L'-h''$ curves constructed from the values of h' from 0.2 to 0.05mm, while Figure 4.16(b) uses the curve of h' = 0.2mm to illustrate the determination of the corresponding value for A_{pl} (area between the two dashed lines that are parallel to each other) which is needed for calculation of J_p using Eq. (4.2), also equal to the area from the subtraction of A_{el} from the area under the $L'-h''$ curve up to the *CIP* point. It should be noted that the above calculation of A_{pl} has ignored the small area for the initial take-off of the curve which occurred due to the acceleration of the crosshead of the test machine to the desired speed.

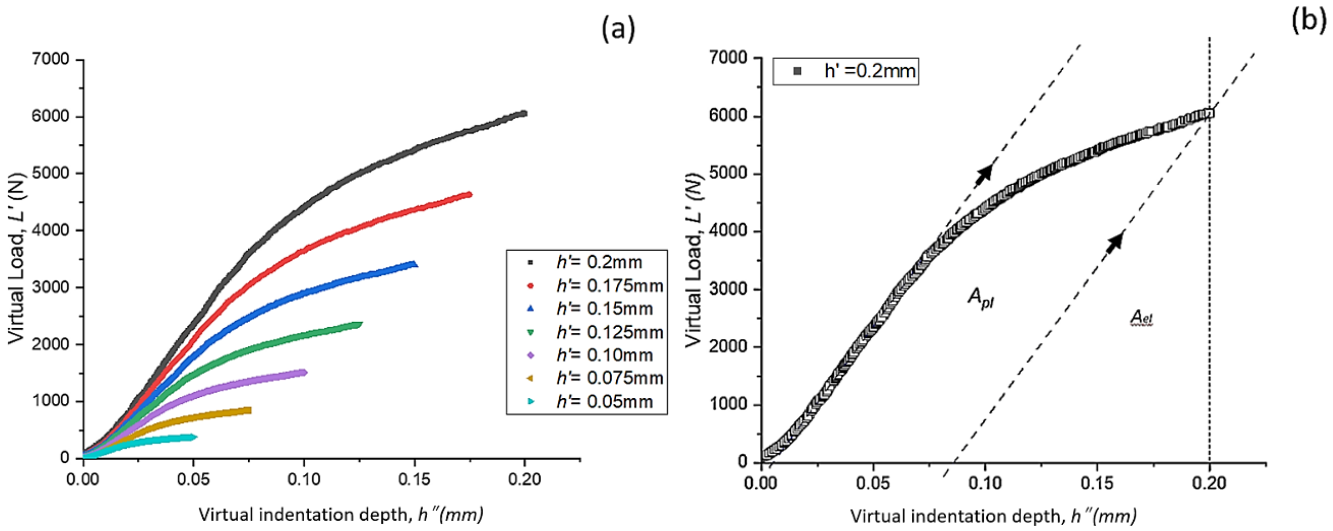

Figure 4.16 Virtual load-depth curve of a 3mm chamfered indentation: (a) variation of virtual load (L') versus virtual depth (h'') with different h' values, and (b) estimation of A_{pl} for the curve in (a) with h' = 0.2mm

The value of η_{pl} in Eq. 4.2 was taken as 0.869 from the previous work [264] which translates from NRB specimens in tension. Table 4.7 provides a summary of virtual NRB parameters from the 3mm chamfered indentation for estimating J and K_J outcomes.

Table 4.7 Virtual indentation estimates for estimating K_J with η_{pl} being taken as 0.869 for the 3mm chamfered indenter.

h' (mm)	a_c' (mm)	*Max L'* (N)	A_{pl} (mm^2)	J_e (N/mm)	J_p (N/mm)	J (N/mm)	K_J (MPa.m$^{0.5}$)
0.200	1.590	9509.225	744.118	22.480	81.456	103.936	91.012
0.175	1.391	7280.500	518.481	19.670	74.131	93.800	86.460
0.150	1.192	5348.939	334.649	16.860	65.125	81.985	80.832
0.125	0.993	3714.541	202.376	14.050	56.713	70.762	75.096
0.100	0.795	2377.306	99.148	11.240	43.413	54.653	65.997
0.075	0.596	1337.235	43.713	8.430	34.028	42.458	58.169
0.050	0.397	594.327	13.178	5.620	23.081	28.701	47.826

Note that J_e was calculated using the J_e term in Eq. (4.2) based on different values of a_c' and the maximum L' in Table 4.7, the latter describing the virtual indentation load at CIP. For J_p, the A_{pl} and a_c' for every $L'-h''$ curve was used, to be combined with J_e for the calculation of J. As shown in Table 4.7, values for all parameters decrease as h' decreases.

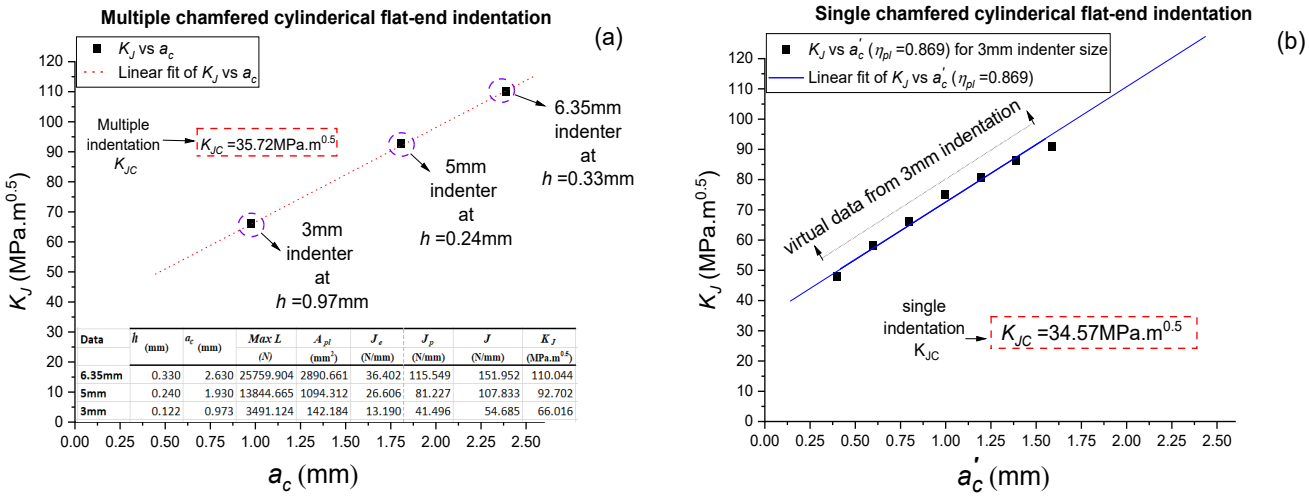

Data	h (mm)	a_c (mm)	Max L (N)	A_{pl} (mm^2)	J_e (N/mm)	J_p (N/mm)	J (N/mm)	K_J (MPa.m$^{0.5}$)
6.35mm	0.330	2.630	25759.904	2890.661	36.402	115.549	151.952	110.044
5mm	0.240	1.930	13844.665	1094.312	26.606	81.227	107.833	92.702
3mm	0.122	0.973	3491.124	142.184	13.190	41.496	54.685	66.016

Figure 4.17 K_{JC} estimation via indentation using a chamfered flat-end indenter.

In Figure 4.17(a), K_J estimation using the three indenter sizes are shown. Extrapolating the different K_J from the 3 indenters with a_c to zero estimated an average K_{JC} of 35.72MPa.m$^{0.5}$. However, Figure 4.17(b) shows the correlation between K_J and (a_c'), which by extrapolating to zero yields K_{JC}. The average fracture toughness estimation using the above modified limit load analysis yields a K_{JC} value of 34.57MPa.m$^{0.5}$, as seen in Figure 4.17(b), which provides a relatively similar value to $K_{\rho c}$ (33.05MPa.m$^{0.5}$), and thus offers an opportunity to estimate fracture toughness from a single indentation loading.

Thus, the approach for virtual indentation from a single indenter for K_{JC} estimation overcomes the challenge of using multiple indenters providing a merit for quick material characterization and assessment. However, more materials need to be investigated and confirmed by using the virtual data from a single indenter for K_{JC} measurement in the future.

4.4.5 Plastic zone size at CIP

Since plasticity occurs at the sub-surface of the circular disk specimens during indentation, it is important to investigate the extent of plasticity especially at the depth corresponding to the CIP. Hence, to study the effect of this local plasticity generated by indentation on the K_{JC} estimation, FE modeling was used to correlate the simulation results with the experimental data of L versus h at the depth and load corresponding to CIP (i.e., h_{CIP} and L_{CIP}, respectively). At the depth of h_{CIP}, the plastic zone size (C) is extracted from the FE model along with the contact radius at CIP ($a_{c,CIP}$). Figure 4.18 shows the outcome of the FE results with experimental data as well as the C illustrated in the FE model at h_{CIP}.

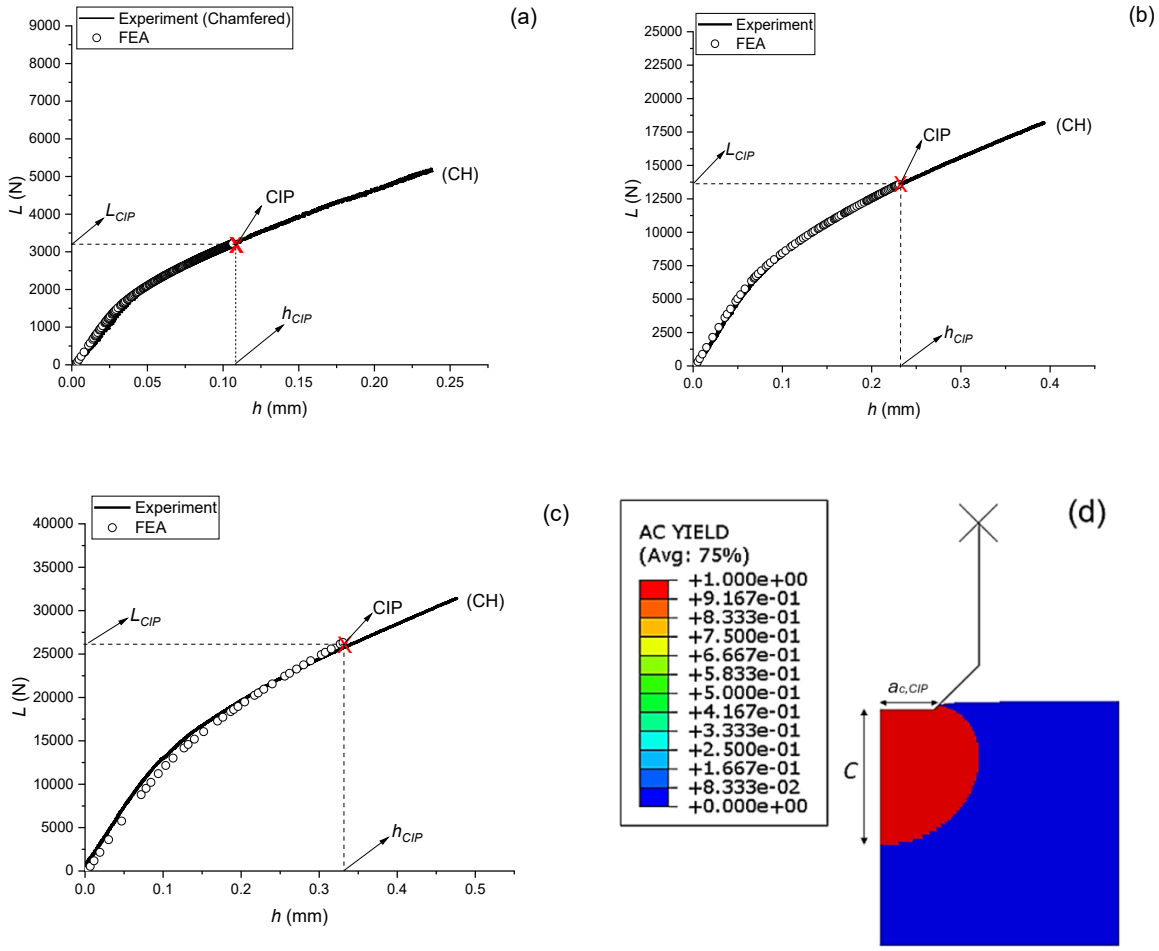

Figure 4.18 Establishing plastic zone size at CIP via FE modelling: (a) 3mm indenter, (b) 5mm indenter, (c) 6.35mm indenter, and (d) an illustration of *C and* $a_{c,CIP}$ estimation via FE modelling.

With *C* and $a_{c,CIP}$ values determined from the FE modelling, the ratio of C/$a_{c,CIP}$ could then be determined and compared for indenters of different sizes. Table 4.8 provides a summary of *C*, $a_{c,CIP}$ and C/$a_{c,CIP}$ for tests using different chamfered indenters, showing that the C/$a_{c,CIP}$ for the different chamfered indenter sizes is ~2.40, which can be regarded as a material property for chamfered indentation of AL2024-T351.

Table 4.8. Indentation parameters and local effect at CIP for different chamfered indenter sizes.

Indenter size (mm)	***C* (mm)**	**$a_{c,CIP}$ (mm)**	***C*/ $a_{c,CIP}$**
3	2.24	0.93	2.408
5	4.35	1.81	2.403
6.35	5.85	2.43	2.407

4.5 Discussion

The estimation of σ_{ys} is different between non-chamfered and chamfered indenters, as seen in Figure 4.13. The σ_{ys} for the chamfered flat-end cylindrical indenter based on Eq. (4.8) has similar values as compared with the yield strength in smooth tensile tests, where (0.0651mm) was taken as the intersection between the elastic and plastic stage for estimating σ_{ys} for the 3mm indenter. However, for the non-chamfered flat-end cylindrical indentation tests, the σ_{ys} values were about 100MPa less than the results from the smooth tensile tests. Similar differences were observed for other non-chamfered indenters. This might be because of the very high non-uniform stress experienced at the local contact region, resulting to an overall reduced average stress of the non-chamfered indenter's base. The approach for σ_{ys} via the method suggested by Riccardi and Montanari [250], which considers attaining the 1st derivative of the P-h/a_c curve [269-270] was also applied in the work. However, the estimation was inconsistent with the yield strength determined from the tensile test.

The nature of the plastic zone developed underneath the indenter tip, as described in Figure 4.14, aids in estimation C. Apart from the estimation of C, another importance of studying the nature of the C development is the development of theoretical models for predicting indentation hardness in terms of uniaxial material properties, which adequately covers the material properties and indenter geometry. It is proposed that any analytical hardness model to be developed in the future via flat-end indenters for elastic-plastic materials should be based on the evolution of the nature of the plastic zone underneath the indenter tip.

K_J values attained from using indentation test were extrapolated to minimize the contribution of J_P in the overall J-integral values as seen in Figure 4.18. In theory, the CIP becomes the underlining indicator for the condition required for the failure of structures. Hence, K_{JC} becomes the critical stress intensity factor resulting from the contribution of J_e with negligible contribution from J_P, thus supporting the linear elastic fracture mechanics (LEFM) principles.

The use of $C/a_{c,CIP}$ at values around 2.40 for the chamfered indentation in fracture toughness estimation also suggests that this parameter can serve as a constant for AL2024-T351 at certain depths irrespective of the indenter size, thus supporting the use of micro indenters for the

possibility of non-destructive testing. This constant value of $C/a_{c,CIP}$ could serve as a combination of mechanical and geometrical relationships and needs to be further examined for the chamfered flat-end cylindrical indentation.

4.6. Conclusions

In this chapter, a non-destructive means is proposed to measure fracture toughness for ductile materials that have low or medium fracture toughness in the LEFM regime, by using just load-depth information from one indenter size. This is achieved by determining the critical J-integral values via virtual indentation. The main conclusions can be summarized as follows:

1. The pressure at the CIP according to von-Mises failure criteria is significant for estimating the required stress for initiating fracture in a structure containing defects.
2. The chamfered flat-end indenter offers less load requirements for indentation testing than the non-chamfered flat-end indenter due to the lower stress concentration generated at the contact region of the chamfered indenter.
3. The study shows virtual indentation from single indentation test results can effectively characterize K_{JC} in contrast to the challenge of using multiple indenters.
4. Several values of $h' \rightarrow 0$ were proposed for the estimation of different K_J values before being extrapolated to zero to attain the K_{JC} value according to the principles of LEFM as little or negligible plastic sizes should be present for $h'<0.2$.
5. Independence of $C/a_{c,CIP}$ with indenter sizes suggests the feasibility of a non-destructive means to measure fracture toughness when micro-sized indenters are employed due to smaller indentation depths and plastic zone size C. The constant $C/a_{c,CIP}$ value also opens the possibility of using direct indentation data for fracture toughness measurement using simple fracture models but needs further studies.

In conclusion, fracture toughness was measured for AL2024-T351 using a chamfered flat-end cylindrical indenter using the limit load analysis, where the CIP according to von Mises criteria for ductile materials was sufficient to measure the indentation energies needed for fracture initiation of different indenter sizes. The CIP, thus becomes the driving pressure via indentation for utilizing the modified limit load analysis approach.

Chapter 5 Fracture Toughness Comparison of AL2024-T351 Using Chamfered Flat-Ended Cylindrical and Spherical Indenters Via Modified Limit Load Analysis[4]

5.1 Introduction

Over the last three decades, the indentation testing method has been used for material characterization and structural integrity assessment with current emphasis on non-destructive testing for static and in-service structures [74, 233, 271–275]. The need for fitness for services (FFS) according to API 579-1/ASME FFS-1 [276] broadens the studies of investigative approaches of materials with flaws, where scheduled and/or real-time conditioning monitoring are paramount to the objectives of investigative engineering. The works of Haggag et al. [77], Murty and Mathew [2] and Haggag [233] implemented the use of a field indentation microprobe for structural integrity evaluation while the works in [178, 274] primarily focuses on attaining the tensile flow curve of metals.

For fracture toughness (K_{IC}), which is a quantitative way of measuring a material to resist the initiation or propagation (unstable) of cracks, several works have looked at estimating fracture toughness for metals using different approaches [66, 104, 178-179, 233-235, 278]. The works of Lee et al. [179] and Yu et al. [104] look at implementing a continuum damage model (CDM) approach by evaluating a critical indentation depth needed for estimating the critical indentation energy for K_{IC} estimation while the works of Haggag and Nanstad [66] and Okocha et al. [237] focuses on estimating K_{IC} using a modified critical fracture strain model originating from the demonstration from the works of Ritchie [61], which observes the microstructural features and characteristic length of carbon steels for fracture initiation. In the work conducted by Kim et al. [235] for the estimation of the critical apparent stress intensity factor from J-integral (K_{JC}), emphasis was directed towards the use of a flat-ended cylindrical indenter via a limit load analysis (LLA) that defines a crack initiation point (CIP) required for structures with defects to fail and relates the flat-end cylindrical indentation with a (CRB) under tension.

[4] This chapter has not been published in the following publication:

Okocha, S. I., Yu, F, Jar, P. Y. B., & Hendry, M. T. (2024). Fracture Toughness Comparison of AL2024-T351 Using Chamfered Flat-Ended Cylindrical and Spherical Indenters Via Modified Limit Load Analysis4, International journal of plasticity. (unpublished)

The concept of CIP originated from the work of Miller [70] that considered Tresca's plane stress limit solutions and depended only on the plane of the ligament [70]. However, due to the conservativeness of the Tresca's plastic yield surface for ductility in metals, Kim et al. [238] considered the use of the von Mises plastic yield surface for the definition of the CIP [235]. Recently, Okocha et al. [278] further modified the limit load analysis (LLA) approach from [238] for high strength aluminum (Al2024-T351) by a virtually determined J-integral (K_J) results via chamfered cylindrical flat-end indentation in the aim of estimating K_{JC} for high strength alloys based on the principle of transiting from elastic-plastic fracture mechanics (EPFM) to linear elastic fracture mechanics (LEFM).

In this work, the modified LLA approach is implemented for AL2024-T351 using both the chamfered flat-end cylindrical indenters and the spherical indenters. The objective is to determine firstly if the modified LLA approach is feasible with spherical indentation owing to their popularity and feasibility towards tensile flow curve determination as well as other mechanical properties. Secondly, it is to ascertain and compare the depth for fracture toughness from both indenter types that is required towards the aim of non-destructive indentation testing, and to investigate the material's sub-surface for the extent of plasticity evolution. Unlike the work of Kim et al [238], where the flat-end cylindrical indenters are virtually compared to a CRB specimens under tension and the work of Okocha et al. [278] where chamfered flat-end indenters are virtually compared to a notch round bar (NRB) specimen in tension, the ball indentation in this study is compared with a single edge notch bend (SENB) specimen under loading since the stress state (stress triaxiality) is similar between the tip of the ball indentation and the sharp crack tip of a SENB specimen in loading [104, 184, 237] as long as the materials are isotropic in nature.

Additionally, a look at the material's deformation stages was considered based on the deformation changes for the estimation of yield strength using spherical indentation. The yield strength estimation, following the ratio of the yield pressure (P_y) and stress constrain factor (δ), saw consistency between different indenter sizes, which was based on the 1st derivative of the average pressure and normalized indentation depth needed for CIP estimation and thus, opening an avenue for using a single indentation loading cycle for material characterization and fracture toughness estimation. In the end, K_{JC} estimation, using either chamfered or spherical indenter, is compared with K_{JC} estimated from literatures.

5.2. Theory and calculation

5.2.1 Parameters needed for K_{IC} estimation via the modified limit load analysis

The K_{JC}, J-integral (J), $P_{CIP,}$ P, $\left(\frac{h}{a_c}\right)_{CIP}$, h' and a_c' as expressed and determined in Chapter 4 [278] are similar in this current chapter. Hence, these parameters will not be deliberated upon in this chapter. However, for the geometrical similarity between the chamfered indenter with the NRB specimen, the spherical indenter is compared with small sizes of spherical indenters.

5.2.2 Measurement via indentation

5.2.2.1. contact area measurement

In order to measure the pressure developed via indentation, the contact area is needed. Eq. (5.1) describes the contact areas and contact radiuses based on the chamfered indenter's edge and spherical indenter's tip. Figure. 5.1 shows an illustration of the indenters contact regions for both the chamfered (CH) cylindrical flat-end indenter and the spherical indenter (S).

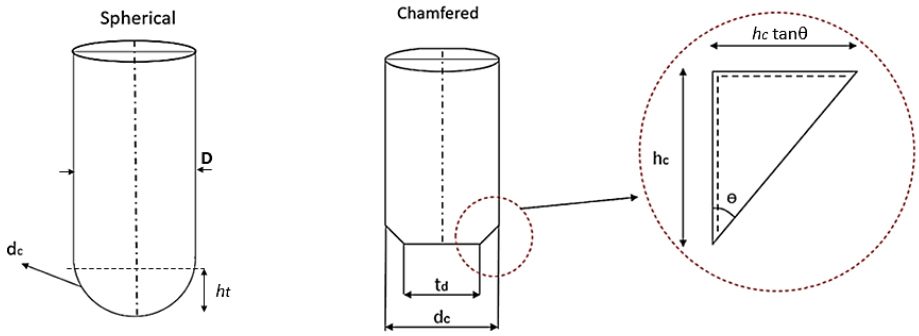

Figure 5.1 Indenter tip geometry for chamfered flat-end cylindrical and spherical indenters.

$$
\begin{aligned}
A_{CH} &= \pi\left[\frac{t_d}{2} + h_c \tan\theta\right]^2 && \text{i}\\
a_{c,CH} &= \frac{t_d}{2} + h_c \tan\theta && \text{ii}\\
A_S &= \pi\left[Dh_c - h_c^2\right] && \text{iii}\\
a_{c,s} &= \sqrt{\frac{A_S}{\pi}} && \text{iv}
\end{aligned}
\qquad (5.1)
$$

A_{CH} and A_S are the contact areas for the chamfered and spherical indenters, respectively while $a_{c,CH}$ and $a_{c,S}$ are the contact radii for the chamfered and spherical indenters, respectively.

For the spherical indentation, h_c is attained by considering the height of pile-up (h_{pile}) created at increased indentation depths with the removal of the elastic recovery component once the specimen is unloaded [94, 183] as seen in Eq. (5.2). This indicates the accurate h_c estimation required for A_S determination.

$$h_c = h_t - h_{pile} - \in \frac{L_{\max}}{S(h_{\max})} \tag{5.2}$$

where $\in$ represents a geometrical constraint and is taken as 0.75 for parabolic or spherical indenters [94, 183], $L_{\max}$ the maximum indentation load for an indentation cycle, $S(h_{\max})$ the material stiffness attained at the maximum indentation depth from the initial portion of the unloading curve, and h_{pile} the height of the pile-up with reference from the surface of the un-indented specimen.

5.2.3.2. Yield strength

For the chamfered flat-end indenter, Eq. (4.8) was used to estimate the yield strength as seen in previous chapter [278]. For the spherical indenter, studies in [269-270] focused on the deformation behaviour of materials using the first (1st) derivative, where materials show different slope changes signifying different deformational stages based on elastic-plastic deformation phenomena [74, 183]. In this study, the 1st derivative of the indentation pressure and normalized depth is used to estimate the yield strength, $\sigma_{y,ind}$ for the spherical indenter based on the yielding pressure, P_y.

$$\sigma_{y,ind} = \frac{P_y}{\delta} \tag{5.3}$$

where δ =2.87 for spherical indenters [127, 247].

5.2.3.3. Indentation Hardness

Conventional methods for hardness measurement, according to ASTM E18 [259], measures the hardness in terms of the ability to withstand a load without forming a dent. However, works from Gao et al. [279-281] demonstrated the hardness evolution using spherical indentation for describing indentation deformations based on the normalized contact area by providing an elastic-plastic solution originating from the ECM, where solutions of the stress, strain, and displacement components of the elastic and plastic domains of an internally pressurized cylindrical cavity were utilized [279–281]. In their work [279-281], the hardness appears to be independent of the strain-hardening level when indentation depth is small such that there is little or no plastic deformation and only affected by strain hardening level at higher depths especially for stiff materials (large ratios of Young's modulus to yield stress). The exact solution is expressed in Eq. (5.4) with the consideration of no strain gradient effect [281] and with a material having an elastic-power-law hardening behaviour [280].

$$H_{ECM} = \sigma_y \frac{2}{3}\left\{1+\frac{1}{n}\left[\left(\frac{1}{4}\frac{E_s}{\sigma_y}\frac{a_c}{R}\right)^n - 1\right]\right\} \tag{5.4}$$

where H_{ECM} is the indentation hardness via the spherical expansion model, n the strain hardening exponent, E_s the Young's modulus of the material measured from indentation, and R the radius of the spherical indenter.

5.2.3.4. Plastic zone size (C)

Plastic deformation occurs almost inevitably during contact between a sharp indenter and a material due to local stress fields exceeding the yield strength of the material. Thus, it is necessary to quantify the plastic zone size especially at the critical depth relating to the CIP of the material. With rising indentation depth, the shape of the plastic zone size (C) is developed within the material's sub-surface following different evolutional trend depending on the type of indenter. Previous works from Gao [279-281] show the shape of the zone for C generated by cone and spherical indenters. However, for the chamfered flat-end cylindrical indenters, the shape of C does not follow an expanding sphere or cylinder [278]. For the chamfered indentation, work presented in [275] describes the plastic zone evolution as a non-circular ellipsoidal solid, which transitions

into a *circular solid* at further indentation depths. For spherical indentation, the work in [258] proposed an analytical model for attaining C, which depends on material properties, the normalized contact radius (a_c/R) and n. In this study, FE modelling is used in this current study to estimate C at different indentation depths as seen in [238, 258, 278] based on the constitutive equation that governs the material deformation behavior for both the chamfered and spherical indentation.

5.3. Experiments, Materials, and Methods

5.3.1. Materials and test program

Test programs involving smooth and notched tensile specimens as well as cylindrical disks for indentations were conducted in ambient temperature. The material used in these tests is AL2024-T351 possesses higher strength and fracture properties in contrast to many other aluminum alloys. The experiments were similar to those done in Chapter 4. Figure 5.2 shows the similarity of the test setup using the two indenters.

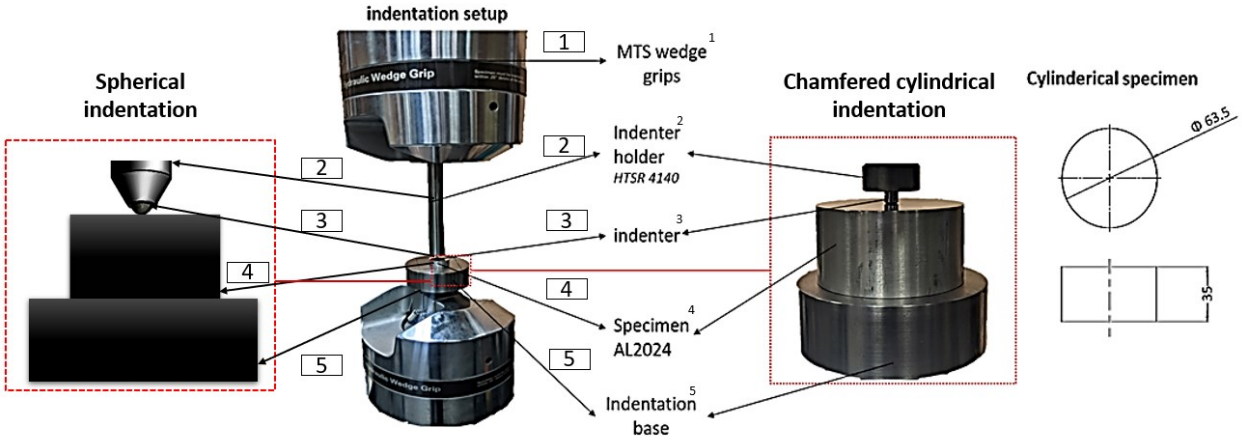

Figure 5.2 Indentation set-up and specimen geometry

5.3.2. Hardness tests

The Rockwell hardness test as defined in ASTM E-18 [259] for metallic materials was conducted using a MACROMET II tester based on B scale hardness test procedure using a steel ball indenter of 1.588mm in diameter. In order to validate the hardness results of AL2024-T351, the Rockwell hardness tester was first calibrated using a standard test block of 34.7 HRB to ensure the hardness measurement followed the right procedure. To achieve this, an initial load application of 98.1N was applied, followed by an additional load to result in a total of 981N, of which the permanent

depth attained is translated to the hardness [259]. Six Rockwell tests were conducted per sample for 2 different samples.

5.3.3 FE modelling of indentation test

FE modelling of indentation test was carried out following the set-up as described in Figure. 5.3 using ABAQUS v.6.14 standard analysis, similar to that described in Chapter 4, section 4.3.5.

The specimen was modelled as similar to what was done in chapters 3 and 4, but the analytical rigid indenter was replaced as a spherical axisymmetric quarter-rigid body. Figure 5.3 shows the comparison between the two indenter types.

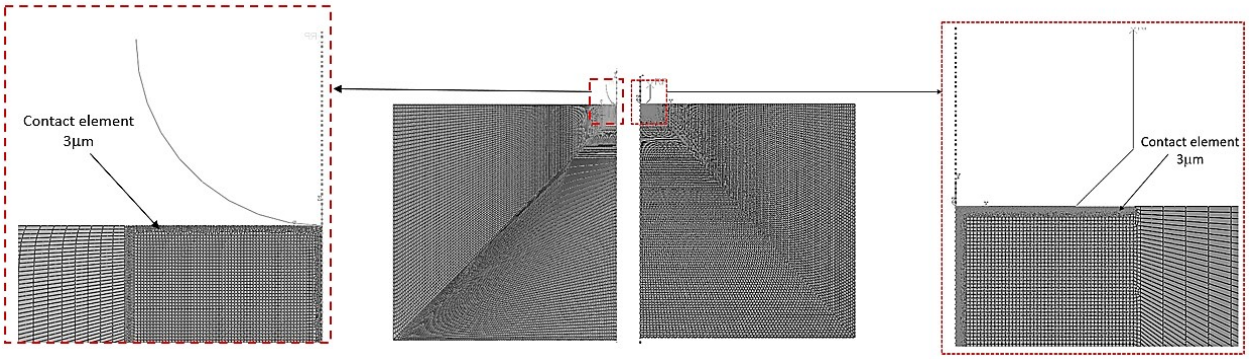

Figure 5.3 FE modelling and mesh orientation of the indentation testing for both indenters.

5.3.4 Fracture toughness description

The fracture toughness estimation using indentation testing results followed a series of procedures from the force-displacement curve to the apparent fracture toughness expressed in Eq. (4.1) as shown and described in Chapter 4. For the spherical indenter, step 2 (S.2) as seen in Figure 4.7 using Eq. (4.5) is replaced with Eq. (5.4) in which the reason will explained later in this chapter.

5.4. Results

5.4.1. Smooth specimen in tension and fracture toughness

A summary of the mechanical and fracture properties for AL2024-T351 is expressed in Table 5.1 from [278], which are results from the smooth and notched tensile tests. For the fracture toughness, information of the stress concentration and application of Irwin's elastic solution for relating notches to cracks of the NRB specimens is explained in detail in [278].

Table. 5.1. A summary of the mechanical properties attained from the tensile tests on smooth and notched specimens of AL2024-T351.

	F_f (KN)	D_f (mm)	σ_{eq}^{f} (MPa)	ε_{eq}^{f}	E (MPa)	σ_y (MPa)	UTS (MPa)	$K_{\rho c}$ (MPa.m$^{0.5}$)
Avg	53.52	10.08	670.39	0.43	71016	360.53	468.03	33.05 [278]

5.4.2 Indentation testing

5.4.2.1 Loading-unloading test

The indentation tests conducted involved using chamfered flat-end cylindrical indenters and spherical indenters of 3 different diameters (3, 5 and 6.35mm). The indentation load-depth data were retrieved from the MTS data analyzer and smoothened using the locally weighted scatterplot smoothing (LOWESS) approach. Loading-unloading curves were generated from the test equipment for each indenter, as shown in Figure 5.4, (a)-(f), and the comparison between the chamfered indenter and spherical indenters at the same depth, (g)-(i).

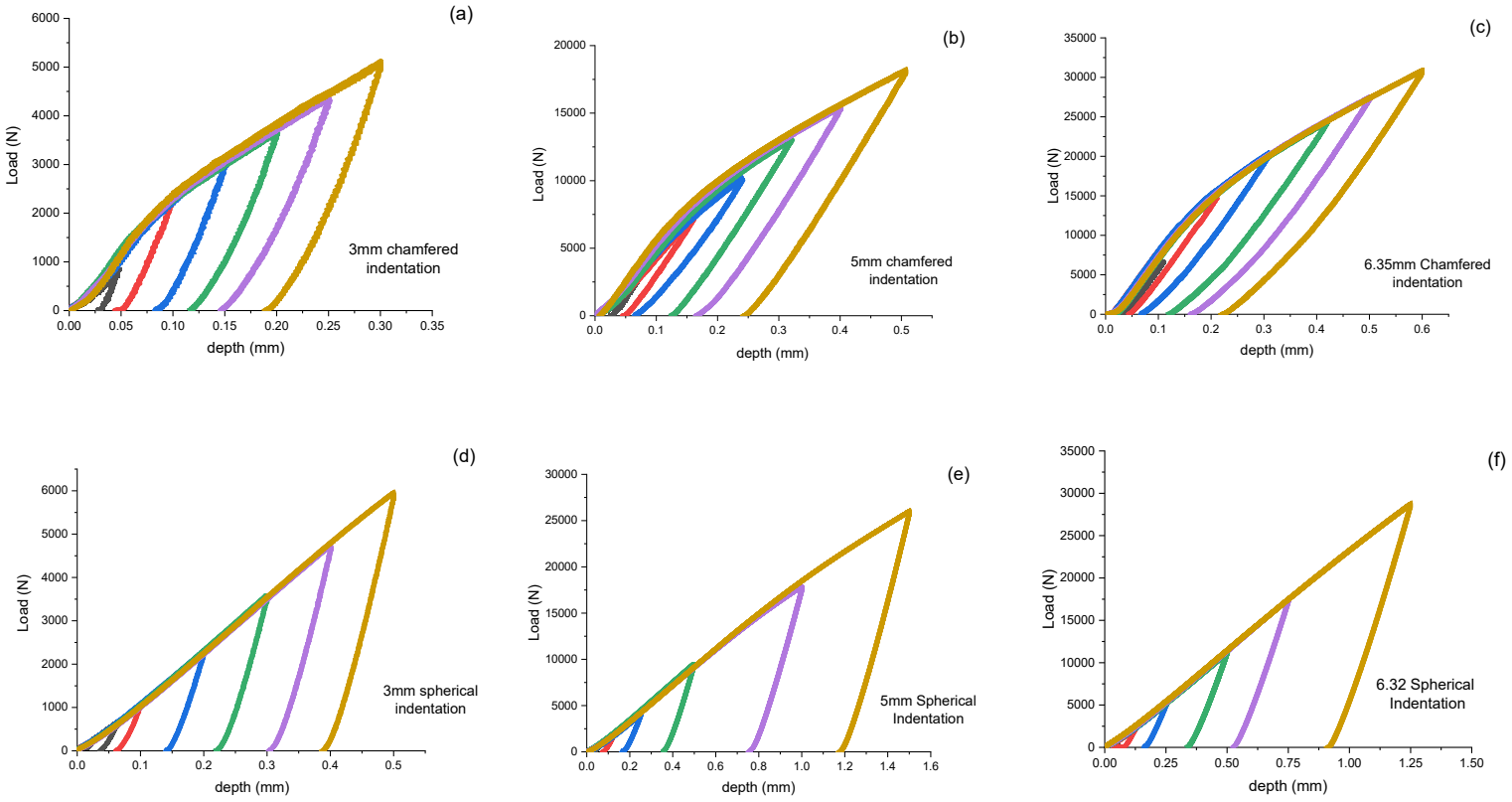

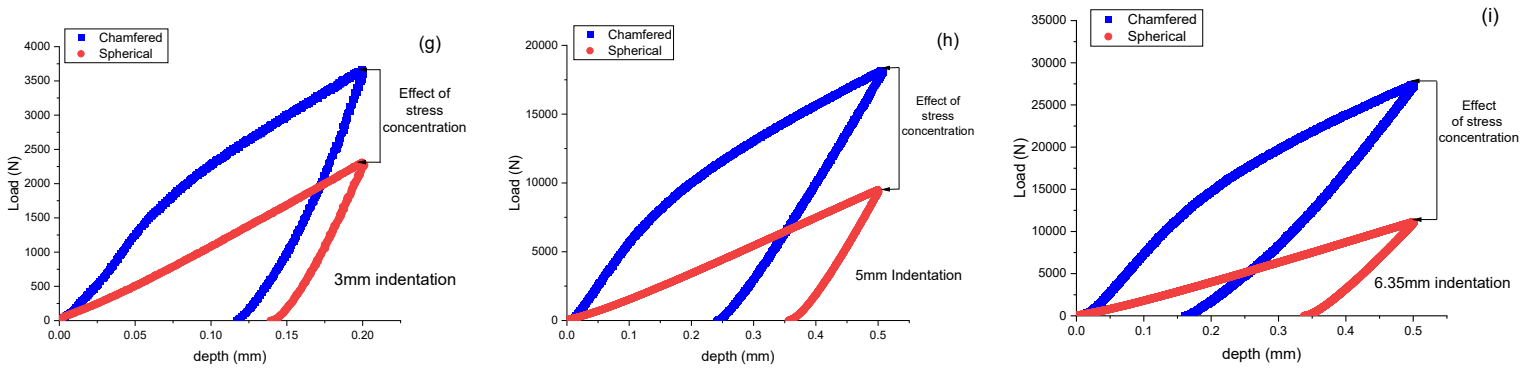

Figure 5.4 Indentation load-depth plots: (a) 3mm chamfered indenter, (b) 5mm chamfered indenter, (c) 6.35 chamfered indenter, (d) 3mm spherical indenter, (e) 5mm spherical indenter, (f) 6.35 spherical indenter, (g) 3mm indentation for difference in stress concentration, (h) 5mm indentation for difference in stress concentration, and (i) 6.35 indentation for difference in stress concentration.

The plots in Figure 5.4, (g)-(i), show the difference in the stress concentration effect and the elastic relaxation due to different sizes of the two types of indenters. These differences are seen to increase as the indenter size increases, which can be attributed to the larger contact area associated with larger indenter sizes and increase of the indentation depth.

For the spherical indenter, the pile-up height (h_{pile}) was also recorded for different indentation depths after unloading. Figure 5.5 shows the relationship of the maximum load (L_{max}) with the resulted pile-up height for different indentation cycles.

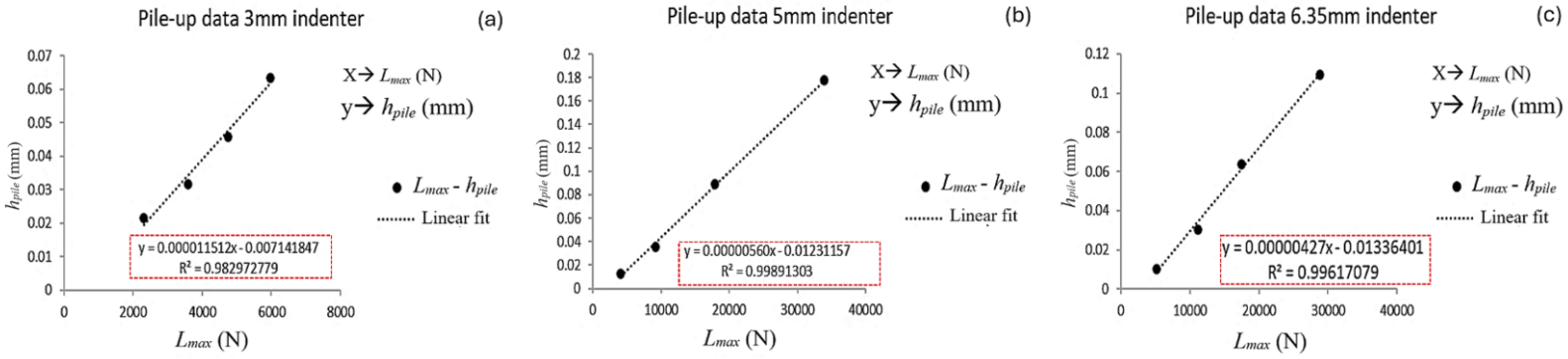

Figure 5.5 h_{pile} *vs* L_{max}*:* (a) 3mm, (b) 5mm, and (c) 6.35mm

5.4.2.2 Yield strength estimation

For the estimation of σ_{ys} using Eq. (5.3), identification of the critical indentation depth (φ) is required to determine the corresponding L_c and a_c values (for the chamfered indenters). As shown in Figure 5.6(a), the φ value was determined from the intersection of two tangent lines for the elastic and the plastic stages of the *L-h* curve as the corresponding L_c and a_c at $h = \varphi$ were used in Eq. (5.8) to estimate σ_{ys}. Figure 5.6(a) shows the location of φ, L_c and a_c and the estimation of σ_{ys} using the 3mm chamfered indenter as an illustration.

For the determination of $\sigma_{y,ind}$ used for the spherical indentation, the first derivatives as suggested in [269-270] is implemented, which is to use the first derivative to indicate the change in the slope of the pressure, P versus $h/a_{c,S}$ to show the transitions of deformational stages. By applying Eq. (5.3), P_y must be located that translates to when an average yielding occurs around the indented substrate.

Four distinct deformation stages were identified as shown in Figure 5.6 (b), where the 1st derivative of P - $h/a_{c,S}$ was determined and provided an observable change in the slope that signals the change of the deformation stage from elastic to full plastic as seen in other studies [269-270]. For the spherical indentation, an interesting observation is demonstrated with local hardening effect occurring at the inception of contact, which causes a rise in the average pressure, followed by a sudden drop in the average stresses with further increase in depth as also observed in [122-124, 183, 279] according to the principle of indenter size effect (ISE). Hence, the estimation of $\sigma_{y,ind}$ is situated after the ISE phenomenon at the *maxima point of the 1st derivative* of P - $h/a_{c,S}$ as seen in Figure 5.6(b). At later indentation depth, we experienced high disturbances in the plastic regime at certain depths as shown in Figure 5.6 (b). Using Eq. (5.3), $\sigma_{y,ind}$ is estimated at the yield pressure, P_y located at the maxima point of the 1st derivative of P - $h/a_{c,S}$. ($\frac{dP}{dh/a_{c,s}} - h/a_{c,s}$). It is to note that initial portion of the P - $h/a_{c,S}$ was truncated due to ISE phenomena.

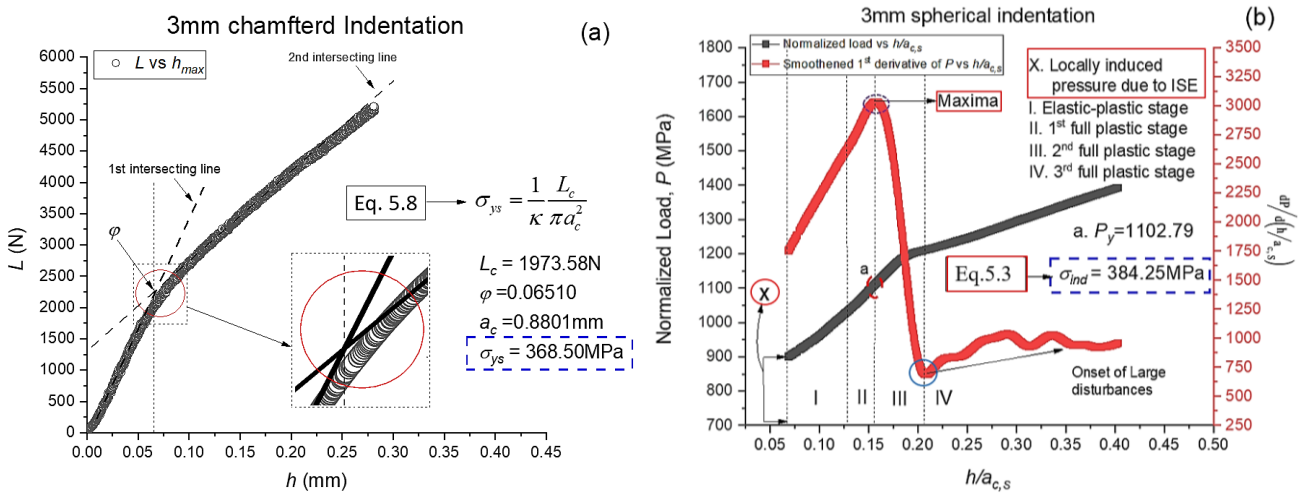

Figure 5.6. P_y location for $\sigma_{y,ind}$ estimation: (a) chamfered cylindrical flat-end indenter, (b) spherical indenter.

The definition of P_y for $\sigma_{y,ind}$ estimation in this study was found to be located at the maxima point of the 1st derivative of P - $h/a_{c,S}$, which is the end of the 1st full plastic stage (II stage). Table 5.2 shows the average value of yield strength for both indenter types and all sizes. Values for σ_{ys} and σ_{ind} determined are summarized in Table 5.2 for the indenter sizes, showing the average (Avg), maximum (Max) and minimum (Min) yield strength values.

Table. 5.2 Yield strength estimation for different indenter sizes.

σ_{ys} (MPa)	***3mm (CH)***	***5mm (CH)***	***6.35mm (CH)***	σ_{ind} (MPa)	***3mm (S)***	***5mm (S)***	***6.35mm (S)***
Max	379	373	372	Max	384	368	381
Min	377	367	368	Min	375	356	371
Avg	*377*	*370*	*370*	Avg	380	363	376

5.4.2.3 Hardness

Experimentation outcomes from the Rockwell hardness tester were used for ascertaining hardness from indentation testing. Table 5.6 shows the hardness value (HRB) and the corresponding Brinell hardness (BHN) value using suitable conversion table as seen in [108, 280].

Table 5.3. Rockwell and Brinell hardness of AL2023-T351

TEST (HRB)	1	2	3	4	5	6	Mean (Std.dev)	BHN (Std.dev)
Specimen 1	77	76.5	77.5	77.25	77.5	77.5	77.21 (0.37)	139.42 (0.73)
Specimen 2	76.5	77.25	77.25	77.5	77.25	77	77.13 (0.31)	139.25 0.63)

5.4.2.4 Nature of the plastic-zone

For the spherical indentation, the plastic zone size, *C*, is developed beneath the indenter, characterized by the ECM as seen in several studies [22, 257-258, 279-281]. However, for the flat-end chamfered indenters, the pressure distribution does not follow the ECM. This is because the stress field developed at the tip of the indenter does not increasingly develop radially with increasing depth at the initial stage of indentation as seen for the spherical or cone indenters [257, 279-281]. Figure 5.7(a) shows that the stress field develops a ring-like pattern initially, and with the increase of indentation depth, as shown in Figure 5.7(c), the ring is evolved into an ellipsoidal shell, surrounding a region that is still subjected to a compressive stress state below the yielding point. As shown in Figures 5.7(c) and 7(e), with the further increase of the indentation depth, the plastic zone eventually evolved into an ellipsoidal solid under the indenter, having a *circular profile* look as seen in Figure 5.7(g). For the spherical indentation, the plastic zone evolves radially from the contact area with increasing depths as seen in Figures 5.7 (b), (d) (f), (h).

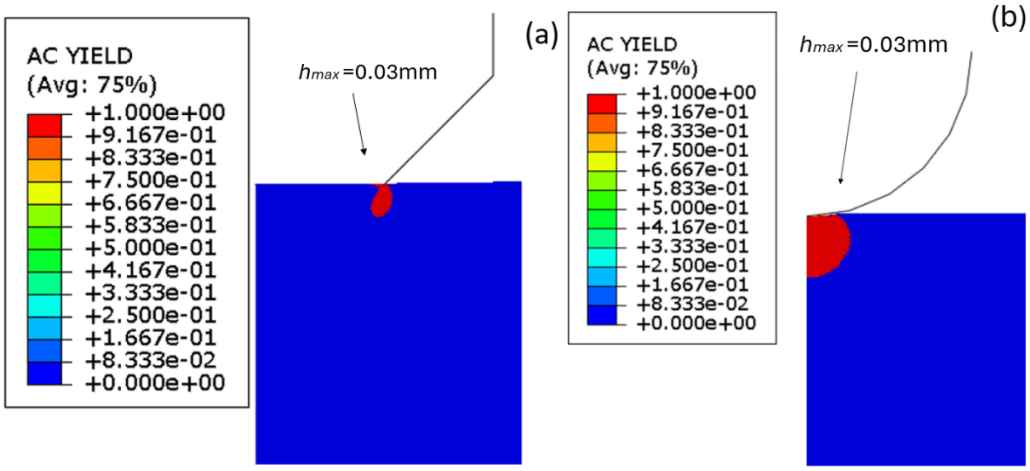

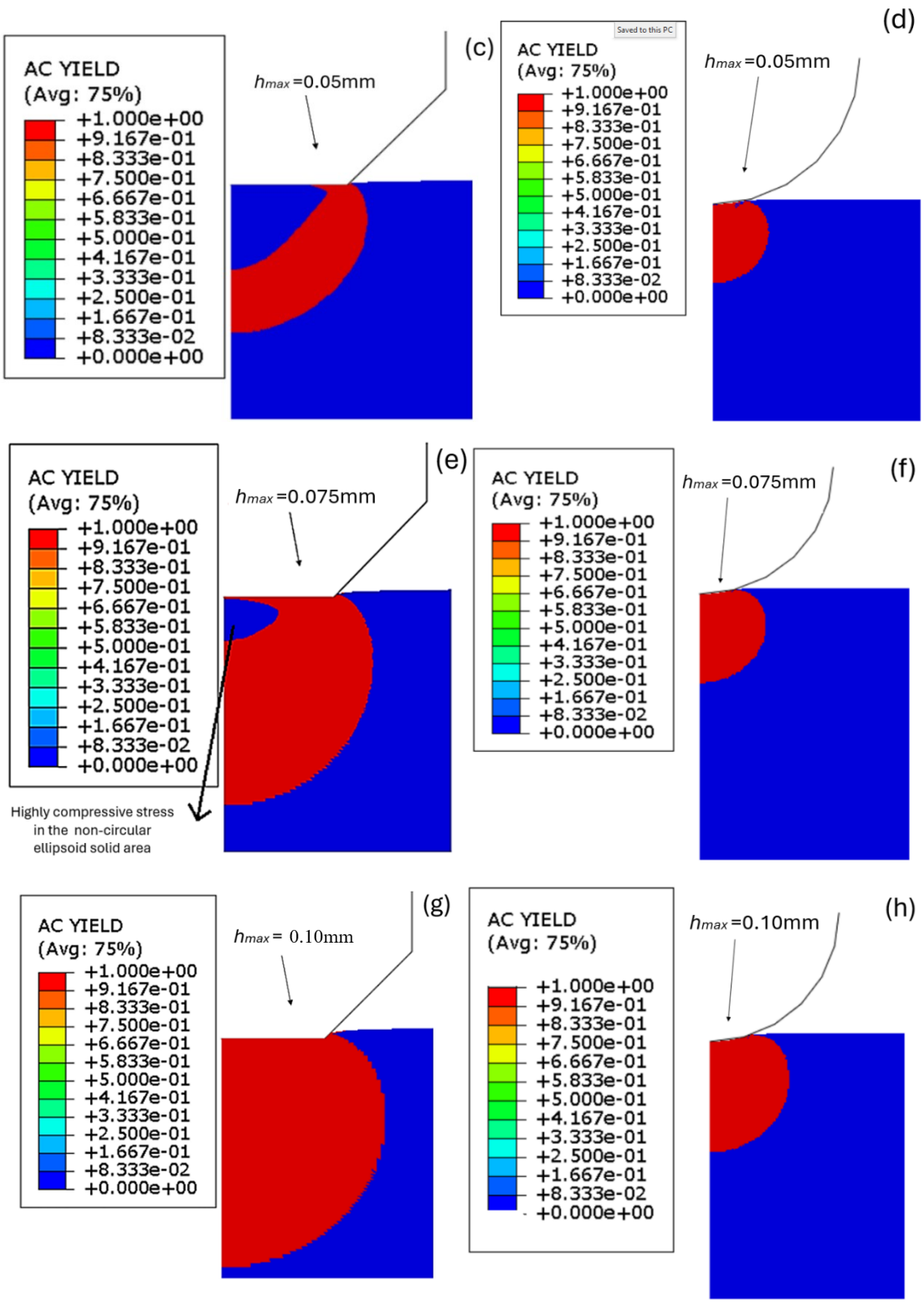

Figure 5.7 Plastic-zone development of the chamfered and spherical indentation using 3mm indenter as an illustration.

5.4.3 Fracture toughness

5.4.3.1 Challenge with spherical indentation for the modified LLA application

As explained in section 5.4.2.2, the ISE phenomena with spherical indentation causing locally induced pressure at contact causing a rise in the average pressure. In order to apply the modified LLA approach, the elastic deformation stage of the entire deformation is needed. As seen in Figure 5.8(a) there is an absence of the elastic deformation portion of the P - $h/a_{c,s}$ curve across the spherical indentation sizes (3mm and 5mm) due to ISE. For the chamfered cylindrical indentation, the P - h/a_c curve initiates closer from the origin and have a visible elastic and plastic deformation portions, where the three indenter sizes show similar P - h/a_c curves as seen in [275]. In Figure 5.8(a), only the 6.35mmn spherical indentation showed less effect of the ISE phenomenon with some presence of the elastic deformation stage in P - $h/a_{c,s}$ curve. The 3mm and 5mm spherical indenters had the ISE phenomenon and an absent of the elastic portion. This suggests that smaller indentation ball causes the localized hardening of pressure as seen in works in [122-124, 178, 283]. It is possible that this phenomenon (ISE) is also present for harder materials even for larger spherical indenter sizes but needs to be looked upon.

The challenge with the spherical indentation for K_{JC} estimation via the modified LLA approach is the absence of the elastic part of the P - $h/a_{c,s}$ curve due to the ISE phenomena. This would nullify the estimation of A_{pl} as seen in Eq. (5.2) in the procedures for K_J as seen in chapter 4. In order to improvise for the absence of the elastic part of the P - $h/a_{c,s}$ curve, a proposition is offered in this study to implement the outcome of H_{ECM} in replacement to P as seen in Figure 5.8(b). This replacement of P with H_{ECM} is done since both are pressures acting on the indented material with the former being the average pressure at the localized indented region, which is the ratio of the applied load and the contact area while the latter describes an incremental indentation pressure representing the ratio of applied load to projected area of the indentation at increase in the normalized contact depth ($h/a_{c,s}$) [283].

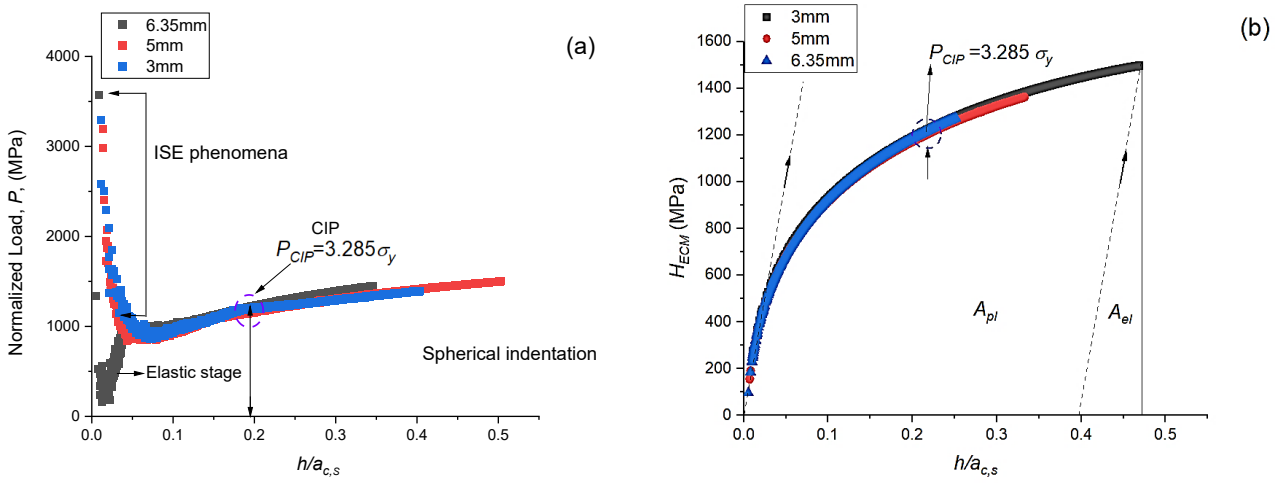

Figure 5.8 Identification of CIP: (a) P - $h/a_{c,s}$ and (b) H_{ECM} - $h/a_{c,s}$

The curve between H_{ECM} - $h/a_{c,s}$ seen in Figure 5.9 (b) shows same profile for the three spherical indenter sizes as suggested in the works of Gao [279-281]. As shown in Figure 5.8(b), an elastic portion can be identified from the curve needed for the estimation of A_{pl} in Eq. 5.2. This suggestion opens the possibility of applying the modified LLA approach to spherical indentation with even small sizes negating the challenges that may arises from ISE phenomena depending on the material.

5.4.3.2 Virtual J-integral for K_J estimation

As explained in section 5.4.4.1 about the challenges with the spherical indentation, a method suggested in this study is the replacement of P - $h/a_{c,s}$ curve with H_{ECM} - $h/a_{c,s}$ curve for step 2 (S.2) in the procedure found in Figure 4.7. Hence, based on the geometrical similarity of relating indentation and NRB specimens for the chamfered cylindrical indenter as well as the similarity in stress-state between the spherical indenter and the SENB specimen, Eq. 5.4 can be used to attain different (a_c') values by varying the values of h' from 0.2 to 0.05, and with this, the new virtual load (L') and virtual depth (h'') curves can be constructed using Eqs. (5.14) and Eq. (5.15), respectively. Figure 5.9 illustrates the virtual load-depth curve constructed from the varying h' from 0.2mm to 0.05mm for both indenter types.

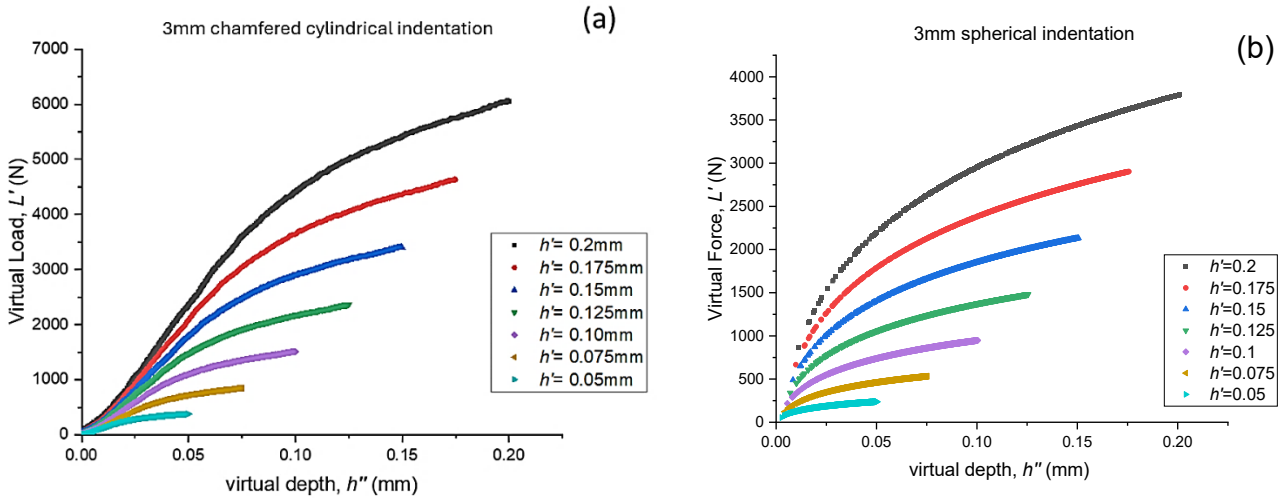

Figure 5.9 Virtual load-depth curve of a 3mm indenter: (a) chamfered cylindrical and (b) Spherical.

The value of η_{pl} as seen in Eq. 5.2 is considered to be taken as 0.869 [275], which is derived from geometrical relationships of NRB specimens for the chamfered indenter [244]. For the spherical indenter, Sharobeam & Pomona [283] suggests that η_{pl} is taken as 0.96 for a sharp crack in the SENB specimen. Thus, η_{pl} is taken as 0.96 for the spherical indentation for the estimation of J using Eq. 5.2 in this study only in the assumption because of the similarity in stress triaxiality between a spherical indenter and SENB specimen [110, 184, 237]. Table 5.4 provides a summary of virtual indentation parameters from the 3mm chamfered indentation outcomes.

Table 5.4. Virtual load-depth estimates from indentation parameters for estimating K_J

Indenter type	h' (mm)	a_c' (mm)	Max L′ (N)	A_{pl} (mm²)	J_e (N/mm)	J_p (N/mm)	J (N/mm)	K_J (MPa.m$^{0.5}$)
CH η_{pl} = 0.869	0.200	1.590	9509.225	744.118	22.480	81.456	103.936	91.012
	0.175	1.391	7280.500	518.481	19.670	74.131	93.800	86.460
	0.150	1.192	5348.939	334.649	16.860	65.125	81.985	80.832
	0.125	0.993	3714.541	202.376	14.050	56.713	70.762	75.096
	0.100	0.795	2377.306	99.148	11.240	43.413	54.653	65.997
	0.075	0.596	1337.235	43.713	8.430	34.028	42.458	58.169
	0.050	0.397	594.327	13.178	5.620	23.081	28.701	47.826
S η_{pl} = 0.96	0.200	1.127	4679.392	384.393	15.160	92.448	107.608	92.934
	0.175	0.986	3582.660	257.513	13.265	80.892	94.157	86.932
	0.150	0.845	2632.158	162.166	11.370	69.336	80.706	80.484
	0.125	0.704	1827.888	93.846	9.475	57.780	67.255	73.471
	0.100	0.564	1169.848	48.049	7.580	46.224	53.804	65.714
	0.075	0.423	658.040	20.271	5.685	34.668	40.353	56.910
	0.050	0.282	292.462	6.006	3.790	23.112	26.902	46.467

Figure 5.10 shows the correlation between K_J and (a_c'), where Figure 5.10(a) shows the K_{JC} estimated via chamfered indentation and Figure 5.10(b) shows K_{JC} estimated via spherical indentation. The average fracture toughness estimation using the above modified limit load analysis yields a K_{JC} value of 34.57MPa.m$^{0.5}$ (CH) and 33.59MPa.m$^{0.5}$ (S) as seen in Figure 5.10, which provides a relatively similar value to $K_{\rho c}$ (33.05MPa.m$^{0.5}$) as seen in Table 5.4, and thus offers an opportunity to estimate fracture toughness from a single indentation loading of both chamfered and spherical indentation.

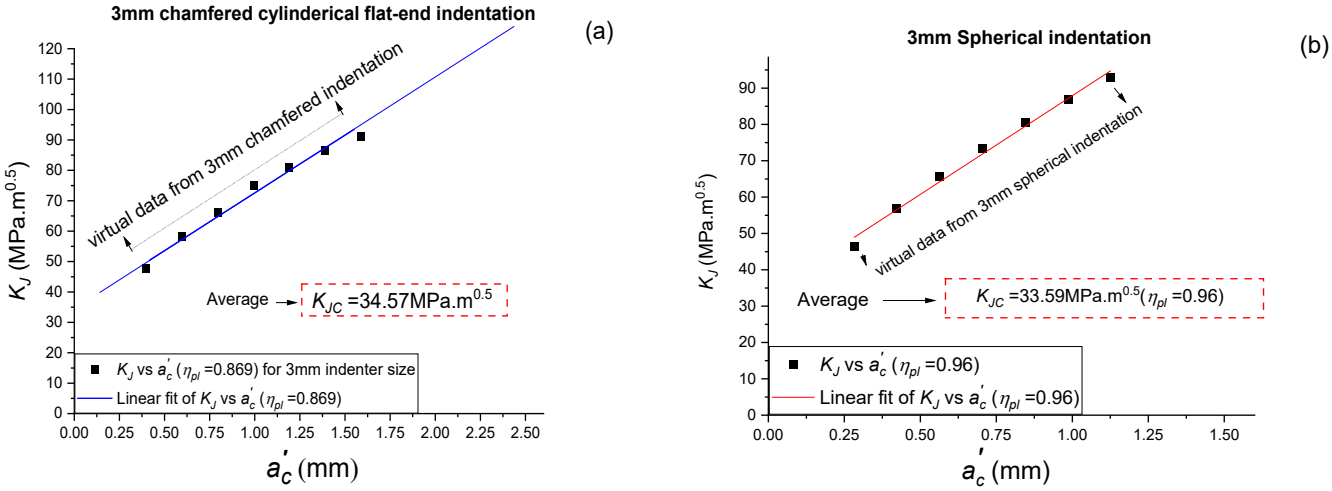

Figure 5.10 K_{JC} estimation via modified LLA approach:
(a) chamfered cylindrical indentation [275], (b) spherical indentation.

The K_{JC} for the chamfered indentation (34.57MPa.m$^{0.5}$) and spherical indentation (33.59MPa.m$^{0.5}$) were close to the value of fracture toughness in [244-245, 278], where standard approach (K_{IC}) from ASTM [69] as well as using Irwin's elastic solution [243] of NRB specimens ($K_{\rho C}$) of AL2024-T351 were used. The extrapolated value when a_c' to zero signifies a sharp crack and is taken as the K_{JC} in relation to K_{IC}. Due to the challenges of ISE in spherical indentation, it is not clear if the use of hardness information for fracture toughness is fully suitable. Thus, further studies are required to ascertain the use of the spherical indentation for fracture toughness estimation via the modified limit load analysis.

5.4.3.3 Plastic zone size at CIP

To study the local effect during indentation corresponding to the K_{JC}, FE modeling is used to correlate simulation results with experimental results of the load and depth at the depth corresponding to CIP ($h_{h/ac}$). $h_{h/ac}$ is attained by plotting P vs h and locating CIP, where the corresponding h value equals $h_{h/ac}$. At this depth, the plastic zone size is extracted from the FE model, measuring the evolution of the plastic zone (C) from the indenter's contact region and the measured contact radius ($a_{c,CIP}$). Figure 5.11 shows the outcome of the FE results with experimental as well as the FE results of the plastic zone sizes.

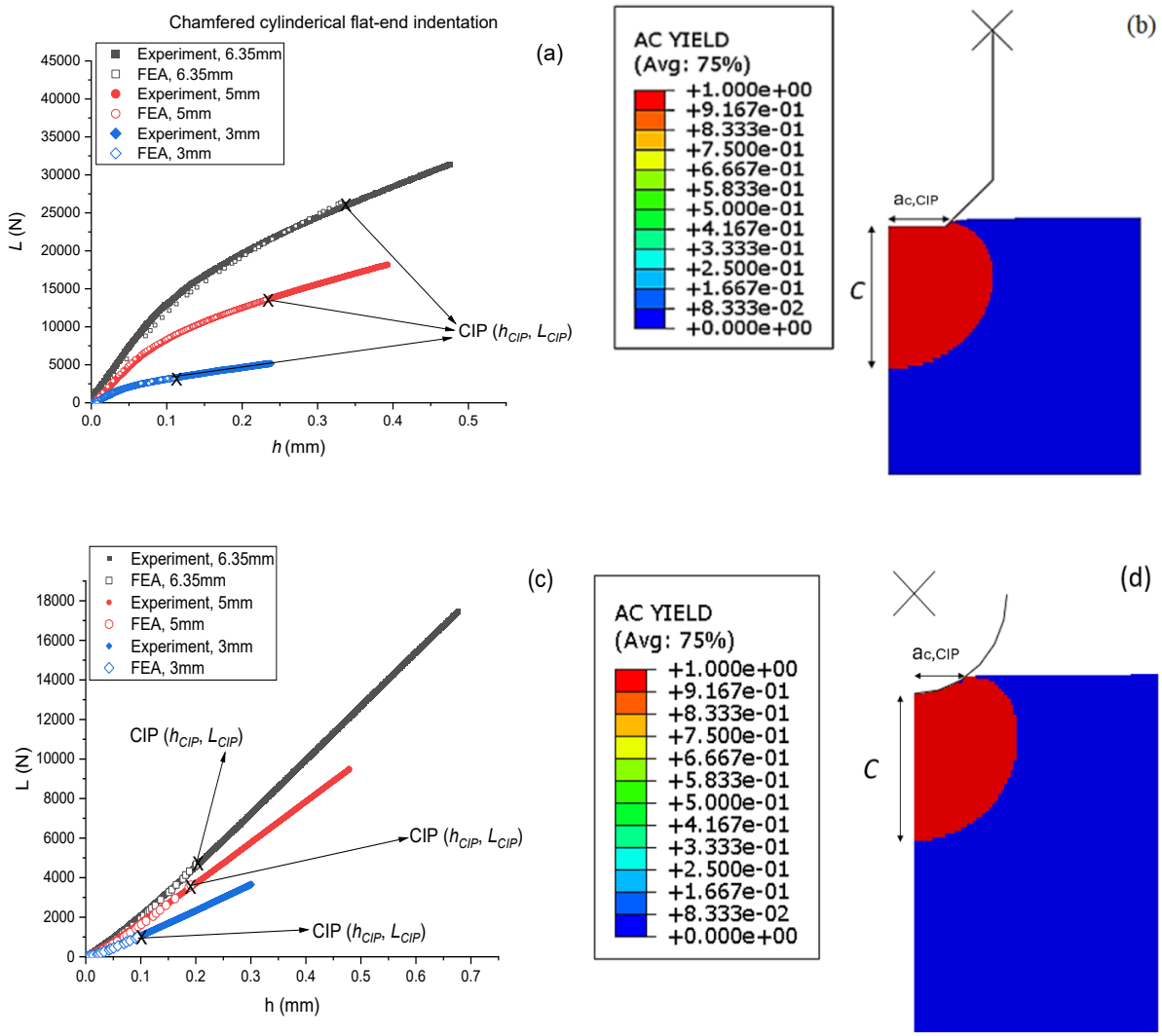

Figure 5.11. Establishing plastic zone size at CIP via FE modelling: (a) chamfered indentation (b) An illustration of C and $a_{c,CIP}$ via FE modelling for chamfered indentation, (c) spherical indentation, (d) An illustration of C and $a_{c,CIP}$ via FE modelling for spherical indentation.

With the estimation of C and $a_{c,CIP}$ from FE modelling, the ratio of C/$a_{c,CIP}$ is estimated and compared for the different indenter types. Figure 5.12 shows the plastic zone sizes from the 3 spherical indenters for the estimation of C and $a_{c,CIP}$ while Table 5.5. provides a summary of C and $a_{c,CIP}$ for the chamfered and spherical indentation tests at CIP. The estimation of C and $a_{c,CIP}$ for the chamfered indenter is taken from [278].

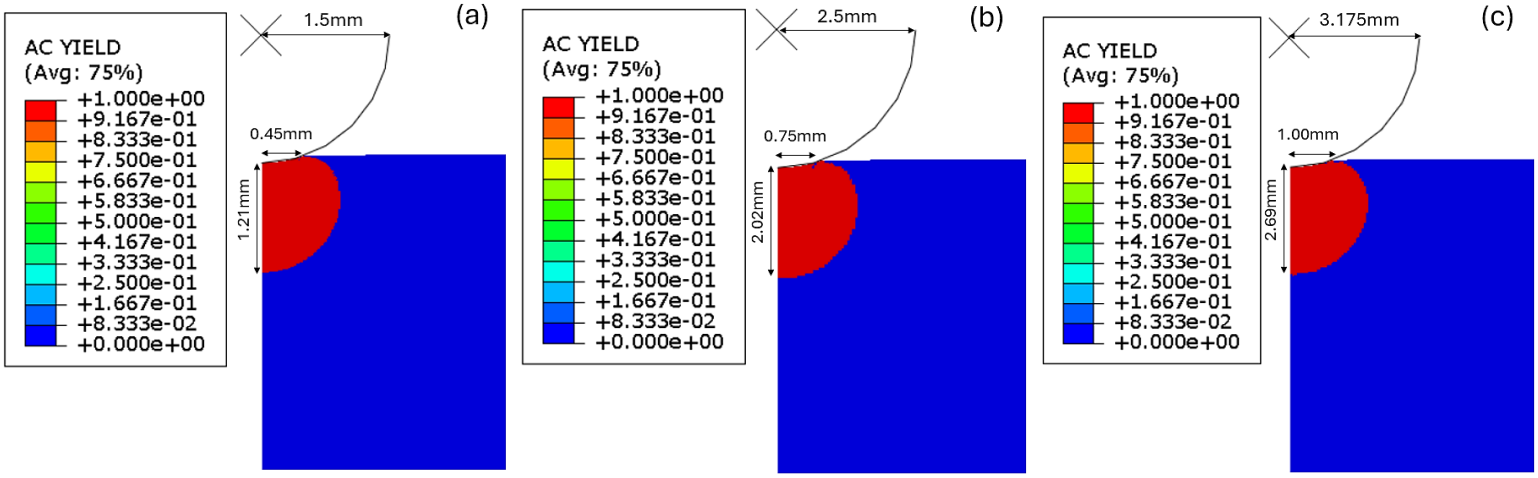

Figure 5.12 Plastic zone sizes for spherical indentation at CIP: (a) 3mm, (b) 5mm, and (c) 6.35mm

Table 5.5. Indentation parameters and local effect at CIP for different chamfered indenter sizes.

	Chamfered Indentation				**Spherical Indentation**				***Ratio of C***
Indenter size	h_{CIP}	C	$a_{c,CIP}$	$C/a_{c,CIP}$	h_{CIP}	C	$a_{c,CIP}$	$C/a_{c,CIP}$	***CH : S***
3mm	0.097	2.24	0.93	2.408	0.094	1.21	0.45	2.688	1.85:1
5mm	0.238	4.35	1.81	2.403	0.187	2.02	0.75	2.693	2.15:1
6.35mm	0.334	5.85	2.43	2.407	0.207	2.69	1	2.690	2.17:1

From table 5.5, it is seen that more indentation depths (h_{CIP}) are needed for attaining CIP using the chamfered indentation as compared to the spherical indentation due the larger contact area from the chamfered indenter. This is supported with the larger stress concentration of the chamfered indentation as seen in Figures 5.7 (i), (j), (k) than the spherical indentation. At the sub-surface level, the value of C is also seen to be larger in the chamfered indenter than the spherical indenter, signifying the extent of plasticity within the substrate since more portion of the substrate tends to reach equivalent stresses beyond the yield strength of the material. The ratio of C comparing both indenters also suggests an increase with an increase in size of the indenter, which is due to the

larger contact area of the chamfered indenter in the elastic-plastic half-space. In [278], the ratio of $C/a_{c,CIP}$ was suggested to be a constant value ~2.4. In this current study, we see the $C/a_{c,CIP}$ being ~2.69 for the spherical indenter for the same material, which entails the contribution of geometrical parameters. Hence, the $C/a_{c,CIP}$ becomes a quantity described from the role of material properties and geometric constraints during indentation that is defined by a critical indentation depth (h_{CIP}).

The ratio of C (CH:S) also provided an insight to plasticity of both indenters. Despite C having a larger magnitude in the chamfered indenter than the spherical indenter, results from table 5.5 show that smaller indenter sizes reduce the ratio of C (i.e CH:S). Hence, in the case of non-destructive testing with micro-indenters, the chamfered indenters might have a C value closely equivalent to spherical indentation, making it more attractive due to its ease in production and application. At microscale indentation, the spherical indenters are posed with the challenge of ISE, which adds another step for fracture toughness estimation unlike chamfered indentation, which creates no ISE effect.

5.5. Conclusions

In this paper, fracture toughness was estimated and investigated using the modified limit load analysis for AL2024-T351 using a chamfered cylindrical indenter and a spherical indenter. The main conclusions can be summarized as follows:

1. The pressure at the CIP according to von-Mises failure criteria is significant for estimating the required stress for simulating fracture toughness in both spherical and chamfered indenters.

2. The spherical indenter offers lesser indentation depth and load requirements for indentation testing than the chamfered flat-end indenter at similar indentation depths making it more suitable for structural assessment.

3. Non-destructive testing is feasible using micro-indenters due to the similarity in stress-field development of different chamfered or spherical indenter sizes as seen from P-h/a_c curves.

4. Replacing H_{ECM} with P can be effectively used to alleviate the ISE challenge experienced via spherical indentation for K_{JC} estimation.

5. Spherical indentation causes less plasticity at the material's sub-surface than chamfered indentation at similar indentation depths or at CIP except at extreme low indentation depths for micro-indenters, where ISE effect may be present causing localized hardening during contact, thus causing larger C than chamfered indenters.

6. The method of fracture toughness estimation via modified LLA approach can be tested for other materials like rail steels that obey LEFM, which is our original intended material meant for structural integrity assessment.

In conclusion, the modified limit analysis is applied to spherical indentation for fracture toughness measurement due to the versatility of the spherical indenter for material characterization in terms of stress-strain curve and material properties. In this case study, a contribution is seen from alleviating the challenges of spherical indentation in the form of ISE especially for micro-sized spherical indenters for fracture toughness measurement. The H_{ECM} is rather used to replace P because of the internal pressure generated due to the expansion of the spherical cavity within the material's substrate. However, the validity for the use of hardness to determine fracture toughness of rail steel is not fully verified and thus a further study is needed. In the end, the fracture toughness measured for AL2024-T351, closely matches the conventional fracture toughness value and opens an opportunity of using spherical indentation to measure fracture toughness directly from load-depth and contact radius information. However, further materials and studies need to be investigated to find the possibility of standardizing the approach.

Chapter 6 Spherical indentation of Heat-treated High Strength Rail Steel for Fracture Toughness and Hardness measurement[5]

6.1 Introduction

The rail industry over the decade has seen enormous improvements in the rail steel characteristics in the aim of alleviating issues concerning wear and fracture of rail steels [3, 10, 284–290]. Studies [4, 139-140] have looked at derailment trends and operational conditions that might attribute to rail fracture and operational safety. Also, several studies [286, 291–292] have shown the importance of continuous health assessment of rail steels during in-service and post-weldment state. Hence, it becomes imperative for a scheduled maintenance scheme to be implemented without relying only on rail properties after the post-manufactured state. However, using the conventional means for hardness and fracture toughness in-situ examination would not be feasible for in-service structures since samples need to be cut off from existing structure to fit the size and shape requirements needed in standards tests. This insinuates a desired need to adopt alternative methods for quickly and efficiently determining the mechanical properties like the Young's modulus, hardness, yield strength and fracture toughness of rail steels.

Works from Godefroid et al. [289], Cannon et al. [3] and Sheinman [294] have demonstrated that the performance of in-service rail steels have reduced life of its components as a result of defects generated by fatigue and wear and thus requiring rail steels to have specific classifications in terms of their tensile strength and hardness [293]. For this reason, the American Railway Engineering and Maintenance-of-Way Association (AREMA) [295] categorize rails depending on their applications. Rails are categorized as general or high-speed railway track usage and according to their chemical composition as standard or low alloy. When it comes to their mechanical properties of hardness and tensile properties, rail steels are thus categorized as standard, intermediate or high strength rail steels.

[5] This chapter is yet to be published:

Okocha, S. I., Yu, F, Jar, P. Y. B., & Hendry, M. T. (2024). Spherical indentation of Heat-treated High Strength Rail Steel for Fracture Toughness and Hardness measurements.

The work of Li et al. [296] suggested that rail wear of a railway curve radius at the straight-circle point, the curve center point and the circle-straight point follows the order of center point > the circle-straight point > the straight-circle point, which intensifies with the rise of running speed. The works in [296–297] have shown that the most critical wear occurs in the outer rails of high curves especially at the flange. Thus, the hardness of rails especially at the railway curve radius becomes crucial in design and for inspection purposes.

For rail fracture and derailments, the transverse detail fracture (TDF), which is a progressive fracture that originates from a longitudinal streak close to the running surface at the upper gage corner of the rail head and spreads transversely [296], is most common. Also, longitudinal cracks occur, which are special types of horizontal cracks induced at the sub-surface just beneath the gage corner of the rail, that has the potentiality to initiate and propagate fracture of the rail [36]. Studies [298-301] investigating cracks in rail have the origin of cracks from the brittle white etching layer (WEL) region due to contact fatigue while its propagation is driven by bending stresses. The international research report [302] reports that the critical crack length (i.e. the length of a surface-initiated crack that causes a rail break) is not a constant value across broken rails investigated internationally. Thus, it becomes imperative for continuous monitoring of rail's health for defects and wear concerns, where fracture toughness and hardness become indispensable towards the quality of an in-service rail steel.

One recent method for quick, cost effective and non-destructive hardness and fracture toughness measurement for post manufactured and/or in-service applications is the spherical instrumented indentation technique. Several researchers have tried using the spherical indentation technique for fracture toughness and hardness estimation [66, 104, 233, 235, 275] of ductile metals. However, the methodologies are still being investigated before they can be utilized for field work in the area of railway engineering. In this current work, spherical indentation is applied to four different rail steel types with different surface heat treatments and microstructure orientation to investigate a method of attaining the hardness and fracture toughness using one indentation loading by using multiple virtual indentation load and depth from geometrically similar spherical indentations. The hardness estimation implements the use of a modified expansion cavity model (ECM) [108, 256] along with conventional Brinell testing while the fracture toughness (K_{JC}) is measured using a modified limit load analysis approach (LLA). The microstructures are also investigated for their

average grain sizes and lamella spacing with their relationship with fracture toughness and strength of the rail steels. In the end, the microstructures are also investigated for their average grain sizes (prior-austenite grain sizes) to investigate its relationship with fracture toughness, which shows a poor relationship and suggests the need for other mechanical properties for a proper fracture toughness estimation if microstructural parameters are needed for fracture toughness estimation as seen in [233]. In the end, hardness estimated using ECM matches Brinell hardness values of the rail steels was attained and closely matched values from standard hardness tests [103,256] while the fracture toughness showed a good trend with K_{JC} values across different rail steels after consideration of the stress triaxiality factor. Thus, providing potentiality of fracture toughness and hardness estimation of rail steels via a single indentation cycle loading in the future.

6.2. Theory and calculation

6.2.1 Parameters needed for K_{IC} estimation via the modified limit load analysis

The parameters needed for estimating fracture toughness using the spherical indenter via the modified limit load analysis are similar to those in chapter 5. The K_{JC}, J-integral (J), $P_{CIP,}$ P, $\left(\frac{h}{a_c}\right)_{CIP}$, h' and a_c' as expressed and determined also in this current chapter. Hence, these parameters will not be deliberated upon in this chapter. Other concerns are the contact area and contact radius measurements, pile-up conditions, yield strength and hardness measurement are similar to the approach used in chapter 5 for the spherical indentation.

6.2.2 A simple novel approach for conventional Hardness measurement

The conventional hardness of the rail steels is also evaluated using the Brinell hardness (H_B) evolution with indentation depth according to ASTM E10. Also, since the indentation diameter (d) can be a function of the indentation depth as expressed ($d = 2(h\,D - h^2)^{0.5}$), the H_B across the indentation depth during loading can be investigated. Eq. 6.10(a) shows the expression for H_B estimation.

$$H_B = 0.102\frac{2L}{\pi D\left(D - \sqrt{D^2 - d^2}\right)} \tag{6.1a}$$

Another simple condition for H_B measurement is suggested in this work from the estimation of H_{ECM}. Due to ISE in spherical indentation, the condition when $\frac{d(H_{ECM})}{d(a_c/R)} = H_{ECM}$ is used in estimating the critical H_{ECM} for H_B estimation, followed by the average stress derived from the critical H_{ECM}. Eq. 6.1(b) shows the expression for H_B estimation from H_{ECM}.

$$H_B = 0.102\kappa C_{ys} \frac{H_{C,ECM}}{\delta} \tag{6.1b}$$

where κ is a fitting parameter for H_{ECM} -h/a_c with P-h/a_c which is caused by frictional effect on P-h/a_c, C_{ys}, the condition of von Mises plastic yield surface. κ is taken as ~1.12 for high strength rail steels (see Appendix 10) while C_{ys} is taken as 3.285.

6.3. Experiments, Materials, and Methods

6.3.1 Materials

The materials used in this chapter are high strength rail steels as used in Chapter 2 and 3. Table 6.1 shows the rail steels used in this study with their microstructures, which were attained using different manufacturing and surface heat treatments, provided by the Canadian National (CN) Railway Company and an undisclosed company (COMPX). Due to the confidentiality of the rail steels provided by COMPX, their names are not mentioned in this paper. A total of four rail steels were used to generate the required data for estimating the mechanical properties [178] and fracture toughness [73, 114]. The rail steels used in this study are similar in the manufacturing process and composition that have been used in the previous work by Yu et al. [73, 119] and Okocha et al. [183, 237].

Table 6.1 Rail samples and their microstructures

Rail Name /Identification number	**Microstructure**	**Location**	**Company**
JP	Deep head hardened	H	CN
EV	Deep head hardened	H	CN
CZ	-	H	CN
Rail #1	Head hardened perlite	H	COMPX

6.3.2 Mechanical tests

6.3.2.1 Destructive smooth tensile and single edge notched bend (SENB) tests

The tensile properties for the high strength rail steels were attained using tensile smooth dog-bone specimens in the longitudinal direction of the rail steels from previous works [73, 119] following the recommendations of ASTM E8/E8M [120]. Similarly, for the conventional fracture toughness, the SENB tests were also conducted according to the guidance of ASTME399 [58] and done from previous work by Yu et al. [73, 119]. The SENB tests were conducted according to measure K_{IC} for the four rail steels, as a reference to validate K_{JC}. The dimensions and methodology for the SENB specimens are recorded in [104, 73, 114].

6.3.2.2 Indentation tests

Two sets of indentation tests were carried out. The first set were conducted using a 1.19mm tungsten carbide balls using an in-house-designed indentation test equipment as shown in Figure 6.1 for extracting the *L-h* curves of the rail steels. This is similar to the test conducted in Chapter 2 and 3.

The second set was conducted using the MTS universal testing machine similar to the test in Chapter 5. Six indentation cycles were conducted based on 6 different indentation depths. The indentation depths were 0.05, 0.1, 0.2, 0.3, 0.4, 0.5mm as a displacement-controlled experiment. Figure 6.1 shows the indentation test set-up and specimen dimensions used, which was for only one indentation test to be conducted in each specimen. In the end, 6 indentation tests were carried out on the different specimens for each indentation sizes, in 3 rounds of experimentation, resulting in a total of 72 indentation tests.

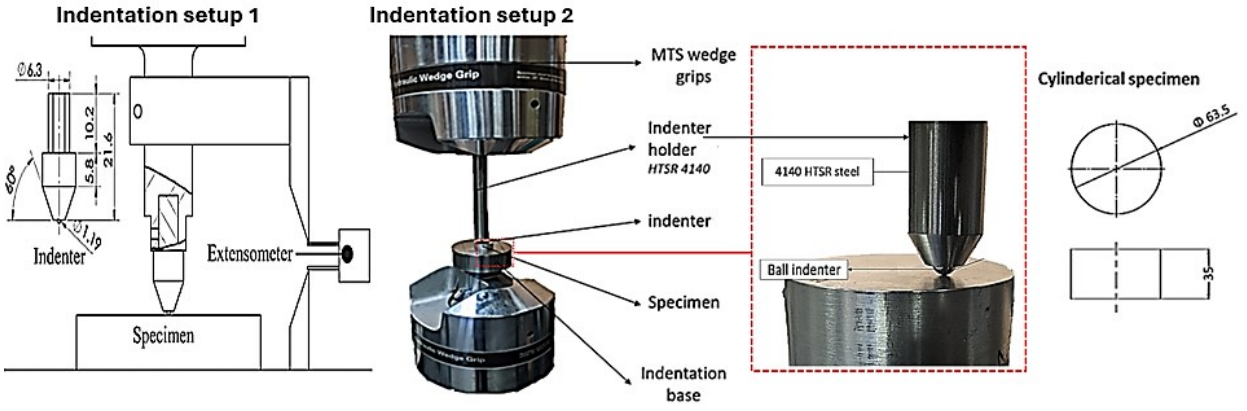

Figure 6.1. Schematics of the instrumented indentation test [275].

6.3.3 Hardness test

The hardness of the rail steels was accessed using the Brinell test from earlier study [183] following procedures in [113]. In this study, a simple approach based on the modification of H_{ECM} is introduced to aid in estimating hardness from indentation cycle. This modification for hardness estimation from H_{ECM} is also considered in this study, which requires an inclusion of Yu and Blanchard's suggestion [257] for estimating hardness for an elastic-perfectly plastic material.

In order to ascertain the modified hardness approach, an additional material AL2024-T351, which has similar fracture toughness with rail steels is also tested. The conventional hardness value is tested using a Rockwell hardness tester as shown in Figure 6.2. The Rockwell hardness test as defined in ASTM E-18 [259] for metallic materials was conducted using a MACROMET II tester, taking into consideration the type of Rockwell test needed for testing steels. The hardness test was conducted based on A scale hardness test procedure using a steel ball indenter of 1.588mm in diameter. In order to validate the hardness results of AL2024-T351, the Rockwell hardness tester was first calibrated using a standard test block of 34.7 HRB to ensure the hardness attained is accurate following the right procedure. To achieve this, an initial load application of 98.1N was first applied, followed by an additional load to result in a total of 981N, of which the permanent depth attained is translated to the hardness.

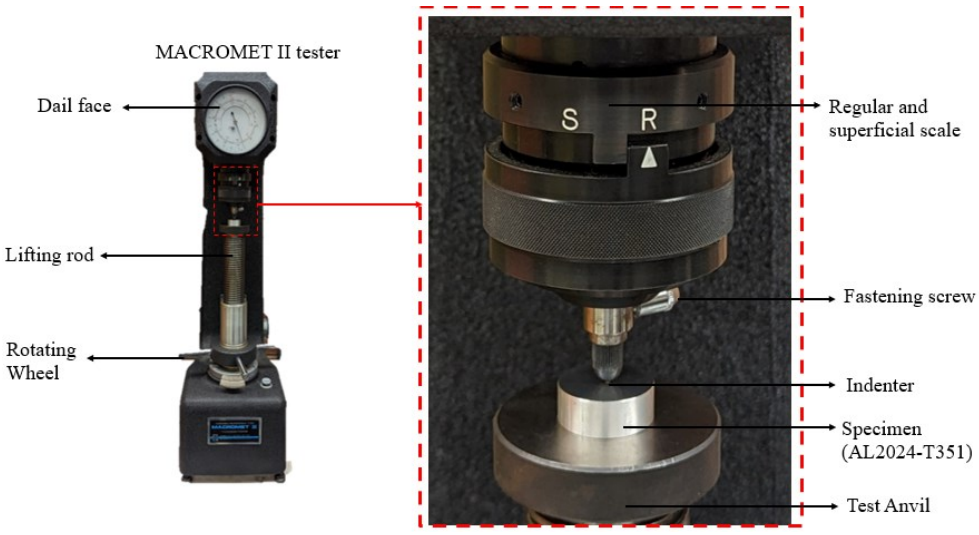

Figure 6.2 Rockwell hardness tester

6.4. Results and Discussions

6.4.1. Outcomes from destructive mechanical testing

A summary of the results from the tensile tests and SENB tests for the mechanical properties and fracture toughness of the rail streels are summarized in Table 6.2, which were conducted as the average values in the works of Yu et al. [73, 119] and Okocha et al. [237]. The variation in the K_{IC} in terms of the standard deviation (std. dev) is also expressed in Table 6.2.

Table 6.2 Mechanical properties and fracture toughness of the high strength rail steels.

Rail Name /Properties	Average E (MPa)	σ_y (MPa)	n	K_{IC} (MPa.m$^{0.5}$) (std. dev)
JP	200,000	820	0.086	39.42 (1.44)
EV	197,000	714	0.085	41.73 (1.29)
CZ	195,000	648	0.082	34.32 (0.62)
Rail #1	185,000	943	0.05009	42.28 (1.33)

The variations in K_{IC} can be attributed to the heat treatments and manufacturing procedures on the rail head resulting to non-uniformity of material properties across the depth of the rail but specifically to improve the properties of the main track at the contact location. This variation is minimal in CZ rail because of the uniformity in microstructure after the hot rolling process. i.e. no heat treatment procedure for surface hardening was done on CZ.

6.4.2 Mechanical properties via spherical indentation

6.4.2.1 Indentation loading-unloading curves

The indentation test consists of 6 load and unloading cycles as shown in Figure 6.3, which are used in estimating the Young's modulus and modulus degradation as seen in previous studies [183]. Each indentation is cycle is further used for yield strength estimation after a considerable indentation depth.

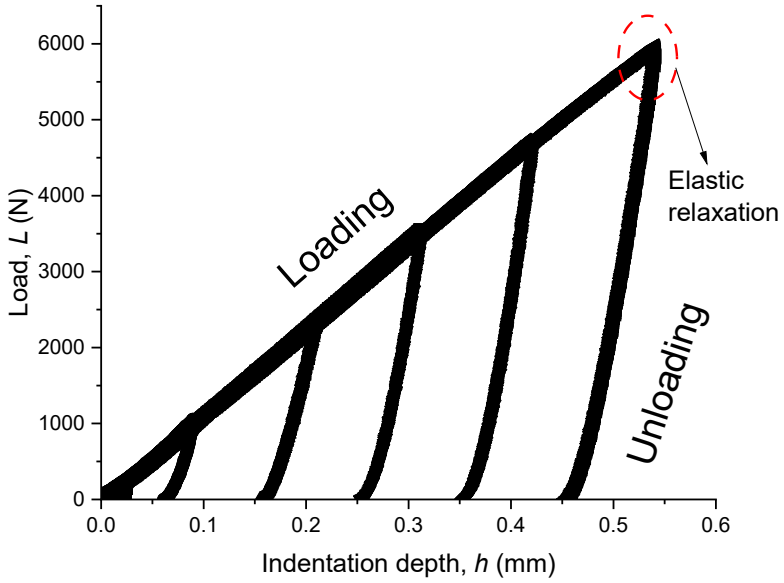

Figure 6.3 Spherical Indentation loading-unloading cycles using 3mm indenter size as an illustration.

6.4.2.2 Yield strength

For the determination of $\sigma_{y,ind}$ used for the spherical indentation as described in Eq. (5.3), the first derivatives as suggested in the works in [269-270] is implemented. The first derivative was used to indicate the change in slope between P- h/a_c curve showing shifts in different deformational stages. By implementing Eq. (5.3), P_y must be located at the point that translates to when an average yielding occurs around the indented substrate. According to previous chapter, the yielding point was found at the maxima point of the 1st derivative and is used in this current study for the high strength rail steels. Figure 6.4. Show the estimation of $\sigma_{y,ind}$ for the four high strength rail steels, where the initial portion of the average stress is truncated due to ISE during initial contact of the indenter with the substrate.

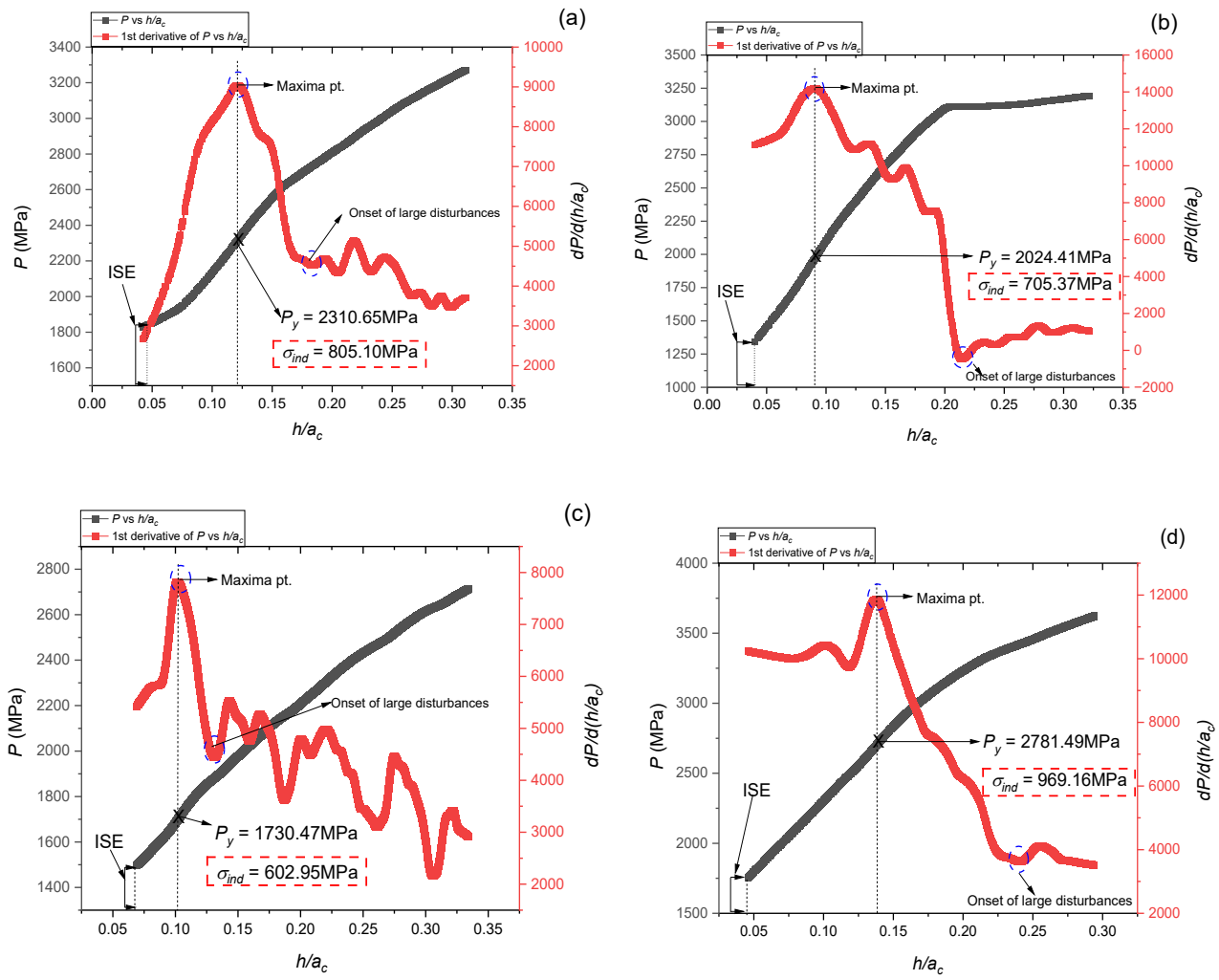

Figure 6.4. Yield strength estimation via spherical indentation using 3mm indenter as an illustration: *(a) JP, (b) EV, (c) CZ, and (d) R#1*

Using 4 different cycles, the average (Avg) and standard deviation (std dev) of the $\sigma_{y,ind}$ are expressed in table 6.3.

Table 6.3 Average and standard deviation of $\sigma_{y,ind}$ estimated via spherical indentation.

Yield strength, $\sigma_{y,ind}$ (MPa)	**1.19mm indenter size Avg (Std dev)**	**3mm indenter size Avg (Std dev)**
JP	839 (5.35)	807 (2.39)
EV	747 (6.15)	709 (2.25)
CZ	650 (1.48)	605 (3.61)
R#1	936 (8.31)	963 (5.38)

6.4.2.3 Brinell Hardness

As suggested in ASTEM E10 [259], the Brinell hardness methodology determines the hardness of the rail steel. In this study, instead of relying on test loads for Brinell hardness estimation, an alternative Brinell hardness was estimated along the depth of the rail steels in which Eq. (6.1a) is applied for all through the indentation load and projected diameter. At first, ISE phenomenon is experienced, followed by a relaxation of stresses due to flow stress effect from spherical indentation [81, 131, 183]. At further depth, the pressure in terms of Brinell hardness is seen to have an approximately steady value. This stability is used for the Brinell hardness estimation. Figure 6.5 describes the Brinell hardness across the depth of the rail steels showing little differences across indenter sizes but differences in rail steel types.

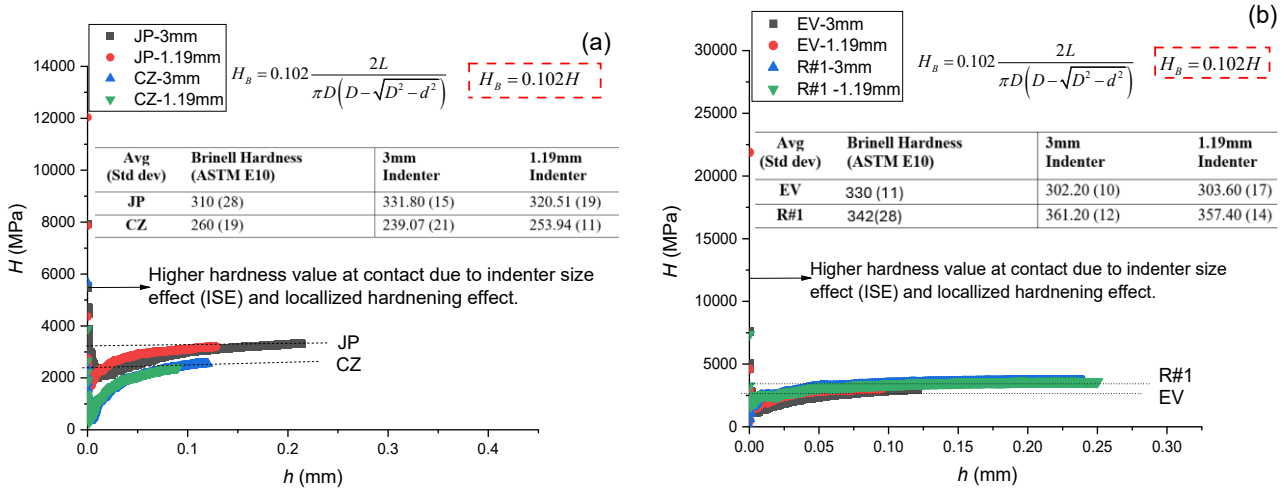

Figure 6.5 Brinell hardness estimation (a) JP and CZ, (b) EV and R#1

CZ rail steel from Figure 6.5(a) shows the least hardness because no surface treatment was applied after manufacture. Although JP and EV are deep head hardened, a relative difference is seen between both rail steels. Although, the chemical composition of all the rail steels is not known (for confidential purposes), it is possible that the cementite grains are affected differently below the eutectic point of the manufacturing phase.

6.4.2.4 H_{ECM} evolution and hardness estimation via H_{ECM}

A simple approach for Brinell hardness estimation is suggested without following the conventional hardness testing method, which can be advantageous for in-service evaluation and inspection. Following the approach of H_B estimation as seen in Figure 6.5, there is the tendency of having the condition of $\Delta H_B = 0$, hence we investigate to find the point where, $\frac{d(H_{ECM})}{d(a_c/R)} = H_{ECM}$ and then apply it to Eq. 6.1(b). Appendix 10 shows the difference between H_{ECM} -h/a_c with P-h/a_c, where κ is used as the fitting parameter for balancing the difference based on frictional effect originating from the tungsten carbide indenter and the rail steel.

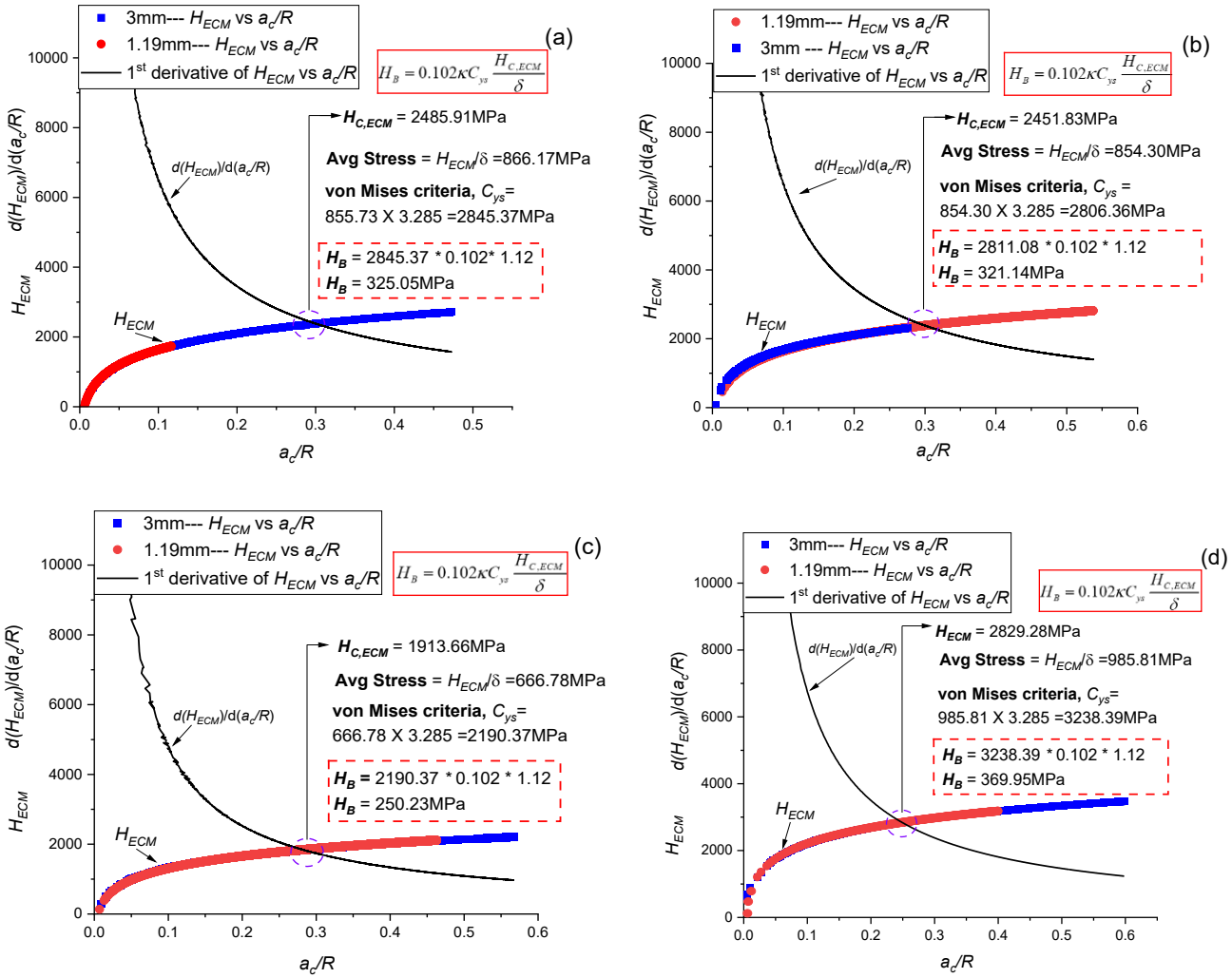

Figure 6.6 Brinell hardness estimation via 1st derivative of H_{ECM} vs a_c/R: (a) JP, (b) EV, (c) CZ, and (d) R#1

The Brinell hardness values estimated using Eq. 6.1(b) shows a close match with conventional Brinell hardness test with CZ having the lowest hardness and R#1 having the highest hardness values. The approach is also applied with another material (AL2024-T351) as seen in Fig A.10 (Appendix 11), which shows the estimated Brinell hardness for AL2024-T351 along with the values of the conventional Brinell hardness test. The similarity of H_{ECM} and a_c/R between indenter sizes as seen in Figure 6.6 also promotes the use of micro-indenters for material characterization as a non-destructive test adding to the advantage of spherical indentation to be used for structural integrity assessment, non-destructively.

6.4.3 K_{JC} estimation

As described in section 5.3.4, the L-h curve is converted to the H_{ECM}-h/a_c curve because of ISE from spherical indentation, from which the P_{CIP} and corresponding h/a_c are determined. Figure 6.7 shows the new virtual load (L') and virtual depth (h'') curves from h' =0.2mm – 0.05mm along with the estimation of A_{pl}, which is an advantage of using H_{ECM} for K_J estimation in contrast to P.

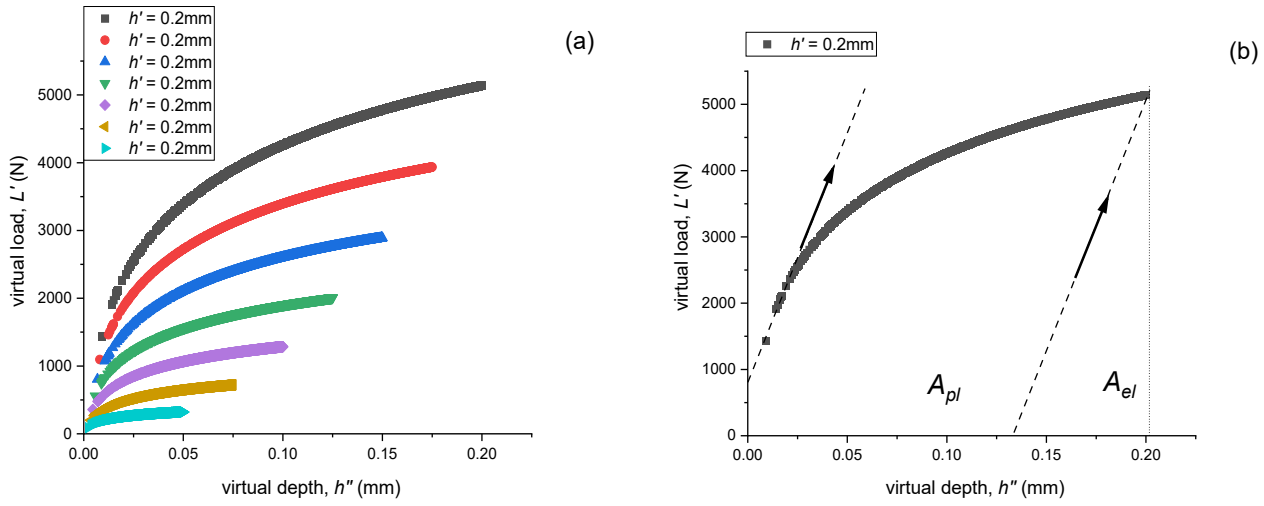

Figure 6.7 Virtual load-depth curve of a 3mm spherical indentation: (a) variation of virtual load (L') versus virtual depth (h'') with different h' values, and (b) estimation of A_{pl} for the curve in (a) with h' = 0.2mm

Following the procedures in section 3.6, Table 6.4 shows the virtual indentation parameters for the four different rail steels.

Table 6.4 Virtual indentation parameters for K_J estimation with η_{pl} = 0.96 for geometrical similarity with SENB

Rail	h'	a_c' (mm)	L' (N)	A_{pl} (mm)	J_e (N/mm)	J_p (N/mm)	J_c (N/mm)	K_J (MPa.m$^{0.5}$)
JP	0.200	0.517	2221.478	306.059	12.931	349.896	362.827	282.386
	0.175	0.452	1700.819	203.611	11.315	304.032	315.346	263.262
	0.150	0.388	1249.582	128.151	9.698	260.454	270.152	243.668
	0.125	0.323	867.765	74.537	8.082	218.145	226.227	222.980
	0.100	0.258	555.370	39.229	6.465	179.392	185.857	202.108
	0.075	0.194	312.395	16.428	4.849	133.553	138.403	174.408
	0.050	0.129	138.842	5.070	3.233	92.744	95.976	145.237
EV	0.200	0.616	2758.339	371.534	11.769	298.910	310.679	261.307
	0.175	0.539	2111.853	244.820	10.298	257.260	267.558	242.495
	0.150	0.462	1551.566	152.300	8.827	217.830	226.657	223.192
	0.125	0.385	1077.476	88.855	7.356	183.005	190.361	204.542
	0.100	0.308	689.585	46.204	5.885	148.689	154.574	184.316
	0.075	0.231	387.891	19.565	4.414	111.933	116.347	159.908
	0.050	0.154	172.396	7.877	2.942	101.399	104.341	151.434
CZ	0.200	1.036	6679.235	896.831	14.532	255.382	269.914	243.561
	0.175	0.906	5113.789	597.612	12.715	222.271	234.987	227.256
	0.150	0.777	3757.070	383.706	10.899	194.248	205.147	212.337
	0.125	0.647	2609.076	217.114	9.082	158.273	167.356	191.785
	0.100	0.518	1669.809	113.674	7.266	129.480	136.746	173.361
	0.075	0.388	939.267	48.670	5.449	98.555	104.004	151.189
	0.050	0.259	417.452	14.975	3.633	68.230	71.863	125.674
R#1	0.200	0.364	1323.959	200.770	13.185	463.602	476.786	323.710
	0.175	0.318	1013.656	135.438	11.536	408.480	420.016	303.828
	0.150	0.273	744.727	84.477	9.888	346.784	356.673	279.981
	0.125	0.227	517.171	49.489	8.240	292.548	300.789	257.114
	0.100	0.182	330.990	25.191	6.592	232.672	239.264	229.315
	0.075	0.136	186.182	10.750	4.944	176.526	181.471	199.709
	0.050	0.091	82.747	3.274	3.296	120.945	124.241	165.244

As seen from Table 6.4, J_P contributes intensively to the overall J-integral value showing the extent of plasticity in the indentation procedure for high strength rail steels. Figure 6.8(a) shows the estimated K_{JC} for the four rail steels while Figure 6.8(b) shows the relationship between K_{JC} and K_{IC} for the four high strength rail steels.

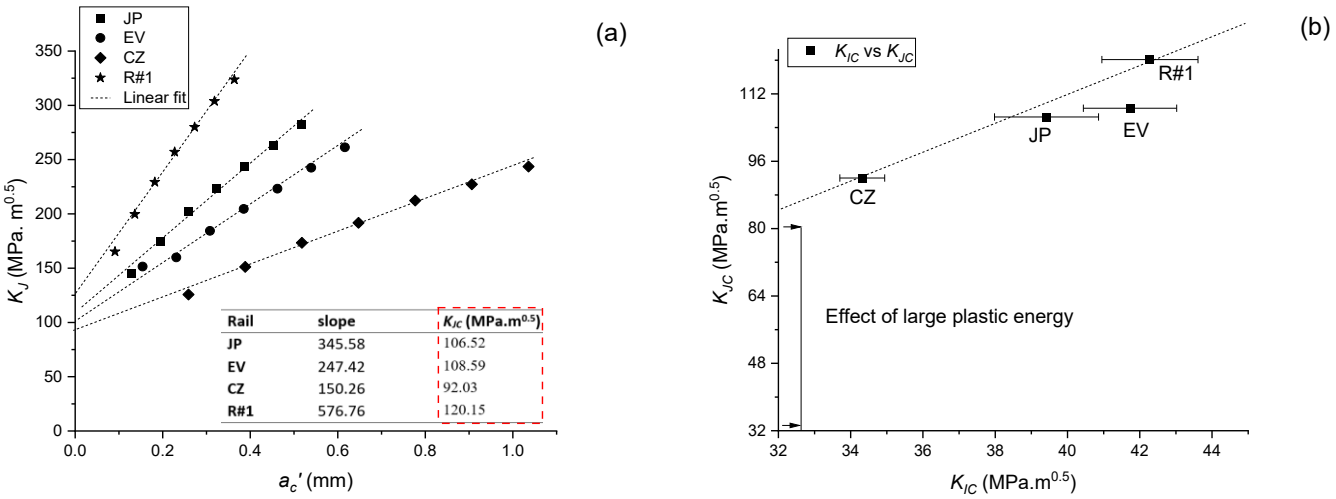

Figure 6.8 Fracture toughness measurement using modified LLA: (a) K_{JC} for the four rail steels, and (b) comparing K_{JC} and K_{IC}

6.4.4. Investigating the plastic J-integral energy for K_{JC} estimation

As seen in Table 6.4, the contribution of J_P to the overall J-integral is very large. Studies from Haggag and Nanstad [66] and Okocha. et. al [237] provide an interesting argument about fracture toughness estimated via spherical indentation using a critical fracture strain model. For the former [32], the indentation energy for fracture was taken as $\sqrt{\sigma_y l_o^* n}$ for A515 grade 70 carbon steel and AS33 grade B class 1 pressure vessel steel with an average of 216.3MPa.m$^{0.5}$ and 217.1MPa.m$^{0.5}$, respectively. However, for the latter [237], the indentation energy, which saw the replacement of n in [32] as $\sqrt{\sigma_y l_o^* \varepsilon_{eq}^{f,\eta_{avg}}}$ was greatly reduced for rail steels because of the influence of the average stress triaxiality (η_{avg}) at the contact region for the estimation of K_{JC}.

In this work, we propose that the influence of η_{avg} was not included in J_P in contrast to the steels analyzed by Haggag and Nanstad [233], where η_{avg} played a negligence role in evaluating the equivalent plastic strain for fracture initiation. Thus, we propose in Eq. 6.2, a new J-integral summation coming from the elastic and plastic components with η_{avg} effect included in J_P as a modification for estimating J-integral using the procedures found in Figure 6.8 as well as Eq. (4,1) and Eq. (4.2).

$$J = J_e + \frac{J_p}{f(\eta_{avg})} \tag{6.2}$$

Thus, for smooth tensile tests where η_{avg} is 0.33, $f(\eta_{avg})$ becomes 1 and plays no role in affecting the overall J-integral. Also, for pressure insensitive materials, η_{avg} effect becomes negligible. Thus, in order to attain the $f(\eta_{avg})$, η_{avg} is required. Figure. 6.9 shows an illustration of the stress triaxiality using ABAQUS software while Table 6.5 shows the stress triaxiality parameters.

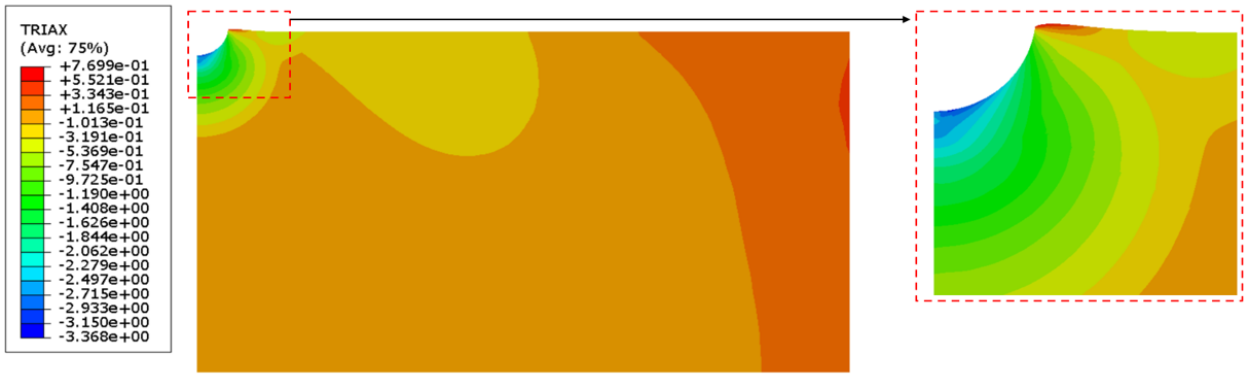

Figure 6.9 Stress triaxiality contour plot of the indentation testing [233]

Table 6.5 Stress triaxiality parameters

Stress triaxiality parameters	**JP**	**EV**	**CZ**	**R#5**
η_{avg} [216]	2.60	2.56	2.73	2.71
$f(\eta_{avg})$	8.979	8.731	9.810	9.680

Having known the estimates for $f(\eta_{avg})$ needed for the four rail steels, new virtual indentation parameters can be estimated, which has J_P effect reduced. Table 6.6 shows the new J-integral estimated from J_e and $J_P/f(\eta_{avg})$ contributions.

Table 6.6 New virtual indentation parameters for K_J estimation with $\eta_{pl} = 0.96$ for geometrical similarity with SENB

Rail	h'	a_c' (mm)	L' (N)	A_{pl} (mm)	J_e (N/mm)	$J_p/f(\eta_{avg})$ (N/mm)	J_c (N/mm)	K_J (MPa.m$^{0.5}$)
JP	0.200	0.517	2221.478	306.059	12.931	39.806	52.737	107.659
	0.175	0.452	1700.819	203.611	11.315	34.588	45.903	100.442
	0.150	0.388	1249.582	128.151	9.698	29.631	39.329	92.972
	0.125	0.323	867.765	74.537	8.082	24.817	32.899	85.033
	0.100	0.258	555.370	39.229	6.465	20.409	26.874	76.853
	0.075	0.194	312.395	16.428	4.849	15.194	20.043	66.370
	0.050	0.129	138.842	5.070	3.233	10.551	13.784	55.040
EV	0.200	0.616	2758.339	371.534	11.769	34.235	46.005	100.553
	0.175	0.539	2111.853	244.820	10.298	29.465	39.763	93.484
	0.150	0.462	1551.566	152.300	8.827	24.949	33.776	86.159
	0.125	0.385	1077.476	88.855	7.356	20.960	28.316	78.888
	0.100	0.308	689.585	46.204	5.885	17.030	22.915	70.966
	0.075	0.231	387.891	19.565	4.414	12.820	17.234	61.544
	0.050	0.154	172.396	7.877	2.942	11.614	14.556	56.561
CZ	0.200	1.036	6679.235	896.831	14.532	26.033	40.565	94.421
	0.175	0.906	5113.789	597.612	12.715	22.658	35.373	88.172
	0.150	0.777	3757.070	383.706	10.899	19.801	30.700	82.141
	0.125	0.647	2609.076	217.114	9.082	16.134	25.216	74.445
	0.100	0.518	1669.809	113.674	7.266	13.199	20.465	67.065
	0.075	0.388	939.267	48.670	5.449	10.046	15.496	58.358
	0.050	0.259	417.452	14.975	3.633	6.955	10.588	48.239
R#1	0.200	0.364	1323.959	200.770	13.185	47.893	61.077	115.860
	0.175	0.318	1013.656	135.438	11.536	42.198	53.735	108.673
	0.150	0.273	744.727	84.477	9.888	35.825	45.713	100.234
	0.125	0.227	517.171	49.489	8.240	30.222	38.462	91.942
	0.100	0.182	330.990	25.191	6.592	24.036	30.629	82.046
	0.075	0.136	186.182	10.750	4.944	18.236	23.180	71.376
	0.050	0.091	82.747	3.274	3.296	12.494	15.790	58.910

Similarly, the fracture toughness using the modified limit load analysis is measured. Figure 6.10 (a) shows the newly estimated K_{JC} for the four rail steels while Figure 6.10(b) shows the relationship between the new K_{JC} and K_{IC} for the four high strength rail steels.

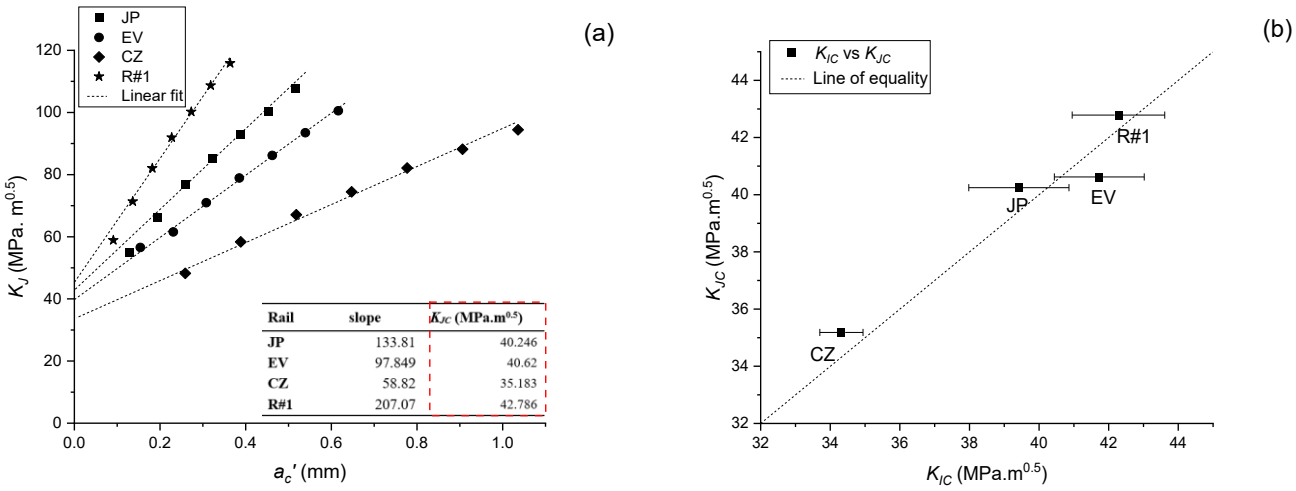

Figure 6.10 A new K_{JC} estimation using modified LLA with stress triaxiality effect: (a) K_{JC} for the four rail steels, and (b) comparing K_{JC} and K_{IC}

Figure 6.10. Shows that the K_{JC} estimated with the influence of the stress triaxiality reduces greatly and matches close to K_{IC} for the four rail steels. This proposition can only be used for high-strength steels and should be further looked into.

6.5 Conclusion

In this paper, fracture toughness and Brinell hardness were estimated and investigated for rail steels post manufactured with heat treatments using ECM approach and the modified limit load analysis, respectively. The main conclusions can be summarized as follows:

1. The pressure at the CIP according to von-Mises failure criteria is significant for estimating the required stress for initiating fracture in a structure containing defects.

2. The effect of ISE can be avoided by using the indentation hardness evolution from H_{ECM} for the estimation of A_{pl} needed for K_{JC}.

3. The size of the prior austenite grain size affects the fracture toughness in a relatively proportional relationship while the interlamellar spacing affects the strength as well as the wear resistance in an inversely proportional relationship.

4. H_{ECM} evolution can be used to estimate Brinell hardness for different metals by taking the 1st derivate and identifying the critical H_{ECM}, where $\frac{d(H_{ECM})}{d(a_c/R)} = H_{ECM}$.

5. For rail steels in this study, J_P is reduced greatly by the influence of stress triaxiality contributed from the loading condition as well as the material's deformation behaviour in compression but needs further study.

6. One indentation cycle can characterize rail steels in this study providing useful information and the strength, wear resistance and energy required to initiate or propagate fracture.

In conclusion, the modified limit load analysis was applied to rail steels, which have similar fracture toughness with AL2024-T351 of which a high J-integral value was observed originating from the plastic component of the J-integral. A major contribution was the inclusion of stress-triaxiality factor effect in the J-integral model due to the pressure-sensitivity of rail steels for fracture toughness measurement via spherical indentation. At this stage, the validity of using indentation hardness information (H_{ECM}) for fracture toughness information is not fully supported but needs further investigation as the definition of H_{ECM} originated for elastic-power law materials. Also, the use of H_{ECM} is only an approximation of the experimental data as the original experimental data from spherical indentation does not generate data that can be used to determine fracture toughness using the approach described in Chapter 4 majorly because of non-repetitive load-depth profiles from different indenter sizes due to ISE. In the end, a reasonable fracture toughness value and trend outcome was observed between different rail steels in comparison with standard fracture toughness value (SENB test) and it is suggested that further studies are explored towards the validity of using spherical indentation for fracture toughness estimation via the modified limit load analysis.

Chapter 7 Conclusions and Future Work

7.1 Conclusions

The ultimate goal of the research is to develop a simple, flexible indentation methodology that can be utilized practically as a non-destructive in-situ technique for the structural assessment of high strength rail steels. In this study, objectives of determining the mechanical properties and fracture toughness in a conventional destructive test were ascertained using purely indentation technique. Different non-destructive indentation testing methods were developed to estimate the fracture toughness of high-strength rail steels and aluminum AL2024-T351 (due to the similarity in fracture toughness value). The main contributions of this thesis can be summarized as follows.

- Mechanical properties such as the Young's modulus, yield strength, strain hardening exponent were attained for 9 high strength rail steels using spherical indentation. This was followed by developing a means of extracting a representative stress and strain similar to what is obtainable in a destructive smooth tensile test using appropriate analytical correlations.

- A new simple Brinell hardness measurement was developed for high strength rail steels and AL2024-T351 using a modification of spherical expansion cavity model (ECM). Favorable results were seen and can be used for categorizing different metallic materials. The Brinell hardness estimated for the high strength rail steels gave an insight to the wear resistance of the rail steels, which was supported by the lamella spacing within the rail's pearlite colonies.

- Fracture toughness measurement was developed using micromechanics approach via a modified critical fracture strain model for 9 high strength rail steels. The model proposes the influence of stress triaxiality not just on the equivalent plastic fracture strain for fracture initialization but also a combined influence on the characteristic distance within the microstructure. Prior austenite grain sizes of the rail steels were investigated, which saw a relative proportionality with fracture toughness. It was seen that the characteristic distance was estimated within the range of 5-7 prior austenite grain sizes, which influenced the

outcomes for fracture toughness via the modified critical fracture strain model. The modified critical fracture strain model proposes that fracture toughness can be estimated using smooth tensile or indentation test as long as the mechanical properties are measured along with consideration of stress triaxiality present at the tip of a sharp crack similar to what is experienced at the sharp crack tip of a single edged notch bend (SENB) specimen.

- Fracture toughness was also measured using a modified limit load analysis. The procedure compares a flat-end cylindrical indenter (a non-chamfered and a chamfered indenter at 45^{o}) and a spherical indenter, where estimation of the crack initiation point (CIP) via the yield strength is paramount to the limit of load and depth needed for fracture toughness estimation. The *J*-integral method was used by utilizing virtual indenters with varying virtual contact radii. The non-chamfered cylindrical indenter was abandoned for fracture toughness measurement because of the very high stress concentration experienced at the indenter's tip along with the high load requirements needed for indentation. The chamfered cylindrical indenter showed a lower stress concentration effect and was successfully used in estimating fracture toughness for AL2024-T351. The spherical indenter was used for the modified limit load analysis and saw the least stress concentration amongst all indenter type and was also successful in estimating the fracture toughness, thus had the lowest load requirement for any future indentation equipment. Comparison between the chamfered indenter and spherical indenter was investigated with preference with the spherical indenter due to lower indentation depth needed for fracture toughness along with less plastic zone development at the sub-surface of AL2024-T351 thus suggesting less damage effect when using micro-indenters. However, the spherical indenter posses a challenge with localized hardening at the inception of contact, also known as the indentation size effect (ISE) especially for small indenter sizes, which can make the chamfered indenter more favorable because the plastic zone size becomes larger for spherical indenters especially when very low depths are required.

- The modified limit load analysis was applied to four (4) high strength rail steels for fracture toughness estimation. A good trend was observed between the measured fracture toughness and the conventional fracture toughness (K_{IC}), however saw the measured fracture

toughness about 3 times the values in K_{IC}. A suggestion was provided as to the non-inclusion of stress triaxiality effect on the plastic component of J-integral along the contact region of indentation, which apparently saw the measured fracture toughness values close to K_{IC}

Hence, for a new rail track, fracture toughness can be estimated via indentation either using the modified critical fracture strain model or the modified limit load analysis. For the former, estimating the E_s, σ_{ys} and n_s is required and then relying on prior information from manufacturers about the average d^* for the estimation of l_o^*. With these parameters and using an η_{avg}, Eq. (3.17iii) can be utilized to estimate the fracture toughness provided C_m is taken as 3 as suggested using spherical indentation. For the latter (spherical or chamfered indenter), fracture toughness does not rely on any microstructural information but rather depends on the estimation of σ_{ys} with geometrical information about the contact radius and indentation depth and η_{pl}. With these parameters, J-integral can be estimated and thus, the critical stress intensity factor attained from J-integral can be estimated either using multiple indenter sizes or virtual indenter sizes from one indentation loading-unloading test.

7.2 Future work

In general, two methods were proposed for estimating fracture toughness of high strength rail steels and still needs more testing and validation before it can be employed for practical cases involving structural assessment of newly manufactured materials and alloys or inspection scenarios for in-service static equipment. The first non-destructive indentation approach is the use of the modified critical fracture strain model, which requires microstructural information, mechanical properties, and the stress triaxiality effect. More testing is needed for a range of steels that obey linear elastic fracture mechanics (LEFM) to elastic-plastic fracture mechanics (EPFM) steel materials.

The second non-destructive indentation approach is the use of a modified limit load analysis approach, which defines virtual indenters for attaining the limit virtual load, depth and contact radius needed for the application of J-integral before the plastic component of J-integral can be minimized to attain the critical value of apparent stress intensity factor.

In order to improve the above two testing methods, the following problems are recommended for future investigation:

- *Material categorization from the tip of spherical indentation:* In view that cracks do not form during indentation testing of ductile materials, it is difficult to determine if a newly developed material will obey LEFM or EPFM for the effect of pressure sensitivity or stress triaxiality to be included when measuring fracture toughness either via the critical fracture strain model or limit load analysis. Hence, the development of a verification approach for material categorization is essential before the implementation of the modified critical fracture strain model and/or limit load analysis approaches. A validation process should require testing different steels ranging from low-high strength with different levels of carbon contents.
- *Angle of chamfered flat-ended indenter effect:* In view that 45^{o} chamfered cylindrical indenter was successful for fracture toughness estimation via the modified limit load analysis, further investigation is needed on the effect of chamfered angle for different materials especially high strength rail steels. This is to examine the condition of the indenter remaining as a rigid material based on contact mechanics principles for high strength alloys and at the same time having the ability to measure fracture toughness effectively by negating the challenges of spherical indentation based on ISE phenomena. The right angle will effectively support non-destructive testing when the indenters are micro-sized.
- *Verification of the fracture toughness across Heat-treated rail head:* In this study, rail samples were extracted on the surface of contact on the rail head. However, head hardened rails has been shown to exhibit different fracture toughness from the surface to the core of the rail head. Thus further studies using the critical fracture strain model and/or the modified limit load analysis is needed to verify the facture toughness difference across the rail head from the surface to the sub-surface towards the core of the rail head.
- *Temperature effect:* In view that all the tests were carried out in ambient temperature, further studies will require testing the mechanical properties and fracture toughness in different temperatures especially at sub-zero critical temperatures (-50^{o}c). The possibility of constructing ductile-brittle transition temperature (DBTT) master curves between fracture toughness and temperature can be attained.

References

[1] R. B. King, “Elastic analysis of some punch problems for a layered medium,” Int. J. Solids Struct., vol. 23, no. 12, pp. 1657–1664, 1987, doi: 10.1016/0020-7683(87)90116-8.

[2] D. F. Cannon, K. Edel, S. L. Grassie, and K. Sawley, “Rail defects : an overview rails, stresses, rail failure and costs,” Fatigue & Fracture of Engineering Materials & Structures, vol. 26, no. 10, pp. 865-886, 2003

[3] E. M. Leishman, M. T. Hendry, and C. D. Martin, “Canadian main track derailment trends, 2001 to 2014,” Can. J. Civ. Eng., vol. 44, no. 11, pp. 927–934, 2017, doi: 10.1139/cjce-2017-0076.

[4] Transportation Safety Board of Canada, “Statistical summary: Rail transportation occurrences in 2018,” Transp. Saf. Board Canada, pp. 1–30, 2019, [Online]. Available: http://www.bst-tsb.gc.ca/eng/stats/aviation/2018/ssea-ssao-2018.html#1.0.

[5] Transport Safety Board of Canada, “Rail transportation safety investigation report R20W0031,” July 28, pp. 1–8, 2020.

[6] S. Subdivision and T. Yard, “Canadian National Freight Train M37231-05 Railway Investigation Report R13D0077 Derailment Canadian National Freight train M37231-05 Mile 144.4 , St-Laurent Subdivision Taschereau Yard , Montréal , Quebec,” no. November, 2013.

[7] R. Lunden and B. Paulsson, “Introduction to wheel–rail interface research. In Wheel–rail interface handbook ”, Woodhead Publishing, pp. 3-33, 2009.

[8] H. Zimmermann, Die Berechnung des Eisenbahnoberbaues. Ernst & Korn, 1888.

[9] Chang, W., Cai, X., & Wang, Q. (2021). “Dynamic characteristic difference of steel-spring floating slab track between single-carriage and multi-carriage models”. Noise & Vibration Worldwide, 52(6), 156-167.

[10] C. Esveld and C. Esveld, “Modern railway track” Zaltbommel, The Netherlands: MRT-productions. Vol. 383, 2001.

[11] M. Hetenyi, “Beams on elastic foundations: Theory with applications in the field of civil engineering,” University of Michigan Press, Ann Arbor, 1946.

[12] L. Fry´ba and C. R. Steele, “Vibration of Solids and Structures Under Moving Loads,” J. Appl. Mech., vol. 43, no. 3, pp. 524–524, 1976, doi: 10.1115/1.3423922.

[13] N. F. Doyle, “Railway Track Design: A Review of Current Practice”. Australian government publishing service, Canberra, 1980.

[14] J. García-Palacios, A. Samartín, and M. Melis, “Analysis of the railway track as a spatially periodic structure,” Proc. Inst. Mech. Eng. Part F J. Rail Rapid Transit, vol. 226, no. 2, pp. 113–123, 2012, doi: 10.1177/0954409711411609.

[15] A. C. Lamprea-Pineda, D. P. Connolly, and M. F. M. Hussein, “Beams on elastic foundations – A review of railway applications and solutions,” Transp. Geotech., vol. 33, 2022, doi: 10.1016/j.trgeo.2021.100696.

[16] L. Frýba, S. Nakagiri, and N. Yoshikawa, “Stochastic finite elements for a beam on a random foundation with uncertain damping under a moving force,” J. Sound Vib., vol. 163, no. 1, pp. 31–45, 1993, doi: 10.1006/jsvi.1993.1146.

[17] O. Orringer, Y. H. Tang, J. E. Gordon, D. Y. Jeong, J. M. Morris, and A. B. Perlman, “Crack propagation life of detail fractures in rails,” (No. DOT/FRA/ORD-88/13). United States. Department of Transportation. Federal Railroad Administration.1988.

[18] U. Zerbst, R. Lundén, K. O. Edel, and R. A. Smith, “Introduction to the damage tolerance behaviour of railway rails - a review,” Eng. Fract. Mech., vol. 76, no. 17, pp. 2563–2601, 2009, doi: 10.1016/j.engfracmech.2009.09.003.

[19] D. Li, J. Hyslip, T. Sussmann, and S. Chrismer, “Railway Geotechnics” Railway geotechnics. CRC Press, 2015.

[20] T. G. Johns, K. B. Davies, and D. P. McConnell, “Introduction To Stresses in Rails: Stresses in Midrail Regions.,” Transp. Res. Rec., no. 694, pp. 10–19, 1978.

[21] G. G. Sirata, H. G. Lemu, K. Waclawiak, and Y. D. Jelila, “Study of rail-wheel contact problem by analytical and numerical approaches,” IOP Conf. Ser. Mater. Sci. Eng., vol. 1201, no. 1, p. 012035, 2021, doi: 10.1088/1757-899x/1201/1/012035.

[22] K. L. Johnson, “Contact Mechanics”. Cambridge: Cambridge University Press, 1985.

[23] J. A. Greenwood, “Formulas for Moderately Elliptical Hertzian Contacts,” J. Tribol., vol. 107, no. 4, pp. 501–504, 1985, doi: 10.1115/1.3261116.

[24] J. J. Kalker, “Rolling Contact Phenomena: Linear Elasticity,” CISM Courses Lect., pp. 1–84, 2000, [Online]. Available: http://ta.twi.tudelft.nl/TWA_Reports/00/00-09bnew.pdf.

[25] F.W.Carter, “On the action of a locomotive driving wheel,” Proc. R. Soc. London. Ser. A, Contain. Pap. a Math. Phys. Character, vol. 112, no. 760, pp. 151–157, 1926, doi: 10.1098/rspa.1926.0100.

[26] B. An, P. Wang, J. Zhou, R. Chen, J. Xu, and B. Wu, “Applying two simplified ellipse-based tangential models to wheel-rail contact using three alternative nonelliptic adaptation approaches: A comparative study,” Math. Probl. Eng., vol. 2019, 2019, doi: 10.1155/2019/3478607.

[27] L. Baeza, S. Bruni, J. Giner-Navarro, and B. Liu, “A linear non-Hertzian unsteady tangential wheel-rail contact model,” Tribol. Int., vol. 181, 2023, doi: 10.1016/j.triboint.2023.108345.

[28] A. Kapoor, F. J. Franklin, S. K. Wong, and M. Ishida, “Surface roughness and plastic flow in rail wheel contact,” Wear, vol. 253, no. 1–2, pp. 257–264, 2002, doi: 10.1016/S0043-1648(02)00111-4.

[29] C. Madshus and A.M. Kaynia, “High speed railway lines in soft ground: Dynamic behaviour at critical train speed.” Journal of Sound and Vibration, vol. 231, no.3, pp. 689-701, 2000.

[30] R. W. Ogden, “Large Deformation Isotropic Elasticity - on the Correlation of Theory and Experiment for Incompressible Rubberlike Solids.,” Rubber Chem. Technol., vol. 46, no. 2, pp. 398–416, 1973, doi: 10.5254/1.3542910.

[31] R. von Mises, “Mechanik der festen {K}orper im plastisch deformation,” Zustand. Nachr. Ges. Wiss. Gottigen, vol. 1, p. 582, 1913, [Online]. Available: http://www.digizeitschriften.de/dms/resolveppn/?PID=GDZPPN002503697.

[32] E. Voce, “The relationship between stress and strain for homogeneous deformation,” J. Inst. Met., vol. 74, pp. 537–562, 1978.

[33] H. Swift, “Plastic instability under plane stress. Journal of the Mechanics and Physics of Solids, 1 (1), 1-18.,” 1952.

[34] H. Hollomon, “Tensile deformation.,” Aime Trans , vol. 12, no. (4), pp. 1–22, 1945.

[35] J. F. Brunel, E. Charkaluk, P. Dufrénoy, and F. Demilly, “Rolling contact fatigue of railways wheels: Influence of steel grade and sliding conditions,” Procedia Eng., vol. 2, no. 1, pp. 2161–2169, 2010, doi: 10.1016/j.proeng.2010.03.232.

[36] N. R. Services, I. Technologies, T. Nordco, and R. Services, “Nordco Rail Flaw Defects Identification Handbook,” FEBS J., vol. 281, no. 19, p. 4556, 2014, [Online]. Available: http://www.ncbi.nlm.nih.gov/pubmed/25270340.

[37] A. Zarembski, “Separating shelling or spalling,” Railw. Tie Assoc., 2016, [Online]. Available: https://www.rta.org/index.php?option=com_content&view=article&id=94:comprehensive-rail-and-track-related-research&catid=20:site-content.

[38] E. Magel, P. Mutton, A. Ekberg, and A. Kapoor, “Rolling contact fatigue, wear and broken rail derailments,” Wear, vol. 366–367, pp. 249–257, 2016, doi: 10.1016/j.wear.2016.06.009.

[39] J. Li, S. I. Doh, and R. Manogaran, “Detection and Maintenance for Railway Track Defects: A Review,” in IOP Conference Series: Earth and Environmental Science, 2023, vol. 1140, no. 1, doi: 10.1088/1755-1315/1140/1/012011.

[40] J. Sadeghi and A. Hasheminezhad, “Correlation between rolling noise generation and rail roughness of tangent tracks and curves in time and frequency domains,” Appl. Acoust., vol. 107, pp. 10–18, 2016, doi: 10.1016/j.apacoust.2016.01.006.

[41] L. Auersch, “Simple and fast prediction of train-induced track forces, ground and building vibrations,” Railw. Eng. Sci., vol. 28, no. 3, pp. 232–250, 2020, doi: 10.1007/s40534-020-00218-7.

[42] X. S. Jin, W. Li, Z. F. Wen, H. Y. Wang, and X. Z. Sheng, “An Investigation into Rail Corrugation, its Mechanisms and Effects on the Dynamic Behavior of Metro Trains and Tracks in China,” Int. J. Railw. Technol., vol. 5, no. 3, pp. 1–29, 2016, doi: 10.4203/ijrt.5.3.1.

[43] X. Du, X. Jin, G. Zhao, Z. Wen, and W. Li, “Rail Corrugation of High-Speed Railway Induced by Rail Grinding,” Shock Vib., vol. 2021, 2021, doi: 10.1155/2021/5546809.

[44] S. L. Grassie and J. A. Elkins, “Corrugation on North American transit lines,” Veh. Syst. Dyn., vol. 28, pp. 5–17, 1998.

[45] G. Diana, F. Cheli, S. Bruni, and A. Collina, “Experimental and numerical investigation on subway short pitch corrugation,” Veh. Syst. Dyn., vol. 29, no. SUPPL., pp. 234–245, 1998, doi: 10.1080/00423119808969562.

[46] A. Böhmer and T. Klimpel, “Plastic deformation of corrugated rails - A numerical approach using material data of rail steel,” Wear, vol. 253, no. 1–2, pp. 150–161, 2002, doi: 10.1016/S0043-1648(02)00094-7.

[47] X. Jin, X. Du, J. Guo, and D. Cui, “State of arts of research on rail grinding,” Xinan Jiaotong Daxue Xuebao/Journal Southwest Jiaotong Univ., vol. 45, no. 1, pp. 1–11, 2010, doi: 10.3969/j.issn.0258-2724.2010.01.001.

[48] R.E Peterson, “Stress Concentration Factors”. John Wiley & Sons, New York, 1974.

[49] S. Timoshenko and L.N. Goodier, “Theory of Elasticity”, 3rd ed. McGraw Hill, McGraw-Hill book company, Inc, New York, 1978.

[50] G. C. Sih and R. Muki, “Stress Analysis of Notch Problems,” J. Appl. Mech., vol. 46, no. 4, pp. 968–969, 1979, doi: 10.1115/1.3424707.

[51] J. Schijve, “Stress gradients around notches”. Fatigue of Eng. Materials and Structures, Vol.3, pp.325-338, 1981.

[52] H. Nisitani and N. A. Noda, “Stress concentration of a cylindrical bar with a V-shaped circumferential groove under torsion, tension or bending,” Eng. Fract. Mech., vol. 20, no. 5–6, pp. 743–766, 1984, doi: 10.1016/0013-7944(84)90084-5.

[53] N. Hironobu and N. Nao-Aki, “Stress concentration of a strip with double edge notches under tension or in-plane bending,” Eng. Fract. Mech., vol. 23, no. 6, pp. 1051–1065, 1986, doi: 10.1016/0013-7944(86)90147-5.

[54] G. R. Irwin, “Analysis of Stresses and Strains Near the End of a Crack Traversing a Plate,” J. Appl. Mech., vol. 24, no. 3, pp. 361–364, 1957, doi: 10.1115/1.4011547.

[55] M. L. Williams, “On the Stress Distribution at the Base of a Stationary Crack,” J. Appl. Mech., vol. 24, no. 1, pp. 109–114, 1957, doi: 10.1115/1.4011454.

[56] T. L. Anderson, “Fracture Mechanics: Fundamentals and Applications,” Fourth Edition (4th ed.). Boca Raton, CRC Press, 2017. https://doi.org/10.1201/9781315370293

[57] P. W. Bridgman, “Studies in Large Plastic Flow and Fracture - With Special Emphasis on the Effects of Hydrostatic Pressure,” Cambridge, MA and London, England: Harvard University Press, 1964. https://doi.org/10.4159/harvard.9780674731349

[58] ASTM Standard, “Standard E399: Standard Test Method for Linear-Elastic Plane-Strain Fracture Toughness KIC of Metallic Materials,” Annu. B. ASTM Stand., p. 33, 2009.

[59] F. Yu, “New Destructive and Non-Destructive Methods to Quantify Fracture Toughness of High-Strength Rail Steels,” Ph.D. Thesis, University of Alberta Libraries 2017. https://doi.org/10.7939/R39G5GT5B

[60] A. A. Griffits, “The phenomena of rupture and flow in solids,” Masinovedenie, no. 1, pp. 9–14, 1995, doi: 10.1098/rsta.1921.0006.

[61] R. O. Ritchie, W. L. Server, and R. A. Wullaert, “Critical fracture stress and fracture strain models for the prediction of lower and upper shelf toughness in nuclear pressure vessel steels,” Metall. Trans. A, vol. 11, no. 2, p. 359, 1980, doi: 10.1007/BF02660643.

[62] E. Orowan, “Fracture and strength of solids,” Reports Prog. Phys., vol. 12, no. 1, pp. 185–232, 1949, doi: 10.1088/0034-4885/12/1/309.

[63] J. F. Knott, “Mechanics and mechanisms of large-scale brittle fracture in structural metals,” Mater. Sci. Eng., vol. 7, pp. 1-36, 1971. 10.1016/j.engfracmech.2018.08.019.

[64] H.A Francis, “Phenomenological Analysis of Plastic Spherical Indentation,” Trans. ASME J. Eng. Mater. Technol., vol. 3, no.98, pp. 272-281, 1976. https://doi.org/10.1115/1.3443378

[65] F. M. Haggag, R. K. Nanstad, J. T. Hutton, D. L. Thomas, and R. L. Swain, “Use of automated ball indentation testing to measure flow properties and estimate fracture toughness in metallic materials,” ASTM Spec. Tech. Publ., no. 1092, pp. 188–208, 1990, doi: 10.1520/stp25039s.

[66] F. M. Haggag and R. K. Nanstad, “Estimating fracture toughness using tension or ball indentation tests and a modified critical strain model,” Am. Soc. Mech. Eng. Press. Vessel. Pip. Div. PVP, vol. 170, pp. 41–46, 1989.

[67] J. Rice, “MATHEMATICAL ANALYSIS IN THE MECHANICS OF FRACTURE,” in Fracture:An Advanced Treatise, vol. 2, 1968, p. 153.

[68] J. A. Begley and J. D. Landes, “The J Integral as a Fracture Criterion,” in ASTM Special Technical Publication, 1972, vol. STP 514, pp. 1–20, doi: 10.1520/STP38816S.

[69] ASTM Standard E1820, “Standard Test Method for Measurement of Fracture Toughness,” ASTM B. Stand., no. January, pp. 1–54, 2013, doi: 10.1520/E1820-13.

[70] A. G. Miller, “Review of limit loads of structures containing defects,” Int. J. Press. Vessel. Pip., vol. 32, no. 1–4, pp. 197–327, 1988, doi: 10.1016/0308-0161(88)90073-7.

[71] R. B. King, “Elastic analysis of some punch problems for a layered medium,” Int. J. Solids Struct., vol. 23, no. 12, pp. 1657–1664, 1987, doi: 10.1016/0020-7683(87)90116-8.

[72] F. Yu, P. Y. B. Jar, and M. T. Hendry, “Indentation for fracture toughness estimation of high-strength rail steels based on a stress triaxiality-dependent ductile damage model,” Theor. Appl. Fract. Mech., vol. 94, pp. 10–25, 2018, doi: 10.1016/j.tafmec.2018.01.003.

[73] F. Yu, P. Y. B. Jar, M. T. Hendry, C. Jar, and K. Nishanth, “Fracture toughness estimation for high-strength rail steels using indentation test,” Eng. Fract. Mech., vol. 204, pp. 469–481, 2018, doi: 10.1016/j.engfracmech.2018.10.030.

[74] E. Martínez-Pañeda, T. E. García, and C. Rodríguez, “Fracture toughness characterization through notched small punch test specimens,” Mater. Sci. Eng. A, vol. 657, pp. 422–430, 2016, doi: 10.1016/j.msea.2016.01.077.

[75] J. B. Ju, J. il Jang, and D. Kwon, “Evaluation of fracture toughness by small-punch testing techniques using sharp notched specimens,” Int. J. Press. Vessel. Pip., vol. 80, no. 4, pp. 221–228, 2003, doi: 10.1016/S0308-0161(03)00042-5.

[76] U. Kaya and E. Schmidova, “Spherical indentation approach to determine mechanical properties of Hadfield’s steel,” Met. 2016 - 25th Anniv. Int. Conf. Metall. Mater. Conf. Proc., pp. 730–734, 2016.

[77] F. M. Haggag, R. K. Nanstad, and D. N. Braski, “Structural integrity evaluation based on an innovative field indentation microprobe,” Am. Soc. Mech. Eng. Press. Vessel. Pip. Div. PVP, vol. 170, pp. 101–107, 1989.

[78] W. Nsengiyumva, S. Zhong, J. Lin, Q. Zhang, J. Zhong, and Y. Huang, “Advances, limitations and prospects of nondestructive testing and evaluation of thick composites and sandwich structures: A state-of-the-art review,” Compos. Struct., vol. 256, 2021, doi: 10.1016/j.compstruct.2020.112951.

[79] P. M. Palermo, “An Overview of Structural Integrity Technology,” Ship Structure Symposium, Washington, D.C., October 6-8, 1975.

[80] B. Raj, T. Jayakumar, and B. P. C. Rao, “Non-destructive testing and evaluation for structural integrity,” Sadhana, vol. 20, no. 1, pp. 5–38, 1995, doi: 10.1007/BF02747282.

[81] A. S. Hamada, F. M. Haggag, and D. A. Porter, “Non-destructive determination of the yield strength and flow properties of high-manganese twinning-induced plasticity steel,” Mater. Sci. Eng. A, vol. 558, pp. 766–770, 2012, doi: 10.1016/j.msea.2012.08.066.

[82] C. Moussa, O. Bartier, X. Hernot, G. Mauvoisin, J. M. Collin, and G. Delattre, “Mechanical characterization of carbonitrided steel with spherical indentation using the average representative strain,” Mater. Des., vol. 89, pp. 1191–1198, 2016, doi: 10.1016/j.matdes.2015.10.067.

[83] M. Beghini, L. Bertini, and V. Fontanari, “Evaluation of the stress-strain curve of metallic materials by spherical indentation,” Int. J. Solids Struct., vol. 43, no. 7–8, pp. 2441–2459, 2006, doi: 10.1016/j.ijsolstr.2005.06.068.

[84] O. Bartier and X. Hernot, “Phenomenological study of parabolic and spherical indentation of elastic-ideally plastic material,” Int. J. Solids Struct., vol. 49, no. 14, pp. 2015–2026, 2012, doi: 10.1016/j.ijsolstr.2012.04.005.

[85] D. TABOR, “A simple theory of static and dynamic hardness,” Proc. R. Soc. London. Ser. A. Math. Phys. Sci., vol. 192, no. 1029, pp. 247–274, 1948, doi: 10.1098/rspa.1948.0008.

[86] E. C. Jeon, J. Y. Kim, M. K. Baik, S. H. Kim, J. S. Park, and D. Kwon, “Optimum definition of true strain beneath a spherical indenter for deriving indentation flow curves,” Mater. Sci. Eng. A, vol. 419, no. 1–2, pp. 196–201, 2006, doi: 10.1016/j.msea.2005.12.012.

[87] H. Lee, J. H. Lee, and G. M. Pharr, “A numerical approach to spherical indentation techniques for material property evaluation,” J. Mech. Phys. Solids, vol. 53, no. 9, pp. 2037–2069, 2005, doi: 10.1016/j.jmps.2005.04.007.

[88] D. R. Barbadikar, A. R. Ballal, D. R. Peshwe, J. Ganeshkumar, K. Laha, and M. D. Mathew, “Investigation on mechanical properties of P92 steel using ball indentation technique,” Mater. Sci. Eng. A, vol. 624, pp. 92–101, 2015, doi: 10.1016/j.msea.2014.11.075.

[89] F. Wang, J. Zhao, N. Zhu, and Z. Li, “A comparative study on Johnson-Cook constitutive modeling for Ti-6Al-4V alloy using automated ball indentation (ABI) technique,” J. Alloys Compd., vol. 633, pp. 220–228, 2015, doi: 10.1016/j.jallcom.2015.01.284.

[90] H. R. Ammar, F. M. Haggag, A. S. Alaboodi, and F. A. Al-Mufadi, “Nondestructive measurements of flow properties of nanocrystalline Al-Cu-Ti alloy using Automated Ball Indentation (ABI) technique,” Mater. Sci. Eng. A, vol. 729, pp. 477–486, 2018, doi: 10.1016/j.msea.2018.05.089.

[91] T. S. Byun, J. H. Hong, F. M. Haggag, K. Farrell, and E. H. Lee, “Measurement of through-the-thickness variations of mechanical properties in SA508 Gr.3 pressure vessel steels using ball indentation test technique,” Int. J. Press. Vessel. Pip., vol. 74, no. 3, pp. 231–238, 1997, doi: 10.1016/S0308-0161(97)00114-2.

[92] J. M. Collin, G. Mauvoisin, and P. Pilvin, “Materials characterization by instrumented indentation using two different approaches,” Mater. Des., vol. 31, no. 1, pp. 636–640, 2010, doi: 10.1016/j.matdes.2009.05.043.

[93] J. M. Collin, G. Mauvoisin, P. Pilvin, and R. El Abdi, “Use of spherical indentation data changes to materials characterization based on a new multiple cyclic loading protocol,” Mater. Sci. Eng. A, vol. 488, no. 1–2, pp. 608–622, 2008, doi: 10.1016/j.msea.2008.01.041.

[94] Ian N. Sneddon, “The relation between load and penetration in the axisymmetric Boussinesq problem for a punch of arbitrary profile,” Int. J. Eng. Sci., vol. 3, no. 1, pp. 47–57, 1965.

[95] R. Solids, P. Chemistry, and S. G. Taylor, “A simple theory of static and dynamic hardness,” Proc. R. Soc. London. Ser. A. Math. Phys. Sci., vol. 192, no. 1029, pp. 247–274, 1948, doi: 10.1098/rspa.1948.0008.

[96] M. F. Doerner and W. D. Nix, “A method for interpreting the data from depth-sensing indentation instruments,” J. Mater. Res., vol. 1, no. 4, pp. 601–609, 1986, doi: 10.1557/JMR.1986.0601.

[97] W. C. Oliver and G. M. Pharr, “An improved technique for determining hardness and elastic modulus using load and displacement sensing indentation experiments,” J. Mater. Res., vol. 7, no. 6, pp. 1564–1583, 1992, doi: 10.1557/jmr.1992.1564.

[98] W. C. Oliver and F. R. Brotzen, “On the generality of the relationship among contact stiffness, contact area, and elastic modulus during indentation,” J. Mater. Res., vol. 7, no. 3, pp. 613–617, 1992, doi: 10.1557/JMR.1992.0613.

[99] S. Biwa and B. Storåkers, “An analysis of fully plastic Brinell indentation,” J. Mech. Phys. Solids, vol. 43, no. 8, pp. 1303–1333, 1995, doi: 10.1016/0022-5096(95)00031-D.

[100] E. G. Herbert, G. M. Pharr, W. C. Oliver, B. N. Lucas, and J. L. Hay, “On the measurement of stress-strain curves by spherical indentation,” Mater. Res. Soc. Symp., vol. 649, p. Q3.4.1-Q3.4.6, 2001, doi: 10.1557/proc-649-q3.4.

[101] A. R. H. Midawi, C. H. M. Simha, M. A. Gesing, and A. P. Gerlich, “Elastic-plastic property evaluation using a nearly flat instrumented indenter,” Int. J. Solids Struct., vol. 104–105, pp. 81–91, 2017, doi: 10.1016/j.ijsolstr.2016.09.036.

[102] A. F. Elmisteri, F. M. Shuaeib, and A. R. H. Midawi, “Mechanical properties evaluation for engineering materials utilizing instrumented indentation: Finite element modelling approach,” J. Mech. Eng. Sci., vol. 15, no. 1, pp. 7671–7683, 2021, doi: 10.15282/jmes.15.1.2021.05.0605.

[103] D. J. Shuman, A. L. M. Costa, and M. S. Andrade, “Calculating the elastic modulus from nanoindentation and microindentation reload curves,” Mater. Charact., vol. 58, no. 4, pp. 380–389, 2007, doi: 10.1016/j.matchar.2006.06.005.

[104] F. M. Xue, F. G. Li, J. Li, and M. He, “Strain energy density method for estimating fracture toughness from indentation test of 0Cr12Mn5Ni4Mo3Al steel with Berkovich indenter,” Theor. Appl. Fract. Mech., vol. 61, no. 1, pp. 66–72, 2012, doi: 10.1016/j.tafmec.2012.08.008.

[105] A. Lenwari, P. Albrecht, and M. Albrecht, “SED method of measuring yield strength of adhesives and other materials,” J. ASTM Int., vol. 2, no. 10, pp. 377–394, 2005, doi: 10.1520/JAI12954.

[106] I. J. Spary, A. J. Bushby, and N. M. Jennett, “On the indentation size effect in spherical indentation,” Philos. Mag., vol. 86, no. 33-35 SPEC. ISSUE, pp. 5581–5593, 2006, doi: 10.1080/14786430600854988.

[107] J. R. Matthews, “Indentation hardness and hot pressing,” Acta Metall., vol. 28, no. 3, pp. 311–318, 1980, doi: 10.1016/0001-6160(80)90166-2.

[108] W. Yan, Q. Sun, and P. D. Hodgson, “Determination of plastic yield stress from spherical indentation slope curve,” Mater. Lett., vol. 62, no. 15, pp. 2260–2262, 2008, doi: 10.1016/j.matlet.2007.11.062.

[109] S. Yang, Z. Yang, and X. Ling, “Fracture toughness estimation of ductile materials using a modified energy method of the small punch test,” J. Mater. Res., vol. 29, no. 15, pp. 1675–1680, 2014, doi: 10.1557/jmr.2014.205.

[110] D. Ma, W. O. Chung, J. Liu, and J. He, “Determination of Young’s modulus by nanoindentation,” Sci. China, Ser. E Technol. Sci., vol. 47, no. 4, pp. 398–408, 2004, doi: 10.1360/03ye0590.

[111] N. Huber, D. Munz, and C. Tsakmakis, “Determination of Young’s modulus by spherical indentation.” Journal of materials research, vol. 9, no .12, pp.2459-2469, 1997

[112] J. E. Zorzi and C. A. Perottoni, “Estimating Young’s modulus and Poisson’s ratio by instrumented indentation test,” Mater. Sci. Eng. A, vol. 574, pp. 25–30, 2013, doi: 10.1016/j.msea.2013.03.008.

[113] ASTM E10-18, “Standard Test Method for Brinell Hardness of Metallic Materials,” 2012.

[114] ASTM, “Standard Practice for Instrumented Indentation Testing,” 2007.

[115] J. B. Pethicai, R. Hutchings, and W. C. Oliver, “Hardness measurement at penetration depths as small as 20 nm,” Philos. Mag. A Phys. Condens. Matter, Struct. Defects Mech. Prop., vol. 48, no. 4, pp. 593–606, 1983, doi: 10.1080/01418618308234914.

[116] T. Zhang, S. Wang, and W. Wang, “A comparative study on fracture toughness calculation models in spherical indentation tests (SITs) for ductile metals,” Int. J. Mech. Sci., vol. 160, pp. 114–128, 2019, doi: 10.1016/j.ijmecsci.2019.06.035.

[117] Oliver.W.C. and Pharr.G.W, “Measurement of hardness and elastic modulus by instrumented indentation : Advances in understanding and refinements to methodology,” J. Mater. Res., vol. 19, no. 1, pp. 3–20, 2004.

[118] R. Hill, B. Storåkers and A. B. Zdunek, “A theoretical study of the Brinell hardness test,” Proc. R. Soc. London. A. Math. Phys. Sci., vol. 423, no. 1865, pp. 301–330, 1989, doi: 10.1098/rspa.1989.0056.

[119] F. Yu, P. Y. B. Jar, and M. Hendry, “Fracture behaviour at the sharp notch tip of high strength rail steels – Influence of stress triaxiality,” Eng. Fract. Mech., vol. 178, pp. 184–200, 2017, doi: 10.1016/j.engfracmech.2017.04.034.

[120] ASTM E8/E8M, “Standard Test Methods for Tension Testing of Metallic Materials,” 2013. [Online]. Available: https://www.astm.org/e0008_e0008m-22.html.

[121] S. Urata, R. Funahashi, T. Mihara, A. Kosuga, and N. Miyasou, “Mechanical properties of oxide materials,” Int. Conf. Thermoelectr. ICT, Proc., pp. 153–156, 2007, doi: 10.1109/ICT.2007.4569446.

[122] T. Mihara, S. Nomura, M. Akino, and K. Yamanaka, “Relations between Crack Opening Behavior and Crack Tip Diffraction Wave,” Proc. 1992 Annu. Meet. JSME/MMD, vol. 2002, no. 0, pp. 517–518, 2002, doi: 10.1299/jsmezairiki.2002.0_517.

[123] Y. Bai, X. Teng, and T. Wierzbicki, “On the application of stress triaxiality formula for plane strain fracture testing,” J. Eng. Mater. Technol., vol. 131, no. 2, pp. 0210021–02100210, 2009, doi: 10.1115/1.3078390.

[124] ASTM E2546-15, “Standard Practice for Instrumented Indentation Testing,” ASTM B. Stand., vol. 1, no. December, pp. 1–23, 2015, doi: 10.1520/E2546-15.

[125] R. V. Prakash, “In-situ damage evaluation using ball indentation test method,” ASME Int. Mech. Eng. Congr. Expo. Proc., vol. 12, pp. 1–6, 2010, doi: 10.1115/IMECE2010-38068.

[126] ASTM A1-00, “Standard Specification for Carbon Steel Tee Rails A 1-100,” ASTM International, 2006.

[127] J. G. Swadener, E. P. George, and G. M. Pharr, “The correlation of the indentation size effect measured with indenters of various shapes,” J. Mech. Phys. Solids, vol. 50, no. 4, pp. 681–694, 2002, doi: 10.1016/S0022-5096(01)00103-X.

[128] G. M. Pharr, E. G. Herbert, and Y. Gao, “The indentation size effect: A critical examination of experimental observations and mechanistic interpretations,” Annu. Rev. Mater. Res., vol. 40, pp. 271–292, 2010, doi: 10.1146/annurev-matsci-070909-104456.

[129] G. Z. Voyiadjis and M. Yaghoobi, “Review of nanoindentation size effect: Experiments and atomistic simulation,” Crystals, vol. 7, no. 10, 2017, doi: 10.3390/cryst7100321.

[130] W. D. Nix and H. Gao, “Indentation size effects in crystalline materials: a law for strain gradient plasticity. Journal of the Mechanics and Physics of Solids,” vol. 46, no. 3, PP. 411-425, 1998.

[131] M. Yetna N’Jock, D. Chicot, X. Decoopman, J. Lesage, J. M. Ndjaka, and A. Pertuz, “Mechanical tensile properties by spherical macroindentation using an indentation strain-hardening exponent,” Int. J. Mech. Sci., vol. 75, no. 33, pp. 257–264, 2013, doi: 10.1016/j.ijmecsci.2013.07.008.

[132] Y. J. Park and G. M. Pharr, “Nanoindentation with spherical indenters: Finite element studies of deformation in the elastic-plastic transition regime,” Thin Solid Films, vol. 447–448, pp. 246–250, 2004, doi: 10.1016/S0040-6090(03)01102-7.

[133] S. Dj Mesarovic, N. A. Fleck, and B. D. SINISA MESAROVICt, “Spherical Indentation of Elastic-Plastic Solids,” Source Proc. Math. Phys. Eng. Sci., vol. 455, no. January 1998, pp. 2707–2728, 1987, [Online]. Available: http://www.jstor.org/stable/53493%5Cnhttp://www.jstor.org/page/info/about/policies/terms.jsp%5Cnhttp://www.jstor.org.

[134] I. Pane and E. Blank, “Role of plasticity on indentation behavior: Relations between surface and subsurface responses,” Int. J. Solids Struct., vol. 43, no. 7–8, pp. 2014–2036, 2006, doi: 10.1016/j.ijsolstr.2005.08.010.

[135] B. Taljat and G. M. Pharr, “Development of pile-up during spherical indentation of elastic-plastic solids,” Int. J. Solids Struct., vol. 41, no. 14, pp. 3891–3904, 2004, doi: 10.1016/j.ijsolstr.2004.02.033.

[136] Y. Tirupataiah and G. Sundararajan, “On the constraint factor associated with the indentation of work-hardening materials with a spherical ball,” Metall. Trans. A, vol. 22, no. 10, pp. 2375–2384, 1991, doi: 10.1007/BF02665003.

[137] Z. Chunyu, Z. Yulong, C. Youbin, C. Nanfeng, and C. Lei, “Understanding indentation-induced elastic modulus degradation of ductile metallic materials,” Mater. Sci. Eng. A, vol. 696, pp. 445–452, 2017, doi: 10.1016/j.msea.2017.04.094.

[138] A. Leitner, V. Maier-Kiener, and D. Kiener, “Essential refinements of spherical nanoindentation protocols for the reliable determination of mechanical flow curves,” Mater. Des., vol. 146, pp. 69–80, 2018, doi: 10.1016/j.matdes.2018.03.003.

[139] F. Yu, P. Y. B. Jar, and M. T. Hendry, “Constitutive analysis of pressure-insensitive metals under axisymmetric tensile loading: A stress triaxiality-dependent plasticity damage model,” Int. J. Mech. Sci., vol. 142–143, pp. 21–32, 2018, doi: 10.1016/j.ijmecsci.2018.04.035.

[140] P.P. Nanekar and B. K. Shah, “Characterization of Material Poperties by ultrasonics,” Natl. Semin. Non-Destructive Eval., no. 249, pp. 25–38, 2003.

[141] Y. Chen, C. Zhang, and C. Varé, “An extended GTN model for indentation-induced damage,” Comput. Mater. Sci., vol. 128, pp. 229–235, 2017, doi: 10.1016/j.commatsci.2016.11.043.

[142] T. W. Clyne and J. E. Campbell, “Indentation Plastometry,” in Testing of the Plastic Deformation of Metals, vol. 1, Cambridge University Press, 2021, pp. 148–191.

[143] C. P. L. Barkan, C. T. Dick, and R. Anderson, “Hazardous Materials Transportation Risk Materials Release Data and Analysis,” Transp. Res. Rec., no. 03, pp. 64–74, 2001.

[144] X. Liu, M. R. Saat, P. Christopher, and L. Barkan, “Analysis of Causes of Major Train Derailment and Their Effect on Accident Rates,” Transp. Res. Rec. 2289.1, no. December 2012, pp. 154–163, 2015.

[145] S. Fallah Nafari, M. Gül, M. T. Hendry, D. Otter, and J. J. Roger Cheng, “Operational Vertical Bending Stresses in Rail: Real-Life Case Study,” J. Transp. Eng. Part A Syst., vol. 144, no. 3, 2018, doi: 10.1061/jtepbs.0000116.

[146] S. Fallah Nafari, M. Gül, M. T. Hendry, and J. R. Cheng, “Estimation of vertical bending stress in rails using train-mounted vertical track deflection measurement systems,” Proc. Inst. Mech. Eng. Part F J. Rail Rapid Transit, vol. 232, no. 5, pp. 1528–1538, 2018, doi: 10.1177/0954409717738444.

[147] D. Behnia, M. T. Hendry, P. Haji Abdulrazagh, and A. Wahba, “Railway Dynamic Load Factors Developed from Instrumented Wheelset Measurements,” J. Transp. Eng. Part A Syst., vol. 148, no. 7, 2022, doi: 10.1061/jtepbs.0000685.

[148] P. Konopík, J. Džugan, and R. Procházka, “Determination of fracture toughness and tensile properties of structural steels by small punch test and micro-tensile test,” Met. 2013 - 22nd Int. Conf. Metall. Mater. Conf. Proc., pp. 772–777, 2013.

[149] H. K. Oh, “Determination of fracture toughness by uniaxial tensile test,” Eng. Fract. Mech., vol. 55, no. 5, pp. 865–868, 1996, doi: 10.1016/0013-7944(96)00238-X.

[150] Y. Feng and T. Zhang, “Determination of fracture toughness of brittle materials by indentation,” Acta Mech. Solida Sin., vol. 28, no. 3, pp. 221–234, 2015, doi: 10.1016/S0894-9166(15)30010-0.

[151] J. R. Foulds, P. J. Woytowitz, T. K. Parnell, and C. W. Jewett, “Fracture Toughness by Small Punch Testing,” J. Test. Eval., vol. 23, no. 1, pp. 3–10, 1995, doi: 10.1520/JTE10392J.

[152] J. A. John Wang, F. Ren, and T. Tan, “Spiral notch torsion test use for determining fracture toughness of structural materials,” Am. Soc. Mech. Eng. Press. Vessel. Pip. Div. PVP, vol. 6, no. PARTS A AND B, pp. 119–124, 2012, doi: 10.1115/PVP2012-78782.

[153] O. W.F. Brown, Jr. (Lewis Reasearch Center, “The circumferentially notched cylindrical bar as a fracture toughness specimen,” Tech. Memo. Nasa Tm X-71551, vol. 71551, 1974.

[154] G. R. Irwin, “Onset of fast crack propagation in high strength steel and aluminum alloys,” in Naval Research Laboratory, 1956, vol. 4763, pp. 1–15.

[155] R. O. Ritchie, J. F. Knott, and J. R. Rice, “On the relationship between critical tensile stress and fracture toughness in mild steel,” J. Mech. Phys. Solids, vol. 21, no. 6, pp. 395–410, 1973, doi: 10.1016/0022-5096(73)90008-2.

[156] C. G. Go and S. E. Swartz, “Energy methods for fracture-toughness determination in concrete,” Exp. Mech., vol. 26, no. 3, pp. 292–296, 1986, doi: 10.1007/BF02320056.

[157] S. Brandstetter, H. Van Swygenhoven, S. Van Petegem, B. Schmitt, R. Maaß, and P. M. Derlet, "From micro- to macroplasticity," Adv. Mater., vol. 18, no. 12, pp. 1545–1548, 2006, doi: 10.1002/adma.200600397.

[158] N. A. Branch, G. Subhash, N. K. Arakere, and M. A. Klecka, "Material-dependent representative plastic strain for the prediction of indentation hardness," Acta Mater., vol. 58, no. 19, pp. 6487–6494, 2010, doi: 10.1016/j.actamat.2010.08.010.

[159] G. C. Sih, "Strain-energy-density factor applied to mixed mode crack problems," Int. J. Fract., vol. 10, no. 3, pp. 305–321, 1974, doi: 10.1007/BF00035493.

[160] C. T. Sun and Z.-H. Jin, "Griffith Theory of Fracture," Fract. Mech., pp. 11–24, 2012, doi: 10.1016/b978-0-12-385001-0.00002-x.

[161] Q. Han, Z. Qu, P. Wang, G. Bi, and G. Qu, "Applications of micro-indentation technology to estimate fracture toughness of shale," Materials (Basel)., vol. 13, no. 18, 2020, doi: 10.3390/MA13184208.

[162] A. A. Baron, "Indentation Determination of the Fracture Toughness of Steels at Various Temperatures," Russ. Metall., vol. 2020, no. 7, pp. 813–816, 2020, doi: 10.1134/S0036029520070022.

[163] K. P. Marimuthu, F. Rickhey, J. H. Lee, and H. Lee, "Spherical indentation for brittle fracture toughness evaluation by considering kinked-cone-crack," J. Eur. Ceram. Soc., vol. 37, no. 1, pp. 381–391, 2017, doi: 10.1016/j.jeurceramsoc.2016.08.014.

[164] F. L. Liang and C. Laird, "Control of intergranular fatigue cracking by slip homogeneity in copper I: Effect of grain size," Mater. Sci. Eng. A, vol. 117, no. C, pp. 95–102, 1989, doi: 10.1016/0921-5093(89)90090-7.

[165] M. Nagumo and H. Matsuda, "Function of hydrogen in intergranular fracture of martensitic steels," Philos. Mag. A Phys. Condens. Matter, Struct. Defects Mech. Prop., vol. 82, no. 17–18, pp. 3415–3425, 2002, doi: 10.1080/01418610208240452.

[166] W. Wang, W. Zhang, H. Wang, X. Fang, and X. Liang, "Influence of Grain Boundary on the Fatigue Crack Growth of 7050-T7451 Aluminum Alloy Based on Small Time Scale Method," Adv. Mater. Sci. Eng., vol. 2016, 2016, doi: 10.1155/2016/7671530.

[167] F. Z. Li, A. Needleman, and C. F. Shih, "Creep crack growth by grain boundary cavitation: crack tip fields and crack growth rates under transient conditions," Int. J. Fract., vol. 38, no. 4, pp. 241–273, 1988, doi: 10.1007/BF00019803.

[168] H. W. Liu and Y. Oshida, "Grain boundary oxidation and fatigue crack growth at elevated temperatures," Theor. Appl. Fract. Mech., vol. 6, no. 2, pp. 85–94, 1986, doi: 10.1016/0167-8442(86)90028-5.

[169] B. Sahoo and S. K. Panigrahi, "Low cycle fatigue behaviour of a turbine blade made of nickel base wrought alloy," Adv. Mater. Res., vol. 891–892, pp. 506–511, 2014, doi: 10.4028/www.scientific.net/AMR.891-892.506.

[170] M. A. Islam and Y. Tomota, "Fatigue strength and fracture mechanisms of IF28 steels," Adv. Mater. Res., vol. 15–17, pp. 804–809, 2007, doi: 10.4028/www.scientific.net/amr.15-17.804.

[171] H. Wu, “Toughening and strengthening mechanisms in ceramic nanocomposites,” Residual Stress. Compos. Mater., pp. 279–311, 2021, doi: 10.1016/B978-0-12-818817-0.00012-3.

[172] I. Milne, “Failure analysis in the presence of ductile crack growth,” Mater. Sci. Eng., vol. 39, no. 1, pp. 65–79, 1979, doi: 10.1016/0025-5416(79)90171-X.

[173] B. L. Bramfitt, “Structure/Property Relationships in Irons and Steels,” in Metals Handbook Desk 2nd ed., Edited by Joseph R. Davis, ASM International, 1998, pp. 153–173.

[174] P. Rama Rao, “Fracture initiation in ductile metals,” Curr. Sci., vol. 70, no. 5, pp. 358–372, 1996.

[175] G. T. Hahn and A. R. Rosenfield, “Metallurgical factors affecting fracture toughness of aluminum alloys,” Metall. Trans. A, vol. 6, no. 3, pp. 653–668, 1975, doi: 10.1007/BF02672285.

[176] F. Zhang, Y. Zhao, Y. Tan, X. Ji, and S. Xiang, “Study on the nucleation and growth of pearlite colony and impact toughness of eutectoid steel,” Metals (Basel)., vol. 9, no. 11, 2019, doi: 10.3390/met9111133.

[177] K. H. Schwalbe, “On the influence of microstructure on crack propagation mechanisms and fracture toughness of metallic materials,” Eng. Fract. Mech., vol. 9, no. 4, pp. 795–832, 1977, doi: 10.1016/0013-7944(77)90004-2.

[178] G. T. Hahn and A. R. Rosenfiled, “Relations between Microstructure and the Fracture Toughness of Metals,” Icf3, p. 20, 1973, [Online]. Available: http://www.icf-wasi.org/documents/conferences/icf3-proceedings/doc_download/2558-relations-between-microstructure-and-the-fracture-toughness-of-metals.html.

[179] G. Hahn and A. Rosenfield, “Plastic Flow in the Locale on Notches and Cracks in Fe-3Si Steel Under Conditions approaching Plane Strain,” 1968. [Online]. Available: http://www.dtic.mil/docs/citations/AD0680123.

[180] J. W. Hancock and A. C. Mackenzie, “On the mechanisms of ductile failure in high-strength steels subjected to multi-axial stress-states,” J. Mech. Phys. Solids, vol. 24, no. 2–3, pp. 147–160, 1976, doi: 10.1016/0022-5096(76)90024-7.

[181] M. Alves and N. Jones, “Influence of hydrostatic stress on failure of axisymmetric notched specimens,” J. Mech. Phys. Solids, vol. 47, no. 3, pp. 643–667, 1999, doi: 10.1016/S0022-5096(98)00060-X.

[182] A. Needleman, “A continuum model for void nucleation by inclusion debonding,” J. Appl. Mech. Trans. ASME, vol. 54, no. 3, pp. 525–531, 1987, doi: 10.1115/1.3173064.

[183] S. I. Okocha, F. Yu, P. Y. B. Jar, and M. T. Hendry, “Indentation Testing Method for Determining Mechanical Properties and Tensile Flow Curve of High-Strength Rail Steels,” Exp. Mech., vol. 63, no. 5, pp. 839–852, 2023, doi: 10.1007/s11340-023-00939-w.

[184] J. S. Lee, J. Il Jang, B. W. Lee, Y. Choi, S. G. Lee, and D. Kwon, “An instrumented indentation technique for estimating fracture toughness of ductile materials: A critical indentation energy model based on continuum damage mechanics,” Acta Mater., vol. 54, no. 4, pp. 1101–1109, 2006, doi: 10.1016/j.actamat.2005.10.033.

[185] P. W. Bridgman, “Studies in Large Plastic Flow and Fracture,” Stud. Large Plast. Flow Fract., vol. 1, no. 2, p. 146, 1964, doi: 10.4159/harvard.9780674731349.

[186] J. Lemaitre, “A continuous damage mechanics model for ductile fracture,” J. Eng. Mater. Technol. Trans. ASME, vol. 107, no. 1, pp. 83–89, 1985, doi: 10.1115/1.3225775.

[187] Y. Bao and T. Wierzbicki, “On fracture locus in the equivalent strain and stress triaxiality space,” Int. J. Mech. Sci., vol. 46, no. 1, pp. 81–98, 2004, doi: 10.1016/j.ijmecsci.2004.02.006.

[188] N. Bonora, “On the effect of triaxial state of stress on ductility using nonlinear CDM model,” Int. J. Fract., vol. 88, no. 4, pp. 359–371, 1997, doi: 10.1023/a:1007479522972.

[189] N. Bonora, G. Testa, A. Ruggiero, G. Iannitti, and D. Gentile, “Continuum damage mechanics modelling incorporating stress triaxiality effect on ductile damage initiation,” Fatigue Fract. Eng. Mater. Struct., vol. 43, no. 8, pp. 1755–1768, 2020, doi: 10.1111/ffe.13220.

[190] A. A. Benzerga and J. B. Leblond, “Ductile Fracture by Void Growth to Coalescence,” Adv. Appl. Mech., vol. 44, pp. 169–305, 2010, doi: 10.1016/S0065-2156(10)44003-X.

[191] T. Yamada and Y. Yamashita, “Ductile crack initiation behavior of prestrained steels,” Am. Soc. Mech. Eng. Press. Vessel. Pip. Div. PVP, vol. 3, pp. 505–513, 2011, doi: 10.1115/PVP2011-57294.

[192] T. Yamada, Y. Yamashita, and S. Kanna, “A study on evaluation of ductile crack initiation using strain hardening exponent for steels,” Procedia Struct. Integr., vol. 2, pp. 2206–2213, 2016, doi: 10.1016/j.prostr.2016.06.276.

[193] A. M. Beese, M. Luo, Y. Li, Y. Bai, and T. Wierzbicki, “Partially coupled anisotropic fracture model for aluminum sheets,” Eng. Fract. Mech., vol. 77, no. 7, pp. 1128–1152, 2010, doi: 10.1016/j.engfracmech.2010.02.024.

[194] Y. Bai and T. Wierzbicki, “Application of extended Mohr-Coulomb criterion to ductile fracture,” Int. J. Fract., vol. 161, no. 1, pp. 1–20, 2010, doi: 10.1007/s10704-009-9422-8.

[195] Z. Li, Y. Zhou, and S. Wang, “Influence of strain and stress triaxiality on the fracture behavior of Gb 35CrMo steel during hot tensile testing,” Adv. Mater. Sci. Eng., vol. 2018, 2018, doi: 10.1155/2018/5124524.

[196] T. Pardoen and J. W. Hutchinson, “Extended model for void growth and coalescence,” J. Mech. Phys. Solids, vol. 48, no. 12, pp. 2467–2512, 2000, doi: 10.1016/S0022-5096(00)00019-3.

[197] M. F. Kanninen, W. F. Adler, A. R. Rosenfield, and R. I. Jaffee, “Inelastic behavior of solids,” Science (80-.)., vol. 167, no. 3926, pp. 1761–1762, 1970, doi: 10.1126/science.167.3926.1761-a.

[198] R. K. Pandey and S. Banerjee, “Strain induced fracture in low strength steels,” Eng. Fract. Mech., vol. 10, no. 4, pp. 817–829, 1978, doi: 10.1016/0013-7944(78)90036-X.

[199] G. Pluvinage and J. Capelle, “On characteristic lengths used in notch fracture mechanics,” Int. J. Fract., vol. 187, no. 1, pp. 187–197, 2014, doi: 10.1007/s10704-013-9924-2.

[200] K. S. Ravichandran and A. K. Vasudevan, “Fracture Resistance of Structural Alloys,” Fatigue Fract., pp. 381–392, 2018, doi: 10.31399/asm.hb.v19.a0002379.

[201] R. JR and Tracey DM, “On the ductile enlargement of voids in triaxial stress fields,” J. Mech. Phys. Solids, vol. 17, pp. 17–201, 1969.

[202] J.R. Rice, G.F. Rosengren, “Plane strain deformation near a crack tip in a power-law hardening material”, . Mech. Phys. Solids, Vol 16, pp 1-12, 1968, https://doi.org/10.1016/0022-5096(68)90013-6.

[203] Y. Huang, “Accurate dilatation rates for spherical voids in triaxial stress fields,” J. Appl. Mech. Trans. ASME, vol. 58, no. 4, pp. 1084–1086, 1991, doi: 10.1115/1.2897686.

[204] A. M. Kanvinde and G. G. Deierlein, “The Void Growth Model and the Stress Modified Critical Strain Model to Predict Ductile Fracture in Structural Steels,” J. Struct. Eng., vol. 132, no. 12, pp. 1907–1918, 2006, doi: 10.1061/(asce)0733-9445(2006)132:12(1907).

[205] C. Feng, Z. Peng, X. Li, S. Bao, and X. Jiang, “Ductile Fracture Prediction of X80 Pipeline Steel Using Void Growth Model,” Metals (Basel)., vol. 12, no. 6, 2022, doi: 10.3390/met12060923.

[206] Y. W. Shi, “Critical void growth for ductile rupture of steel welds,” Eng. Fract. Mech., vol. 34, no. 4, pp. 901–907, 1989, doi: 10.1016/0013-7944(89)90226-9.

[207] W. M. Garrison, “A microstructural interpretation of the fracture strain and characteristics fracture distance,” Scr. Metall., vol. 18, no. 6, pp. 583–586, 1984, doi: 10.1016/0036-9748(84)90345-4.

[208] W. M. Garrison and A. W. Thompson, “Micromechanistic Expressions of Continuum Microscale Parameters for Stable Crack Growth.,” Metall. Trans. A, Phys. Metall. Mater. Sci., vol. 17 A, no. 12, pp. 2249–2253, 1986, doi: 10.1007/BF02645922.

[209] W. Conshohocken, “Standard Test Method for Measurement of Fracture Toughness 1,” Annu. B. ASTM Stand., vol. i, no. April 2000, pp. 1–56, 2001, doi: 10.1520/E1820-18AE01.

[210] M. V. Pereira, F. A. Darwish, and E. Campelo, “On the relationship between J-integral and crack tip opening displacement in elastic-plastic fracture mechanics,” J. Mater. Eng. Perform., vol. 22, no. 8, pp. 2271–2276, 2013, doi: 10.1007/s11665-013-0503-5.

[211] J. R. Kilpatrick, A. O. Benscoter, and A. R. Marder, "'Tint etching improves resolution and contrast of microstructures", Metal progress vol 100, pp 79-81, 1971.

[212] J. L McCall and W.M Mueller. Metallographic specimen preparation: optical and electron microscopy (Ed. 1), Springer New York, NY, p. 358, 2012. https://doi.org/10.1007/978-1-4615-8708-8

[213] K. B. Small, D. A. Englehart, and T. A. Christman, “Guide to etching specialty alloys,” Adv. Mater. Process., vol. 166, no. 2, pp. 32–37, 2008.

[214] F. S Lepera, “Improved etching technique for the determination of percent martensite in high-strength dual-phase steels”. Metallography. Vol 12(3), pp 263-268, 1979.

[215] C. T. Rueden and K. W. Eliceiri, “ImageJ for the Next Generation of Scientific Image Data,” Microsc. Microanal., vol. 25, no. S2, pp. 142–143, 2019, doi: 10.1017/s1431927619001442.

[216] ASTM E112-13, “Standard Test Methods for Determining Average Grain Size ASTM International: West Conshohocken, PA, USA, 2013.

[217] F. M. Burdekin and D. E. W. Stone, “The crack opening displacement approach to fracture mechanics in yielding materials,” J. Strain Anal. Eng. Des., vol. 1, no. 2, pp. 145–153, 1966, doi: 10.1243/03093247V012145.

[218] P. van Liempt and J. Sietsma, “A physically based yield criterion I. Determination of the yield stress based on analysis of pre-yield dislocation behaviour,” Mater. Sci. Eng. A, vol. 662, pp. 80–87, 2016, doi: 10.1016/j.msea.2016.03.013.

[219] F. Yu, P. Y. B. Jar, and M. Hendry, “Effect of temperature on deformation and fracture behaviour of high strength rail steel,” Eng. Fract. Mech., vol. 146, pp. 41–55, 2015, doi: 10.1016/j.engfracmech.2015.07.039.

[220] T. Børvik, O. S. Hopperstad, and T. Berstad, “On the influence of stress triaxiality and strain rate on the behaviour of a structural steel. Part II. Numerical study,” Eur. J. Mech. A/Solids, vol. 22, no. 1, pp. 15–32, 2003, doi: 10.1016/S0997-7538(02)00005-0.

[221] F. Yu, P. Y. B. Jar, and M. Hendry, “Fracture behaviour at the sharp notch tip of high strength rail steels – Influence of stress triaxiality,” Eng. Fract. Mech., vol. 178, pp. 184–200, 2017, doi: 10.1016/j.engfracmech.2017.04.034.

[222] T. S. Byun, J. W. Kim, and J. H. Hong, “A theoretical model for determination of fracture toughness of reactor pressure vessel steels in the transition region from automated ball indentation test,” J. Nucl. Mater., vol. 252, no. 3, pp. 187–194, 1998, doi: 10.1016/S0022-3115(97)00338-3.

[223] K. Wallin, “The scatter in KIC-results,” Eng. Fract. Mech., vol. 19, no. 6, pp. 1085–1093, 1984, doi: 10.1016/0013-7944(84)90153-X.

[224] H. K. D. H. Bhadeshia and A. A. B. Sugden, “Microstructural entropy and the scatter in toughness,” in Recent Trends Weld. Sci. Technol (TWR'89)’, (ed. David S A, and Vitek J M),Materials Park, OH, ASM International, pp. 745–748, 1989.

[225] S. K. Chaudhuri and R. Brook, “Influence of prior-austenite grain size and fracture mode on the fracture toughness of 12% Cr steel,” Int. J. Fract., vol. 12, no. 1, pp. 101–106, 1976, doi: 10.1007/BF00036013.

[226] E. Werner, “Influence of grain size, alloying, and cold deformation on fracture toughness,” Zeitschrift fuer Met. Res. Adv. Tech., vol. 79, no. 9, 1988.

[227] H. Couque, J.W. Duffy and, R. J. Asaro. Effects of prior austenite and ferrite grain size on fracture properties of a plain carbon steel. Technical rept (ARO 18414.6-EC), Brown University, Division of Engineering Providence, RI 02912 , 1984.

[228] J. Pacyna and A. Mazur, “Relationship between grain size and fracture toughness of tool steel,” Steel Res., vol. 57, no. 11, pp. 577–585, 1986, doi: 10.1002/srin.198600828.

[229] B. L. Bramfitt, “Structure/PropH. erty Relationships in Irons and Steels,” Met. Handb. Desk Ed., pp. 153–173, 2018, doi: 10.31399/asm.hb.mhde2.a0003090.

[230] F. P. L. Kavishe, “the Correlation of Microstructure with Strength and Fracture Toughness in Pearlitic rail steels,” PhD diss., University of London 1986.

[231] C. F. Shih, “Relationship between the J-integral and the COD for stationary and extending cracks,” J. Mech. Phys. Solids, vol. 29, no. 4, pp. 305–326, 1981.

[232] F. Liao, M. Wang, L. Tu, J. Wang, and L. Lu, “Micromechanical fracture model parameter influencing factor study of structural steels and welding materials,” Constr. Build. Mater., vol. 215, pp. 898–917, 2019, doi: 10.1016/j.conbuildmat.2019.04.155.

[233] Z. Wen, “Modeling of Ductile Fracture in Steel Structures for Monotonic and Cyclic Loading,” PhD diss., Carleton University, 2012.

[234] A. M. Kanvinde and G. G. Deierlein, “Micromechanical Simulation of Earthquake-Induced Fracture in Steel Structures,” PhD diss., Stanford University. 2004.

[235] M. F. Kanninen, W. F.Adler, A. R. Rosenfield, & R. I Jaffee, “Inelastic behavior of solids”. Science vol. 167, no. 3926, pp. 1761-1762, 1970.

[236] P. A Hess, S.J Poon, G.J Shiflet, R.H Dauskardt, “Indentation fracture toughness of amorphous steel”, Journal of materials research. 20 vol 4, pp 783-6, 2005.

[237] S. I. Okocha, F. Yu, P. Y. B. Jar, and M. T. Hendry, “Use of a modified critical fracture strain model for fracture toughness estimation of high strength rail steels,” Theor. Appl. Fract. Mech., vol. 127, 2023, doi: 10.1016/j.tafmec.2023.104069.

[238] W. Kim, S. Choi, J. Kim, S. won Jeon, M. J. Choi, and D. Kwon, “Estimation of Fracture Toughness Using Flat-Ended Cylindrical Indentation,” Met. Mater. Int., vol. 27, no. 9, pp. 3186–3194, 2021, doi: 10.1007/s12540-020-00753-2.

[239] F. Yu, J. Fang, D. Omacht, M. Sun, and Y. Li, “A new instrumented spherical indentation test methodology to determine fracture toughness of high strength steels,” Theor. Appl. Fract. Mech., vol. 124, 2023, doi: 10.1016/j.tafmec.2022.103744.

[240] F. M. Haggag, “Field indentation microprobe for structural integrity evaluation,” U.S. Patent No. 4,852,397. Washington, DC: U.S. Patent and Trademark Office. 1989.

[241] J. H. Lee, T. Kim, and H. Lee, “A study on robust indentation techniques to evaluate elastic-plastic properties of metals,” Int. J. Solids Struct., vol. 47, no. 5, pp. 647–664, 2010, doi: 10.1016/j.ijsolstr.2009.11.003.

[242] R. Hurst, Y. Li, and K. Turba, “Determination of fracture toughness from the small punch test using circular notched specimens,” Theor. Appl. Fract. Mech., vol. 103, 2019, doi: 10.1016/j.tafmec.2019.102238.

[243] G. R. Iriwn, “Structural Aspects of Brittle Fracture.,” Appl. Mater. Res., vol. 3, no. 2, pp. 65–81, 1964.

[244] C. D. Wilson and J. D. Landes, “Fracture toughness testing with notched round bars,” in ASTM Special Technical Publication, 1999, no. 1360, pp. 69–82, doi: 10.1520/stp13396s.

[245] I. The Aluminum Association, “Aluminum 2024-T4; 2024-T351,” Aluminum Standards and Data 2000. https://asm.matweb.com/search/SpecificMaterial.asp?bassnum=ma2024t4.

[246] W. D. Pilkey, “Peterson’s Stress Concentration Factors”(2nd Ed.), John Wiley & Sons, p.544, 1997.

[247] Y. Murakami, “Theory of elasticity and stress concentration” (1st Ed.), John Wiley & Sons, p.818, 2016.

[248] C. S. Shin, K. C. Man, and C. M. Wang, “A practical method to estimate the stress concentration of notches,” Int. J. Fatigue, vol. 16, no. 4, pp. 242–256, 1994, doi: 10.1016/0142-1123(94)90338-7.

[249] J. H. Lee, Y. Gao, A. F. Bower, H. Xu, and G. M. Pharr, “Stiffness of frictional contact of dissimilar elastic solids,” J. Mech. Phys. Solids, vol. 112, pp. 318–333, 2018, doi: 10.1016/j.jmps.2017.12.010.

[250] B. Riccardi and R. Montanari, “Indentation of metals by a flat-ended cylindrical punch,” Mater. Sci. Eng. A, vol. 381, no. 1–2, pp. 281–291, 2004, doi: 10.1016/j.msea.2004.04.041.

[251] H. Y. Yu, M. A. Imam, and B. B. Rath, “Study of the deformation behaviour of homogeneous materials by impression tests,” J. Mater. Sci., vol. 20, no. 2, pp. 636–642, 1985, doi: 10.1007/BF01026536.

[252] Y. C. Lu, S. N. V. R. K. Kurapati, and F. Yang, “Finite element analysis of cylindrical indentation for determining plastic properties of materials in small volumes,” J. Phys. D. Appl. Phys., vol. 41, no. 11, 2008, doi: 10.1088/0022-3727/41/11/115415.

[253] J. Won, S. Kim, O. M. Kwon, Y. C. Kim, and D. Kwon, “Evaluation of tensile yield strength of high-density polyethylene in flat-ended cylindrical indentation: An analytic approach based on the expanding cavity model,” J. Mater. Res., vol. 35, no. 2, pp. 206–214, 2020, doi: 10.1557/jmr.2019.387.

[254] Z. Hu, K. Lynne, and F. Delfanian, “Characterization of materials’ elasticity and yield strength through micro-/nano-indentation testing with a cylindrical flat-tip indenter,” J. Mater. Res., vol. 30, no. 4, pp. 578–591, 2015, doi: 10.1557/jmr.2015.4.

[255] A. R. H. Midawi, C. H. M. Simha, and A. P. Gerlich, “Novel techniques for estimating yield strength from loads measured using nearly-flat instrumented indenters,” Mater. Sci. Eng. A, vol. 675, pp. 449–453, 2016, doi: 10.1016/j.msea.2016.08.056.

[256] G. Eason and R. T. Shield, “The plastic indentation of a semi-infinite solid by a perfectly rough circular punch,” Zeitschrift für Angew. Math. und Phys. ZAMP, vol. 11, no. 1, pp. 33–43, 1960, doi: 10.1007/BF01591800.

[257] W. Yu and J. P. Blanchard, “An elastic-plastic indentation model and its solutions,” J. Mater. Res., vol. 11, no. 9, pp. 2358–2367, 1996, doi: 10.1557/JMR.1996.0299.

[258] M. Mata, O. Casals, and J. Alcalá, “The plastic zone size in indentation experiments: The analogy with the expansion of a spherical cavity,” Int. J. Solids Struct., vol. 43, no. 20, pp. 5994–6013, 2006, doi: 10.1016/j.ijsolstr.2005.07.002.

[259] ASTM E18, “Standard test methods for Rockwell hardness of metallic materials,” 2008.

[260] K. F. Quach, W. M., Teng, J. G., & Chung, “Three-stage full-range stress-strain model for stainless steels,” J. Struct. Eng., vol. 134, no. 9, 2008, doi: https://doi.org/10.1061/(ASCE)0733-9445(2008)134:9(1518).

[261] M. Kamaya, “Ramberg-Osgood type stress-strain curve estimation using yield and ultimate strengths for failure assessments,” Int. J. Press. Vessel. Pip., vol. 137, pp. 1–12, 2014, doi: 10.1016/j.ijpvp.2015.04.001.

[262] R. Walter and William R. Osgood, “Description of stress-strain curves by three parameters,” Natl. Advis. Comm. Aeronaut., pp. 1–29, 1943, [Online]. Available: http://www.apesolutions.com/spd/public/NACA-TN902.pdf.

[263] K. -H Schwalbe and B. Neale, “A Procedure for Determining the Fracture Behaviour of Materials—the Unified Fracture Mechanics Test Method Efam Gtp 94,” 1995. doi: 10.1111/j.1460-2695.1995.tb01185.x.

[264] C. D. Wilson, "Fracture Toughness Testing with Notched Round Bars. " PhD diss., University of Tennessee, 1997.

https://trace.tennessee.edu/utk_graddiss/2512

[265] J. R. Davis, “Alloying: understanding the basics,” ASM International, pp. 193–202, 2001. https://doi.org/10.31399/asm.tb.aub.9781627082976

[266] J. Sun, Y. Xu, and L. Wang, “Evaluation of the Elastic Modulus and Plateau Stress of a 2D Porous Aluminum Alloy Based on a Convolutional Neural Network,” Metals (Basel)., vol. 13, no. 2, 2023, doi: 10.3390/met13020284.

[267] B. Bahrami Babamiri, H. Askari, and K. Hazeli, “Deformation mechanisms and post-yielding behavior of additively manufactured lattice structures,” Mater. Des., vol. 188, 2020, doi: 10.1016/j.matdes.2019.108443.

[268] N. A. Noda, M. Sera, and Y. Takase, “Stress concentration factors for round and flat test specimens with notches,” Int. J. Fatigue, vol. 17, no. 3, pp. 163–178, 1995, doi: 10.1016/0142-1123(95)98937-X.

[269] X. Xu, T. W. J. Kwok, P. Gong, and D. Dye, “Tailoring the deformation behaviour of a medium Mn steel through isothermal intercritical annealing,” Materialia, vol. 22, 2022, doi: 10.1016/j.mtla.2022.101422.

[270] S. F. Gharaibeh and A. Aburub, “Use of first derivative of displacement vs. force profiles to determine deformation behavior of compressed powders,” AAPS PharmSciTech, vol. 14, no. 1, pp. 398–401, 2013, doi: 10.1208/s12249-013-9928-2.

[271] K. L. Murty and M. D. Mathew, “Nondestructive monitoring of structural materials using automated ball indentation (ABI) technique,” Nucl. Eng. Des., vol. 228, no. 1–3, pp. 81–96, 2004, doi: 10.1016/j.nucengdes.2003.06.006.

[272] H. Fadil, D. Jelagin, and M. N. Partl, “Spherical indentation test for quasi-non-destructive characterisation of asphalt concrete,” Mater. Struct. Constr., vol. 55, no. 3, 2022, doi: 10.1617/s11527-022-01945-5.

[273] A. Karimzadeh, S. S. R. Koloor, M. R. Ayatollahi, A. R. Bushroa, and M. Y. Yahya, “Assessment of Nano-Indentation Method in Mechanical Characterization of Heterogeneous Nanocomposite Materials Using Experimental and Computational Approaches,” Sci. Rep., vol. 9, no. 1, 2019, doi: 10.1038/s41598-019-51904-4.

[274] H. Mei, H. Q. Li, J. X. Tao, and L. F. Cheng, “Non-destructive investigation of quasi-static indentation damage to C/SiC composites and its effects on compressive properties,” Adv. Appl. Ceram., vol. 111, no. 8, pp. 495–501, 2012, doi: 10.1179/1743676112y.0000000044.

[275] F. Cellini, Y. Gao, and E. Riedo, “Å-Indentation for non-destructive elastic moduli measurements of supported ultra-hard ultra-thin films and nanostructures,” Sci. Rep., vol. 9, no. 1, 2019, doi: 10.1038/s41598-019-40636-0.

[276] T. L. Anderson and D. A. Osage, “API 579: A comprehensive fitness-for-service guide,” Int. J. Press. Vessel. Pip., vol. 77, no. 14–15, pp. 953–963, 2000, doi: 10.1016/S0308-0161(01)00018-7.

[277] S. K. Kang, Y. C. Kim, K. H. Kim, J. Y. Kim, and D. Kwon, “Extended expanding cavity model for measurement of flow properties using instrumented spherical indentation,” Int. J. Plast., vol. 49, pp. 1–15, 2013, doi: 10.1016/j.ijplas.2013.02.014.

[278] S. I. Okocha, F. Yu, P.-Y. B. Jar, and M. T. Hendry, “Fracture Toughness Estimation of High strength allloys using Flat-end Cylindrical Indenter Via Modified Limit Load Analysis, Engineering Fracture Mechanics,” Eng. Fract. Mech. (to be submitted)

[279] X. L. Gao, “An expanding cavity model incorporating strain-hardening and indentation size effects,” Int. J. Solids Struct., vol. 43, no. 21, pp. 6615–6629, 2006, doi: 10.1016/j.ijsolstr.2006.01.008.

[280] X. lin Gao, “An exact elasto-plastic solution for an open-ended thick-walled cylinder of a strain-hardening material,” Int. J. Press. Vessel. Pip., vol. 52, no. 1, pp. 129–144, 1992, doi: 10.1016/0308-0161(92)90064-M.

[281] X. L. Gao, X. N. Jing, and G. Subhash, “Two new expanding cavity models for indentation deformations of elastic strain-hardening materials,” Int. J. Solids Struct., vol. 43, no. 7–8, pp. 2193–2208, 2006, doi: 10.1016/j.ijsolstr.2005.03.062.

[282] ASTM E140-07, “Standard Hardness Conversion Tables for Metals Relationship Among Brinell Hardness, Vickers Hardness, Rockwell Hardness, Superficial Hardness, Knoop Hardness, and Scleroscope Hardness,” ASTM International, 2013.

[283] M. H. Sharobeam and N. J. Pomona, “The load separation technique in the elastic-plastic fracture analysis of two- and three- dimensional geometries,” In NASA Conference Publication 7274, FAA/NASA International Symposium on Advanced Structural Integrity Methods for Airframe Durability and Damage Tolerance , pp. 703–724, 1994.

[284] U. Zerbs, K. Mädler, & H. Hintze, “Fracture Mechanics in Railway Application,” An overview. Engng Fract Mech Vol 72, no. 2, pp. 1–46, 2004.

[285] J. M. Hyzak and I. M. Bernstein, “The role of microstructure on the strength and toughness of fully pearlitic steels,” Metall. Trans. A, vol. 7, no. 8, pp. 1217–1224, 1976, doi: 10.1007/BF02656606.

[286] S. S. Sahay, G. Mohapatra, and G. E. Totten, “Overview of pearlitic rail steel: Accelerated cooling, quenching, microstructure and mechanical properties,” J. ASTM Int., vol. 6, no. 7, 2009, doi: 10.1520/JAI102021.

[287] J. Plu, S. Bondeux, D. Boulanger, and R. Heyder, “Application of fracture mechanics methods to rail design and maintenance,” Eng. Fract. Mech., vol. 76, no. 17, pp. 2602–2611, 2009, doi: 10.1016/j.engfracmech.2009.02.025.

[288] R. R. Porcaro, G. L. Faria, L. B. Godefroid, G. R. Apolonio, L. C. Cândido, and E. S. Pinto, “Microstructure and mechanical properties of a flash butt welded pearlitic rail,” J. Mater. Process. Technol., vol. 270, pp. 20–27, 2019, doi: 10.1016/j.jmatprotec.2019.02.013.

[289] L. B. Godefroid, G. L. Faria, L. C. Cândido, R. M. Santos, and T. C. G. Vilela, “Mechanical properties of two different pearlitic steels for railroad application,” ICF 2017 - 14th Int. Conf. Fract., vol. 1, pp. 263–264, 2017.

[290] L. B. Godefroid, A. T. Souza, and M. A. Pinto, “Fracture toughness, fatigue crack resistance and wear resistance of two railroad steels,” J. Mater. Res. Technol., vol. 9, no. 5, pp. 9588–9597, 2020, doi: 10.1016/j.jmrt.2020.06.092.

[291] P. Yilmazer, A. Amini, and M. Papaelias, “The structural health condition monitoring of rail steel using acoustic emission techniques,” 51st Annu. Conf. Br. Inst. Non-Destructive Test, Northamptonshire, UK, pp. 51–62, 11-13 sept, 2012.

[292] K. Morton, D. F. Cannon, P. Clayton, and E. G. Jones, "The Assessment of Rail Steels," Rail Steels—Developments, Processing, and Use, ASTM STP 644, D. H. Stone and G. G. Knupp, Ed., American Society for Testing and Materials, Denver, Colo., 17-18 Nov 1978, pp. 80-98.

[293] K. Wang, X. Zhang, S. Song, Y. Wang, Y. Shen, and P. D. Wilcox, “Rail Steel Health Analysis Based on a Novel Genetic Density-based Clustering Technique and Manifold Representation of Acoustic Emission Signals,” Appl. Artif. Intell., vol. 36, no. 1, 2022, doi: 10.1080/08839514.2021.2004346.

[294] E. Sheinman, “Wear of rails. A review of the American press,” J. Frict. Wear, vol. 33, no. 4, pp. 308–314, 2012, doi: 10.3103/S1068366612040101.

[295] AREMA, Manual for Railway Engineering (MRE), American Railway Engineering and Maintenance-of-Way Association, 2010, Chapter 4.

[296] H. Li, J. Sun, and G. Zhao, “Research on rail wear of small radius curve in EMU depot,” Railw. Sci., vol. 1, no. 1, pp. 16–39, 2022, doi: 10.1108/rs-04-2022-0014.

[297] S. Mojumder, K. Mishra, K. Singh, C. Qiu, P. Mutton, and A. Singh, “Microstructural investigation along the transverse section of the lower gauge corner flow lips formed in high rails of mild curves,” Wear, vol. 494–495, 2022, doi: 10.1016/j.wear.2022.204267.

[298] T. Jendel and M. Berg, “Prediction of Wheel Profile Wear,” Veh. Syst. Dyn., vol. 37, no. sup1, pp. 502–513, 2002, doi: 10.1080/00423114.2002.11666258.

[299] U. Olofsson and T. Telliskivi, “Wear, plastic deformation and friction of two rail steels - A full-scale test and a laboratory study,” Wear, vol. 254, no. 1–2, pp. 80–93, 2003, doi: 10.1016/S0043-1648(02)00291-0.

[300] S. Mojumder, H. Su, C. Qiu, P. Mutton, A. Singh, and W. Yan, “The role of bending stress on the initiation of reverse transverse defects,” in Proceedings of the Institution of Mechanical Engineers, Part F: Journal of Rail and Rapid Transit, 2021, vol. 235, no. 1, pp. 61–72, doi: 10.1177/0954409720904329.

[301] S. Mojumder, K. Mishra, K. Singh, C. Qiu, P. Mutton, and A. Singh, “Effect of track curvature on the microstructure evolution and cracking in the longitudinal section of lower gauge corner flow lips formed in rails,” Eng. Fail. Anal., vol. 135, 2022, doi: 10.1016/j.engfailanal.2022.106117.

[302] A. Ekberg, “Surface fatigue initiated transverse defects and broken rails- an International Review,” pp. 1–24, Research report, Gothenburg, Sweden 2014.

[303] G. Testa, N. Bonora, A. Ruggiero, G. Iannitti, and D. Gentile, “Stress triaxiality effect on cleavage fracture stress,” Theor. Appl. Fract. Mech., vol. 109, 2020, doi: 10.1016/j.tafmec.2020.102689.

[304] “Carbide Probes Inc.” https://www.carbideprobes.com/wp-content/uploads/2019/07/TungstenCarbideDataSheet.pdf.

Appendix 1-Stress Beneath the Surface of A Semi-Infinite, Elastic Plastic Material Indented with A Rigid Sphere

$$\frac{\sigma_r}{p_m}=\frac{3}{2}\left\{\frac{1-2v_s}{3}\frac{a^2}{r^2}\left[1-\left(\frac{z}{u^{1/2}}\right)^3\right]+\left(\frac{z}{u^{1/2}}\right)^3\frac{a^2u}{u^2+a^2z^2}+\left(\frac{z}{u^{1/2}}\right)\left[u\frac{1-v_s}{a^2+u}+(1+v_s)\frac{u^{1/2}}{a}\tan^{-1}\left(\frac{a}{u^{1/2}}\right)-2\right]\right\} \quad \text{(A1.1)}$$

$$\frac{\sigma_\theta}{p_m}=-\frac{3}{2}\left\{\frac{1-2v_s}{3}\frac{a^2}{r^2}\left[1-\left(\frac{z}{u^{1/2}}\right)^3\right]+\left(\frac{z}{u^{1/2}}\right)\left[u\frac{1-v_s}{a^2+u}+(1+v_s)\frac{u^{1/2}}{a}\tan^{-1}\left(\frac{a}{u^{1/2}}\right)+2v_s\right]\right\} \quad \text{(A1.2)}$$

$$\frac{\sigma_z}{p_m}=-\frac{3}{2}\left(\frac{z}{u^{1/2}}\right)^3\frac{a^2u}{u^2+a^2z^2} \quad \text{(A1.3)}$$

$$\frac{\tau_{zr}}{p_m}=-\frac{3}{2}\left(\frac{rz^2}{u^2+a^2z^2}\right)\left(\frac{a^2u^{1/2}}{a^2+u}\right) \quad \text{(A1.4)}$$

Where p_m is the mean pressure beneath the indenter;

$$u=\frac{1}{2}\left[\left(r^2+z^2-a^2\right)+\left[\left(r^2+z^2-a^2\right)^2+4a^2z^2\right]^{1/2}\right]$$

The principal stresses in the r_z plane can be expressed as:

$$\sigma_{1,3}=\frac{\sigma_r+\sigma_z}{2}\pm\left[\left(\frac{\sigma_r-\sigma_z}{2}\right)^2+\tau_{zr}^2\right]^{1/2} \quad \text{(A1.5)}$$

$$\sigma_2=\sigma_\theta \quad \text{(A1.6)}$$

The maximum stress occur on the z axis and the corresponding principal stresses can be expressed as:

$$\sigma_1=\sigma_2=\sigma_x=\sigma_y=-p_{\max}\left[\left(1-|\xi_a|\right)\tan^{-1}\left(\frac{1}{\xi_a}\right)\right](1+v)-\frac{1}{2(1+\xi_a^2)} \quad \text{(A1.7)}$$

$$\sigma_3=\sigma_z=\frac{-p_{\max}}{1+\xi_a^2} \quad \text{(A1.8)}$$

where: ξ_a=z/a: a non-dimensional parameter for depth below the surface

Appendix 2- Development of the Plastic Diameter After Unloading

If ρ is the radius of the plastic indent and R is the radius of the indenter, the plastic indentation depth (h_p)

$$h_p = \rho - \sqrt{\rho^2 - a^2} \quad \text{and} \quad \frac{1}{\rho} = \frac{2h_p}{h_p^2 + a^2} \tag{A2.1}$$

From the elastic hertzian contact theory:

$$\frac{1}{R} - \frac{1}{\rho} = \frac{3P}{4a^3 E_r} \tag{A2.2}$$

$$a = \left[\frac{3PR(h_P^2 + a^2)}{4E_r(h_P^2 + a^2 - 2h_p R)} \right]^{1/3}$$

Taking a =d_p/2, R=D/2

$$d_p = \left\{ \left[3PD\left(4h_p^2 + d_p^2\right) \right] / \left[E_r\left(4h_p^2 + d_p^2 - 4h_p D\right) \right] \right\}^{1/3} \tag{A2.3}$$

Appendix 3- Damage Initiation Threshold Strain

Repeated loading-unloading smooth tensile tests were conducted to determine if there was a deterioration of the Young's Modulus by calculating the slope of the unloading curve as seen in Figure A1 (a). Figure A1(b) also shows the degradation of the Modulus using the smooth tensile specimen, which occurred way before the necking strain and closely at the onset of plastic strain. This supports the theory of material behaviour, where damage can occur before or at the onset of necking depending on the material of study.

Finite element modelling of smooth tensile and short-gauge notched specimen were conducted showing variation of damage evolution as a function of equivalent plastic strain from the elements located at the centre, quarter of diameter from the centre, and along the circumference on the minimum cross section of smooth specimen and short, notched gauge was conducted. It is shown that the damage initiation occurs from equivalent strains, where three curves of damage evolution overlap with each other during the uniform deformation and deviate around the necking strain for the smooth tensile specimen. This means that the nucleation strain is insensitive to stress triaxiality (i.e. γ =0). Also, for the short, notched gauge specimen, where stress triaxiality plays a larger role, it is shown that the damage initiation occurred from equivalent strains close to 0.002 as seen in

Figure A2(b). Although stress triaxiality affects the p_{th}, the value is close to ε_{th} for our study. Hence, we then assumed 0.002 for both p_{th} and ε_{th} as a conservative value for the damage threshold strain [232] for high multiaxial stress states. However, the γ at high stress triaxiality needs more study.

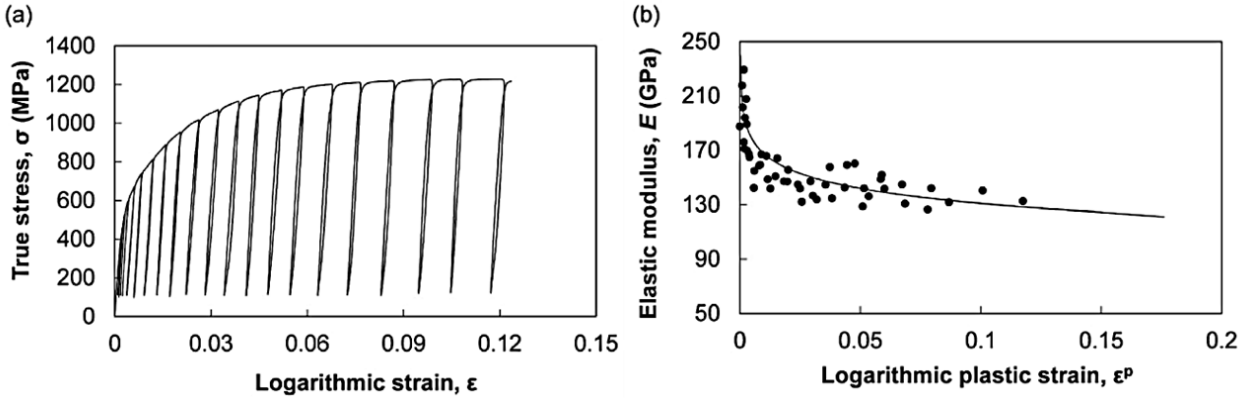

Figure A3.1Results from the experiment of loading-unloading smooth tensile tests: (a) true stress-logarithmic strain curve, and (b) calibration of damage parameter using deterioration of the elastic Modulus [232].

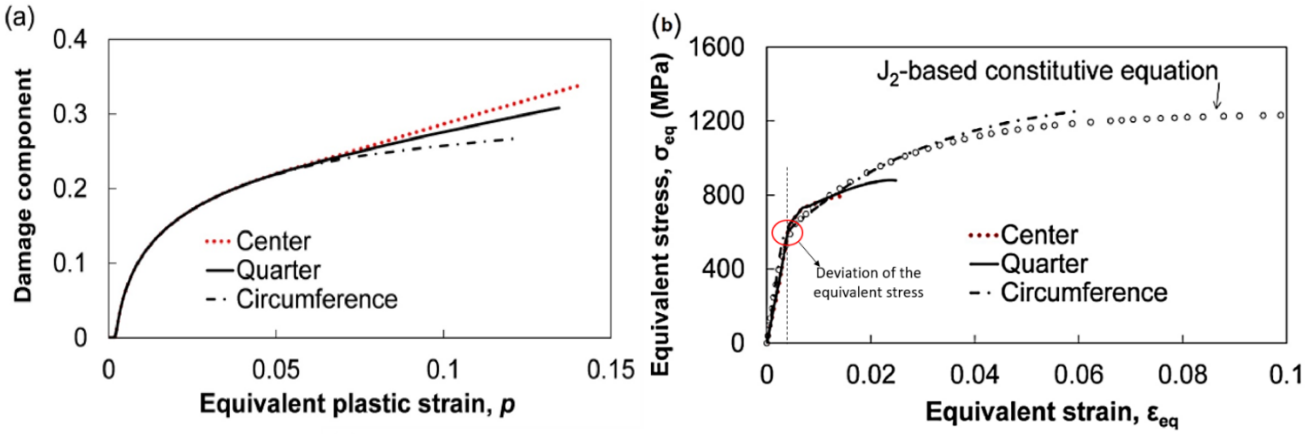

Figure A.3.2 Equivalent plastic strain evolution of tensile tests: (a) Smooth tensile testing, and (b) Short gauge notched specimen [232].

$$\varepsilon_{eq}^{f,\eta_{avg}} = \frac{p_{th}}{f\left(\eta_{avg}\right)^{\gamma}}\left(\frac{n}{\varepsilon_{th}}\right)^{\frac{1}{f\left(\eta_{avg}\right)^{1-\gamma}}} \qquad \text{A(3.1)}$$

Since $\gamma = 0$ (is assumed for this study), A3.1 reduces back to A3.2

$$\varepsilon_{eq}^{f,\eta_{avg}} = p_{th}\left(\frac{\varepsilon_f^*}{\varepsilon_{th}}\right)^{\frac{1}{f\left(\eta_{avg}\right)}} \qquad \text{A(3.2)}$$

Since, p_{th} would depend on η especially at very high η, the particle separation would occur when an interface strength, σ_c, reaches a critical value [177, 233]. This σ_c would depend on the mean stress (stress triaxiality) and the von Mises stress.

$$\sigma_c = \sigma_{eq}\left(1 + c\eta\right) \qquad \text{A(3.3)}$$

where $0 \leq c \leq 1$

From the outcome of p_{th} in [232], it can be speculated that c would contribute very little ($c \rightarrow 0$) to the de-bonding of the particle from the rail steels' matrix. This can be based of manufacturing constituents and because the material deformation of the rail steel at that plastic strain (ε_{th}), follows a different constitutive equation [73, 104, 119] (Ogden model), where plastic regime has not been fully attained (transition between elastic and plastic) unlike the assumption of the material behaviour in the studies in [183, 237]. So plastic strain would be contributing less to the overall equivalent strain and thus the η. However, at larger equivalent strains, plastic strain and η increases contributing to the damage evolution while very limited plastic strain surrounding the particle in the matrix contributes to the debonding mechanism. Hence, the void nucleation using a micromechanical model in which particle–matrix separation occurs by failure of a cohesive interface needs to be further studied for the rail steels as proposed in the works of Testa et al. [303].

$$p_{th} = C_1 \exp\left(-\frac{4}{3}\eta\right) + C_2 \qquad \text{A(3.4)}$$

where C_2 is the minimum p_{th} expected at extremely high stress triaxiality and C_1 is a fitting parameter.

Appendix 4 Mesh Sensitivity Analysis

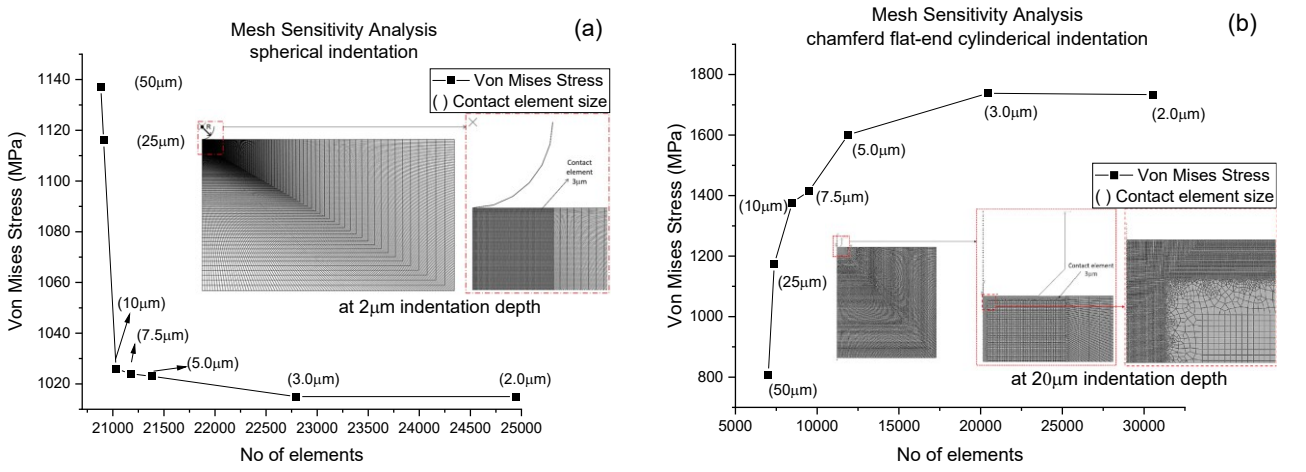

Figure A.4.1 Mesh sensitivity analysis of indentation testing: (a) spherical indenter; (b) Chamfered indenter

Appendix 5 Force-Cmod For 9 Rail Steels

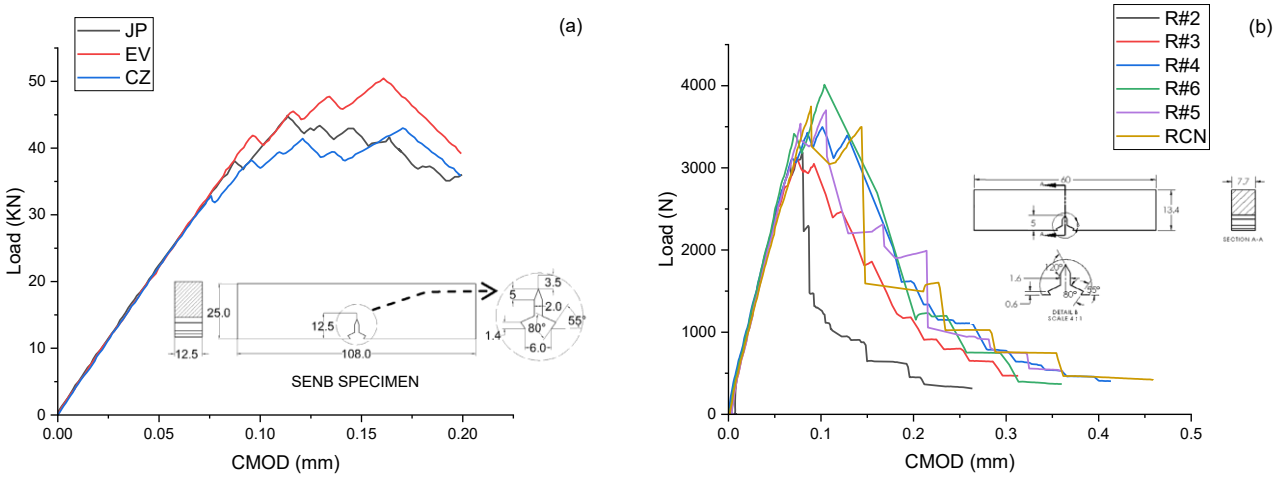

Figure A.5.1Force to CMOD curve for the rail steels: (a) company CN rail steels, and (b) company COMPX rail steels [73, 119]

Appendix 6 Indentation Force-Depth Curves For 9 Rail Steels

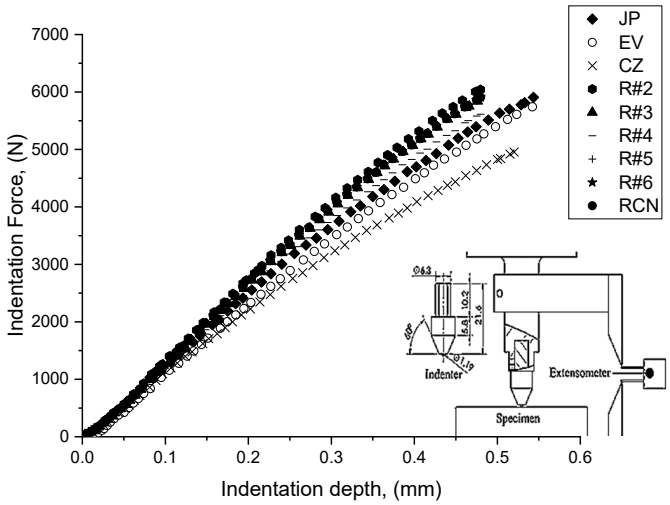

Figure A.6.1 Indentation force to depth loading curve for the 9 rail steels

Appendix 7 Stress-Strain Curves For 9 Rail Steels

Tensile tests were conducted on smooth dog-bone specimens in the longitudinal direction of the rail steels following the recommendations of ASTM E8/E8M. The stress-strain were done in ambient temperature and a crosshead speed of 8.5×10^{-3}mm/s, equivalent to an initial strain rate of 2.36×10^{-4}/s. The outcome of the test showed an obvious necking of the specimen with dimples appearing the fracture surface. This is evident that the fracture was governed by ductile failure mechanism at a low stress triaxiality such as that experienced in smooth tensile tests. However, for SENB specimen, where high stress triaxiality is experienced, in Figure 3.8, brittle cleavage fracture is stimulated and at the same time dimple formation an otherwise ductile fracture mechanism [234, 235].

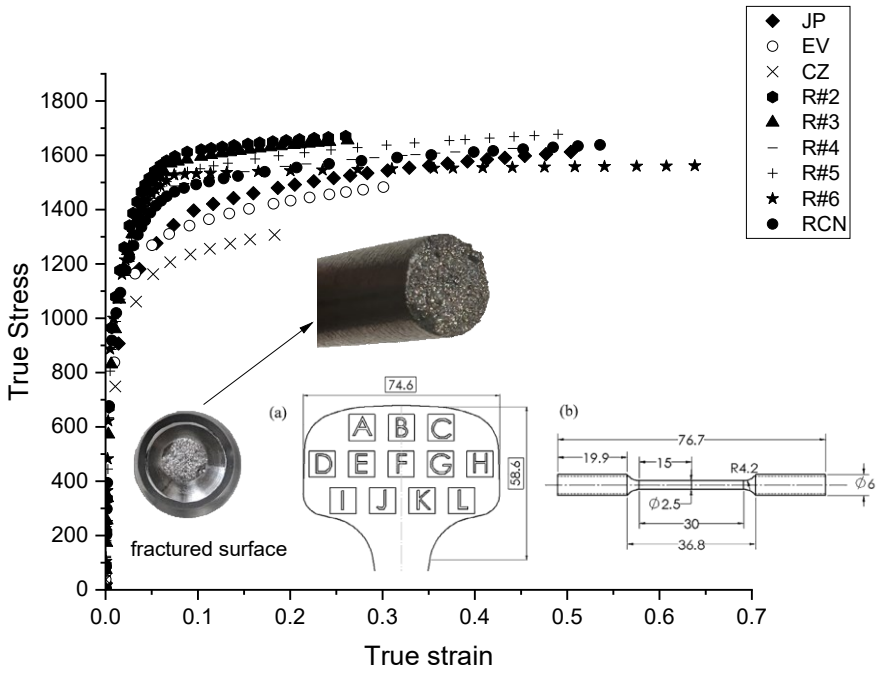

Figure A.7.1 True stress to strain curve for the 9 rail steels

Appendix 8 Load Frame Compliance Calibration

The load frame compliance, C_f, of the indentation testing system used in this study was calibrated using a CZ rail steel block a Brinell hardness of 289 MPa (HBW 10/3000) and a Young's modulus of 195GPa. The indentation tests were conducted using a the different indenter sizes and types with a maximum force of 2000N for both the rail steel and the aluminum Figure A7(a) shows results from an indentation loading-unloading test, where the unloading curves are best fit using a power-law function, $L=A(h-h_{cf})^m$, in which A, h_{cf} and m are fitting parameters determined using the least squares fitting method. The properties of tungsten carbide were accessed from Carbide probes Inc. [304]

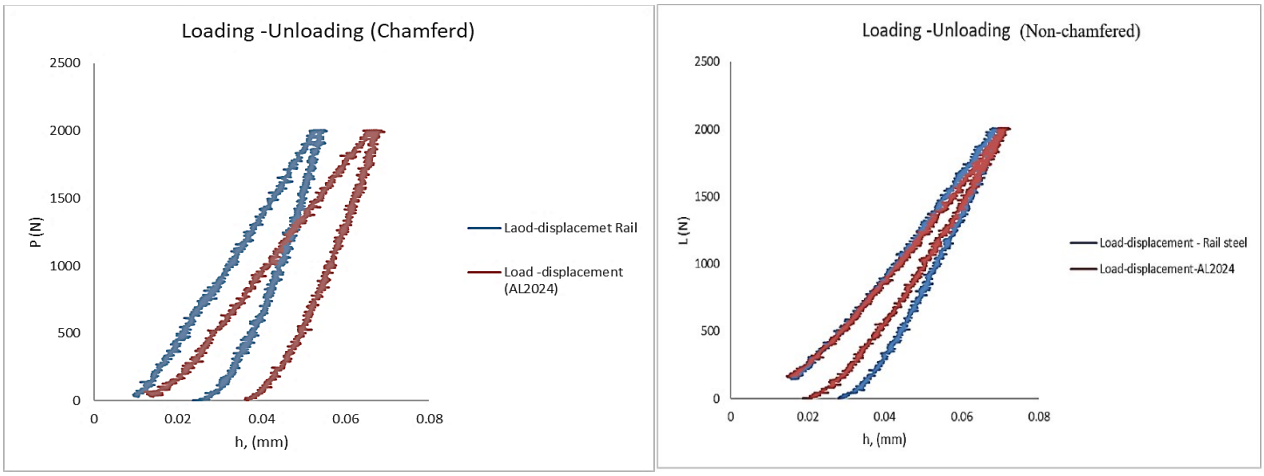

Figure A8.1 Loading-unloading of AL2024-T351 and steel used for load frame compliance estimation: (a) chamfered flat-end indenter; (b) non-chamfered flat-end indenter

From both materials and both tests, the total compliance, C_T was calculated, and the difference was employed to calculate the load frame compliance, C_f on the assumption that the CT attained from the rail steel is approximated to the compliance of the MTS machine since the base platform for testing materials was made using high strength steel similar to the CZ rail steel with approximately similar modulus and hardness. Hence, $\boldsymbol{C_f = C_{T(AL2024)} - C_{T(rail)}}$. Table A.1 C_f of the different indenters used. Once the compliance of the specimen, C_s, is attained the young's modulus for the rail steel can be calculated using Eq. (4.7) as well as for the AL2024-T351 specimens.

Table A.1. Summary of the load-frame compliance outcome for each indenter

Compliance(mm/N)	**3mm (CH)**	**5mm (CH)**	**6.35mm (CH)**	**3mm (F)**	**5mm (F)**	**6.35mm (F)**
$\boldsymbol{C_{T(AL2024)}}$	1.05E-05	1.31E-05	1.34E-05	1.19E-05	1.29E-05	1.39E-05
$\boldsymbol{C_{T(rail)}}$	7.68E-06	8.58E-06	9.89E-06	6.05E-06	6.10E-06	6.21E-06
$\boldsymbol{C_f}$	6.40E-07	2.13E-06	4.20E-06	5.85E-06	6.80E-06	7.69E-06

Appendix 9 Smoothening Operation Using the LOWESS Approach

The experimental data were smoothened using one of the signal processing smoothening techniques. We found that the locally weighted scatterplot smoothing (LOWESS) approach provided a mean value of the high and low experimental peak results due to experimental noises created from the MTS equipment. A span of 0.1 was used in the smoothening approach as seen in Figure A.9.

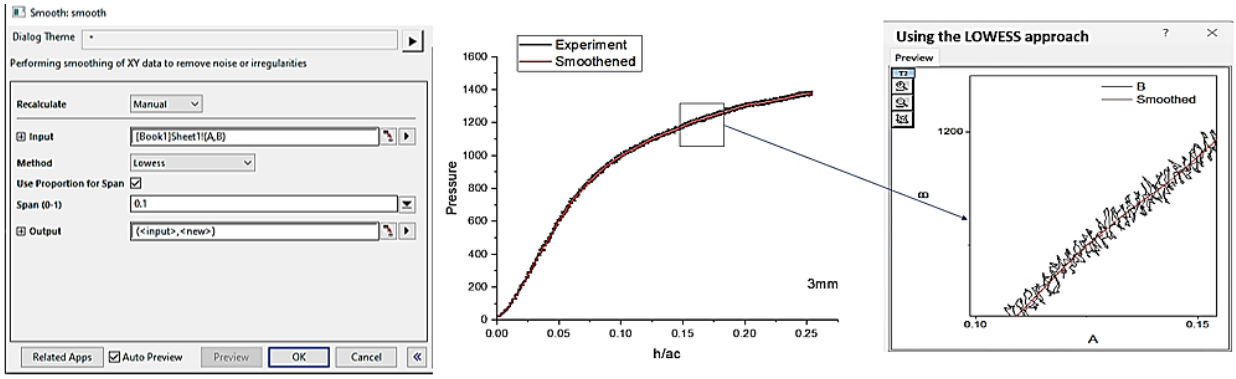

Figure A.9.1 A sample of the smoothing operation for an indentation test with a 3mm chamfered indenter

Appendix 10 Difference In h_{ECM} -h/a_c with P-h/a_c and the Application OF κ

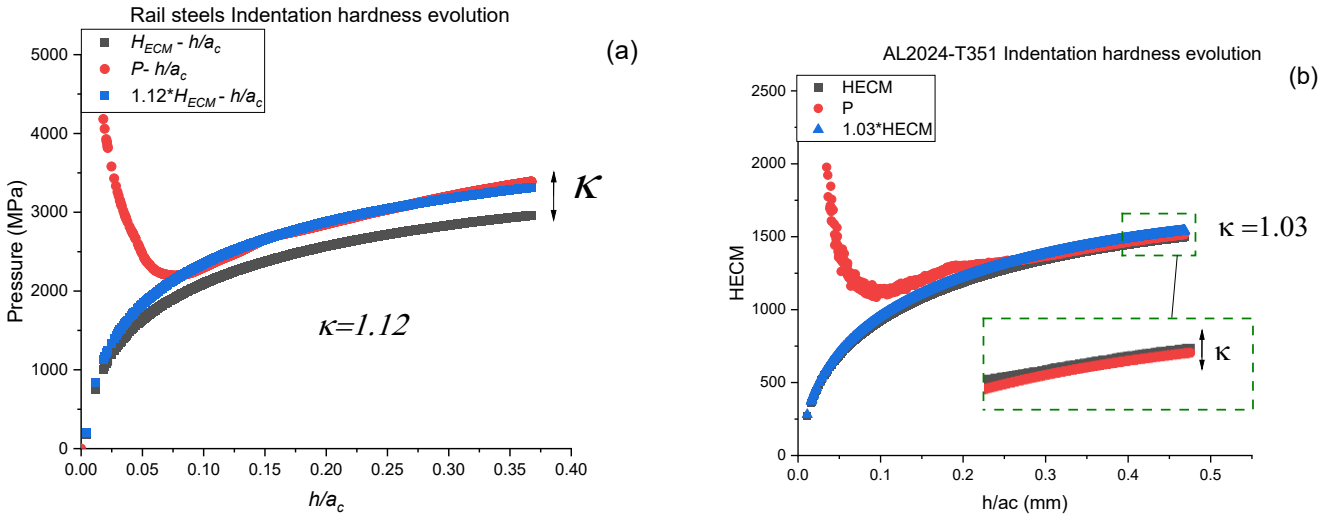

Figure A9.1 κ as a fitting parameter for H_{ECM} -h/a_c with P-h/a_c: *(a) JP and (b) AL2024-T351*

Appendix 11 Hardness Estimation of AL2024-T351

TEST (HRB)	1	2	3	4	5	6	Mean (Std.dev)	BHN (Std.dev)
Specimen 1	77	76.5	77.5	77.25	77.5	77.5	77.21 (0.37)	139.42 (0.73)
Specimen 2	76.5	77.25	77.25	77.5	77.25	77	77.13 (0.31)	139.25 0.63)

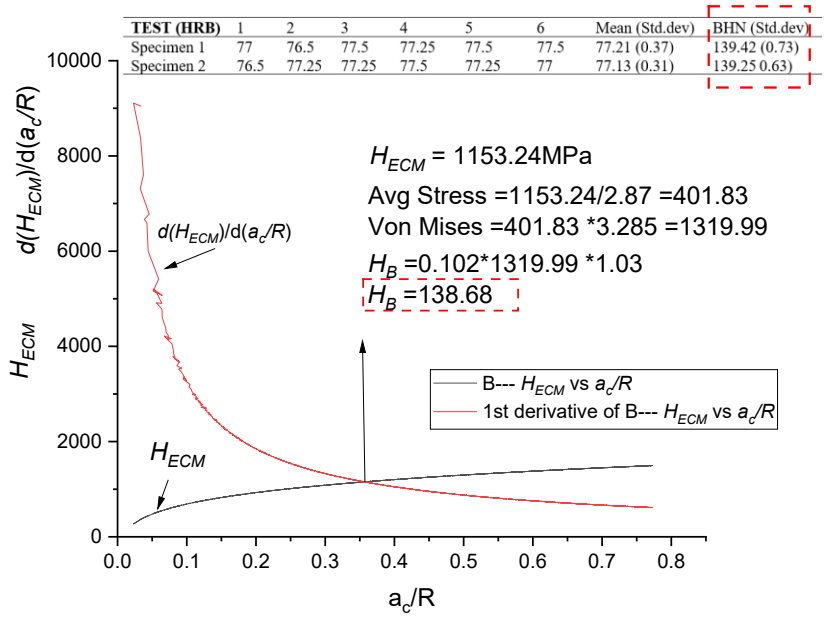

Figure A.11.1 Brinell hardness estimation via 1st derivative of H_{ECM} vs a_c/R for AL2024-T351